Design, Development and Structure of Liquid and Solid Electrolytes for Lithium Batteries

Hilal Al-Salih

Thesis submitted to the University of Ottawa
in partial Fulfillment of the requirements for the Degree of Doctor of Philosophy

Department of Chemical and Biological Engineering

Faculty of Engineering

University of Ottawa

Abstract

Energy storage is crucial for intermittent renewable energy sources, electric vehicles, and portable devices. The continuously increasing energy consumption in these industries necessitates the enhancement of commercial lithium-ion batteries (LIB), especially regarding their safety and energy density. Historically, aqueous electrolytes were the norm in the battery industry. Prior to the development of lithium batteries, most commercially significant batteries used water as the solvent. In the past decade, "highly concentrated" electrolytes resurrected the notion of an aqueous lithium-ion battery (ALIB). Significant efforts have been made since then to comprehend the interfacial stability of these high-concentration electrolytes, and make them suitable for use in batteries especially high voltage ones. Another candidate for future batteries is All-Solid-State Batteries (ASSB) as they have the potential to double, or even triple, the energy density figures we currently achieve in LIBs mainly due to their ability to utilize lithium metal anode which has the highest specific capacity among anodes (3860 mAh g^{-1}), lowest reduction potential (-3.04 V vs SHE), and low density (0.53 g cm^{-3}).

This thesis first proposes a phenomenological model to describe the microstructure of aqueous electrolyte and the relation between their phase diagrams with ionic conductivity; highlighting a common correlation between the eutectic composition and peak ionic conductivity in conductivity isotherms. we then propose an empirical model correlating ionic conductivity with both molar concentration and temperature. The aim of this portion of the thesis is to provide an in depth understanding of aqueous electrolytes' physical properties in a way that can help researchers optimize the energy density and the cost of ALIBs.

Moving further, the thesis presents two novel composite solid electrolytes (CSE) that were developed and fully characterized. Both of which were composed of the following four components; polyethylene oxide (PEO), lithium bis(trifluoromethanesulfonyl)imide (LiTFSI) salt, lithium lanthanum titanate (LLTO) perovskite inorganic ceramic and the polymer plasticizer succinonitrile (SN). The careful formulation of these CSEs was based on the trade-off between film forming ability and ionic conductivity. The optimized polymer rich CSE proved to have better characteristics when compared to its ceramic rich alternative. ASSBs employing both CSEs were successfully charged and discharged when coupled with lithium metal anode and in-lab prepared composite cathode. The developed thin and flexible CSEs could be utilized in small applications (Wh-KWh) such as in consumer electronics and flexible biomedical devices (e.g., pacemakers) or larger applications (kWh-MWh) such as in EVs and large format storage for the electrical grid.

Résumé

Pour lutter contre le changement climatique et la demande exponentielle en matière de transport électrifié, l'amélioration et le développement de batteries renouvelables sûres à haute densité d'énergie et de puissance sont d'une importance capitale. Historiquement, les électrolytes aqueux étaient la norme dans l'industrie des batteries. Avant le développement des batteries au lithium, la plupart des batteries commerciales utilisaient l'eau comme solvant. Au cours de la dernière décennie, les électrolytes "hautement concentrés" ont ressuscité l'idée d'une batterie lithium-ion aqueuse (ALIB). Depuis lors, des efforts considérables ont été déployés pour comprendre la stabilité interfaciale de ces électrolytes à haute concentration et les rendre aptes à l'utilisation dans des batteries, en particulier celles à haute tension. Un autre candidat pour les batteries futures est les batteries tout solides (ASSB) car elles ont le potentiel de doubler, voire de tripler les densités énergétiques que nous atteignons actuellement avec les LIBs. Ceci, principalement en raison de leur capacité à utiliser l'anode en métal lithium ayant la plus grande capacité spécifique parmi les anodes (3860 mAh g-1), le potentiel de réduction le plus bas (-3.04 V par rapport à SHE) et une faible densité (0.53 g cm-3).

Cette thèse propose d'abord un modèle phénoménologique pour décrire la microstructure de l'électrolyte aqueux et la relation entre leurs diagrammes de phase et la conductivité ionique ; mettant en évidence une corrélation commune entre la composition eutectique et la conductivité ionique maximale dans les isothermes de conductivité. Nous proposons ensuite un modèle empirique corrélant la conductivité ionique à la fois avec la concentration molaire et la température. L'objectif étant de fournir une compréhension approfondie des propriétés physiques des électrolytes aqueux d'une manière qui peut aider les chercheurs à optimiser la densité énergétique et le coût des ALIBs.

De plus, la thèse présente deux nouveaux Électrolytes Solides Composites (CSE) qui ont été développés et entièrement caractérisés. Tous deux étaient composés des quatre composants : Oxyde de Polyéthylène (PEO), Sel de bis(trifluorométhanesulfonyl), imide de Lithium (LiTFSI), Pérovskite inorganique en céramique de Titanate de Lanthane de Lithium (LLTO) et le plastifiant polymère Succinonitrile (SN). La formulation de ces CSE était basée sur le compromis entre la capacité de formation de film et la conductivité ionique. Le CSE riche en polymère optimisé a obtenu les meilleures caractéristiques par rapport à son alternative riche en céramique. Les ASSBs utilisant les deux CSE ont été chargées et déchargées avec succès

lorsqu'elles étaient couplées avec une anode en métal lithium et une cathode composite préparée en laboratoire. Les CSE minces et flexibles développés pourraient être utilisés dans de petites applications (Wh-KWh) telles que dans l'électronique grand public et les dispositifs biomédicaux flexibles (les stimulateurs cardiaques) ou dans de plus grandes applications (kWh-MWh) telles que dans les véhicules électriques et le stockage de grand format pour le réseau électrique.

Statement of Contributions of Collaborators

I hereby declare that I am the sole author of this thesis.

Chapters 1 and 2 were written entirely by myself, with editorial corrections from Dr. Yaser Abu-Lebdeh and Professor Elena Baranova.

Chapter 3 was written by me with editorial corrections from Dr. Yaser Abu-Lebdeh, Prof Gillian Goward and Professor Elena Baranova. Electrolyte preparation, cathode preparation, battery cycling, and all characterization except NMR measurements were conducted by me with some assistance from CO-OP student Allan Huang. Conductivity data analysis and contour figures development was done by Research Council Officer Chae-Ho Yim. Pulsed Field Gradient Nuclear Magnetic Resonance (PFG NMR) measurements were done by Dr. Annica I. Freytag

Chapter 4 was written by me with editorial corrections from Dr. Yaser Abu-Lebdeh, Prof Gillian Goward and Professor Elena Baranova. Electrolyte preparation, cathode preparation, battery cycling, and all characterization except NMR measurements was conducted by me with some assistance from PhD student Shuo Yan and Research Officer Zouina Karkar. Conductivity data analysis and contour figures development was done by Research Council Officer Chae-Ho Yim. Pulsed Field Gradient Nuclear Magnetic Resonance (PFG NMR) measurements were done by PhD candidate Mengyang Cui and Dr. Zoya Sadighi.

Chapter 5 was co-written by Dr. Yaser Abu-Lebdeh and myself with editorial corrections from Prof. Elena Baranova.

Appendices was entirely written by me with editorial corrections from Dr. Yaser Abu-Lebdeh and Prof. Elena Baranova. Dr. Mohamed Houache helped me construct Schematics and figures in Appendix B

Acknowledgements

I would like to start by expressing my sincere gratitude to my supervisors; Professor Elena A. Baranova and Dr. Yaser Abu-Lebdeh for all their guidance and support throughout the years. Special thanks to Dr. Abu-Lebdeh, not only for being my supervisor but because he became my older brother as well. His patience, valuable lessons and advice each time I knocked his door will never be forgotten. I will never forget the Alchemist book he made sure I read!

I would like to thank Dr. Kelly Meek, Dr. Ghassan Jabbour, Dr. Benoît Lessard and Dr. Ali Abouimrane for being my Ph. D. defense committee and I would also love to thank all the Battery Material Innovation team at the National Research Council for their support and help throughout the years: Chae-Ho, Svetlana, Zouina, Mohamed, Shuo, James and Gina. I would also love to thank Parvin for her guidance during her time with the team.

Furthermore, I would like to thank my friends who have been my mental health backbone throughout the years. Those include AbuBaker, Andrew, Ali Khayyat, Rania Ali Taha, Tahseen, Khaldoon, Sammer, Fatima, and many others whom I have been very lucky to befriend.

I also cannot forget my uncle who was always my Idol, Muzahim AlMukhtar, who made me love the field of academia from a young age. He also helped me translate the abstract to French! Big thanks to his friend at the university of Ottawa Dr. Sai Vanapalli, who helped my wife and I a lot through the admission process.

My deepest gratitude goes to my parents who are the reason I embarked on this journey in the first place. Leaving them left a big hole in my life that would never heal unless I reunite with them. My days are always missing something without you!

Special thanks to my wife, Asma Shubair, who is also doing her Ph. D right now. I am extremely lucky to have you in my life. I can never thank you enough for all things you have done and I hope we continue to live life to the fullest. I wish to travel the world with you and convince you one day of skydiving together.

Finally, how can I end this acknowledgment without mentioning my daily source of dopamine, Leen my daughter? You are my biggest motivator in this life. May god protect you and bless you, always!

Nomenclature

ASSLB	All-Solid-State Lithium Batteries
ATR	Attenuated Total Reflection
CE	Coulombic Efficiency
CIP	Contact Ion-Pairs
CPE	Composite Polymer Electrolytes
CSE	Composite Solid Electrolytes
DBP	Dibutyl Phthalate
DMC	Dimethyl Carbonate
DSC	Differential Scanning Calorimetric
EC	Ethylene Carbonate
EDS/EDX	Energy-Dispersive X-Ray Spectroscopy
EIS	Electrochemical Impedance Spectroscopy
ESW	Electrochemical Stability Window
EV	Electric Vehicles
FTIR	Fourier Transform Infrared Spectra
HER	Hydrogen Revolution Reaction
IP	Ion Pairs
ISE	Inorganic Solid Electrolytes
LAGP	Lithium Aluminium Germanium Phosphate
LE	Liquid Electrolytes
LFP	Lithium Iron Phosphate
LCO	$LiCoO_2$
LGPS	$Li_{10}GeP_2S_{12}$
LIB	Lithium-Ion Batteries
LISICON	Lithium Super Ionic CONductor
LLTO	Lithium Lanthanum Titanate
LLZO	Lithium Lanthanum Zirconium Oxide
LMO	Lithium Manganese Oxide
LTO	Lithium Titanium oxide
LSV	Linear Sweep Voltammetry
MD	Molecular Dynamic Simulations
NMC	Lithium Nickel-Manganese-Cobalt

NASICON	Sodium Super Ionic CONductor
NiCd	Nickel/Cadmium
NiMH	Nickel/Metal-Hydride
NMR	Nuclear Magnetic Resonance
OER	Oxygen Evolution Reaction
PEG	Polyethylene Glycol
PEO	Polyethylene Oxide
PFG	Pulsed Field Gradient
PVDF	Poly(Vinylidene Fluoride)
RT	Room Temperature
SCIP	Solvated-Contact Ion Pairs
SDC	Specific Discharge Capacity
SE	Solid Electrolyte
SEI	Solid-Electrolyte Interphase
SEM	Scanning Electron Microscopy Imaging
SN	Succinonitrile
SOC	State Of Charge
SIP	Solvent-Shared Ion Pairs
SPE	Solid Polymer Electrolytes
SSIP	Solvent Separated Ion Pairs
SSB	Solid-State Batteries
SSE	Solid-State Electrolytes
TGA	Thermo-Gravimetric Analysis
UCIP	Un-solvated Contact Ion Pair
WIBS	Water-In-Bi-Salt
WIS	Water-In-Salt
XRD	X-Ray Diffraction

Table of Content

List of Figures

List of tables

Chapter 1. Introduction

Background and motivation

The demand for efficient energy storage batteries has increased exponentially due to the rapid growth of portable electronics, electric vehicles (EVs), and renewable energy sources. Lithium-ion batteries (LIBs) have been the dominant choice in the past few decades for these applications due to their decent energy density, long cycle life, and low self-discharge rate. However, concerns over the safety, cost, and sustainability on top of increased energy density demand beyond the theoretical limits of LIBs (state-of-the art LIB: 280 Wh kg^{-1} vs. demand: > 400 Wh kg^{-1})[1] have prompted research into alternative battery technologies. Examples of those that are focused on in this thesis are aqueous lithium-ion batteries (ALIBs) and all-solid-state batteries (ASSBs)

ALIBs offer several advantages over conventional LIBs, including improved safety, lower cost, and a wider temperature range of operation. The use of aqueous electrolytes in ALIBs eliminates the risk of thermal runaway, a significant safety concern associated with organic electrolytes in LIBs. However, the energy density of ALIBs is limited by the inherently narrow electrochemical stability window of water, which restricts the voltage range and leads to lower energy densities compared to LIBs. The understanding and optimization of aqueous electrolytes' microstructure and ionic conductivity are critical for improving the energy density and reducing the cost of ALIBs.

ASSBs have also emerged as a promising alternative to traditional LIBs due to their potential for higher energy density, improved safety, and longer cycle life The use of solid electrolytes in ASSBs eliminates the need for volatile and flammable organic liquids, reducing the risk of thermal runaway. Composite solid electrolytes (CSEs) specifically, have gained rapidly growing attention for their potential to combine the benefits of both polymeric and ceramic electrolytes.

The continuous development and optimization of ALIBs and ASSBs will undoubtfully result in scientific breakthroughs that will transform our future to a greener one. I hope this thesis can be a helpful stepping stone on this path.

Research objectives

The primary objective of this thesis is the development of safe and high energy

density batteries, specifically focusing on the inherently safe aqueous lithium-ion batteries (ALIBs) and the high energy density all-solid-state batteries (ASSBs) with composite solid electrolytes (CSEs). In order to address the challenges and opportunities in this field, the thesis is divided into several interconnected objectives:

a. Investigate the microstructure of aqueous electrolytes in order to helps developing the next generation of liquid electrolytes: The aim is to develop a novel phenomenological model that explains the microstructure of these electrolytes especially at high salt concentrations which is still unknown despite the advancements of characterization techniques that can unravel the structure in the liquid state .

b. Establish a connection between aqueous electrolytes' phase diagrams and their ionic conductivity: By identifying and analyzing trends, the thesis proposes a semi-empirical model that links ionic conductivity to both molar concentration and temperature. This model will serve as a valuable tool for researchers aiming to optimize ALIB performance.

c. Develop and fully characterize novel composite solid electrolytes (CSEs) for ASSBs: Two CSE formulations will be synthesized, one being polymer-rich and the other is ceramic-rich, both consisting of Polyethylene oxide (PEO), Lithium bis(trifluoromethanesulfonyl)imide (LiTFSI) salt, Lithium Lanthanum Titanate (LLTO) Perovskite inorganic ceramic, and the polymer plasticizer Succinonitrile (SN).

d. Evaluate the performance of ASSBs with novel CSEs: The prepared CSEs will be integrated into ASSBs with lithium metal anode and in-lab prepared 'Catholyte' containing composite cathode. The charging and discharging behavior of the resulting batteries will be assessed to determine their viability for practical applications.

In summary, this thesis aims to advance our understanding of aqueous electrolytes' microstructure and its relation to ionic conductivity and develop novel composite solid electrolytes for application in safe and high energy dense batteries. The research objectives will contribute to the improvement of existing battery technologies and open new avenues for the development of innovative energy storage solutions.

Thesis structure and organization

This thesis is divided into 6 main chapters followed by Appendices as follows:

- Chapter 1: represents a general introduction to this thesis. It mainly discusses the background and motivation for the work within and, presents the objectives accomplished.
- Chapter 2: starts with an introduction to batteries history and an overview of the

dominant lithium ion-batteries and their challenges. It then provides a comprehensive literature review about aqueous electrolytes and solid-state electrolytes.

- Chapter 3: refine and extend the understanding of a model on the long-debated topic of microstructure of highly concentrated liquid electrolyte system and presents an investigation of four nitrate aqueous electrolytes. In addition, it highlights an oversighted link between the salt/water phase diagram and the ionic conductivity behavior in these systems.
- Chapter 4: presents the novel polymer-rich composite solid electrolyte prepared and reports on its characteristics and battery performance.
- Chapter 5: presents the novel ceramic-rich composite solid electrolyte prepared and reports on its characteristics and battery performance.
- Chapter 6: A conclusion of all the research data described in the previous chapters, alongside the future research recommendations related for the fields of aqueous electrolytes and SSE.
- Appendix A: Includes supplementary information for Chapter 3
- Appendix B: Review paper titled: “Composite Cathodes for Solid-State Lithium Batteries: “Catholytes” the Underrated Giants”
- Appendix C: Presents a figure comparing the electrochemical stability window of the highest conductive aqueous electrolyte vs the highest conductive solid electrolyte prepared during the thesis.
- Appendix D: Includes a list of the publications, conference meetings and poster presentations related to this thesis.

References

[1] P. Mandade, M. Weil, M. Baumann, Z. Wei, *Chem. Eng. J. Adv.* **2023**, *13*, 100439.

Chapter 2. Literature Review

Introduction to batteries history

For over 2 centuries, aqueous batteries have been the prevalent battery technology. In the early 1800s, Italian physicist Alessandro Volta was the first to invent a battery by stacking alternating layers of Zinc, salt water saturated paper and copper in what we call now the 'Voltaic pile'.[1] Shortly after, Nicholson and Carlisle reported the first "electrolytic breakdown of water" by using the Volta pile.[2] Davy examined the effect of electrical current on materials and discovered that decomposition starts when a certain voltage is exceeded. Faraday later developed the "law of electrolysis" after studying the electrochemical decomposition of water.[3]

Despite the fact that the Volta pile electrochemical reaction was irreversible, this initial battery served as the foundation for several battery systems. In 1860, Gaston Planté made a significant milestone with the discovery of the rechargeable lead acid battery.[4] In the late 19th century, this technique sparked the world's industrial revolution and is still in use today. Additional battery innovations evolved in the decades that followed:

- Nickel/cadmium (NiCd) secondary batteries in 1890s [5]
- zinc/manganese Primary Alkaline batteries in the 1950s [6]
- nickel/metal-hydride (NiMH) secondary batteries in the 1960s [7]
- Lithium-Ion Batteries (LIBs) in 1970s [8]

After NiCd was the sole rechargeable battery technology for portable applications for many years, concerns regarding the use and disposal of cadmium encouraged the market introduction of a replacement which was the more environmentally sustainable NiMH battery in late 20th century, Apart from LIBs, these technologies have two characteristics in common: I the struggle against water electrolysis. water decomposition at high voltage which limits the cell voltage and energy density. In addition, (ii) these cell chemistries utilize conversion electrodes, which involve a chemical interaction between the electrode and electrolyte. Substantial volume growth, permanent morphological changes during intercalation and deintercalation of active material, and side reactions degrade the cycle life of electrodes.[9]

Nonetheless, the lead acid battery, which is one of the most common types of batteries used today, has an aqueous electrolyte and works at a nominal voltage of 2 V. Lead acid

batteries is in high demand because of its longevity, cheap cost, easy production method, and well-established supply chains. Lead-acid batteries are frequently used in autos and telephone backup systems especially when just a few deep charge/discharge cycles are necessary. However, the relatively short cycle life, low energy density (30–50 Wh/kg on the cell level), and usage of hazardous lead make lead-acid batteries a poor contender for large scale energy storage system and portable devices. The overall global battery market was valued at $108.4 billion in 2019 and is anticipated to increase by 14.1% from 2020 to 2027. in 2019, the market share of lead acid batteries is the largest at 29%. As illustrated in Fig. 2.1, it is anticipated that the market share of Li-ion batteries would exceed that of lead acid batteries by 2027.[10,11]

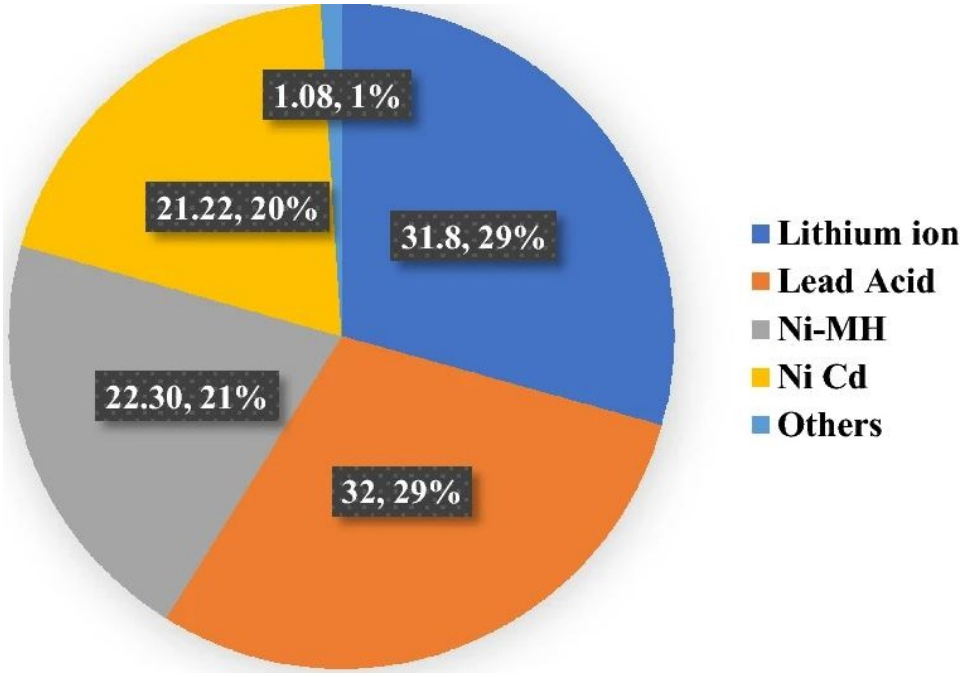

Figure 2.1: Market share of different batteries in 2019. Adapted with permission from [10] Copyright © 2022, Indian Institute of Science

Lithium-Ion Batteries (LIBs)

Unlike all prior battery technologies, LIBs store energy using a rocking chair mechanism. The electrodes no longer suffer dissolution/deposition processes, but instead function as hosts for Li^+ that intercalate and de-intercalate to and from the electrolyte during charge/discharge, resulting in an increase in cycle life. Profs. M. Stanley Whittingham, John B. Goodenough, and Akira Yoshino were awarded the 2019 Nobel Prize in Chemistry for developing these batteries.[12] The standard LIB consists of a graphitic intercalation anode and layered transition metal oxide cathodes. As seen in Fig 2.2, Li^+ de-intercalates from the positive electrode and intercalates into the negative electrode during charging and vice versa during discharging. Physically separating the two electrodes is the 'separator' which is a

porous membrane typically saturated with an organic liquid electrolyte. The electrolyte is vital to the functioning of a battery. The extremely oxidizing and reducing potentials of today's 4 V-class LIBs cannot be sustained by water, hence several non-aqueous electrolytes were developed. Commercial electrolytes are a mixture of several compounds, each of which serves a different function. Typically, electrolyte solvents are a combination of aprotic carbonate esters, such as ethylene carbonate (EC), dimethyl carbonate (DMC), and ethyl methyl carbonate (EMC). EMC and DMC have low viscosities, which is beneficial for ionic conductivity. While EC's high dielectric constant makes salt dissociation and Li+ solvation possible.[13]

Moving over to salts, Lithium hexafluorophosphate ($LiPF_6$) is one of the preferred conducting salts due to its high degree of dissociation and capacity to generate a passivation layer on the surface of the negative electrode. this layer is called the solid-electrolyte interphase (SEI) [13]. Despite the fact that carbonate-based electrolytes become unstable below 1 V vs. Li^+/Li, their decomposition products create a stable SEI that is electronically insulating in nature which prevents further electrolyte decomposition while maintaining sufficient Li-ion conductivity.[14] In the last 40 years, many electrolyte additives were developed to improve and optimize the developed SEI layer.[15] For instance, vinylene carbonate (VC) and fluoroethylene carbonate (FEC) are well-known for extending the lifespan of LIBs because they generate polymeric SEI components.[16]

A major drawback of LIBs is the flammability and volatility of the organic chemicals used as electrolyte solvents. These electrolytes can cause the rapid transition from a small thermal vent to a dangerous thermal runaway of the battery. Many mistreatments and failures may initiate such catastrophic accidents Such as short circuiting and overheating either by dendritic development or mechanical impacts, and deep discharging that results in oxidation of the copper current collector and then its re-deposition in the anode during the following charge, hence promoting dendrite formation. Hence, LIBs must be properly handled, transported at low states of charge, and monitored throughout operation to ensure Individual battery cells are never overcharged or undercharged. Furthermore, the moisture sensitivity of $LiPF_6$ necessitates dry manufacturing lines, which has a substantial effect on manufacturing expenses and energy usage.[17] These limitations become notably apparent and significant for large-scale applications that are cost-driven in particular. Unlike consumer electronics and electric cars, stationary storage applications do not have substantial volumetric or gravimetric limits. Nonetheless, safe battery operation and low levelized cost of stored energy throughout the lifespan of the battery system are critical.

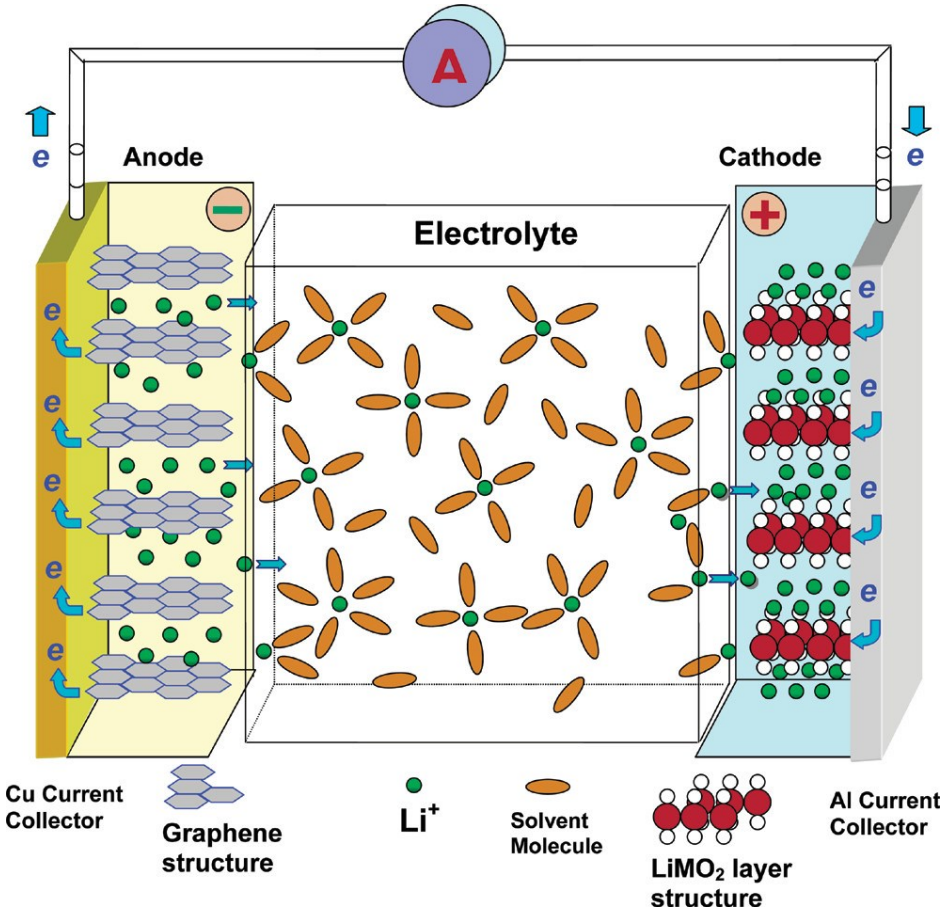

Figure 2.2: A schematic of a "(lithium ion) rocking-chair" cell with graphitic carbon as the anode and layered transition metal oxide as the cathode. Lithium ion de-intercalates from the graphene, travels through the electrolyte and intercalates into the layered structure of the cathode. This demonstrates the discharge of the cell, since the reaction is spontaneous. Adapted with permission from [13] Copyright © 2023, American Chemical Society

Aqueous electrolytes for aqueous lithium-Ion batteries

In addressing these obstacles, water-based electrolytes for LIBs provide a number of distinct benefits. Water is non-toxic, non-combustible, inexpensive, and inexhaustible. In addition, water's high relative permittivity and low viscosity allow for increased salt dissociation and increased mobility of ions, resulting in higher ionic conductivity in comparison to organic electrolytes. In addition, moisture-free production conditions are no longer required, and the inherently greater level of safety allow for minimization of the cost of safety measures like as temperature control and flame retardant materials. On the other hand, the narrow electrochemical stability window (ESW) of water, which is just 1.23 V at 25 °C from a thermodynamic standpoint, has prevented its use as an electrolyte in LIBs. High voltages result in electrolysis and the release of H2 and O2. The hydrogen Revolution reaction (HER) and Oxygen Evolution Reaction (OER) occur at 2.63 V and 3.86 V versus Li/Li^+, respectively. At neutral pH. these redox potentials are connected to the difference in Gibbs free energy between the reactants and products, which is controlled by the solvation structure and hydrogen bonding.[18] Marcel Pourbaix was the first to observe that the onset potentials for HER and OER move in accordance with the Nernst equation (59 mV per pH unit) when the pH value of the solution is altered. A Pourbaix diagram depicts the phase behavior of a system as a function of electrode voltage and solution pH. (Fig 2.3). It depicts conditions of equilibrium between coexisting phases in an electrochemical system. In this diagram, water is positioned between the anode OER and the cathode HER previously stated, defining the potential window within which an aqueous battery may function without kinetic overpotentials.[19]

Li and Dahn et al.[20] presented the first aqueous LIB in 1994 using a saturated solution of $LiNO_3$ (pH adjusted with 0.001 M LiOH). They utilized a $VO_2/LiMn_2O_4$ (LMO) electrode combination with a charge-discharge plateau of 1.5 V and energy density of 55 Wh/kg, which was superior than lead-acid batteries (30 Wh/kg) and comparable to NiCd (50 Wh/kg) at the time. This battery chemistry was never industrialized, since it was unable to compete with the well-established and reliable NiMH and lead acid batteries at the time.[21] VO_2 has a relatively high redox potential of around 2.5 V compared to Li/Li^+. ref. the NASICON-type anode $LiTi_2(PO_4)_3$ (LTP) was developed in 2007, but reliable cycling was only accomplished by coating the anode with a nanometer-thick layer of carbon.[19] Unlike anode materials, the vast majority of typical LIB cathode materials are compatible with traditional dilute aqueous

electrolytes. Spinel LMO has been widely utilized for a long time, and its interfacial Li^+ transfer reaction was even quicker than carbonate electrolytes. in 2015, Suo et al.[22] demonstrated stable cycling of Mo_6S_8 with a redox potential below the Pourbaix diagram's thermodynamic limit. The group employed a highly concentrated solution of lithium bis(trifluoromethanesulfonyl)imide (LiTFSI) in water, which has revived the ALIB research world.

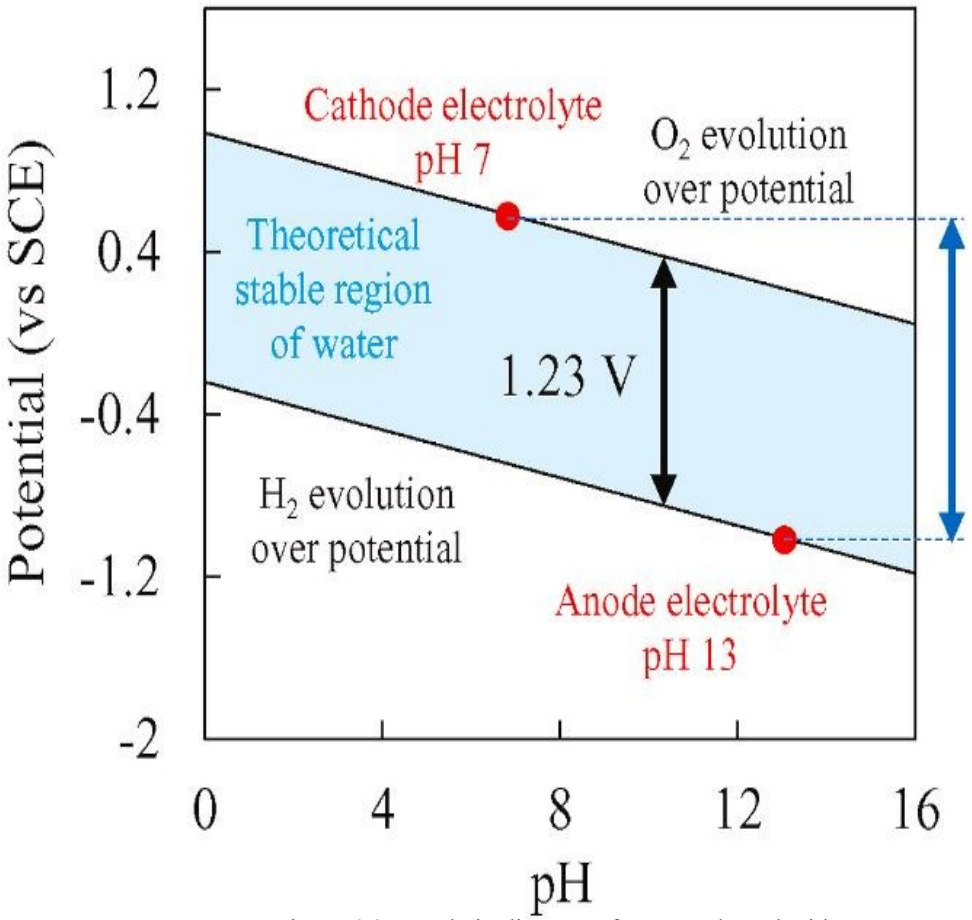

Figure *2*.3: Pourbaix diagram of water Adapted with permission from [19] *© 2020 Elsevier B.V.*

High concentrated aqueous Electrolytes

Molecular dynamic simulations (MD) can be used to explain the structural variations that occur in aqueous electrolyte solutions. Zheng et al.[23] used this technique to explore aqueous lithium nitrate system. Super-concentrated aqueous solutions present entirely new realms of solutions[24], with local structures that differ significantly from those established for

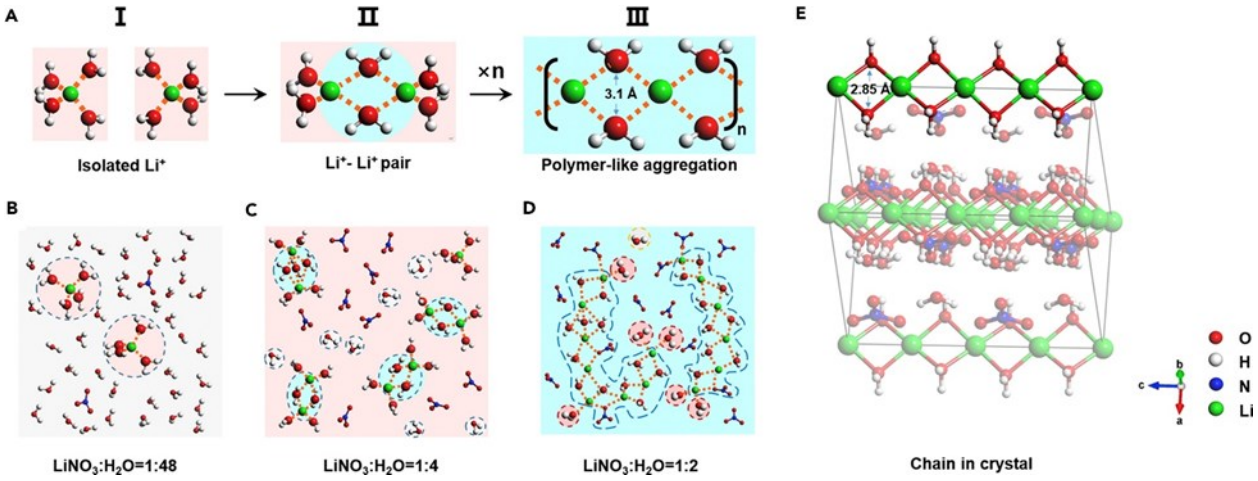

Figure 2.4: Molecular Dynamics (MD) Simulations of the LiNO3 Aqueous Solution with Increasing Concentration Adapted with permission from [23] © 2023 Elsevier Inc.

dilute aqueous solutions, and thus directly dictate the thermodynamic states of water molecules and salt anions, and hence the corresponding electrochemical behavior. Zheng et al. [23] reported on a super-concentrated (unsaturated) aqueous electrolyte based on a common Li salt, $LiNO_3$ that efficiently increases the aqueous stability window to 2.55 V without the formation of a protective SEI. They found the solution local structure by combining theoretical and experimental methodologies. All models and tests were done at 35 degrees Celsius on the basis of the well-researched
force fields for NO_3[25–27] and water systems H_2O[28,29], they initially utilized MD simulations to describe the structural development of $LiNO_3$ aqueous solutions as their concentration increased. In traditional aqueous solutions in which $LiNO_3$ molar ratio is < 0.09, Li^+ forms a $Li^+(H_2O)_4$ complex and travels with this initial solvation sheath formed of four water molecules[30], with each individual Li^+ ion randomly dispersed throughout the solution. This is the image captured by the MD simulation for a $LiNO_3$ solution at 200 ns, where $LiNO_3$ x = 0.02 (Fig 2.4 A-I and 1B) and the individual NO_3 molecules are randomly spread among the water molecules with no coordination. Yet, even in such a very dilute solution, Li^+ distribution retains a degree of short-range regularity. The initial Li^+ peak is positioned at 4.5A° and a minor quantity of Li^+ pairs are visible in the picture of dilute solution, where two Li^+ ions coordinate with two to three water molecules to form $Li^{2+}(H2O)_6$ dimer (Fig 2.4A-II). In this dilute solution, just 1.9% of water molecules are coordinated by Li+ couples, whereas 16.1% are coordinated by Li^+ ions alone. The majority of Li^+ ions carry their entire solvation sheaths with at least four water molecules, whereas 82% of water molecules stay free and only interact through hydrogen bonds.[23]

As the salt concentration rises to x = 0.2, the number of free water molecules

decreases quickly to 10.6% (Fig 2.4 C); at x = 0.33, just 1.2% of water molecules remain free (Fig 2.4 D). In contrast, when salt concentration rises, an increasing number of Li^+ ions appear in pairs because they prefer to partly share the main water sheaths; hence, the number of water molecules shared by Li^+ also increases. In addition, when x is between 0.2 and 0.33, a linear chain of Li^+ and water molecules develops (Fig 2.4 A-III), with the majority of the $Li^+(H_2O)_4$ complex condensing into $(Li^+(H_2O)_2)n$ (Fig 2.4 D) and hydrogen bonds disappearing entirely. This dynamic image derived from MD simulations demonstrates the significant change in local structure from dilution to hyper-concentration. $LiNO_3$ may crystallize with three water molecules at room temperature to create the solvate lattice $LiNO_3.3H_2O$ (Fig 2.4 E), which can be precipitated from a super-concentrated $LiNO_3$ aqueous solution. In this solvate crystal lattice, $(Li^+(H_2O)_2)n$ chains are retained intact by electrostatic interactions with NO_3 and may be seen as a "living fossil" of the local liquid structure throughout its precipitation from a super-concentrated solution. Yet, the distance between two oxygen atoms belonging to the two closest water molecules (d(OH–OH)) in the Li^+-H_2O chains of the $LiNO_3.3H_2O$ crystal structure is 2.85A°, but it is 3.1A° in the Li^+-H_2O chains of super-concentrated $LiNO_3$ solution (Fig 2.4 A-III). Comparatively to dilute $LiNO_3$ solution and a $LiNO_3.3H_2O$ crystal, the local structure of aggregated $(Li^+(H_2O)_2)n$ chains assume a significantly more relaxed conformation; hence, Li^+ ions might still be mobile in such formations. It is destined to manifest itself in macroscopic physical and chemical characteristics as a unique property of the super-concentrated $LiNO_3$ solution, which is halfway between a crystal and a traditional solution having advantages from both. [23]

In 2013, The use of TFSI anion in aqueous electrolytes for LIBs was first proposed. At a concentration of 2 M, the TFSI anion is stable at any pH values up to 60 °C.[31] In addition, LiTFSI has an exceptional solubility of 20m at 20 °C, which is more than that of $LiNO_3$ (14m)[32], and Li_2SO_4 (3.1m).[33] At concentrations over 5m, LiTFSI has a greater mass and volume than water, which justifies the name Water-In-Salt (WIS) electrolyte.[22] In dilute aqueous solutions of LiTFSI, an extensive hydrogen-bond (H-bond) network dominates but at concentrations greater than 20m, the majority of water molecules reside as isolated clusters with chain-like configurations.[34] The proportion of residual "free" water molecules in a 21m LiTFSI solution is approximately only 15%. In dilute solutions, four water molecules form the main solvation sheath around a lithium cation. At 21m, the ratio of H_2O to Li^+ is insufficient to fully solvate each cation. As seen in Fig 2.5, the principal solvation sheath of Li^+ also includes anions.[22]

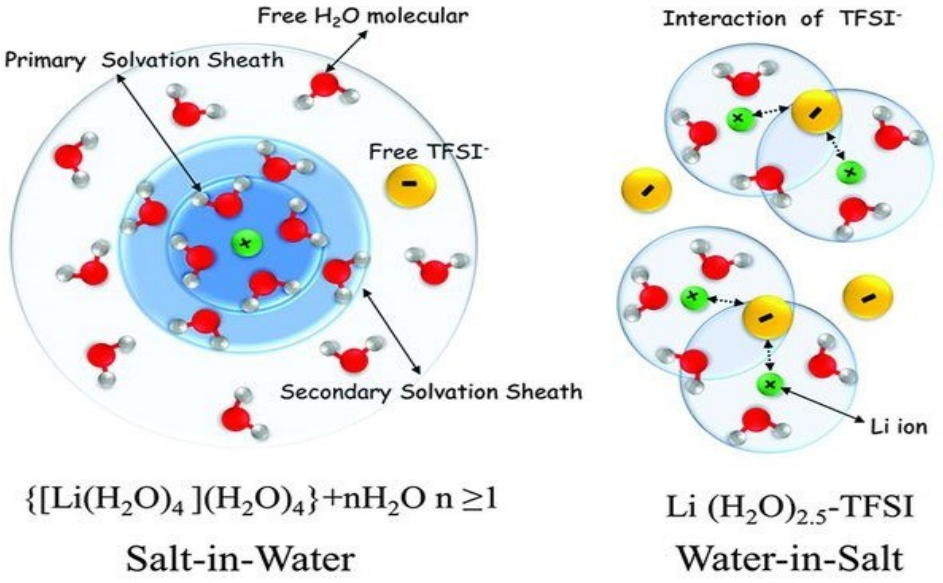

Figure 2.5: the solvation shell of Li^+ in water at low and high concentrations Adapted with permission from [22] Copyright © 2023, The American Association for the Advancement of Science

The lack of solvent molecules can also result in a nano-heterogeneous structured solution. Borodin et al. concluded, via the use of molecular dynamic simulations (MD) the emergence of a percolating network of essentially fully water-solvated Li cations surrounded by anion rich domains with a reduced water content.[35] According to simulations, around 40% of all Li ions lack $TFSI^-$ in their main solvation shell, and 25% are not coordinated by any water. Li^+ in water rich domains are much more mobile than Li^+ in $TFSI^-$ rich domains, where the bulky TFSI anions are immobilized. The most mobile species, as determined by NMR studies and MD simulations, is water, followed by Li^+ and $TFSI^-$. This explains the high Li^+ transport numbers t^+ of around 0.7 in WIS electrolytes when derived from diffusion coefficients.[35,36]

Whether the expanded ESW of WIS electrolyte is kinetic or thermodynamic in origin is still a hot debate in the scientific literature.[37–39] Early literature commonly refer to the reduced electrochemical activity of water to explain the wider ESW at high salt concentration.[22,40] Yamada et al. owed the reduced activity (0.5 kPa compared to 4.25 kPa for pure water at 30 °C) to the low vapor pressure of a $(LiTFSI)_{0.7}(LiBETI)_{0.3}.2H_2O$ electrolyte (about 28m, also known as hydrate melt electrolyte).[40] Besides that, the close coordination of water molecules in WIS electrolytes increases the energy required for de-solvation, slowing the kinetics of water splitting.[39] Its increased oxidative stability may be

partly explained by the changed electronic structure of water in highly concentrated solutions. Upon coordination, the lone pairs of the oxygen atom in water transfer a portion of their electron density to Li^+. Thus, the energy of the highest occupied molecular orbital (HOMO) decreases, making oxygen atoms less susceptible to oxidation.[40,41] Nonetheless, water's lowest unoccupied molecular orbital (LUMO) undergoes similar shift, making water more vulnerable to reduction.[39] When a solution becomes more concentrated, the activity of protons rises, which thermodynamically shifts the HER potential higher which facilitates HER.[37]

WIS electrolytes offer superior reductive stability compared to diluted aqueous electrolytes. similar LUMO shift also happens for $TFSI^-$ in the main solvation sheath of Li^+, which reduces the anion's reductive stability. On the basis of density functional theory (DFT) calculations, it is hypothesized that the electrochemical reduction of TFSI should occur prior to water decomposition at higher concentrations.[22] The reduction of $[Li_2TFSI(H_2O)_6]^+$ clusters was projected to occur at 2.14 V vs. Li/Li^+ through a TFSI defluorination process, generating a LiF-rich SEI production at high salt concentration.[22,42] SEI generation in aqueous electrolytes was initially believed to be impossible due to the fact that water electrolysis only resulted in gas production.[43,44] it is still debatable whether the anion decomposition occur electrochemically through the reduction of dissolved gases such as CO,[45,46] or chemically by hydroxide ions that are formed as a by-product of HER.[47,48] Regardless of how this protective layer is made, it is mostly made up of inorganic products of TFSI's decomposition, like LiF and Li_2CO_3, which are insoluble in the WIS electrolyte and form stable SEI. The low electronic conductivity of the SEI makes the potential drop across the electrode/electrolyte interphase. This is the mainly why some WIS electrolytes are more electrochemically stable than traditional dilute aqueous electrolytes, which can't form SEIs.

Abu-Lebdeh et al.[49] proposed a model for electrolyte solutions that connect the structure of the liquid to its ionic conductivity through the binary phases diagram. Briefly, it postulates that:

(1) the microstructure of the liquid, above the liquidus line of the phase diagram, is a heterogeneous mixture similar to that of the solid state below the corresponding solidus line.

(2) the heterogeneous microstructures vary with composition into molten solvent-rich, eutectic-rich and salt-rich domains.

(3) each domain is made up of charge carries/solvent molecules formed from the fragmentation of the bulk solid structure into its basic building units of ion pairs (IPs), ionic

clusters (ICs) or solvent aggregates.

(4) the charge carriers are kinetically-stable entities that continuously undergo a rapid dynamic exchange of ions and solvents and conduct ions in their respective domains through accessible free volume by overcoming energy barriers under the influence of an electric field.

(5) Changes in the type of charge carriers, free volume, activation energy plays a key role in controlling the throughout the compositional range with the conductivity mechanism varying from being dominated by vehicular mechanism to an ion hopping one on crossing the eutectic composition .

They successfully applied the model to aqueous and non-aqueous (nitriles) solutions of LiCl, LiTFSI and NaTFSI salts.

High-voltage ALIBs

The first report of a battery with 21m LiTFSI as electrolyte had 97% average Coulombic efficiency (CE) for 100 cycles 0.15C, an energy density of 84 Wh kg^{-1} and an CE approaching 99.5% at 4.5C over 1000 cycles.[22] The kinetic aspect of the widened ESW by the SEI is seen by the variation in CE between rapid and slow cycling, since the electrode stays considerably longer at more unfavorable voltages at the lower C-rate. Slow kinetics and mass transfer cause HER activity to be lowered at high rates. Low C-rates are thus essential to show compatibility between the electrolyte and the active material. The same 21m LiTFSI electrolyte but with lower pH (pH = 5 instead of pH = 7) facilitated cycling of a LNMO cell demonstrated high energy density values of 125 Wh kg-1 but lower CE of around 96% at C/2.[50] According to another study, $LiCoO_2$ (LCO) cathodes may be successfully stabilized at high voltages by adding tris(trimethylsilyl) borate (TMSB), which creates a cathode electrolyte interphase (CEI).[51]

Lowering the water content, for example, by raising the salt concentration, increases kinetic barriers against hydrolysis. This can be done by using a dual salt method, which involves dissolving a second salt in the LiTFSI-H_2O matrix and has a similar structure to LiTFSI, higher lithium-ion concentrations can be achieved. This research was based on a study by Angell et al. that demonstrated the ability of a hydrated salt to dissolve a non-hydrated salt that contains an identical anion.[52] Suo et al. added 7m LiOTf to 21m LiTFSI solution to raise the Li salt concentration from 21m to 28m. The water-in-bisalt electrolyte (also known as WIBS) allows for the use of an anode with a lower redox potential, such as TiO_2.[53] In this WIBS electrolyte, the residual free water percentage fell even further, from

15% to 11%. In this case, The TiO_2 anode works at the extreme edge of the 28m WIBS electrolyte's stability limit, and stable cycling can only be achieved upon carbon coating the titanium dioxide particles. This system was able to achieve 99% CE at 0.5C and an energy density of 100Wh/kg. Yamada et al. developed the system introduced before; which is the hydrate melt electrolyte.[40] $Li_4Ti_5O_{12}$ (LTO) anodes, which have an even lower redox potential of 1.55 V vs. Li/Li^+, were able to cycle thanks to a 28-molar combination of lithium bis(pentafluoroethanesulfonyl)imide (LiBETI) and LiTFSI. This cell was able to provide an energy density of 130 Wh kg^{-1} at C/5 when coupled with LCO, however low CEs compromised cycle stability. Only fast cycling rates; > 0.1C enabled reliable cycling. This electrolyte functions outside of its ESW when combined with LTO, as it exhibits comparatively low CE and apparent capacity fading upon cycling. In an electrolyte known as mono-hydrate melt, where the molar fraction of Li^+ is equal to that of water,[54] the salt concentration has recently been raised to levels as high as 55.5m. LiBETI has been replaced by an asymmetric lithium salt LiPTFSI, which has a much greater solubility at room temperature than all previously known imide-type salts.[55] At such high salt concentrations, the OER and HER exhibit much larger kinetic overpotentials. Yet, considerably higher viscosity and poor conductivity come at the expense of the enhanced ESW. The authors of this work may have chosen to provide cycle data for a battery using this electrolyte only at high temperatures due to the slow transport capabilities. Despite the existence of asymmetric anions, this electrolyte may only be meta-stable at room temperature and may have a significant inclination to crystallize.

Hybridizing an aqueous electrolyte with organic solvents like DMC or acetonitrile improved batteries cycling with LTO anodes.[56,57] Few advantages result from hybridizing WIS electrolytes including lower water content, which increases the lithium-to-water molar ratio and disrupts the hydrogen bonding network more; and the ability of the organic molecules to create SEIs. A DMC-hybridized WIS electrolyte did in fact exhibit reductive stability of up to 2 V vs. Ag/AgCl, which the authors primarily ascribed to an enhanced SEI containing DMC decomposition products.[57] using this electrolyte, an LTO cell operating at 3.2 V with an energy density of 165 Wh kg^{-1} was reported to cycle at 0.5C achieving CE of more than 99% for 200 cycles. The incorporation of acetonitrile enabled an LTO/LMO cell to operate at zero degrees Celsius and an LTO/$LiNi_{0.8}Co_{0.15}Al_{0.05}O_2$ (NCA) cell to achieve high-capacity retention at 1C after 100 cycles with an initial energy density of 173 Wh kg^{-1}.[56] As adding organic solvents would ultimately risk losing the aqueous virtue of non-flammability, other strategies were tried, like adding non-flammable organic salts or ionic liquids.[58–60] 42m

LiTFSI and 21m Me_3EtN-TFSI[59] were combined to form a 63m electrolyte. Low ionic conductivity (0.9 mS/cm), a low transport number (0.5), and a high viscosity (407 mPa s) were found for this electrolyte, which came at the expense of the increased electrochemical stability.

To limit the amount of hydrogen bonding in the bulk electrolyte and therefore enable lower LiTFSI concentrations, it is wise to attempt to confine water molecules in an organic matrix instead of the hydration shell of Li ions.[61,62] Due to its novel design approach, the molecular crowding electrolyte, which used poly(ethylene glycol) to lower the water activity, has received a lot of interest. It did not, however, demonstrate enhanced cycle stability of LTO/LMO cells.[63] The use of urea as a crowding agent that functions as a hydrogen bond acceptor and donor led to significantly increased cycle stability.[61]

Most anode materials for WIS electrolytes, as previously mentioned, are based on titanium. However , TiO_2 has been known as a strong photocatalyst for water splitting and LTO is thought to catalyze catalytic decomposition reactions of non-aqueous electrolytes. Thus, several studies investigated coating techniques to keep water off the anode's surface. For instance, carbon[53,58] or $LiTi_2(PO_4)_3$[64–66] were used to coat TiO_2. Similarly, several coatings were suggested for LTO anodes such as carbon[67], LATP[63], Al_2O_3, NbOx[58,68] PAN-LiTFSI polymer[59], and zinc.[19] Even a 4 V aqueous battery was made possible by an artificial SEI created by a fluorinated ether on graphite or lithium metal.[69]

Only few research articles have documented the cycling of WIS electrolytes without the anode's surface being coated. When combined with LMO cathodes (2 V), Mo_6S_8[22] and TiS2[70] have high enough redox potentials to prevent the need for a coating, but their energy density is poorer; usually less than 100 Wh/kg. A super concentrated electrolyte of 75m (50m LiTFSI and 25m ionic liquid) was cycled without coating with polymorph of TiO_2; TiO_2-B.[71] In the literature, there are instances of uncoated LTO electrodes as well, but these either exhibited stable cycling only at high rates or used WIS electrolytes that had undergone polymerization or hybridization with organic solvents.[40] A 63m consisting of 42m LiTFSI and 21m ionic liquid hybrid WIS electrolyte as well as ternary LiTFSI-water-urea/methyl urea electrolytes,[61] also showed stable cycling of uncoated LTO electrodes. LTO anode cycling was also facilitated by the barley liquid monohydrate-melt electrolyte.[54] In conclusion, titanium-based anodes need either a protective coating to permit stable cycling with WIS electrolytes or organic solvents to create enhanced SEI. Going to really high salt concentrations, the third alternative, is less practical since it results in excessively viscous liquids with subpar transport qualities.

Solid-State Electrolytes

Solid-state electrolytes can be divided into 3 main classes and those are, solid polymer electrolytes (SPEs), inorganic solid electrolytes (ISEs) and composite solid electrolytes (CSE). This chapter will focus on discussing the ionic conduction mechanism in each, the primary characteristics and drawbacks of each and explain the superiority of CSEs as the better candidate for solid electrolyte in lithium metal batteries.

Solid Polymer Electrolytes (SPEs)

The development of SPEs first sparked in 1973 when Wright et. al reported on the discovery of ionic conductive complexes between polyethylene oxide (PEO) and alkali metal ions. [72] Few years after, Armand et. al suggested the utilization of these polymer-alkali complexes in high energy density batteries because of their solid-state chemistry, flexibility and ease of processing. [73]

Polymers are typically semi-crystalline structures meaning they exhibit a crystalline structure, usually at low temperatures, and an amorphous structure, usually at high temperatures. Whether the amorphous or the crystalline phase is better for ionic conductivity has been a hot debate for researchers. [74] Earlier attempts to explain ionic conduction predicted that ions transport in polymer helices in the crystalline phases. [75] Some researchers still back this stance such as Bruce et al [76] who have proposed that lithium ions can transport in crystalline polymers by hopping across crystalline spiral cylindrical chains. However, another theory came out suggesting the opposite and has the support of most researchers. This mechanism, sometimes termed as the *hopping mechanism,* is best explained by Meyer et al. [77] Lithium salt ions interact with suitable coordination sites on polymer chains to form Lewis acid or Lewis base complexes, then the cations and anions dissociate, hop and coordinate on adjacent polymer chains. This with the propelling dynamics of the polymer chain and an external electric field yield to the ionic transport of lithium across the electrolyte. Based on this interpretation, many studies have concluded that ionic transport is best when the polymer chains are activated (at temperature above glass transition temperatures) and that the crystalline phases impede ionic conductivity. [74][78] Fig 2.6 presents schematic of the two conduction mechanism discussed above.

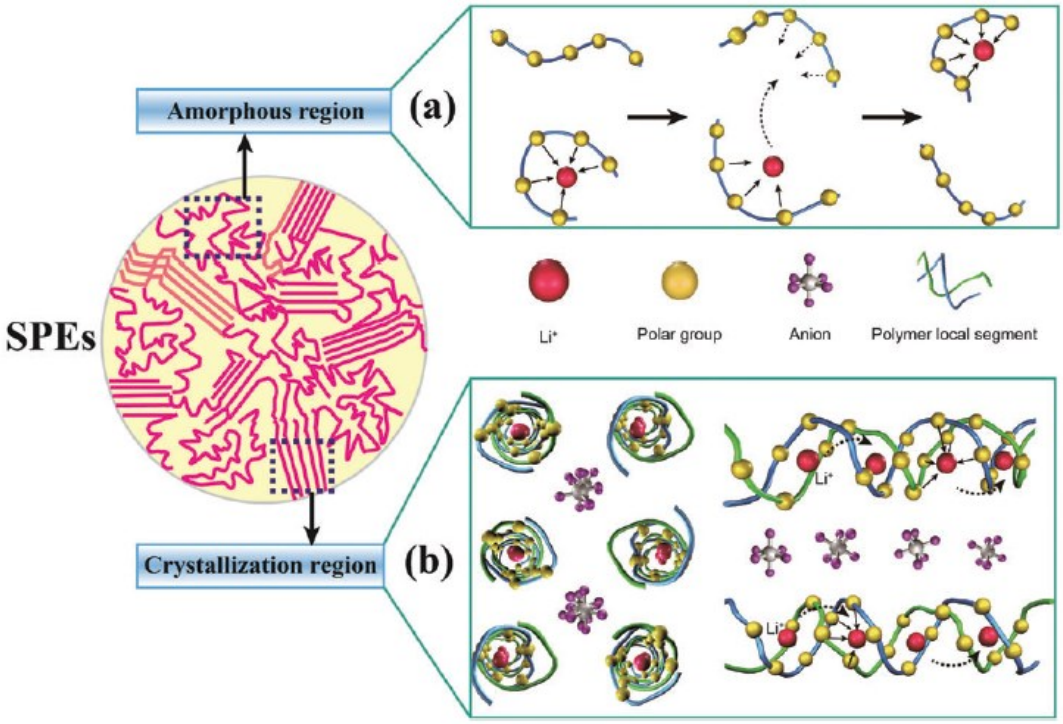

Figure 2.6: schematic of ionic conduction mechanism in (a) amorphous phase proposed by Meyer et al[77] (b) crystalline phase proposed by Bruce et al[76] Adapted with permission from [74]Copyright © 2016, Royal Society of Chemistry

Efforts into exploring the link between polymer chains dynamics and ionic conductivity started since the 1980s and have continued till this date. However, the application of SPEs is heavily hindered by the low room temperature conductivity (10^{-6}–10^{-8} S cm^{-1}) which is partly because of the high degree of crystallinity of polymers at ambient conditions. [79] To enhance the ionic conductivity of polymers at ambient operating conditions, researchers have tried employing different additives and were able to raise the conductivity up to 10^{-4} S cm^{-1} and beyond. The additives used can be simply divided into two classes*: active fillers* and *passive fillers*. Active fillers are typically inorganic particles that offer alternative conduction pathways to the polymer and thus, they provide a direct contribution to conductivity. When active fillers are used with polymers, they create what is called *composite solid electrolytes* (CSEs). Those are the third class of solid electrolytes and are going to be discussed further later in this report. On the other hand, passive fillers (sometimes called *plasticizers)* just prevent the recrystallization of the semi-amorphous polymers which in turn improves the conductivity of the polymers.

For example, Ito et al. [80] studied the effect of poly (ethylene glycol) (PEG) as a plasticizer on PEO-$LiCF_3SO_3$ complexes and they noticed an increase in ionic conductivity with content increase of PEG. The conductivity enhancement was attributed to the

crystallinity reduction and free volume increase in the system. [80] PEG was able to raise the conductivity of PEO- $LiCF_3SO_3$ from 1.3 x 10^{-7} to 2.8 x 10^{-5} S/cm at 25 °C. Also, Benedict et al. [81] observed the effectiveness of dibutyl phthalate (DBP) as a plasticizer. DBP was added to PEO-$LiAsF_6$ complex. Figure 2.7 shows the effect of DBP molar ration on the ionic conductivity of the polymer/salt complex.

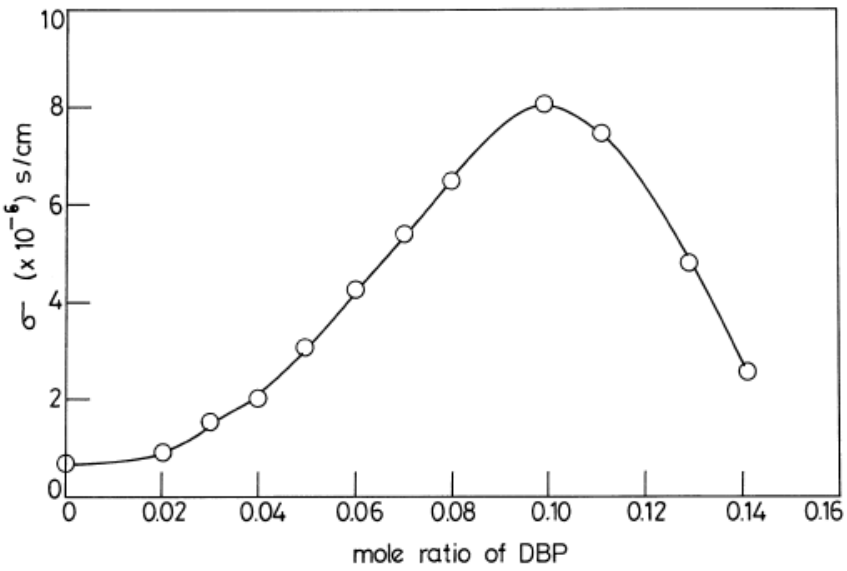

Figure 2.7: ionic conductivity at room temperature of PEO-$LiAsF_6$ with different molar ratios of DBP Adapted with permission from [81] Copyright © 2023 Elsevier Science S.A.

Other studies have proved the effectiveness of various inorganic particles as plasticizers. Croce et al [82] have proven the effectiveness of titania and alumina (TiO_2 and Al_2O_3) as solid ceramic plasticizers. TiO_2 and Al_2O_3 kinetically inhibit the crystallization of PEO as it cools down from temperatures above 60 °C. Fig 2.8 below presents the Arrhenius plots of ceramic free polymers versus polymer with the ceramic additives. It is clearly observable that the addition of the ceramic passive fillers provides 2-3 orders of magnitude increase in ionic conductivity. Another passive filler that proved to be excellent is silica (SiO_2). Xiong et al [83] reported very similar findings as Croce in terms of conductivity enhancement. SiO_2 enhances the ionic conductivity of PEO/$LiClO_4$ by 2-3 orders of magnitude. the conductivity enhancement achieved by the addition of those ceramic passive fillers is ascribed to the interaction between the Lewis acidic sites on the fillers and both the PEO segments and the lithium salt anions (e.g.: $TFSI^-$ or ClO_4^-), which aid the release of additional free Li^+ ions and generate more amorphous pathways for the charge transfer. [84] In addition, Croce et al also demonstrated that passive fillers with Lewis basic sites such as ZnO are also effective in improving room temperature ionic conductivity. [85] Despite all the

success in bringing up the ionic conductivity to acceptable levels, it is mostly done by reducing the crystallinity of polymers which in turn weakens the robust structure of polymers. Mechanical strength of electrolytes is in fact its biggest advantage and thus the biggest challenge for SPEs application is finding the optimal balance between ionic conductivity and mechanical strength.

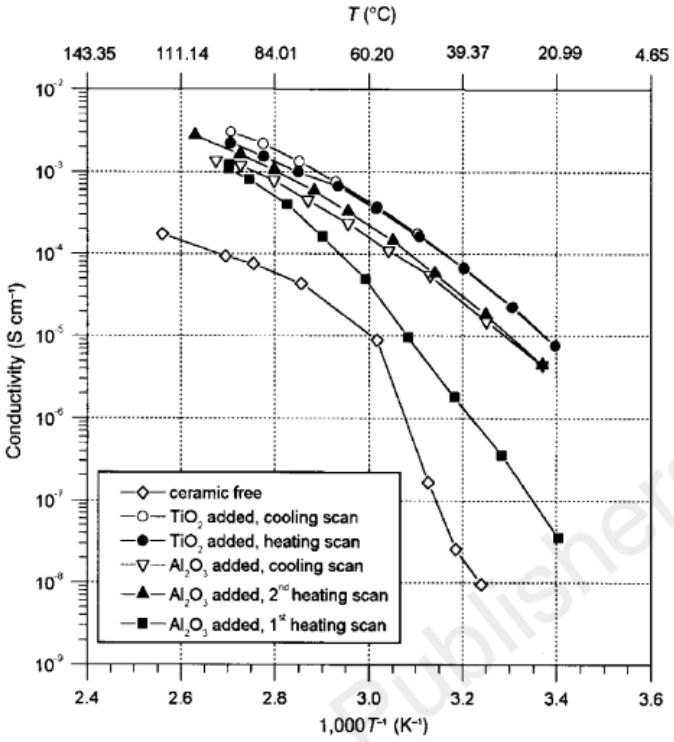

Figure 2.8: Ionic conductivity Arrhenius plot for SPEs with and without ceramic passive fillers Adapted with permission from [82] Copyright © 2023, Springer Nature - Macmillan Magazines Ltd.

Polymer-salt complex formation

For any salt to dissociate in any solvent, whether polymer or liquid, and at constant temperature and pressure, this process must result in an overall reduction in Gibbs free energy. As a reminder change in Gibbs free energy is calculated as follows:

$$\Delta G = \Delta H - T\Delta S \qquad (1)$$

The first part of equation (1), is the change of enthalpy and this must be minimized for the dissolution to be more favorable. The higher the electrostatic interactions between the solvated ions and interactions between the salt cation and the polymer coordinating groups, the lower the change in enthalpy which favors the polymer-salt complex formation. On the other hand, ions with small radii and high charge possess higher lattice energies which leads to a larger change in enthalpy upon dissolving making the complex formation less favorable. [86]

As for the second term of equation (1), which is the change in entropy, it must be as high as possible for the dissolution to be more favorable. Entropy increases as the salt crystal structure break and ions dissolve in the polymer. Simultaneously, entropy decreases as polymer chains stiffen when coordinating with ions. This slows down the polymeric chains segmental motion. It had been proven that typically the entropy decrease because of polymers chain stiffing is more than the increase in entropy caused by the salt crystal structure breaking down. Thus, the typical net entropy change is negative which is not in favor of the polymer-salt complex formation. [87]

For an SPE to have decent ionic conductivity at room temperature, the polymer must possess the lowest glass transition temperature (T_g). This is because polymers with low T_g have more amorphous regions and more tangled polymer chains. Similarly, having a lower melting point (T_m) is also associated with higher room temperature conductivity. In addition, for polymers to solvate lithium ions more easily, they must have a high dielectric constant, high concentration of polar group on its polymer chains such as ether (-O-), sulfide (-S-), phosphide (-P-), amine (-N-) and carbonyl (C=O). and appropriate distancing between coordinating centers. Lastly, polymers must also have low steric hinderance for bond rotation and a flexible back bone. [72,73,88]

Table 2.1: The most common polymers used in SPEs, their chemical formulas and their thermal properties (their T_g and T_m). [89]

Polymer host point	Repeat unit	Glass transition temperature T_g (°C)	Melting T_m (°C)
Poly(ethylene oxide)	$-(CH_2CH_2O)_n-$	−64	65
Poly(propylene oxide)	$-(CH(-CH_3)CH_2O.)_n$	−60	—[a]
Poly(dimethylsiloxane)	$-[SiO(-CH_3)_2]_n$	−127	−40
Poly(acrylonitrile)	$-(CH_2CH(-CN))_n-$	125	317
Poly(methyl methacrylate)	$-(CH_2C(-CH_3)(-COOCH_3))_n-$	105	—[a]
Poly(vinyl chloride)	$-(CH_2CHCl)_n-$	82	—[a]
Poly(vinylidene fluoride)	$-(CH_2CF_2)_n-$	−40	171
Poly(vinylidene fluoride-hexafluoropropylene)	$-(CH_2CF_2)_n$-$[CF_2CF(CF_3)]_m$-	−65	135

[a] Amorphous polymer.

Poly(ethylene oxide) (PEO) is the polymer that has gained the most attention among researchers for that fact that it excels in all the above-mentioned criteria and for its ease of processability. In fact, PEO-based SPEs can be made from the simplest techniques such as solution casting. [90] Other polymers such as Poly(propylene oxide) (PPO) for example, has a T_g close to that of PEO, yet its solvation ability falls far behind PEO because of its low dielectric constant coordination geometry. Polymers like poly(ethylene) amine or polysiloxanes have a decent capacity for polymer-salt complex formation but they are limited

by their weak chemical stability. [73] PEO is a water-soluble polymer that is synthesized by ring polymerization of ethylene oxide. It is also soluble in most organic solvents such as dimethylforamide, acetonitrile, anisole and ethylene dichloride. The ether oxygen atoms on the polymer chains are correctly placed with appropriate distancing between each other to allow for polarizability and maximum solvation of lithium ions which makes PEO an ideal solvent for Alkali and transition metal cations. [91,92].

Despite SPEs impressive characteristics, their room temperature conductivity is still relatively low compared to liquid electrolytes (10^{-7}-10^{-6} S cm^{-1} compared to 10^{-3}-10^{-2} S/cm). This is mainly because the polymer's T_m and T_g are well above ambient conditions and thus, the crystalline phase dominates. [90]

Inorganic Solid Electrolytes (ISEs)

The second class of solid-state electrolytes are ISEs. The ionic conduction mechanism in ISEs is significantly different from that in SPEs and liquid electrolytes where lithium ions get solvated in an aprotic medium. According to Stokes-Einstein equation, conductivity in liquid electrolytes or SPEs can simply be enhanced by choosing liquid/polymer electrolytes with higher dielectric constant and/or lower viscosity. [13] The potential energy profile for mobile lithium ions is almost flat which is because of the relatively easy exchange of ions between the solvent molecules in aprotic liquids/polymers. [93] However, this is not the case in crystalline inorganic solid electrolytes (ISEs) where the ions must overcome energy barriers before they can transfer from one crystallographic site to another. The magnitude of this energy barrier or sometimes referred to as migration energy E_m, heavily impacts the ionic mobility in ISEs. In addition, the ionic conductivity in ISEs also depends on the number of vacancies and interstitials which is determined by the defect formation energy, E_f (this is known as intrinsic regime). Vacancies and interstitials can sometimes be created in a process governed by trapping energy, E_t (this is known as extrinsic regime). The overall conductivity of ISEs abides the following equation:

$$\sigma = \frac{\sigma_o}{T} e^{-E_A/k_B T}$$

where k_B is Boltzmann constant E_A is the activation energy of diffusion which equals to $E_m + E_f/2$ and $E_m + E_t/2$ in intrinsic and substituted ISEs, respectively. [93]

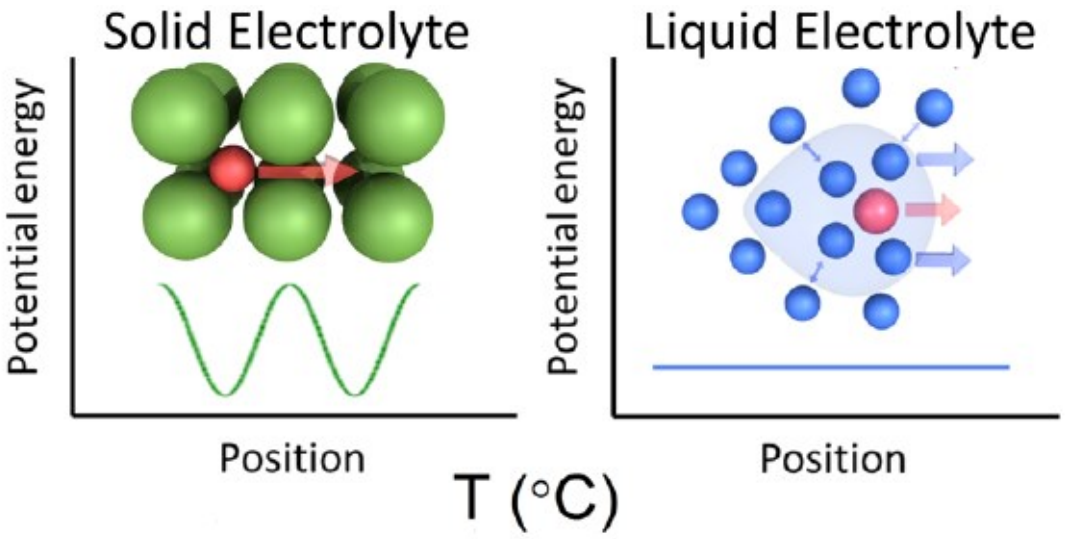

Figure 2.9: Potential energy profile of lithium ions in liquid versus crystalline solid electrolytes Adapted with permission from [93]. Copyright 2023 American Chemical Society.

ISEs are usually divided to many sub-classes, Fig 2.10 below shows a schematic of ISE sub-classes which are going to be discussed briefly below:

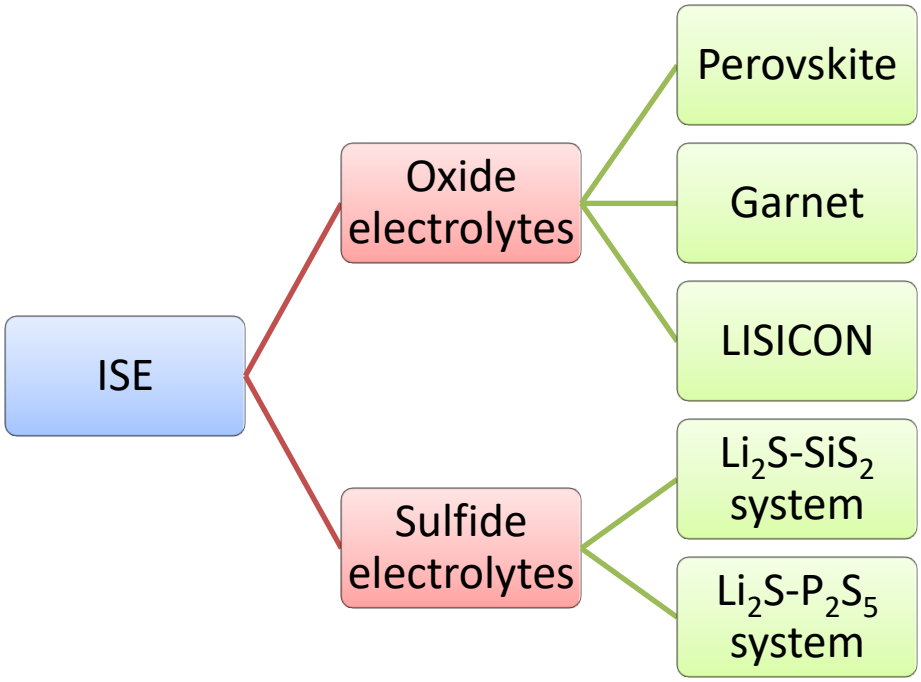

Figure 2.10: A simple schematic showing ISE most researched classes and subclasses

Oxide solid electrolytes

Perovskite type structure

Perovskite ISEs are electrolytes that share the same structure with $CaTiO_3$ and have the general formula ABO_3 where A represents an alkaline rare or earth ion and B represents a transition metal ion. [94,95] A schematic of a typical perovskite structure can be seen in Fig

2.11.

One of the most famous perovskite ISEs is $Li_{3x}La_{2/3-x}TiO_3$ (LLTO). Here in this electrolyte, both Li and La occupy the A position while Ti occupies the B position. Inaguma et al. was able to synthesize LLTO electrolyte that possessed ionic conductivity of around 10^{-3} S cm^{-1} at ambient conditions. [96] This high conductivity is comparable to that of liquid electrolytes and it drew much interest around it. LLTO can be made into a cubic, tetragonal or orthogonal structure depending on its composition and its preparation technique. On the other hand, its conductivity is mainly depending on the atoms occupying A positions. The presence of high valence La atoms in A positions create A vacancies thus, boosting conductivity. [94] Despite its superb ionic conductivity, LLTO cannot be used as an electrolyte in lithium metal batteries since it is very unstable against lithium metal. Lithium can easily intercalate into LLTO structure reducing Ti^{4+} to Ti^{3+}. However, LLTO is typically used in CSEs to boost their ionic conductivity. (Will be discussed further later in the report)

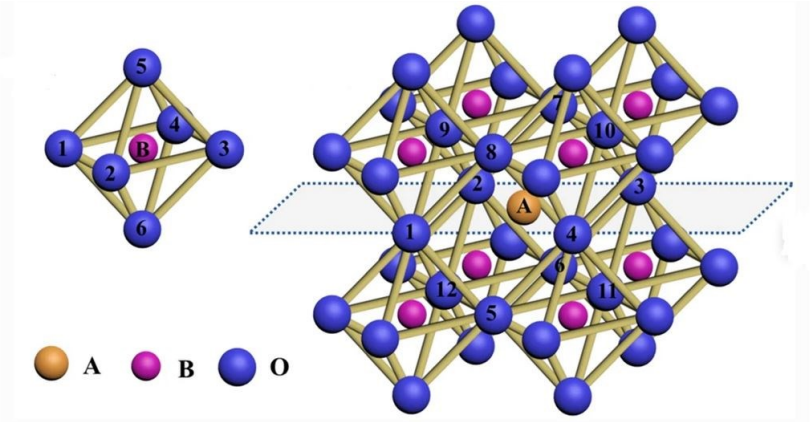

Figure 2.11: Schematic of perovskite structure. Adapted from [132] Copyright © 2023, Springer Science Business Media, LLC, part of Springer Nature

LISICON type structure

LISICON ISEs are made by replacing Li ions in place of Na ions in the parent NASICON structure. NASICON ISEs were first synthesized by Goodenough et al. [97] in 1976 and they have the general formula of $AM_2(PO_4)_3$ (x = 0-3) where A sites are occupied by Na^+ or Li^+ (called LISICON in the latter case) and M sites are occupied by tetra-valence ions (Ti^{4+}, Ge^{4+}, Zr^{4+}) Their name stands for Sodium (NA)/ Lithium (Li) super (S) ionic (I) conductor (CON) because of their exceptionally high ionic conductivity. [94] The structure of LISICONs can be seen in the schematic in Fig. 2.12.

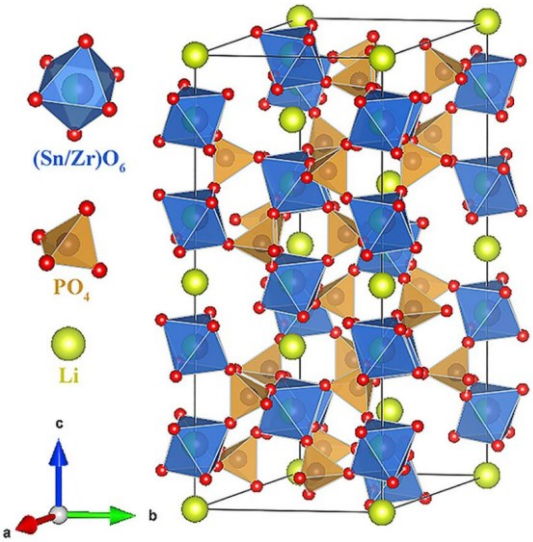

Figure 2.12: A schematic of LISICON structure. Adapted from [98] © 2023 Elsevier B.V. All rights reserved.

The ionic conductivity in LISICONs depends on the similarity between the ions size and the channels size in the crystal structure. highest ionic conductivity is obtained when these two sizes match each other.[99] For example, the ionic conductivity reported for $LiZr_2(PO_4)_3$ is very low and was boosted remarkably when Zr atoms were replaced by Ti atoms to make $LiTi_2(PO_4)_3$.[100] The $LiTi_2(PO_4)_3$ electrolyte gained a lot of interest because of its high ionic conductivity and efforts were focused on improving it even more. Aono et al. tried substituting one of the Ti^{4+} atoms with one M^{3+} atom (M= Cr, Al, Ga, Sc, Fe, In, Lu, La, Y). They were able to boost the ionic conductivity by one order of magnitude with the electrolyte $Li_{1.3}Ti_{1.7}Al_{0.3}(PO_4)_3$ (LATP) that has a conductivity is 7×10^{-4} S cm^{-1} at 298K.[101] However, the Ti^{4+} atom in LATP electrolytes gets easily reduced to Ti^{3+} at low potentials and thus, LATPs are not electrochemically stable.[102] Another highly investigated LISICON ISE is the $Li_{1+x}Al_xGe_{2-x}(PO_4)_3$ (LAGP) system because of its wide electrochemical stability window, low activation energy [103] and high ionic conductivity of 6.2×10^{-4} S cm^{-1} especially at x = 0.5-0.6.[104] in 2011, Kamaya et al synthesized $Li_{10}GeP_2S_{12}$, a solid electrolyte with an extremely high ionic conductivity of 1.2×10^{-2} S cm^{-1}. Notably, Ge is an expensive metal, and this hinders the wide-scale application of Ge-containing CSEs. Besides, LAGP and LGPS long term stability in contact with lithium metal is uncertain.[102]

Garnet type structure

Garnet type ISEs for Lithium batteries were first studied in 1969 by Kasper et al and they had the general formula of $Li_3M_2Ln_3O_{12}$ where M was W or Te. Later in 1988, Mazza et al reported on a new garnet structure with the general formula $Li_5La_3M_2O_{12}$ where M is Nb or Ta.[105] A schematic of this structure is shown in Fig 2.13 below.[106]

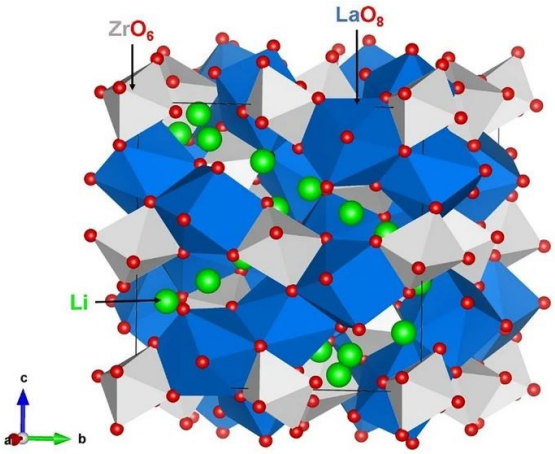

Figure 2.13: Schematic of garnet structure. Adapted from [133] licensed under a Creative Commons

$Li_5La_3M_2O_{12}$ exhibited a conductivity of 10^{-6} S cm^{-1} at room temperature and wide electrochemical stability window. Further research was able to find that the replacement of La atoms with low valence atoms such as Sr, Ca or Ba is able to further improve the ionic conductivity.[107,108] Precisely, ionic conductivity of 4 x 10^{-5} S cm^{-1} was reported for $Li_6BaLa_2Ta_2O_{12}$.[107] the latest most impressive improvement to garnet ISEs was achieved by Weppner et al in 2007 when they replaced La atoms with Zr atoms to make $Li_7La_3Zr_2O_{12}$ (LLZO). LLZO has ionic conductivity of 3 x 10^{-4} S cm^{-1}.[109] In comparison, LLZO with tetragonal structure exhibit ionic conductivity of 1.63 x 10^{-6} S cm^{-1}.[110] The difference in ionic conductivity is attributed to the vacancies arrangement in both structures. In Garnet structured LLZO, Li-vacancies are completely disordered which creates more pathways for lithium ions when compared to the tetragonal LLZO where the vacancies are completely in order.[110] In the last decade, researchers continued their efforts to slightly improve the garnet LLZO further by the substitution of other metals for Zr atoms. [111–113] Despite the amazing properties garnets exhibit and include high ambient ionic conductivity and stability against lithium metals, they suffer from severely high interfacial resistance at both the anode and cathode side. This is attributed to the poor contact between the materials as they are both hard solids and this can lead to large overpotential building inside the battery during cycling.[114]

Sulfide solid electrolytes

Li_2S-SiS_2 system

This system was first discovered in 1986 by Kennedy et al. by the melting-quench technique and its conductivity was first reported at 1.2×10^{-4} S cm^{-1} at 25°C and it increases when doped with different lithium halides. The highest ionic conductivity (1.8 x 10^{-3} S cm^{-1})

was achieved by doping the electrolyte system with LiI but this electrolyte did not show great electrochemical stability [115] Since then, many researchers have tried different synthesis and doping techniques to try and improve the ionic conductivity and stability including synthesis by high energy ball milling technique and doping with Al_2S_3, $LiPO_4$ and Li_2SO_4.[116–119] All dopants assisted in stabilizing the solid electrolyte against electrochemical reduction but, none were able to surpass the ionic conductivity reported first by Kennedy in 1986.

Li_2S-P_2S_5 system

Despite the conductivity of pure Li_2S-P_2S_5 prepared by solid phase reaction has very low conductivity, amorphous Li_2S-P_2S_5 prepared by melt quenching or mechanical milling has very high ionic conductivity and could improve even further when crystal phases are formed by glass crystallization.[120] This further enhancement in ionic conductivity in glass-ceramics is due to the formation metastable crystalline phase.[121] 80%Li_2S-20%P_2S_5 (mol%) highly dense glass-ceramics reported ionic conductivity of 10^{-3} S cm^{-1} at room temperature. It is important to note that small changes in preparation conditions can lead to different structures of Li_2S-P_2S_5. When preparing Li_3PS_4 using high temperature solid reaction, the highly conductive β-Li_3PS_4 is obtained above 190 °C but is transformed to the poorly conductive γ-Li_3PS_4 below that temperature.[122] However, in 2013 Liu et al. were able to stabilize β-Li_3PS_4 in a porous structure at room temperature attaining a conductivity of 1.6 x 10^{-4} S cm^{-1} that can be improved up to 6.3 x 10^{-4} S cm^{-1} with LiI doping.[123] Unfortunately, most Li_2S-P_2S_5 systems are chemically unstable and susceptible to reactions with water producing H_2S gas.[124]

Composite solid-state electrolytes (CSE)

In pursuit to find the ultimate solid electrolyte that will radically solve the issues of safety, enable high energy density lithium batteries and enable us to transition to EVs with confidence, researchers have found no solution better than combining the advantages of both ISEs and SPEs together to make CSEs. An ideal CSE would be one that exhibit high ionic conductivity, mechanical flexibility, high energy density, chemical and electrochemical stability, long cycle life and ease of processability. Generally, CSEs can be labelled as either ‘polymer-in-ceramic’ or ‘ceramic-in-polymer’ depending on the dominant phase in the electrolyte. Notably, most CSEs developed to date are composed of polymers, salts and ceramics as active fillers (or as the dominant phase). Seldom to find CSEs that employ these 3 components along with passive fillers as well to create quaternary CSEs.

The ion conduction mechanism across CSEs where both a polymer matrix and a ceramic crystalline structure are present is a debatable topic. One of the best attempts to

explain it practically was done by He et al [125] by tracing the lithium ions pathway through a CSE by $^{6,7}Li$ nuclear magnetic resonance (NMR). Their CSE consisted of PEO as the polymer, $LiClO_4$ salt and LLZO as the ceramic active filler. NMR technique has proved to be of adequate sensitivity to detect lithium ion dynamics and local structural environments. [126][127] They first applied high resolution NMR to establish the local structural environment of the ions in the polymer matrix, the ceramic phase and polymer-ceramic interphase. This was possible as both ^{6}Li and ^{7}Li are active NMR isotopes which allowed them to detect the pathways by observing isotope exchange. As presented in Fig 2.14 a, both pure PEO-$LiClO_4$ polymer and LLZO ceramic have single ^{6}Li resonance peaks while the CSE has an additional ^{6}Li resonance peak which indicates the presence of a third phase. Fig. 2.14 b presents the potential lithium ions local environment inside the CSE. The CSE was then electrochemically cycled while sandwiched between ^{6}Li foil. The ions were stripped from one side and deposited on the opposite side because of an applied potential. As ^{6}Li ions move through the electrolyte, they momentarily replace ^{7}Li inside the different CSE phases which leaves a detectable trail for the ions path. Further, comparing the NMR data for pristine and cycled CSE allows us to accurately know the Li ion pathway through the CSE. Fig. 2.14 c indicates the LLZO resonance intensification after cycling while no similar intensification was observed for the polymer and the polymer-ceramic interface. Fig 2.14 d provides the quantification of the resonance change before (pristine) and after cycling. These results suggest that Li ions prefer to diffuse through LLZO phase rather than the polymer or the polymer-ceramic phase. However, it is worth to note the LLZO concentration in this study was 50% and that a study with less ceramic concentration (5%) showed totally different results. Chan et al [128] used the same NMR technique on a CSE consisting of Polyacrylonitrile PAN polymer, $LiClO_4$ salt and 5 wt. % LLZO nanowires. They explained the low concentration was essential to maintain the best ionic conductivity. Adding more LLZO nanowires led to reduction in ionic conductivity because of agglomeration. In this case, the comparison between the ^{6}Li NMR of the pristine and the cycled CSE indicated that the Li ions preferred to transfer through the modified PAN interface instead of the ceramic phase as depicted in Fig 2.14 f. The difference in results between the studies was attributed to the fact that a connected percolation network of ceramic phase did form when the active ceramic concentration was high (50%) but not when it was low (5%).

Recently, Fu et al[129] created a novel 3D hierarchical CSE using $Li_{6.28}La_3Zr_2Al_{0.24}O_{12}$ (LLZAO) as the ceramic active filler. They inserted a flexible film of PEO/$LiClO_4$ in a 3d porous network of LLZAO network by using a cleanroom wiper as the template. The obtained

3D CSE showed almost 31 times higher conductivity (2.25 x 10^{-5} S/cm) than the pristine PEO/$LiClO_4$ electrolyte at 30 °C. The main contributor to conductivity enhancement in this 3D CSE is the porous LLZAO structure which provides faster ionic transport pathways. Fu et al also reported that the 3D network successfully inhibits lithium dendrite formation which led to the desired safety and superb stability during lithium cycling. Charging and discharging the battery at 1 C rate using this CSE kept 86% of its initial discharge capacity of 143.8 mAh.g^{-1} after 200 cycles. Cai et al [130] reported on a very similar 3D CSE. It is only different because it uses PEO/LiTFSI as the base polymer. They reported a conductivity of 2.51 x 10^{-4} S/cm at room temperature, an initial discharge capacity of 165.9 mAh.g^{-1} at 0.2 C and 80% capacity retention after 100 cycles.

Moreover, Zhang et al [131] have reported on one of the few quaternary CSEs that employ both active and passive fillers. The active filler they used was the inorganic ceramic lithium aluminate (LAO) in the form of micro-rods while the passive filler was the solid plasticizer succinonitrile (SN). They varied the concentrations of both fillers and reported 10% and 15% active and passive filler as optimum concentrations, respectively. The resulting quaternary CSE has a maximized conductivity of 1.36 x 10^{-5} S/cm at 30 °C. The solid-state lithium batteries delivered an initial discharge capacity of 141.3 mAh.g^{-1} and maintained a coulombic efficiency of around 97 % after 25 cycles. Al-Salih et al[90] reported on another CSE that incorporates a different active filler. The active filler they used is lithium lanthanum Titanium Oxide (LLTO). However, this quaternary CSE reported a higher ionic conductivity at around 2 x 10^{-4} S/cm at room temperature. The all-solid-state battery delivered 143.2 mAh.g^{-1} and maintained a coulombic efficiency of around 99% after 30 cycles.

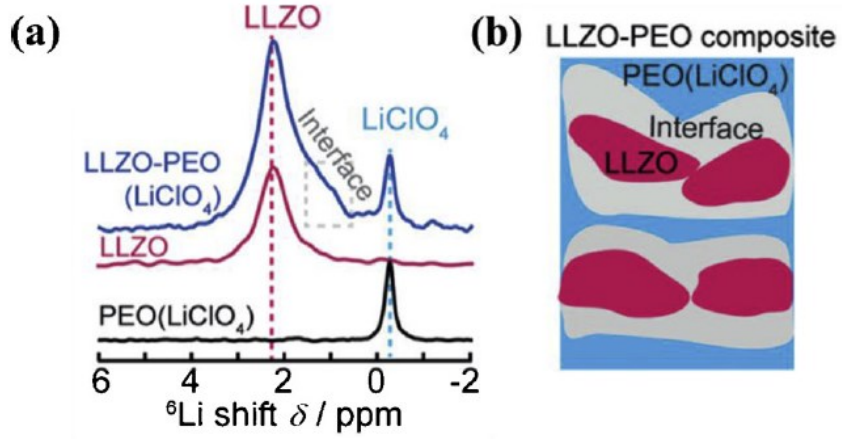

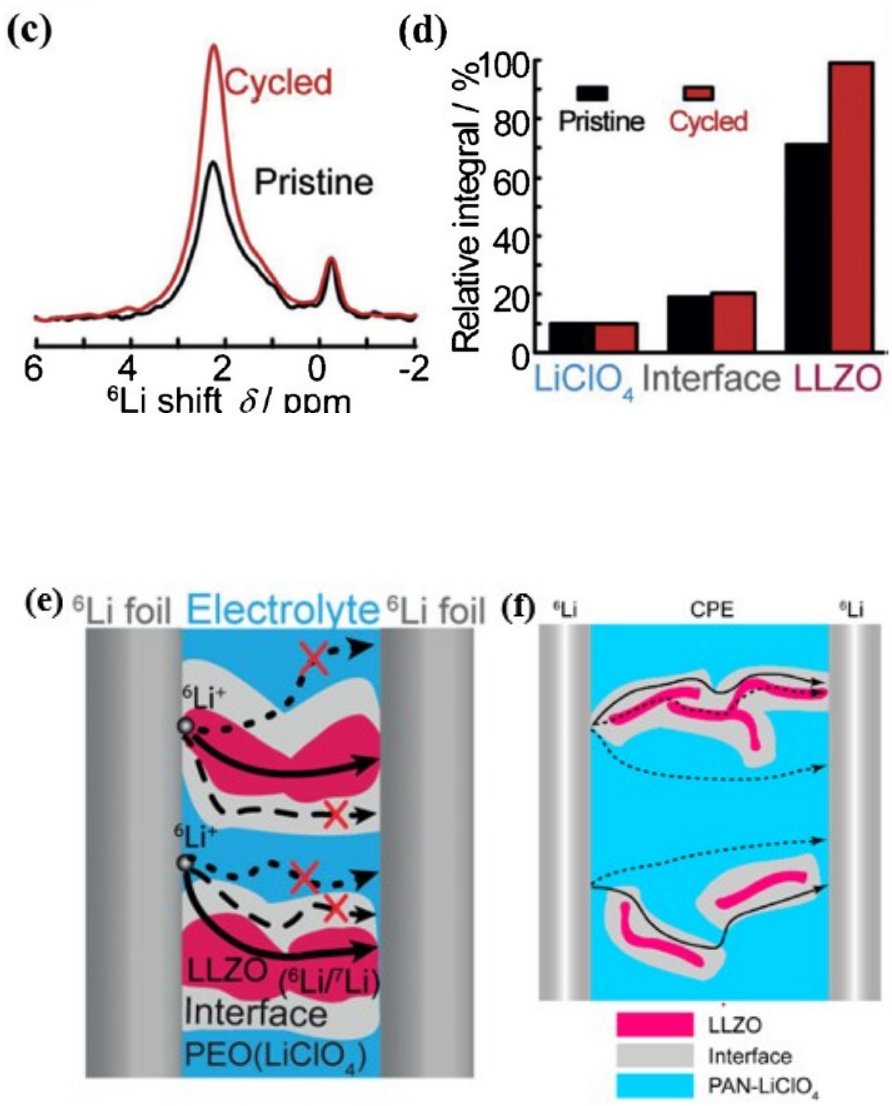

Figure 2.14: (a) ^{6}Li NMR of $LiClO_4$ in PEO, cubic LLZO, and

LLZO/PEO(LiClO4) CSE (b) Sketch of local Li environments in LLZO/PEO (LiClO4) CSE (c) Comparison of the ^{6}Li NMR spectra of the LLZO/PEO(LiClO4) CSEs before and after cycling (d) Analysis of ^{6}Li amount in LiClO4, interface, and LLZO of the LLZO/PEO(LiClO4) before and after cycling (e) Illustration of the possible Li+ transport pathways within the CSE upon cycling the battery by He et al[125] (f) Illustration of the possible Li+ transport pathways within the CSE upon cycling the battery by Chan et al Adapted with permission from [128] Copyright ©

References

[1] W. M. Sudduth, *Ambix* **1980**, *27*, 26.

[2] T. Smolinka, H. Bergmann, J. Garche, M. Kusnezoff, *Electrochem. Power Sources Fundam. Syst. Appl. Hydrog. Prod. by Water Electrolysis* **2022**, 83.

[3] A. A. Mills, *http://dx.doi.org/10.1080/00033790110117566* **2010**, *60*, 373.

[4] P. Kurzweil, *J. Power Sources* **2010**, *195*, 4424.

[5] S. Petrovic, *Batter. Technol. Crash Course* **2021**, 73.

[6] S. Raghav, J. Raghav, P. K. Yadav, D. Kumar, 357.

[7] N. Furukawa, *J. Power Sources* **1994**, *51*, 45.

[8] W. van Schalkwijk, B. Scrosati, *Adv. Lithium-Ion Batter.* **2002**, 1.

[9] H. Wang, S. Chen, C. Fu, Y. Ding, G. Liu, Y. Cao, Z. Chen, *ACS Mater. Lett.* **2021**, *3*, 956.

[10] K. Yanamandra, D. Pinisetty, A. Daoud, N. Gupta, *J. Indian Inst. Sci.* **2022**, *102*, 281.

[11] Grand View research, Battery Market Size, Share, Growth & Trends Report, 2030, https://www.grandviewresearch.com/industry-analysis/battery-market.

[12] A. Yoshino, *https://doi.org/10.1246/bcsj.20210338* **2022**, *95*, 195.

[13] K. Xu, *Chem. Rev.* **2004**, *104*, 4303.

[14] E. Peled, S. Menkin, *J. Electrochem. Soc.* **2017**, *164*, A1703.

[15] A. M. Haregewoin, A. S. Wotango, B. J. Hwang, *Energy Environ. Sci.* **2016**, *9*, 1955.

[16] T. Jaumann, J. Balach, U. Langklotz, V. Sauchuk, M. Fritsch, A. Michaelis, V. Teltevskij, D. Mikhailova, S. Oswald, M. Klose, G. Stephani, R. Hauser, J. Eckert, L. Giebeler, *Energy Storage Mater.* **2017**, *6*, 26.

[17] Y. Liu, R. Zhang, J. Wang, Y. Wang, *iScience* **2021**, *24*, 102332.

[18] T. Lv, L. Suo, *Curr. Opin. Electrochem.* **2021**, *29*, 100818.

[19] H. Seki, K. Yoshima, Y. Yamashita, S. Matsuno, N. Takami, *J. Power Sources* **2021**, *482*, 228950.

[20] E. DeJong, K. Edwards, E. Fischer, R. Garstang, A. Harch, S. Kadel, R. Kirk, J. Moersch, J. Plutchak, M. Robinson, R. Sullivan, W. Sullivan, J. Sunshine, S. Vail, L. Wainio, D. Wil-liams, J. Yoshimizu, W. Li, J. R. Dahn, D. S. Wainwright, W. Li, S. Crescent, M. Ridge, *Science (80-.).* **1994**, *264*, 1115.

[21] A. von Wald Cresce, K. Xu, *Carbon Energy* **2021**, *3*, 721.

[22] L. Suo, O. Borodin, T. Gao, M. Olguin, J. Ho, X. Fan, C. Luo, C. Wang, K. Xu, *Science (80-.).* **2015**, *350*, 938.

[23] J. Zheng, G. Tan, P. Shan, T. Liu, J. Hu, Y. Feng, L. Yang, M. Zhang, Z. Chen, Y. Lin, J. Lu, J. C. Neuefeind, Y. Ren, K. Amine, L. W. Wang, K. Xu, F. Pan, *Chem* **2018**, *4*, 2872.

[24] E. Brini, C. J. Fennell, M. Fernandez-Serra, B. Hribar-Lee, M. Lukšič, K. A. Dill, *Chem. Rev.* **2017**, *117*, 12385.

[25] K. P. Jensen, W. L. Jorgensen, *J. Chem. Theory Comput.* **2006**, *2*, 1499.

[26] W. L. Jorgensen, J. Tirado-Rives, *Proc. Natl. Acad. Sci. U. S. A.* **2005**, *102*, 6665.

[27] G. A. Kaminski, R. A. Friesner, J. Tirado-Rives, W. L. Jorgensen, *J. Phys. Chem. B* **2001**, *105*, 6474.

[28] A. D. MacKerell, D. Bashford, M. Bellott, R. L. Dunbrack, J. D. Evanseck, M. J. Field, S. Fischer, J. Gao, H. Guo, S. Ha, D. Joseph-McCarthy, L. Kuchnir, K. Kuczera, F. T. K. Lau, C. Mattos, S. Michnick, T. Ngo, D. T. Nguyen, B. Prodhom, W. E. Reiher, B. Roux, M. Schlenkrich, J. C. Smith, R. Stote, J. Straub, M. Watanabe, J. Wiórkiewicz-Kuczera, D. Yin, M. Karplus, *J. Phys. Chem. B* **1998**, *102*, 3586.

[29] H. J. C. Berendsen, J. P. M. Postma, W. F. van Gunsteren, J. Hermans, **1981**, 331.

[30] J. Mähler, I. Persson, *Inorg. Chem.* **2012**, *51*, 425.

[31] S. F. Lux, L. Terborg, O. Hachmöller, T. Placke, H.-W. Meyer, S. Passerini, M. Winter, S. Nowak, *J. Electrochem. Soc.* **2013**, *160*, A1694.

[32] D. Zeng, J. Ming, W. Voigt, *J. Chem. Thermodyn.* **2008**, *40*, 232.

[33] J. Sohr, W. Voigt, D. Zeng, *J. Phys. Chem. Ref. Data* **2017**, *46*.

[34] Y. Zhang, N. H. C. Lewis, J. Mars, G. Wan, N. J. Weadock, C. J. Takacs, M. R. Lukatskaya, H. G. Steinrück, M. F. Toney, A. Tokmakoff, E. J. Maginn, *J. Phys. Chem. B* **2021**, *125*, 4501.

[35] O. Borodin, L. Suo, M. Gobet, X. Ren, F. Wang, A. Faraone, J. Peng, M. Olguin, M. Schroeder, M. S. Ding, E. Gobrogge, A. Von Wald Cresce, S. Munoz, J. A. Dura, S. Greenbaum, C. Wang, K. Xu, *ACS Nano* **2017**, *11*, 10462.

[36] M. McEldrew, Z. A. H. Goodwin, S. Bi, A. A. Kornyshev, M. Z. Bazant, *J. Electrochem. Soc.* **2021**, *168*, 050514.

[37] D. Degoulange, N. Dubouis, A. Grimaud, *J. Chem. Phys.* **2021**, *155*, 064701.

[38] L. Droguet, A. Grimaud, O. Fontaine, J. M. Tarascon, *Adv. Energy Mater.* **2020**, *10*, 2002440.

[39] N. Dubouis, A. Serva, E. Salager, M. Deschamps, M. Salanne, A. Grimaud, *J. Phys. Chem. Lett.* **2018**, *9*, 6683.

[40] Y. Yamada, K. Usui, K. Sodeyama, S. Ko, Y. Tateyama, A. Yamada, *Nat. Energy 2016 110* **2016**, *1*, 1.

[41] K. Yoshida, M. Nakamura, Y. Kazue, N. Tachikawa, S. Tsuzuki, S. Seki, K. Dokko, M. Watanabe, *J. Am. Chem. Soc.* **2011**, *133*, 13121.

[42] H.-G. Steinrück, C. Cao, M. R. Lukatskaya, C. J. Takacs, G. Wan, D. G. Mackanic, Y. Tsao, J. Zhao, B. A. Helms, K. Xu, O. Borodin, J. F. Wishart, M. F. Toney, *Angew. Chemie* **2020**, *132*, 23380.

[43] D. Çirmi, R. Aydin, F. Köleli, *J. Electroanal. Chem.* **2015**, *736*, 101.

[44] F. Habashi, S. A. Mikhail, K. V. Van, *https://doi.org/10.1139/v76-524* **2011**, *54*, 3646.

[45] L. Suo, D. Oh, Y. Lin, Z. Zhuo, O. Borodin, T. Gao, F. Wang, A. Kushima, Z. Wang, H. C. Kim, Y. Qi, W. Yang, F. Pan, J. Li, K. Xu, C. Wang, *J. Am. Chem. Soc.* **2017**, *139*, 18670.

[46] S. Ko, Y. Yamada, A. Yamada, *ACS Appl. Mater. Interfaces* **2019**, *11*, 45554.

[47] N. Dubouis, P. Lemaire, B. Mirvaux, E. Salager, M. Deschamps, A. Grimaud, *Energy Environ. Sci.* **2018**, *11*, 3491.

[48] R. Bouchal, Z. Li, C. Bongu, S. Le Vot, R. Berthelot, B. Rotenberg, F. Favier, S. A. Freunberger, M. Salanne, O. Fontaine, R. Bouchal, C. Bongu, S. Le Vot, R. Berthelot, F. Favier, O. Fontaine, Z. Li, B. Rotenberg, M. Salanne, S. A. Freunberger, *Angew. Chemie* **2020**, *132*, 16047.

[49] C.-H. Yim, J. Tam, H. Soboleski, Y. Abu-Lebdeh, *J. Electrochem. Soc.* **2017**, *164*, A1002.

[50] F. Wang, L. Suo, Y. Liang, C. Yang, F. Han, T. Gao, W. Sun, C. Wang, F. Wang, L. Suo, Y. Liang, C. Yang, F. Han, T. Gao, W. Sun, C. Wang, *Adv. Energy Mater.* **2017**, *7*, 1600922.

[51] F. Wang, Y. Lin, L. Suo, X. Fan, T. Gao, C. Yang, F. Han, Y. Qi, K. Xu, C. Wang, *Energy Environ. Sci.* **2016**, *9*, 3666.

[52] C. A. Angell, *J. Electrochem. Soc.* **1965**, *112*, 1224.

[53] L. Suo, O. Borodin, W. Sun, X. Fan, C. Yang, F. Wang, T. Gao, Z. Ma, M. Schroeder, A. von Cresce, S. M. Russell, M. Armand, A. Angell, K. Xu, C. Wang, *Angew. Chemie* **2016**, *128*, 7252.

[54] S. Ko, Y. Yamada, K. Miyazaki, T. Shimada, E. Watanabe, Y. Tateyama, T. Kamiya, T. Honda, J. Akikusa, A. Yamada, *Electrochem. commun.* **2019**, *104*, 106488.

[55] M. Becker, R.-S. Kü, C. Battaglia, R. Li, / Chemcomm, C. Communication, *Chem. Commun.* **2019**, *55*, 12032.

[56] J. Chen, J. Vatamanu, L. Xing, O. Borodin, H. Chen, X. Guan, X. Liu, K. Xu, W. Li, J. Chen, L. Xing, H. Chen, X. Guan, X. Liu, W. Li, J. Vatamanu, O. Borodin, K. Xu, *Adv. Energy Mater.* **2020**, *10*, 1902654.

[57] F. Wang, O. Borodin, M. S. Ding, M. Gobet, J. Vatamanu, X. Fan, T. Gao, N. Edison, Y. Liang, W. Sun, S. Greenbaum, K. Xu, C. Wang, *Joule* **2018**, *2*, 927.

[58] M. Becker, D. Rentsch, D. Reber, A. Aribia, C. Battaglia, R. S. Kühnel, *Angew. Chemie Int. Ed.* **2021**, *60*, 14100.

[59] L. Chen, J. Zhang, Q. Li, J. Vatamanu, X. Ji, T. P. Pollard, C. Cui, S. Hou, J. Chen, C. Yang, L. Ma, M. S. Ding, M. Garaga, S. Greenbaum, H. S. Lee, O. Borodin, K. Xu, C. Wang, *ACS Energy Lett.* **2020**, *5*, 968.

[60] J. Yue, L. Lin, L. Jiang, Q. Zhang, Y. Tong, L. Suo, Y. sheng Hu, H. Li, X. Huang, L. Chen, *Adv. Energy Mater.* **2020**, *10*, 2000665.

[61] J. Xu, X. Ji, J. Zhang, C. Yang, P. Wang, S. Liu, K. Ludwig, F. Chen, P. Kofinas, C. Wang, *Nat. Energy 2022 72* **2022**, *7*, 186.

[62] R. Lin, C. Ke, J. Chen, S. Liu, J. Wang, *Joule* **2022**, *6*, 399.

[63] J. Xie, Z. Liang, Y. C. Lu, *Nat. Mater. 2020 199* **2020**, *19*, 1006.

[64] X. Hou, X. Ju, W. Zhao, J. Wang, X. He, L. Du, B. Yan, J. Li, E. Paillard, J. Sun, H. Lin, M. Winter, J. Li, *J. Power Sources* **2021**, *484*, 229255.

[65] X. Hou, R. Wang, X. He, T. P. Pollard, X. Ju, L. Du, E. Paillard, H. Frielinghaus, L. C. Barnsley, O. Borodin, K. Xu, M. Winter, J. Li, *Angew. Chemie Int. Ed.* **2021**, *60*, 22812.

[66] X. Hou, T. P. Pollard, W. Zhao, X. He, X. Ju, J. Wang, L. Du, E. Paillard, H. Lin, K. Xu, O. Borodin, M. Winter, J. Li, *Small* **2022**, *18*, 2104986.

[67] M. R. Lukatskaya, J. I. Feldblyum, D. G. Mackanic, F. Lissel, D. L. Michels, Y. Cui, Z. Bao, *Energy Environ. Sci.* **2018**, *11*, 2876.

[68] D. Reber, O. Borodin, M. Becker, D. Rentsch, J. H. Thienenkamp, R. Grissa, W. Zhao, A. Aribia, G. Brunklaus, C. Battaglia, R.-S. Kühnel, D. Reber, M. Becker, D. Rentsch, R. Grissa, W. Zhao, A. Aribia, C. Battaglia, R.-S. Kühnel Empa, O. Borodin, E. Zurich, J. H. Thienenkamp, G. Brunklaus, *Adv. Funct. Mater.* **2022**, *32*, 2112138.

[69] C. Yang, J. Chen, T. Qing, X. Fan, W. Sun, A. von Cresce, M. S. Ding, O. Borodin, J. Vatamanu, M. A. Schroeder, N. Eidson, C. Wang, K. Xu, *Joule* **2017**, *1*, 122.

[70] W. Sun, L. Suo, F. Wang, N. Eidson, C. Yang, F. Han, Z. Ma, T. Gao, M. Zhu, C. Wang, *Electrochem. commun.* **2017**, *82*, 71.

[71] A. Zhou, Y. Liu, X. Zhu, X. Li, J. Yue, X. Ma, L. Gu, Y. S. Hu, H. Li, X. Huang, L. Chen, L. Suo, *Energy Storage Mater.* **2021**, *42*, 438.

[72] D. E. Fenton, J. M. Parker, P. V. Wright, *Polymer (Guildf).* **1973**, *14*, 589.

[73] M. Armand, *Solid State Ionics* **1983**, *9–10*, 745.

[74] R. Chen, W. Qu, X. Guo, L. Li, F. Wu, The pursuit of solid-state electrolytes for lithium batteries: From comprehensive insight to emerging horizons. *Mater. Horizons* **2016**, *3*, 487–516.

[75] I. E. Animitsa, A. L. Kruglyashov, O. V. Bushkova, V. M. Zhukovsky, *Solid State Ionics* **1998**, *106*, 321.

[76] Z. Gadjourova, Y. G. Andreev, D. P. Tunstall, P. G. Bruce, *Nature* **2001**, *412*, 520.

[77] W. H. Meyer, *Adv. Mater.* **1998**, *10*, 439.

[78] Y. Wang, W.-H. Zhong, *ChemElectroChem* **2015**, *2*, 22.

[79] J. G. Kim, B. Son, S. Mukherjee, N. Schuppert, A. Bates, O. Kwon, M. J. Choi, H. Y. Chung, S. Park, A review of lithium and non-lithium based solid state batteries. *J. Power Sources* **2015**, *282*, 299–322.

[80] Y. Ito, K. Kanehori, K. Miyauchi, T. Kudo, *J. Mater. Sci.* **1987**, *22*, 1845.

[81] T. J. Benedict, S. Banumathi, A. Veluchamy, R. Gangadharan, A. Z. Ahamad, S. Rajendran, *J. Power Sources* **1998**, *75*, 171.

[82] F. Croce, G. B. Appetecchi, L. Persi, B. Scrosati, *Nature* **1998**, *394*, 456.

[83] H. M. Xiong, K. K. Zhao, X. Zhao, Y. W. Wang, J. S. Chen, *Solid State Ionics* **2003**, *159*, 89.

[84] F. Croce, R. Curini, A. Martinelli, L. Persi, F. Ronci, B. Scrosati, R. Caminiti, *J. Phys. Chem. B* **1999**, *103*, 10632.

[85] H. M. Xiong, X. Zhao, J. S. Chen, *J. Phys. Chem. B* **2001**, *105*, 10169.

[86] M. Hema, S. Selvasekarapandian, D. Arunkumar, A. Sakunthala, H. Nithya, *J. Non. Cryst. Solids* **2009**, *355*, 84.

[87] M. Armand, *Solid State Ionics* **1994**, *69*, 309.

[88] M. B. Armand, *Annu. Rev. Mater. Sci.* **1986**, *16*, 245.

[89] G. P. P. R C Agrawal, *J. Phys. D. Appl. Phys.* **2008**, *41*.

[90] H. Al-Salih, A. Huang, C.-H. Yim, A. I. Freytag, G. R. Goward, E. Baranova, Y. Abu-Lebdeh, *J. Electrochem. Soc.* **2020**, *167*, 070557.

[91] E. Quartarone, P. Mustarelli, A. Magistris, *Solid State Ionics* **1998**, *110*, 1.

[92] C. Berthier, W. Gorecki, M. Minier, … M. A.-S. S., undefined 1983, *academia.edu*.

[93] J. C. Bachman, S. Muy, A. Grimaud, H. H. Chang, N. Pour, S. F. Lux, O. Paschos, F. Maglia, S. Lupart, P. Lamp, L. Giordano, Y. Shao-Horn, Inorganic Solid-State Electrolytes for Lithium Batteries: Mechanisms and Properties Governing Ion Conduction. *Chem. Rev.* **2016**, *116*, 140–162.

[94] B. H. X. Yao, *Chinese Phys. B* **2015**, *25*.

[95] A. S. Bhalla, R. Guo, R. Roy, The perovskite structure - A review of its role in ceramic science and technology. *Mater. Res. Innov.* **2000**, *4*, 3–26.

[96] Y. Inaguma, C. Liquan, M. Itoh, T. Nakamura, T. Uchida, H. Ikuta, M. Wakihara, *Solid State Commun.* **1993**, *86*, 689.

[97] L. Hagman, P. Kierkegaard, P. K.-A. C. Scand, undefined 1968, *actachemscand.org*.

[98] T. Pareek, S. Dwivedi, B. Singh, D. Kumar, P. Kumar, S. Kumar, *J. Alloys Compd.* **2019**, *777*, 602.

[99] V. Thangadurai, W. Weppner, *Ionics (Kiel).* **2006**, *12*, 81.

[100] M. A. Subramanian, R. Subramanian, A. Clearfield, *Solid State Ionics* **1986**, *18–19*, 562.

[101] H. Aono, E. Sugimoto, Y. Sadaoka, N. Imanaka, G. ya Adachi, *Solid State Ionics* **1990**, *40–41*, 38.

[102] M. Hou, F. Liang, K. Chen, Y. Dai, D. Xue, *Nanotechnology* **2020**, *31*, 132003.

[103] X. Xu, Z. Wen, X. Wu, X. Yang, Z. Gu, *J. Am. Ceram. Soc.* **2007**, *90*, 2802.

[104] J. Fu, *Solid State Ionics* **1997**, *104*, 191.

[105] D. Mazza, *Mater. Lett.* **1988**, *7*, 205.

[106] E. J. Cussen, *Chem. Commun.* **2006**, 412.

[107] V. Thangadurai, W. Weppner, *Adv. Funct. Mater.* **2005**, *15*, 107.

[108] V. Thangadurai, W. Weppner, *J. Am. Ceram. Soc.* **2005**, *88*, 411.

[109] R. Murugan, V. Thangadurai, W. Weppner, *Angew. Chemie - Int. Ed.* **2007**, *46*, 7778.

[110] J. Awaka, N. Kijima, H. Hayakawa, J. Akimoto, *J. Solid State Chem.* **2009**, *182*, 2046.

[111] R. Murugan, S. Ramakumar, N. Janani, *Electrochem. commun.* **2011**, *13*, 1373.

[112] S. Ohta, T. Kobayashi, T. Asaoka, *J. Power Sources* **2011**, *196*, 3342.

[113] C. Deviannapoorani, L. Dhivya, S. Ramakumar, R. Murugan, *J. Power Sources* **2013**, *240*, 18.

[114] B. Liu, Y. Gong, K. Fu, X. Han, Y. Yao, G. Pastel, C. Yang, H. Xie, E. D. Wachsman, L. Hu, *ACS Appl. Mater. Interfaces* **2017**, *9*, 18809.

[115] J. H. Kennedy, S. Sahami, S. W. Shea, Z. Zhang, *Solid State Ionics* **1986**, *18–19*, 368.

[116] H. Morimoto, H. Yamashita, M. Tatsumisago, T. Minami, *J. Am. Ceram. Soc.* **2004**, *82*, 1352.

[117] V. K. Deshpande, A. Pradel, M. Ribes, *Solid State Ionics* **1988**, *28–30*, 756.

[118] S. Kondo, K. Takada, Y. Yamamura, *Solid State Ionics* **1992**, *53–56*, 1183.

[119] F. Mizuno, A. Hayashi, K. Tadanaga, T. Minami, M. Tatsumisago, "All-solid-state lithium secondary batteries using Li2S-SiS 2-Li4SiO4 glasses and Li2S-P 2S5 glass ceramics as solid electrolytes," Solid State Ionics, Elsevier, 30 November **2004**.

[120] F. Mizuno, A. Hayashi, K. Tadanaga, M. Tatsumisago, *Adv. Mater.* **2005**, *17*, 918.

[121] F. Mizuno, A. Hayashi, K. Tadanaga, M. Tatsumisago, *Solid State Ionics* **2006**, *177*, 2721.

[122] M. Tachez, J. P. Malugani, R. Mercier, G. Robert, *Solid State Ionics* **1984**, *14*, 181.

[123] Z. Liu, W. Fu, E. A. Payzant, X. Yu, Z. Wu, N. J. Dudney, J. Kiggans, K. Hong, A. J. Rondinone, C. Liang, *J. Am. Chem. Soc.* **2013**, *135*, 975.

[124] H. Muramatsu, A. Hayashi, T. Ohtomo, S. Hama, M. Tatsumisago, *Solid State Ionics* **2011**, *182*, 116.

[125] J. Zheng, M. Tang, Y.-Y. Hu, *Angew. Chemie Int. Ed.* **2016**, *55*, 12538.

[126] A. J. Ilott, N. M. Trease, C. P. Grey, A. Jerschow, *Nat. Commun.* **2014**, *5*, 1.

[127] W. Schmidt, P. Bottke, M. Sternad, P. Gollob, V. Hennige, M. Wilkening, *Chem. Mater.* **2015**, *27*, 1740.

[128] T. Yang, J. Zheng, Q. Cheng, Y. Y. Hu, C. K. Chan, *ACS Appl. Mater. Interfaces* **2017**, *9*, 21773.

[129] X. Fu, Y. Li, C. Liao, W. Gong, M. Yang, R. K. Y. Li, S. C. Tjong, Z. Lu, *Compos. Sci. Technol.* **2019**, *184*, 107863.

[130] D. Cai, D. Wang, Y. Chen, S. Zhang, X. Wang, X. Xia, J. Tu, *Chem. Eng. J.* **2020**, 124993.

[131] N. Zhang, J. He, W. Han, Y. Wang, *J. Mater. Sci.* **2019**, *54*, 9603.

[132] S. Peng, F. Zeng, Y. Wang, Q. Liu, A. Xue, E. Cai, F. Mou, *J. Mater. Sci. Mater. Electron.* **2020**, *31*, 16235.

[133] N. Kuganathan, M. J. D. Rushton, R. W. Grimes, J. A. Kilner, E. I. Gkanas, A. Chroneos, *Sci. Reports 2021 111* **2021**, *11*, 1.

Chapter 3: Unraveling the Phase Diagram-Ion Transport Relationship in Aqueous Electrolyte Solutions and Correlating Conductivity with Concentration and Temperature by Semi-Empirical Modeling

Adapted from: Al-Salih, H.; Baranova, E.; Abu-Lebdeh, Y. communications chemistry **2023**

Abstract

The relationship between structure and ion transport in liquid electrolyte solutions is not well understood over the whole concentration and temperature ranges. In this work, we have studied the ionic conductivity (κ) as a function of molar ratio (x) and Temperature (T) for aqueous solutions of salts with nitrate anion and different cations (proton, lithium, calcium, and ammonium) along with their liquid-solid phase diagrams. The connection between the known structural changes in the phase diagrams and the ionic conductivity isotherms is established with an insight on the conductivity mechanism. Also, known isothermal (κ vs. x) and iso-compositional (κ vs. T) equations along with a newly proposed two variables semi-empirical model (κ = f (x, T)) were fitted to the collected data to validate their accuracy. The role of activation energy in controlling ionic conductivity is discussed. This work brings us closer to the development of a phenomenological model to describe the structure and transport in liquid electrolyte solutions.

Keywords: nitrates, aqueous electrolyte, liquid solution structure, phase diagram, ionic conductivity, electrolyte model

Introduction

The exact structure of liquid electrolyte solutions is still not known due to their very disordered nature despite recent advancements in characterization techniques.[1] In their review of the structure of electrolyte solutions, Enderby and Neilson[2] highlighted the challenges in understanding the microstructure of liquid solutions, a sentiment shared by many scientists at the time. C. Angel, one prominent scientist in the field, described the lack of a model or theory that can successfully extend or replace the long-standing Debye-Hückel theory, which only applies to very low concentrations (mM), as the most celebrated failure in physical chemistry.[3] However, over the years there have been many serious attempts to extend and apply the theory to higher concentrations but were not overly successful. This topic has become of great interest recently as high concentrations (c) or molar ratios (x) of electrolyte solutions are required so that practical high ionic conductivities of 10^{-3} - 10^{-2} S cm^{-1} are achieved which often occurs at a concentration or molar ratio of highest (maximum) conductivity (c_{max} or x_{max}) in the isothermal conductivity vs composition plots. This concentration has not been given much significance in the past but recently a lot of research is focused on electrolyte solutions with higher concentrations beyond x_{max} due to improved physiochemical and electrochemical performance.[4,5]

It was shown by many researchers that the structure of liquid electrolyte solutions depends on the type of the salt and solvent and their concentration and temperature.[6] It is widely accepted that at very low concentration ions are well separated into free ions while at low concentrations the salt dissociates into ions that are separated into solvated and unsolved ion pairs (IP) of different types (contact, solvent separated and solvent shared) into a bulk solvent. As the concentration is increased fewer solvent molecules are available so the IPs can associate into larger ion clusters (ICs). Fig 3.1 shows possible structures of the different IPs and ICs that can exist in electrolyte solutions at different concentrations. This change in ion speciation has an impact on transport properties of the solution. Ionic conductivity in particular is one of the most important transport properties of liquid electrolyte solutions that qualify them for applications in many electrochemical devices.

Abu-Lebdeh et al[7] have recently showed that the strong dependence of ionic conductivity on electrolyte concentration in aqueous and non-aqueous solutions can be correlated to the liquid -solid (salt/solvent) binary phase diagram. It was shown that the presence of a maxima in the bell-shaped, isothermal conductivity vs. concentration plots is a common feature in liquid electrolyte solutions and also solid electrolytes.[5] This was given a significance, contrary to what was proposed by Angel,[8] and was attributed to a transition in the structure of the solution from the ionic atmosphere structure where transport is dominated by solvated ionic species (different types of IPs) diffusing or migrating by a vehicular

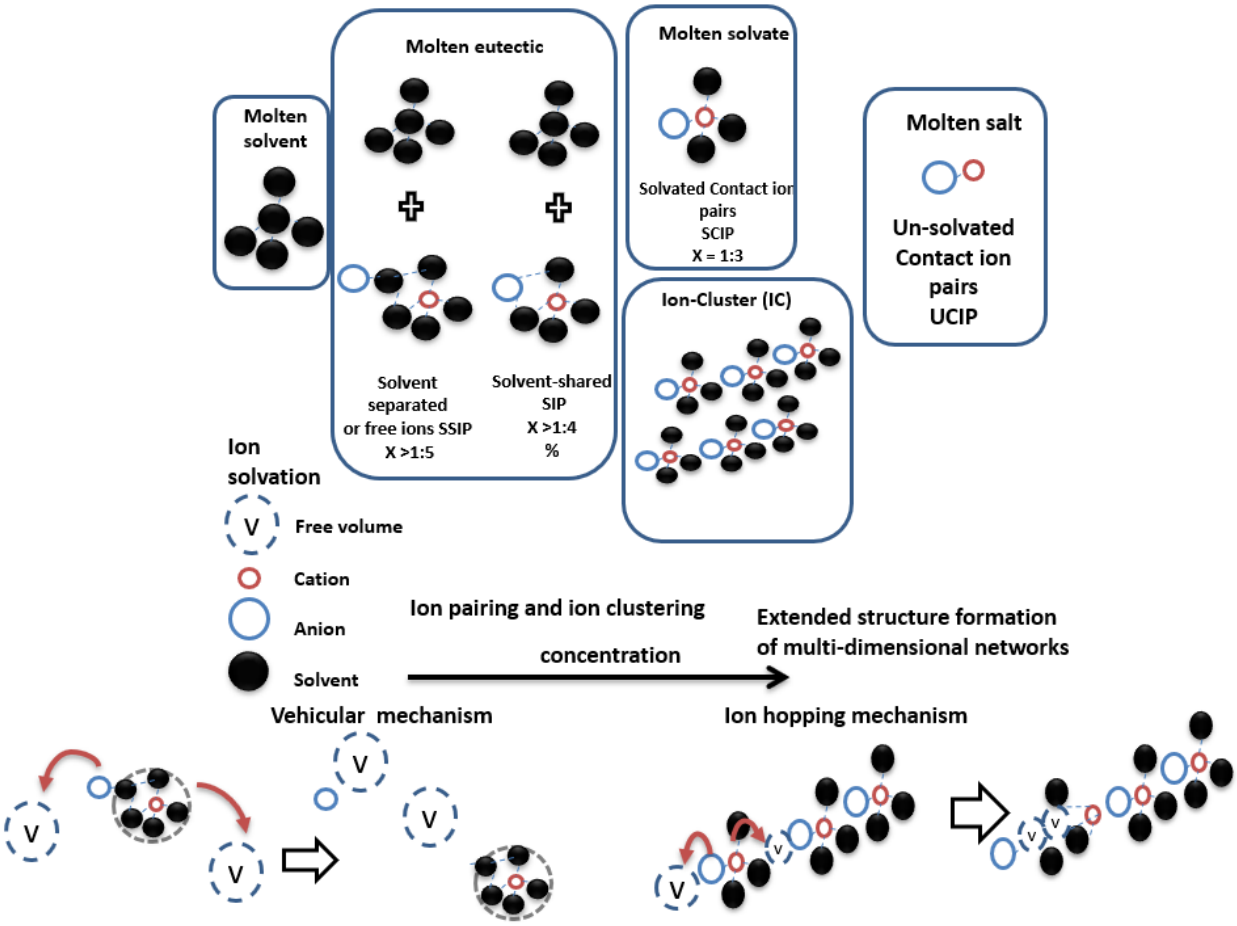

Figure 3.1: (a) possible structures of the different IPs and ICs that can exist in electrolyte solutions at different concentrations. (b) illustration of vehicular type and ion hopping type conduction mechanisms

mechanism to a loose lattice structure where transport is dominated by ion hopping mechanism where naked ions hop along the extended structure (different types of ICs) (Fig 3.1). Abu-Lebdeh proposed a model for electrolyte solutions where the change in liquid structure and hence transport mechanism can be understood by observing changes in solid microstructure in the (salt/solvent) phase diagram for a given concentration or molar ratio.[7,9,10] It assumes that, at the sub-micron level, the structure of the liquid, above the liquidus line, is a heterogeneous

mixture similar to that of the solid state below the solidus line and each component of the mixture is made up of charge carries formed from the fragmentation of the bulk structure into its basic building units (IPs, ICs or solvent aggregates). The isothermal structural variation at high and low temperatures in a phase diagram with no solvate formation and in a phase diagram with a solvate formation are presented in Fig S.1 and S.2, respectively. As shown, the main features of the heterogeneous structure are (1) a molten solvent (Hydrogen bonded tetrahedral structure with tetrahedron building units in the case of water) and molten eutectic (water and IPs) below the eutectic composition ($x_{eutectic}$) which can be represented as a molten eutectic-in-water, (2) a molten eutectic only at the eutectic composition ($x_{eutectic}$) with a distinct melting point ($T_{eutectic}$) and a distinct structure of alternate layered molten solvent and molten salt, (dominated by un-solvated contact ion pairs (UCIP)) or solvate (dominated by solvated contact ion pairs (SCIPs and ICs), (3) a mixture of molten eutectic as in (2) and a molten solvate (dominated by SCIPs and ICs) or molten salt (dominated by CIPs and ICs)-if there is no solvate formation above $x_{eutectic}$, which can be presented as molten eutectic-in-molten salt or molten eutectic-in-molten solvate. It was emphasized that the building units or charge carriers are kinetic entities that undergo a rapid dynamic exchange among each other and that free volume and activation energy play a key role in controlling the transport specially when crossing $x_{eutectic}$ which shows the lowest activation energy for transport. This idea of liquid heterogeneity is not new and in fact mounting evidence of recent studies point to nano-heterogeneity in liquids.[11] It was even suggested that at low enough temperatures liquid-liquid separation could take place due to incompatibility between the two solvent-rich and solvate-rich or molten salt-rich components.[12] Individual schematic illustrations of the salt/water structure at all possible concentration-temperature combinations for both kind of phase diagrams (with and without solvent formation) according to the model can also be found in the supplementary information section of this work (Fig S.4).

In this work, we use this model, which was previously applied to aqueous and non-aqueous (nitriles) solutions of LiCl, LiTFSI and NaTFSI salts, in order to understand the structure and ionic conductivity of four selected nitrate-based electrolyte solutions. The four solutions were carefully selected so that they have diverse phase diagrams with and without solvate formation and diverse isotherms with a conductivity maximum that does and does not drop beyond the onset maximum molar ratio. Below is a brief description for the chemistries under study:

1- Ammonium nitrate/water (NH_4NO_3/H_2O): This system's phase diagram has a simple eutectic and no solvate formation and a conductivity isotherm with a maximum conductivity that drops slightly thereafter.

2- Lithium nitrate/water ($LiNO_3/H_2O$): This system's phase diagrams have a solvate forming and two eutectic points and their conductivity isotherms have a maximum conductivity that drops thereafter.

3- Nitric acid/water (HNO_3/H_2O): This system's phase diagram has two solvate formation points and three eutectic points and a conductivity isotherm with a maximum conductivity that drops thereafter.

4- Calcium nitrate/water ($Ca(NO_3)_2/H_2O$): This system's phase diagram has 3 solvate forming with the latter 2 forming within a very narrow compositional range. For simplicity, we modified the phase diagram to include one solvate formation. This system becomes similar to that of Lithium nitrate/water

First, we examine the conductivity isotherms and the phase diagrams and show that the correlations follow the model. Next, we use well-established one-variable, isothermal and iso-compositional equations to fit the data. We then propose a novel two-independent-variables equation that fits the data well as indicated by the coefficient of determination, R^2.

Experimental The ionic conductivity data of NH_4NO_3, HNO_3, Ca $(NO_3)_2$ solutions were obtained from Wahab et al.[13], Spencer et al.[14] and Angel et al.[3] respectively. NH_4NO_3 data was obtained in S m^{-1} through the digitization of the plots using Automeris software and converted to mS cm^{-1}. HNO_3 data was directly taken from tables and required no digitization or conversion. For Ca $(NO_3)_2$, Data was digitized and converted from equivalent conductance units (Ω^{-1} cm^{-1} eq^{-1}) into mS cm^{-1} data points. In our search for $LiNO_3$ data, we found conductivity plots reported by Li et al.[15] that exhibited two peaks in conductivity at different molar concentrations, specifically x = 0.11 and x = 0.19. In this set of data specifically the second peak in the conductivity isotherm does not correlate to the phase diagram given that it is at a molar ratio between a eutectic point and solvate forming at x = 0.25. We hypothesize that a drop in conductivity must occur after the first peak. For this reason, we decided to run our own experiment to obtain $LiNO_3$ conductivity vs. x and T data. $LiNO_3$ electrolyte solutions were prepared by dissolving known amounts of $LiNO_3$ salt (Aldrich) in de-ionized water, represented in salt to solvent molar ratios (x), and left to equilibrate overnight. Ionic conductivity measurements were carried out using conductivity meter RL060C from Thermo Scientific equipped with a water bath to control the temperature between 20 °C and 80 °C. The estimated error in measurement is ± 1%. The variation between our data and Li et al data is presented in Fig 3.2. The phase diagrams were obtained by direct digitization from literature.[3,16–19]

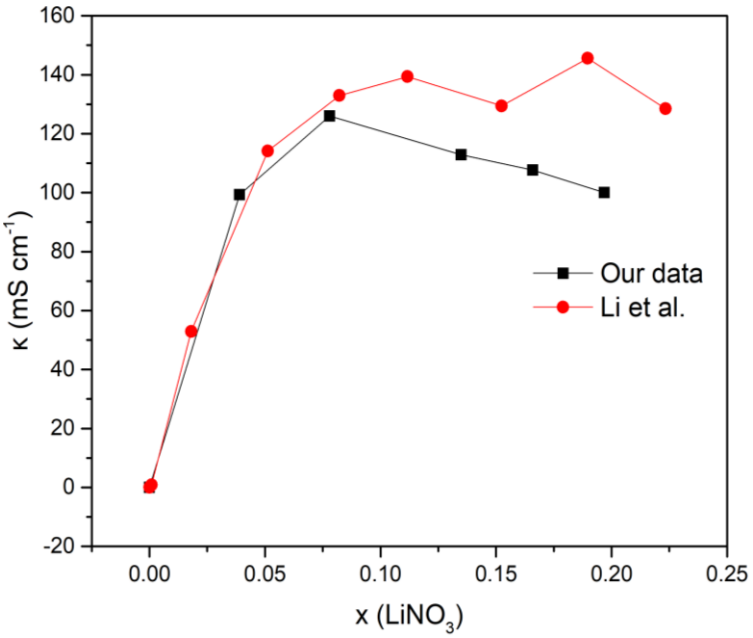

Figure 3.2: comparison of our LiNO3 conductivity data with Li et al data[15]

Results and Discussion

Ionic conductivity of aqueous nitrate electrolyte solutions in relation to their phase diagrams:

Fig 3.3 a-d show plots of conductivity isotherms *i.e.*, the specific ionic conductivity (κ), versus molar ratio (x) at 298 K of the four aqueous electrolyte solutions along with their respective phase diagrams. In order to better understand the observed isotherms, let us have a closer look at the binary phase diagrams and extract as much information as we can about the structure of the liquid from those of the corresponding solids for a given composition at lower temperatures.

1) The phase diagram with simple eutectic and no solvate formation: NH_4NO_3/H_2O

Fig 3.3a shows the phase diagram which is a simple eutectic with no solvate formation. The melting point of the electrolyte solution decreases from 273.2 K($T_{m\,(H2O)}$) with increasing the amount of salt, as represented by the molar ratio x, until it reaches a minimum 257 K (T_e), at the eutectic molar ratio 0.14, then increases again up until that of the pure salt 443 K ($T_{m\,(NH4NO3)}$). The electrolyte solution is liquid above T_m and liquid and solid between T_m and T_e and solid below T_e. In order to understand the structure of the liquid it is better to understand that of the solid. Below T_e at x_e, the solid is made of pure eutectic while at concentrations below x_e it is made of a mixture of solid eutectic and pure solid solvent and above x_e it is made of solid eutectic and pure salt. The structure of solid eutectics has been studied in many systems and more so in metal alloys.[20] It is clear that due to kinetic and thermodynamic limitations the eutectic tends to adopt certain peculiar structures where the two end compounds, in this case the solvent and the salt, tend to alternate into a lamellar structure in most systems. We can hypothesize that this structure is carried over upon melting to the liquid state. Therefore, at x_{max} in the conductivity isotherm, which is essentially x_e, the alternate structure has the highest conductivity (the maximum of the product of mobility and charge carriers). Ongoing below or above this concentration a diluting effect occurs where the composition of eutectic in the mixture is reduced and replaced by the less conductive bulk solvent (molten eutectic-in-water or molten eutectic-in-molten salt). However, the drop in the lower end goes to approximately zero due to the poor conductivity of pure, bulk solvents while in the higher end does not drop to zero due to the more conductive molten salt. These drops in conductivity on both sides of the x_{max} explains the observed maximum.

2) The phase diagram with solvate formation: $LiNO_3/H_2O$ and $Ca(NO_3)_2/H_2O$

Fig 3.3 (b) and 3.3 (d) show the phase diagrams which illustrate a solvate formation. The following is a description of $LiNO_3/H_2O$ phase diagram which share the same characteristics

as $Ca(NO_3)_2/H_2O$ phase diagram. Fig 3.3 (b) shows a solvate formation at x = 0.25 (x_s) molar ratio corresponding to $LiNO_3.3H_2O$. The phase diagram now is split into two simple eutectic phase diagrams like the one in Fig 3.3 (a) but on both sides of the $LiNO_3.3H_2O$ solvate. *i.e.,* $H_2O/LiNO_3.3H_2O$ and $LiNO_3.3H_2O/LiNO_3$. The melting point of the electrolyte solution decreases from 273K ($T_{m\ (H2O)}$) at x = 0 with increasing the amount of salt until it reaches 250 K (T_{e1}) at the first eutectic point (x_{e1}), then increases again up until that of the $LiNO_3.3H_2O$ solvate (T_{ms}) of 304 K, at x_s of 0.25. T_{e1} remains almost constant throughout this range at 304 K. Going higher in x, T_m decreases again until it reaches 301 K at the second eutectic point (T_{e2}), then increases again up until that of the $LiNO_3$ salt at T_{m2} of 526 K. T_{e2} remains constant throughout this range at 301 K. In this case the electrolyte solution is liquid above T_m and liquid and solid between T_m and T_{e1} and in between T_m and T_{e2} while solid below T_{e1} and T_{e2}. The structure of the liquid resembles that of the solids below T_{e1} and T_{e2}. At x_{e1} and x_{e2}, the solids are made of pure eutectics while below x_{e1} it is made of a mixture of solid eutectic and pure solid solvent while above x_{e1} and below x_s it is a mixture of a solid eutectic and a solvate. Between x_s and $x_{e2,\ i}$t is a mixture of a solid eutectic and a solvate. While above x_{e2} it is a mixture of a solid eutectic and pure salt. Now, in this type of phase diagram the eutectic is made up of the solvent and the $LiNO_3.3H_2O$ solvate and shows the highest conductivity at x_{max} in the conductivity isotherm. Also, ongoing below or above this concentration the structure changes from molten eutectic-in-water to molten eutectic-in-molten $LiNO_3.3H_2O$ solvate accompanied by a drop in conductivity at both ends but the lower end goes to approximately zero due to the poor conductivity of pure water while in the higher end does not drop to zero due to the more conductive molten $LiNO_3.3H_2O$ solvate. The $Ca(NO_3)_2/H_2O$ phase diagram shows the same features but with a $Ca(NO_3)_2.4H_2O$ solvate forming at higher (T_{ms}) temperature than $LiNO_3.3H_2O$ solvate at 315 K and x_s of 0.2. In this case however, the conductivity in the higher end drops to zero indicating lower conductivity of the molten $Ca(NO_3)_2.4H_2O$ solvate due to tis higher stability.

3) The phase diagram with two solvate formation: HNO_3/H_2O

Fig 3.3 (c) shows the phase diagram which illustrates two solvate formations at x_{s1} = 0.25 and x_{s2} = 0.5 corresponding to $HNO_3.3H_2O$ and $HNO_3.2H_2O$ respectively. The phase diagram is now split into three simple eutectic phase diagrams like the one in Fig 3.3 (a). The first is to the left of the $HNO_3.3H_2O$ solvate i.e., $H_2O/HNO_3.3H_2O$ and the other two are on both sides of $HNO_3.2H_2O$ solvate i.e., $HNO_3.3H_2O/HNO_3.2H_2O$ and $HNO_3.2H_2O/HNO_3$. The melting point

of the electrolyte solution decreases from 273K ($T_{m\,(H2O)}$) at x = 0 with increasing amount of salt until it reaches 230 K (T_{e1}), then increases again up until that of the $HNO_3.3H_2O$ solvate (T_{ms1}) of 254 K at x = 0.25. T_{e1} remains constant throughout this range at 230 K. between x_{e1} and x_{e2}, T_m decreases again until it reaches 231 K (T_{e2}), then increases again up until that of the HNO3.2H2O solvate T_{ms2} of 235 K. T_{e2} remains constant throughout this range at 231 K. beyond x_{e2}, T_m decreases again until it reaches 207 K (Te_3), then increases again up until that of pure HNO_3 salt of 231 K ($T_{m\,(HNO3)}$). T_{e3} remains constant throughout this range at 207 K. In this case, the electrolyte solution is liquid above T_m and liquid and solid between T_m and T_{e1}, between T_m and T_{e2}, and in between T_m and T_{e3} while solid below T_{e1}, T_{e2}, and T_{e3}. The structure of the liquid resembles that of the solids below T_{e1}, T_{e2}, and T_{e3}. At the eutectic molar ratios, the solids are made of pure eutectics while below x_{e1} it is made of a mixture of solid eutectic and pure solid solvent while above x_{e1} and below x_{s1} it is a mixture of a solid eutectic and the $HNO_3.3H_2O$ solvate. Between x_{s1} and x_{e2} it is a mixture of a solid eutectic and $HNO_3.3H_2O$ solvate. While above x_{e2} and below x_{s2}, it is a mixture of a solid eutectic and $HNO_3.2H_2O$ solvate. Similarly, above x_{s2} and below x_{e3}, it is a mixture of a solid eutectic and $HNO_3.2H_2O$ solvate while above x_{e3}, it is a mixture of a solid eutectic and pure HNO_3 salt. Similar to $LiNO_3/H_2O$ and $Ca(NO_3)_2/H_2O$ phase diagrams the eutectic is made up of the solvent and the $HNO_3.3H_2O$ solvate and shows the highest conductivity at x_{max} in the conductivity isotherm. Also, ongoing below or above this concentration the structure changes from molten eutectic-in-water to molten eutectic-in-molten $HNO_3.3H_2O$ solvate then to molten eutectic-in-molten $HNO_3.2H_2O$ solvate. However, in this case the drop in conductivity at both ends goes to approximately zero due to the poor conductivity of pure water and pure HNO_3.

Generally, the first eutectic point ($x_{eutectic}$) for each of the solutions typically corresponds to the molar ratio with the highest ionic conductivity (x_{max}). This can be seen clearly in the case of ammonium nitrate, lithium nitrate and nitric acid. In the case of calcium nitrate, x_{max} lies slightly after $x_{eutectic.}$ This behavior is typically witnessed only for the first eutectic point (at lower concentration of salts) and is not observed for subsequent eutectic points. One exception to this observed behaviour is exhibited by sulfuric acid in water system where a second peak is seen in the conductivity isotherms at subsequent eutectic point that corresponds to its third eutectic point at x = 0.71.[21,22] Table 1 gathers the information about the cation in the nitrate salts studied, eutectic compositions and corresponding conductivity at these compositions, eutectic temperatures and the solvate compositions.

(a)

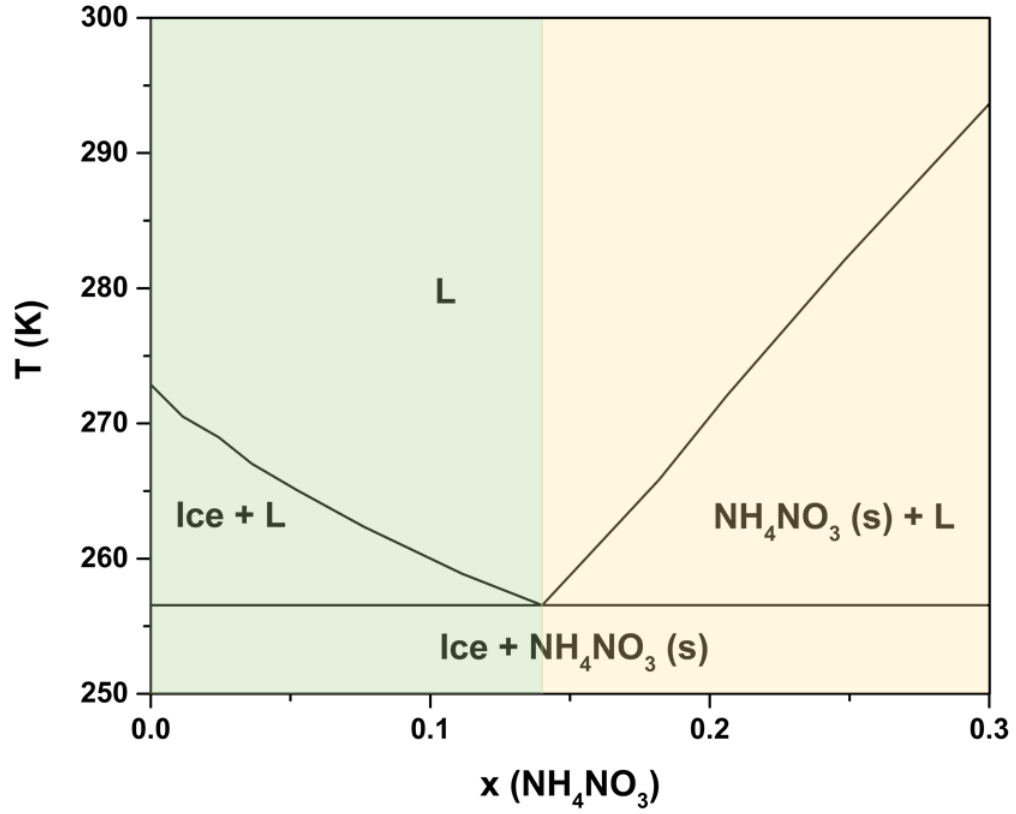
300
290
280
270
260
250
T (K)
L
Ice + L
NH4NO3 (s) + L
Ice + NH4NO3 (s)
0.0
0.1
0.2
0.3
x (NH4NO3)

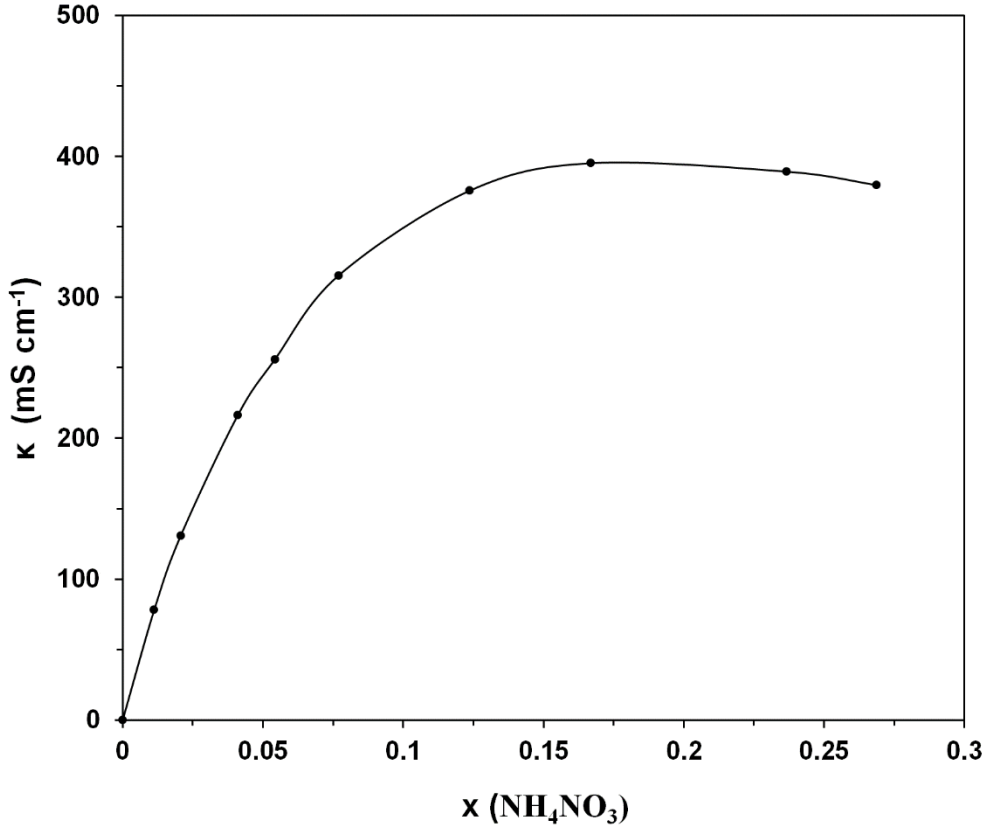
500
400
300
200
100
0
κ (mS cm-1)
0
0.05
0.1
0.15
0.2
0.25
0.3
x (NH4NO3)

(b)

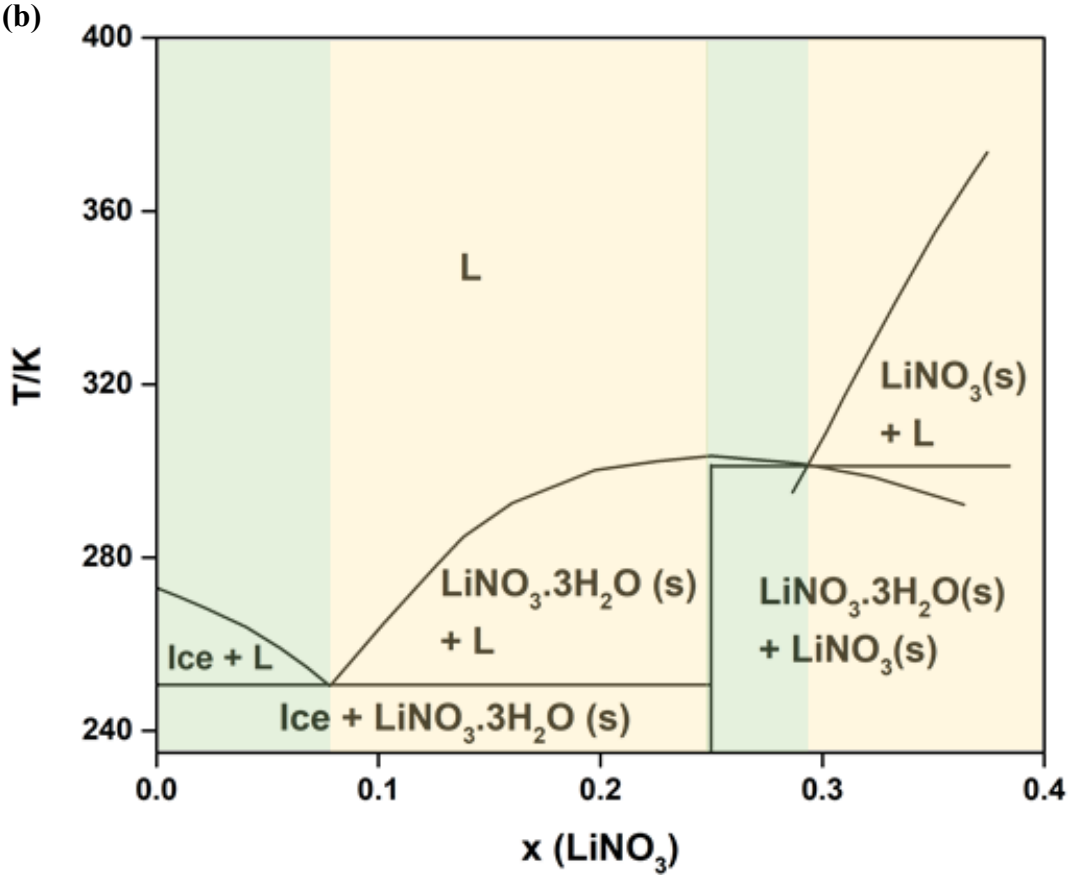
400
360
320
280
240
T/K
L
LiNO3(s)
+ L
LiNO3.3H2O (s)
+ L
LiNO3.3H2O(s)
+ LiNO3(s)
Ice + L
Ice + LiNO3.3H2O (s)
0.0
0.1
0.2
0.3
0.4
x (LiNO3)

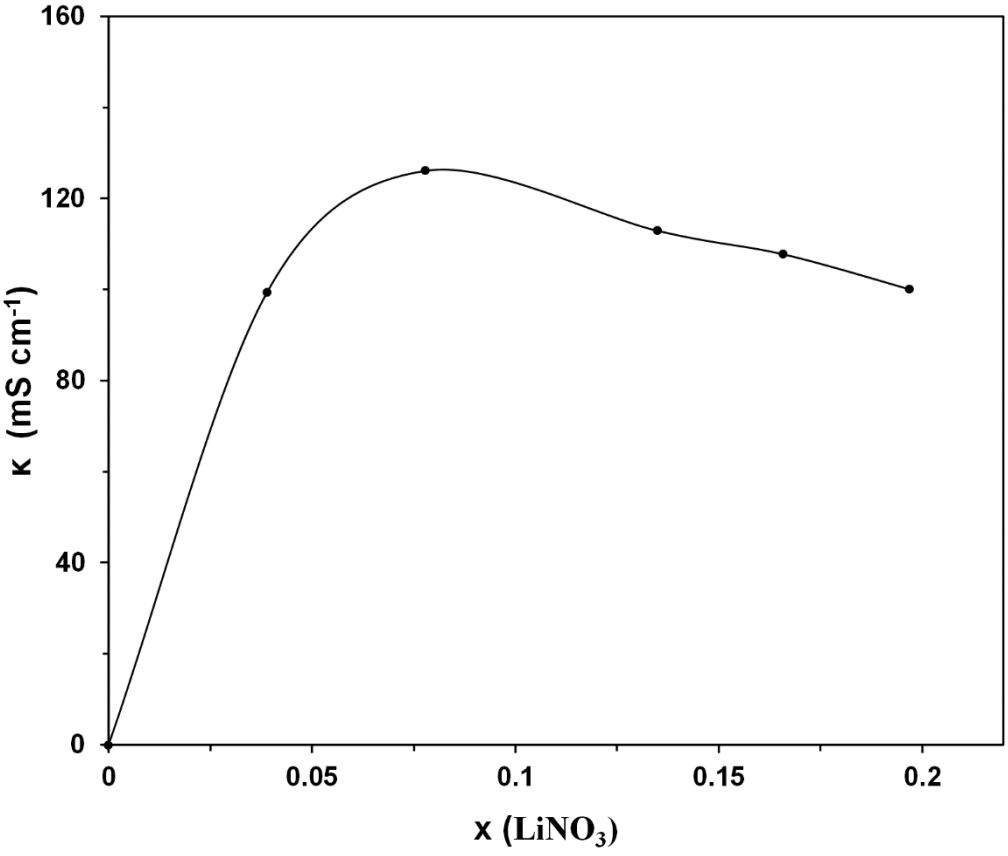
160
120
80
40
0
κ (mS cm-1)
0
0.05
0.1
0.15
0.2
x (LiNO3)

(c)

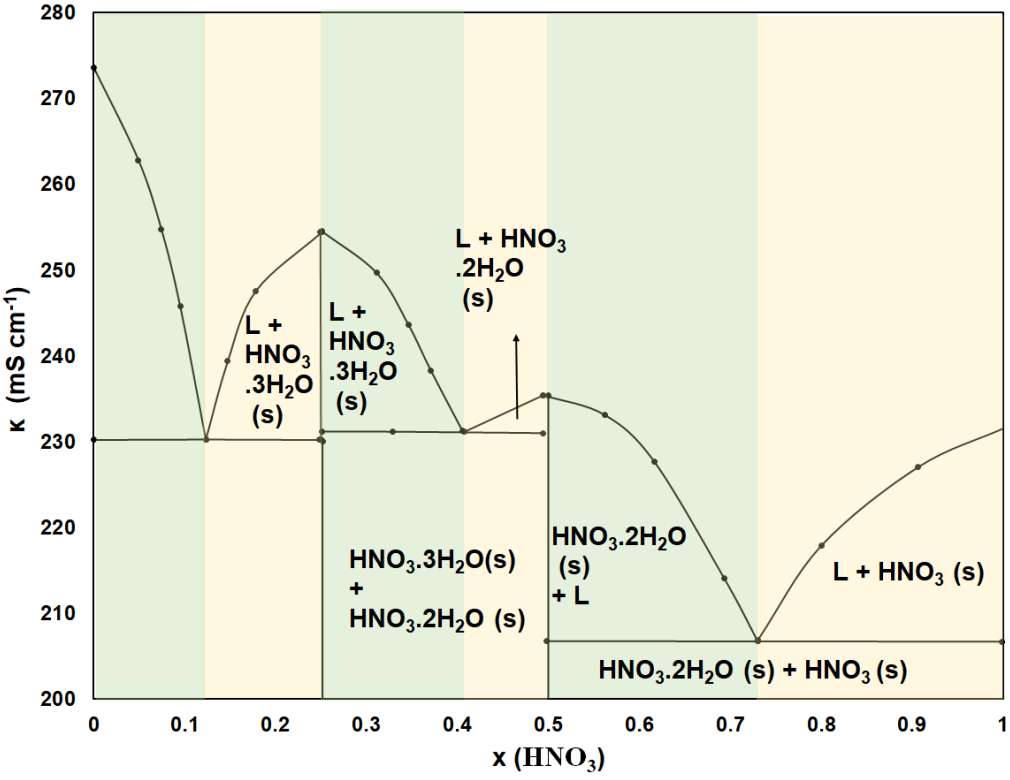
280
270
260
250
240
230
220
210
200
κ (mS cm-1)
0
0.1
0.2
0.3
0.4
0.5
0.6
0.7
0.8
0.9
1
x (HNO3)
L + HNO3 .3H2O (s)
L + HNO3 .3H2O (s)
L + HNO3 .2H2O (s)
HNO3.3H2O(s) + HNO3.2H2O (s)
HNO3.2H2O (s) + L
L + HNO3 (s)
HNO3.2H2O (s) + HNO3 (s)

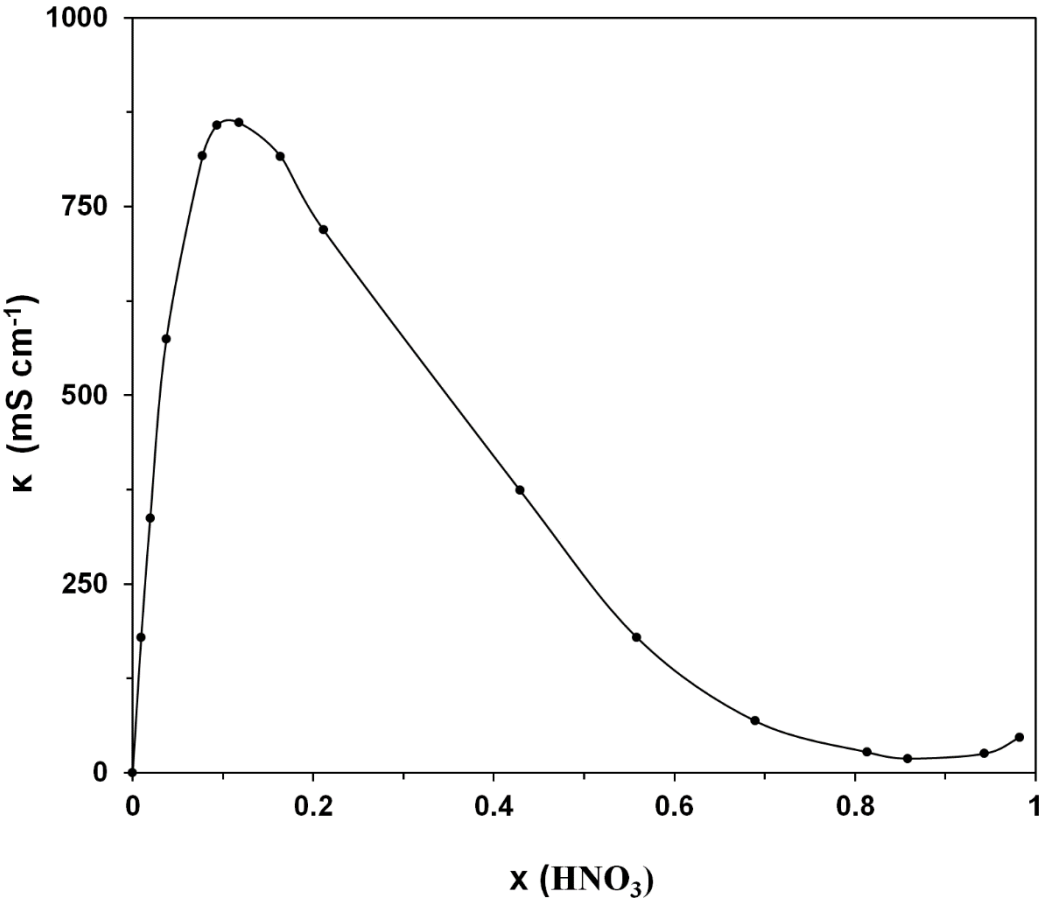
1000
750
500
250
0
κ (mS cm-1)
0
0.2
0.4
0.6
0.8
1
x (HNO3)

(d)

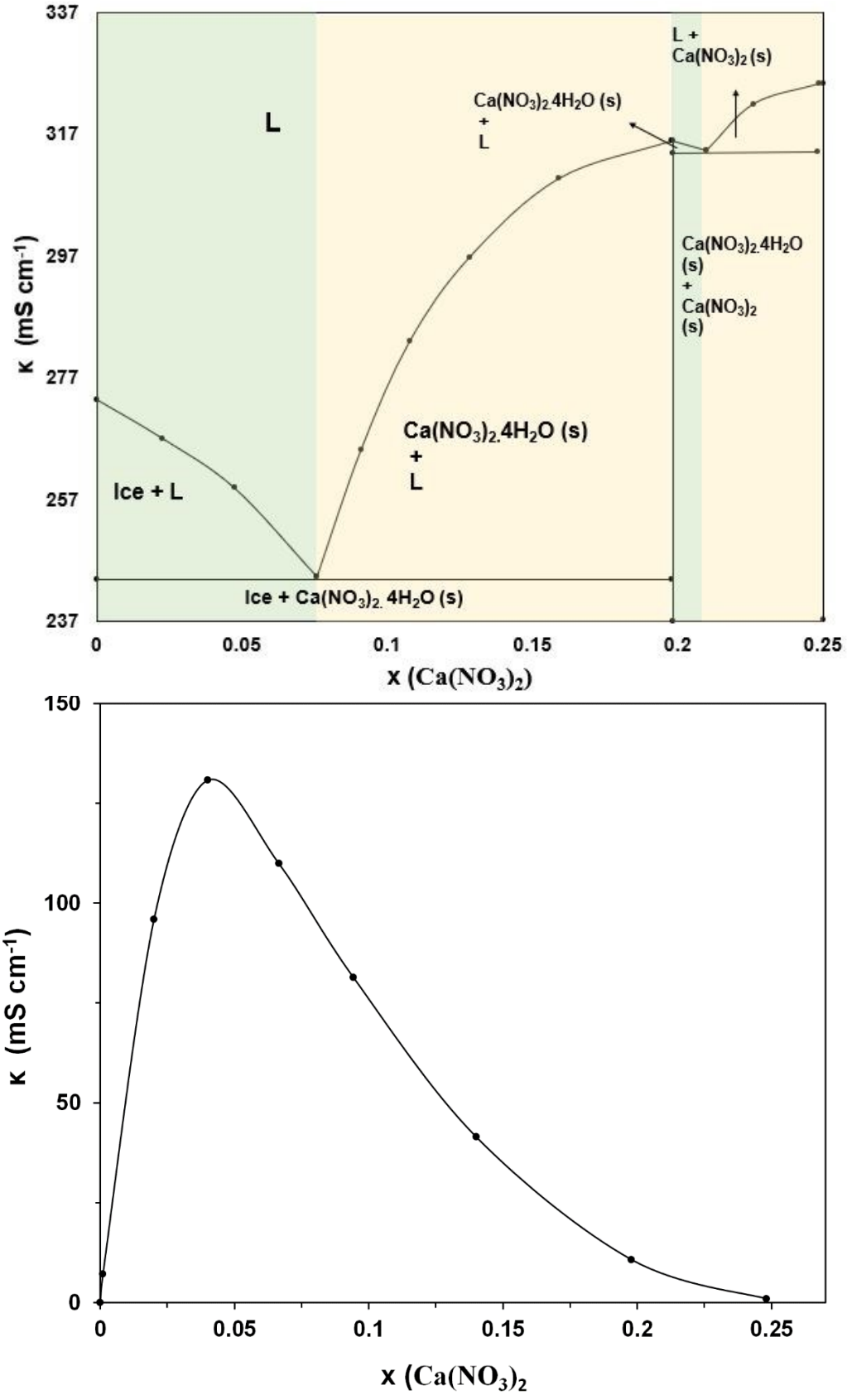

Figure 3.3: Phase diagram and room temperature ionic conductivity isotherms for (a) Ammonium nitrate (b) Lithium nitrate (c) Nitric acid (d) Calcium nitrate

Table 3.2: lists the cation charge density, Gibbs free energy of interaction (ΔG^{int}), eutectic molar concentrations ($x_{eutectic}$) and temperatures ($T_{eutectic}$), maximum ionic conductivities (κ_{max}) and corresponding molar concentrations (x_{max}), as well as the solvate formation molar ratios ($x_{solvate}$) for all the aqueous electrolyte solutions:

solute	Chemical structure	Cation charge density (e Å^{-3})	ΔG^{int} (kJ mol^{-1})	$x_{eutectic}$	$T_{eutectic}$ (K)	x_{max}	κ_{max} (mS cm^{-1})	$x_{solvate}$
Ammonium nitrate	NH_4NO_3	0.048[23]	-45.40[23]	0.14	256	0.16	396	-
Lithium nitrate	$LiNO_3$	0.327[23]	-115.8[23]	0.08	250	0.08	126	0.25
Nitric acid	HNO_3	-	-	0.12 0.41 0.73	230 231 206	0.12	860	0.25 0.5
Calcium nitrate	$Ca(NO_3)_2$	0.322[23]	-192.5[23]	0.07 0.25	244 314	0.04	131	0.2

NO_3: charge density =0.015 e Å^{-3} and interaction energy $\Delta G^{int} = -17.8770$ kJ mol^{-1}. [23]

From the table we can see that the ionic conductivity of all the aqueous electrolyte solutions (κ_{max}) follows the order: H^+ (860 mS cm^{-1}) > NH_4^+ (396 mS cm^{-1}) > Ca^{2+} (131 mS cm^{-1}) > Li^+ (126 mS cm^{-1}). This could be understood based on the charge density of the cations as shown in Table 1. The higher the charge density (e.g., Li and Ca) the stronger the interactions with water molecules as evidenced by the interaction energy (ΔG^{int}) as shown in table 1. Also, the stronger the interaction the higher the activation energy and the lower the mobilities of the cations. We here assumed that the anion has little interaction with water as evidenced by the low ΔG^{int} of the nitrate anion which reported to be −17.88 kJ mol^{-1}.[23] For both x_{max} and $x_{eutectic}$ the trend is the same as follows: $NH_4^+ > H^+ > Li^+ > Ca^{2+}$. This corroborates the correlation between the two parameters. The trend however for the position of x_{max} and $x_{eutectic}$ is still not understood. Empirically it is found that solutions of salt of higher valence cations and anions

show lower x_{max} and $x_{eutectic}$.[3] Possible explanation is again that the higher charge density of the cation and/or the anion attracts more solvent molecules from the water layer into the molten salt or solvate layer hence increasing the number of charge carriers (IPs and ICs). This causes a faster drop in the ratio of ice to eutectic shifting x to the left of the phase diagram. Similar line of thought can be applied to $T_{eutectic}$. Herein the trend is $NH_4^+ > Li^+ > Ca^{2+} > H^+$ which again can be explained by differences in their charge density as faster break up in water bulk structure and larger number of IPs leads to lower $T_{eutectic}$. It is worth mentioning that proton conductivity in acids is given special attention and it is believed that the very high proton conductivity is due to Grotthuss mechanism where the proton can hop into the water network and contribute to the total conductivity along with the vehicular mechanism of the protonated water molecules. *i.e.* both mechanisms are at play.[24] It is also worth noting that the water-molten salt eutectic of NH_4^+ has higher conductivity than that of the water-solvate of Li^+ and Ca^{2+}. This implies that the UCIPs and possibly ICs are getting more dissociated by water molecules (or more mobile) than the more stable SCIPs.

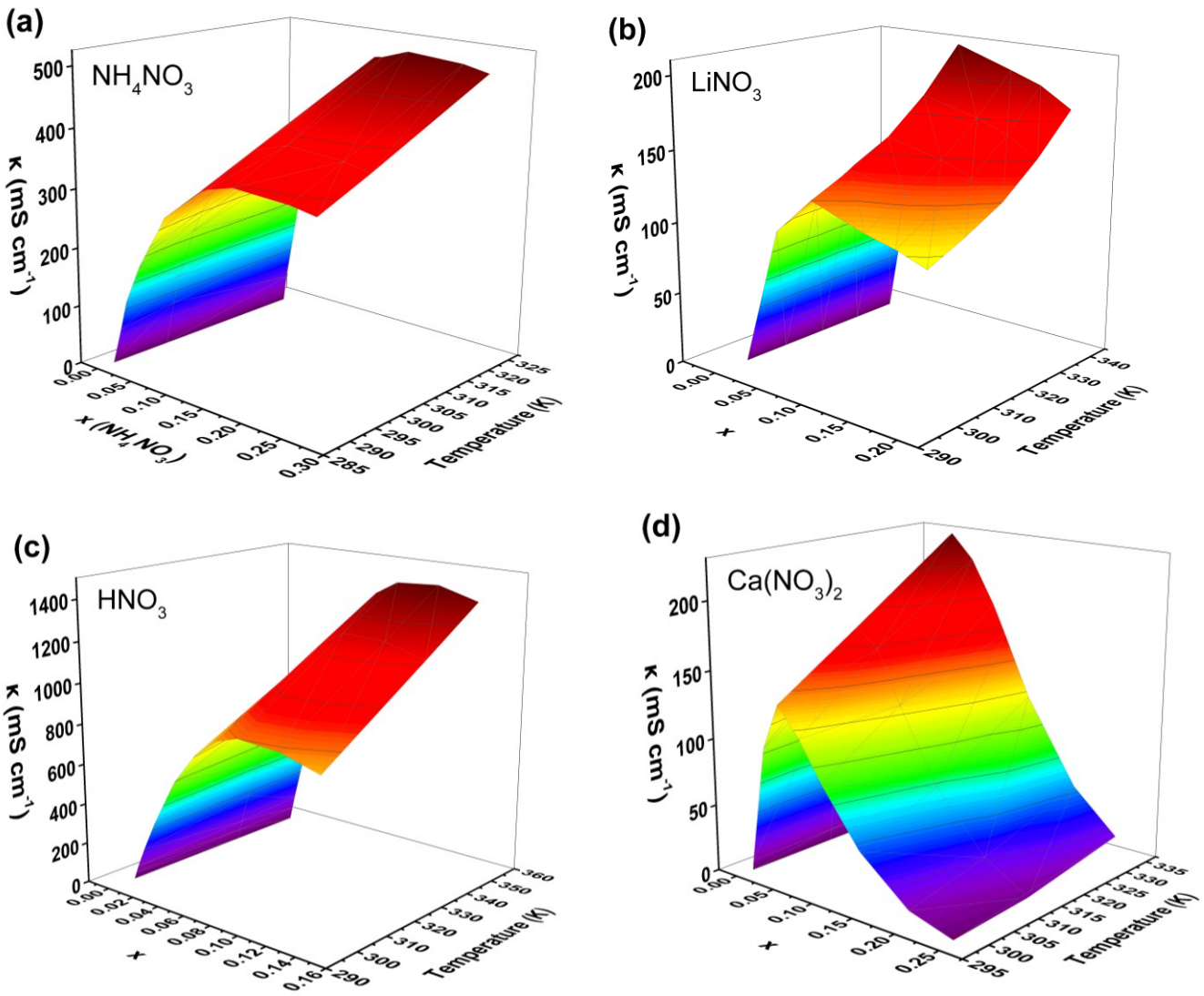

Figure 3.4: The variation of ionic conductivity (κ) with molar ratio (x) and temperature (T) for each of the nitrate solutions

Fig 3.4 illustrates the ionic conductivity behavior versus molar ratio of the nitrate salts in the aqueous electrolyte solutions at different temperatures. Notably, there is no shared trend in behavior across the four salts other than the observation that κ_{max} increases with temperature. Nitric acid has the highest κ reaching well above 1 S cm^{-1} around its x_{max} at temperatures higher than 60 °C. Fig 3.4 (c) Shows a small plateau in κ values around x_{max} (x = 0.08 – 0.12) before they drop down again at x > 0.12. As mentioned above, the conductivity in acid solutions needs more attention as the very high conductivity is always explained by a combination of vehicular and ion hopping mechanisms taking place concurrently in solution. The electrolyte with the second highest κ is ammonium nitrate, with values reaching up to 0.5 S cm^{-1} around its x_{max} at temperatures higher than 50 °C. The plateau behavior is once again observed but this time it

persists at all compositions with x >x_{max}. This can be taken as an indirect proof that the conductivity does not drop because the structure of the liquid does not approach a lower value of the pure molten salt as there is little to no dilution effect. The solution structure is dominated by (UCIPs)) of the molten NH_4NO_3 originating from the molten eutectic, which is composed of molten NH_4NO_3/H_2O and molten NH_4NO_3. This is corroborated by the phase diagram which is a simple eutectic with no formation of a solvate. Lithium nitrate and calcium nitrate are the electrolytes with the least ionic conductivity reaching a maximum of 0.2 S cm^{-1} around their x_{max} at temperatures above 60 °C. Both electrolytes do not show any plateau in κ values beyond their $x_{max.}$ Rather, their ionic conductivity keeps decreasing with increasing x after x_{max}. Again, this can be explained by the dilution effect when the structure switches from molten eutectic-in water to molten eutectic-in-molten solvate. In this case the molten solvate (dominated by SCIPs) being less conductive than the molten salt (dominated by UCIPs) due to the high energy density of the cations. Fig S.3 in the Supplementary Information (S.I) present the variation of conductivity with temperature for the different nitrates in 2D scatter plots.

Analysing Isothermal trends, we can notice that the conductivity of the nitrates-water system increases with the increase in the electrolyte concentration at the same temperature. This increase is steeper at x values way below x_{max} and becomes more moderate when x approaches x_{max}.[10,25] After x_{max}, $Ca(NO_3)_2$ exhibits a parabolic behavior as its conductivity decreases after approaching x_{max}. This behavior differs from the one observed in NH_4NO_3-H_2O or HNO_3-H_2O systems. Possible explanation is that Ca^{2+}, being a divalent ion, is subject to stronger electrostatic forces and short-range interactions during ion migration under the influence of an external electric field than monovalent NH_4^+ or H^+. Hence, a quick drop in its mobility due to higher activation energies may be noticed in regions of high electrolyte concentration.

Analysing the iso-compositional trends, we can see the conductivity of the solution rises with increasing temperature with varying proportionality as a function of x. In the dilute region, the increase in temperature results in subtle increase in conductivity while in the more concentrated region near solubility, temperature change results in a substantial increase in conductivity. This is mainly because at the high concentration regions, the number of ion pairs and clusters (IPs and ICs) is larger than that at the dilute region, and the ion association decreases with rising temperature, leading to more mobile “free” ions. Hence, the conductivity of the high concentration region is more temperature-sensitive.[10,25] Also, temperature expands the liquid and increases its free volume and lowers activation energy hence improving ion mobility.

Ionic conductivity Model Description

In the low concentration regions, κ of the aqueous electrolyte solutions is equal to the total of the conductivities of the ions in the solution, according to the equation below.[26]

$$\kappa = \sum n_i q_i \mu_i \quad (1)$$

where κ is conductivity, q_i is the charge of the ion, n_i is the number of ions and μ_i is the mobility of the ions. It can be demonstrated in eq.1 that the conductivity is impacted by both the quantity of ions in the solution and their mobility. To further expand the validity of the equation to medium and high concentrations, eq.1 must be adjusted to account for the effect of electrolyte concentration on the number of free ions and, accordingly, ion mobility.

In solutions of moderate and high concentrations, the distance between anions and cations decreases, and less mobile or non-conductive ion pairs are created by ion association, resulting in a reduction in the number of free ions involved in vehicular conduction. Hence, the quantity of free ions as a function of electrolyte concentration follow a linear relationship.[25] The following equation may be used to explain the number of free ions in relation to the molar ratio x:

$$n = ax \quad (2)$$

where *a* is a constant and *n* is effectively the speed of ions per unit electric field intensity and is the product of the combined effects of the external electric field force and ion movement resistance. Considering the ion and its hydration layer as a whole, the resistance to movement during migration when an external electric field is applied consists of ion-ion, ion-solvent, and solvent-solvent forces. The first is a long-range interaction induced by electrostatic forces, while the second and third are short-range interactions. At low concentrations, long-range interactions dominate while short-range interactions are often neglected. When the electrolyte concentration in the solution rises, the distance between molecules drops, and it becomes harder to neglect short-range interactions; hence, ion migration resistance rises quickly.[27] Therefore, ion mobility often decreases as electrolyte concentration rises. Zhang et al.[25] have proposed an empirical equation to relate μ and x that can be applied to electrolytic solutions in any concentration region:

$$\mu_i = \mu_{io} \exp(-bx) \quad (3)$$

where b is a constant.

Substituting eq. 2 and 3 into eq. 1, we arrive to the following equation relating κ and x which was introduced before by Abu-Lebdeh et al.:[10]

$$\kappa = Axexp(-Bx) \quad (4)$$

where A and B are constants. To test the validity of eq 4 on the different aqueous electrolyte system, we have fitted the data obtained from literature and our own experimental conductivity data for $LiNO_3$ to the equation. The parameters obtained and the R^2 values are tabulated in Table 2 below. R^2 column indicates the model fits the data well with $R^2 > 0.98$ for all the systems at different temperatures except for $Ca(NO_3)_2$ at the highest temperature (333K; $R^2 \approx 94\%$).

Table 3.3: fitted parameters for eq 4 for different systems at different temperatures

		Parameters			
System	T	A	B	R^2	Data source
NH_4NO_3	288.15	5394	5.515	0.9963	
	298.15	6355	5.720	0.9947	[28]
	323.15	8496	5.950	0.987	
$LiNO_3$	298.15	3642	10.38	0.9865	
	308.15	4067	10.26	0.9903	
	318.15	4622	10.35	0.9847	This work
	328.15	5066	9.99	0.9895	
	338.15	5948	9.99	0.9868	
HNO_3	298.15	23290	10.11	0.9976	
	333.15	32430	9.777	0.9984	[14]
	358.15	37270	9.595	0.999	
$Ca(NO_3)_2$	298.15	8143	23.84	0.9958	
	313.15	10770	22.56	0.9987	[3]
	333.15	10443	16.41	0.9377	

While eq 4 represent the effect of electrolyte concentration on conductivity, it can only be applied to the study of different electrolyte solutions isothermally as conductivity also depends on temperature as illustrated in the famous Arrhenius equation:

$$\kappa = A_o exp(\frac{-E_a}{RT}) \tag{5}$$

Or also by the Vogel–Fulcher–Tammann (VTF) equation:

$$\kappa = \frac{A_o}{\sqrt{T}} exp(\frac{-E_a}{R(T-T0)}) \tag{6}$$

where A_o is the pre-exponential factor, E_a is the activation energy R is the gas constant and T is the temperature in Kelvin and T_o is an empirical temperature related to T_g, the glass transition temperature.

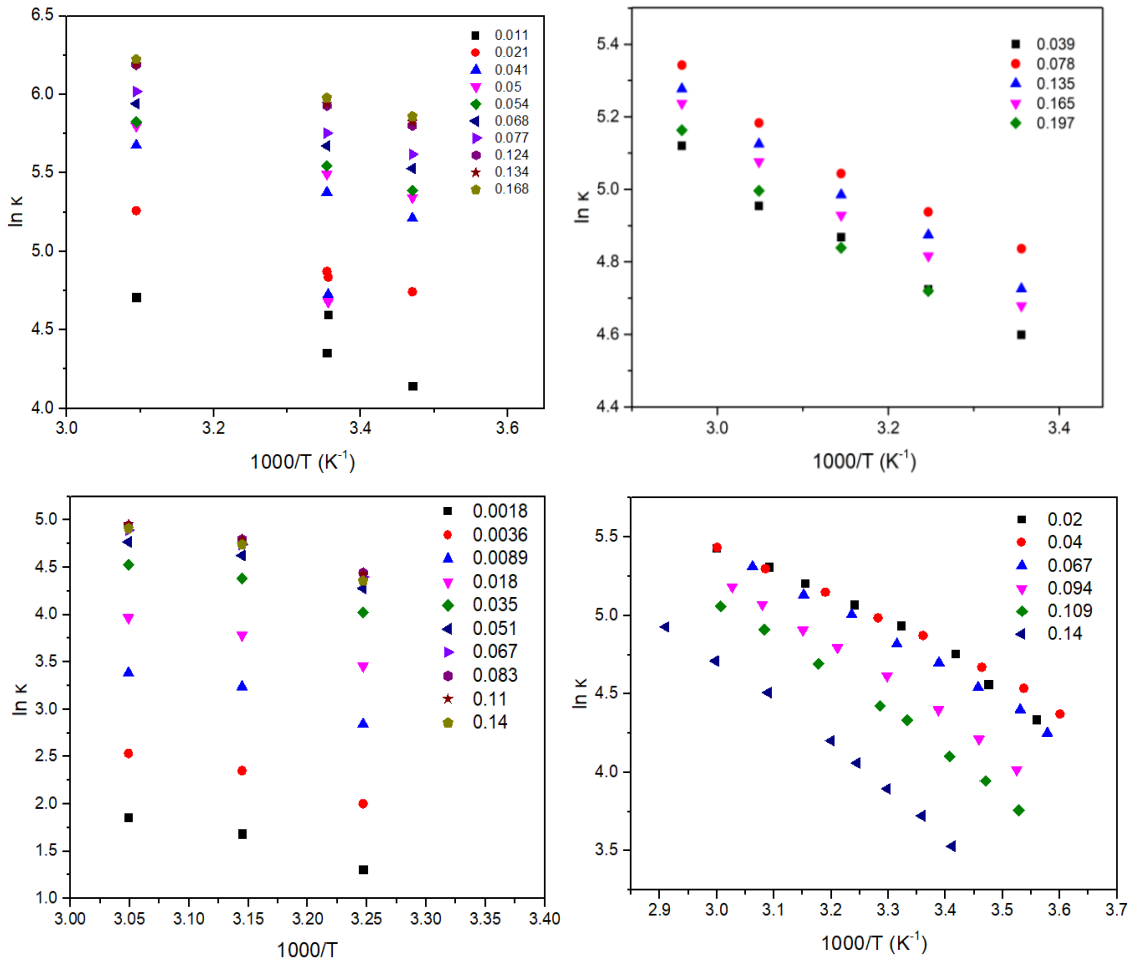

Figure 3.5: conductivity, ln (κ), of the different nitrate solutions as a function of temperature

Fig 3.5 presents the ionic conductivity variation of the four electrolyte solutions on a logarithmic scale versus the reciprocal of the temperature. The temperature dependence of ln κ

shows a similar linear trend across all electrolytes indicating that they all obey the classical Arrhenius behavior given by eq 5.

Using Fig 3.5, we calculated the activation energies and the pre-exponential factor for each of the nitrates aqueous electrolytes and plotted each against the molar concentration, x.

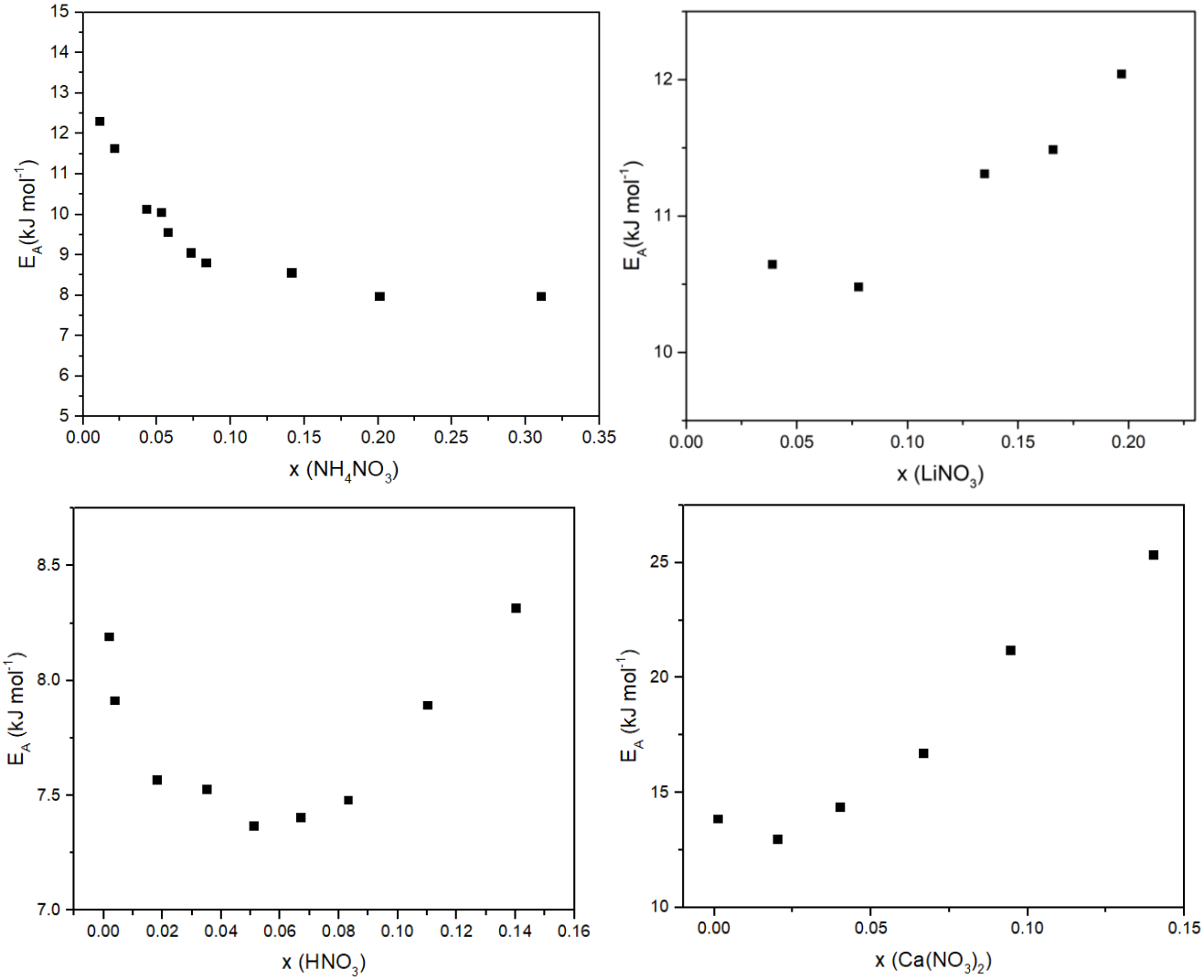

Figure 3.6: Activation energy for the different nitrate solutions as a function of molar ratio

Fig 3.6 depicts the change in activation energy as the electrolyte molar ratio in solution (x) increase. The general trend observed is a decrease in activation energy as we approach $x_{eutectic}$ which is the expected behavior that accompanies the increase in ionic conductivity. This is then

followed by an increase in the activation energy as we pass the eutectic point ($x > x_{eutectic}$) in all the electrolytes except ammonium nitrate where the activation energy plateaus and does not

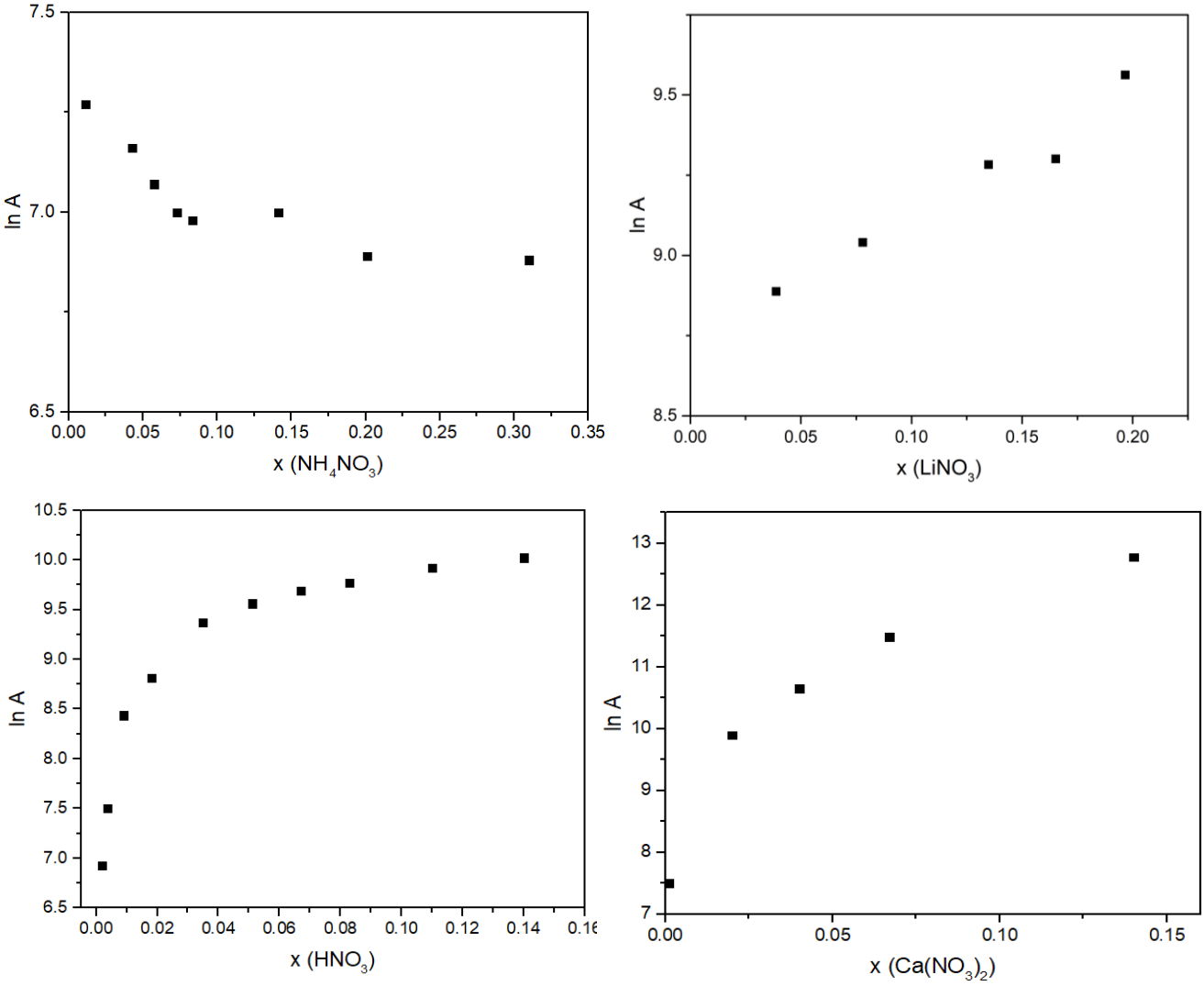

Figure 3.7: Pre-exponential factor for the different nitrate solutions as a function of molar ratio

increase as we pass $x_{eutectic.}$ This explains the plateauing of ionic conductivity of ammonium nitrate beyond $x_{eutectic}$ as observed in Fig 3.3 (a). In addition, we have found that nitric acid has the least activation energy at dilute concentration ($x < 0.01$), followed by ammonium nitrate and lastly calcium nitrate (we do not have the dilute activation energy data for lithium nitrate). This observed trend indicates that electrolytes with highest conductivity tend to have the lowest activation energy at low concentration, x, values. We therefore expect lithium nitrate to have a similar activation energy value at lower x values as calcium nitrate because of their similar ionic conductivity. The increase in the activation energy can be simply attributed to the higher number of the ion-ion interactions at the expense of solvent-solvent and ion-solvent interactions as the structure changes from molten eutectic-in water to molten eutectic-in molten solvate or

molten eutectic-in-molten salt. Also, a drop in the free volume can also contribute to this behaviour.

The intercept of Fig. 3.5, or the pre-exponential factor (A) was calculated and plotted against molar concentration (x) as shown in Fig. 3.7. Once again, not all nitrates share the same trend. For instance, Ammonium nitrate's A decreased with an increase in molar ratio until it hit a plateau at around x = 0.2 While all the other electrolytes' A increased with an increase in molar ratio. Lithium nitrate A increased gradually at first before rising up significantly after x = 0.2 while nitric acid and calcium nitrate's A increased significantly at dilute solutions until x = 0.04 and then continued to ramp gradually after that concentration. The continuous increase of E_a and A after $x_{eutectic}$ can explain the drop in ionic conductivity beyond that ratio. Upon observing ammonium nitrate's unique E_a and A behavior, one can understand the reason behind the stagnation of ionic conductivity at $\kappa_{max.}$ For the rest of the salt solutions, both activation energy and pre-exponential factor increase significantly at high concentrations and might be responsible for the severe drop in conductivity at high concentrations beyond x_{max} and eutectic composition.

The degree of ion dissociation in the solution and the number of free ions both increase as the temperature rises.

$$n = a'T \tag{7}$$

Furthermore, when the temperature rises, the intermolecular force reduces, which causes the barrier to ion movement to decrease and thus, ion migration speeds up:

$$\mu_i = \mu_{io} \exp\left(\frac{-b\prime}{T}\right) \tag{8}$$

The dependance of ionic conductivity on temperature in the pre-exponential term could take many forms. Herein, we tested three different empirical equations listed in Table 3 alongside their calculated parameters and the R^2 values when fitted against $LiNO_3$ κ vs T data.

Table 4.3: fitted parameters for three possible κ vs T empirical equations at different concentration regions.

		Parameters		
Model	x region	A	B	R^2
$\boldsymbol{\kappa = ATexp(\frac{-B}{T})}$	Dilute	8.967	984.5	0.9893
	Near x_{max}	11.55	996.6	0.9823
	Concentrated	14.38	1105	0.9914
$\boldsymbol{\kappa = \frac{A}{\sqrt{T}} exp(\frac{-B}{T})}$	Dilute	229186	1463	0.9885
	Near x_{max}	295284	1475	0.9805
	Concentrated	367972	1583	0.9903
$\boldsymbol{\kappa = A\sqrt{T}exp(-Bx)}$	Dilute	264.1	1143	0.9890
	Near x_{max}	340.2	1156	0.9817
	Concentrated	423.8	1264	0.9910

It can be observed that there is only a slight advantage for the first linear model when comparing R^2. For this slight edge and the sake of simplicity, the linear dependence will be used in this work:

$$\kappa = ATexp(\frac{-B}{T}) \quad (9)$$

where A and B are constants

following the observed correlation of κ with x and T in eq 4 and 9, we propose the following novel semiempirical equation:

$$\kappa = ATxexp(\frac{-Bx}{T}) \quad (10)$$

Note that this is not the first time such a model is proposed. Lin et al.[29] have analyzed the conductivity data for the ionic liquids [EMIM][C_2N_3] and [EMIM][CF_3SO_3] in aqueous solutions and developed a six-parameter empirical model, as shown in eq 11, that concurrently connected conductivity, electrolyte concentration, and temperature:

$$\kappa = x \exp (A_1 + A_2 T^{0.5} + A_3 x^{0.5}) + A_4 + A_5 T^{0.5} + A_6 x^{0.5} \quad (11)$$

where $A_1 - A_6$ are empirical parameters that can be obtained through data regression. Similarly, eq 8 is a seven-parameter model developed by Fu et al.[30] that is used to correlate ionic conductivity of ionic liquids in organic solvents:

$$\kappa = B_1 x^{B2} \exp \left(- \frac{B_4 x^{0.5} + B_5 x + (B_6 x' + B_7)^2}{T - B_3}\right) \quad (12)$$

where $B_1 - B_7$ are also empirical parameters and x' is a parameter related to solvent composition. Further, Zhang et al.[25] have proposed a five-parameter model that correlates the same components and is suitable for both pure and mixed solvent systems premised on how the electrolyte concentration and temperature affect the quantity and mobility of free ions:

$$\kappa = (P_1 T + P_2)\, m^n \exp \left(- \frac{P_3 m}{T - P_4}\right) \quad (13)$$

where $P_1 - P_5$ are also empirical parameters and n is a parameter related to solvent species. All of the mentioned models do a great job when fitting data with great degree of accuracy. The R^2 value for all the aforementioned studies is above 99%. Our model exhibited slightly less yet accepted accuracy with R^2 values always exceeding 95%.

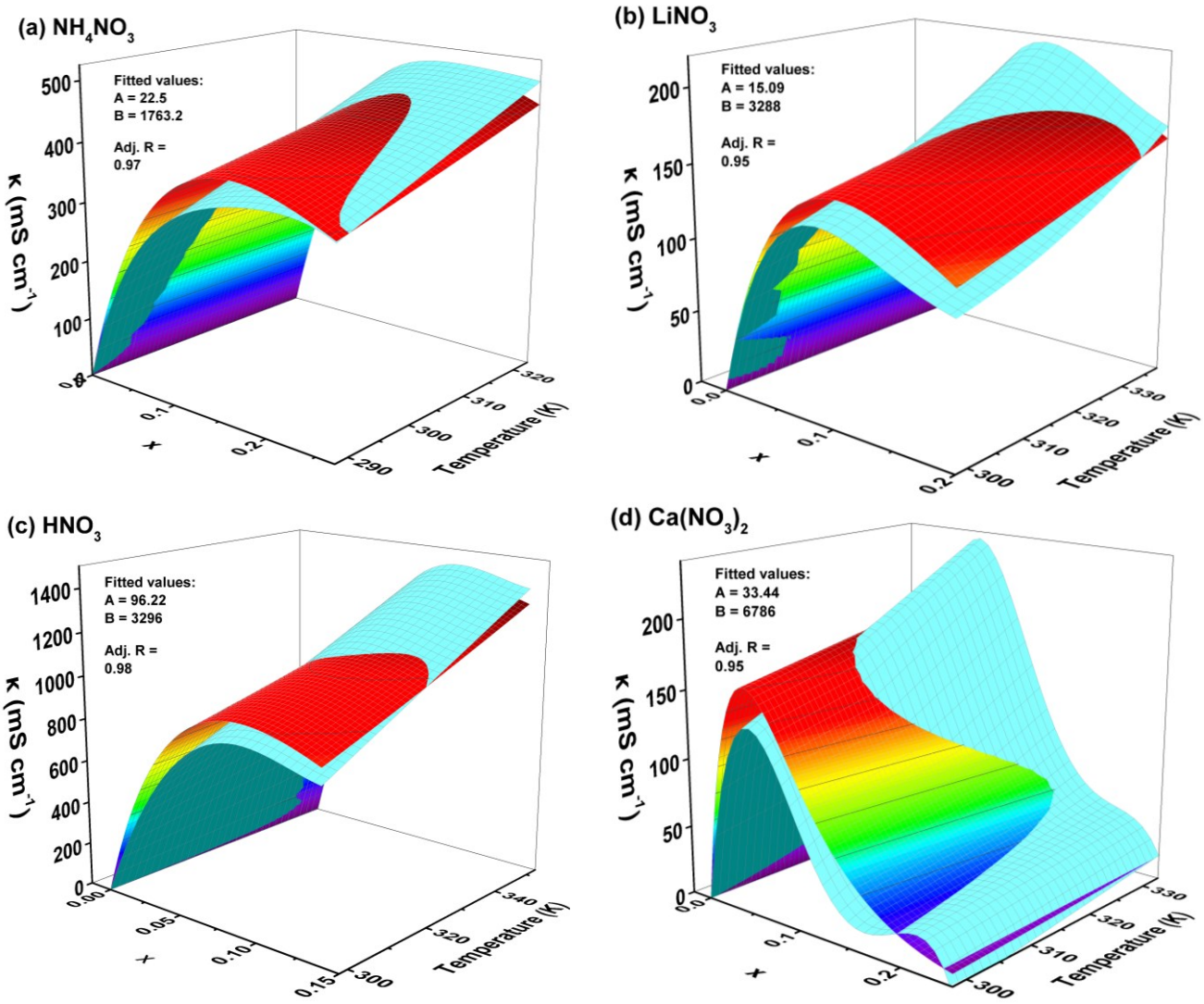

Figure 3.8: 3D graphs of κ vs T and x for each of the nitrate systems plotted next to the fitted curve of eq 10

Fig 3.8 presents the 3D graphs representing the collected data from literature and our experimental work (colored curves) next to the fitted model data (light blue curves). The parameters A, B and R^2 values for each of the nitrate aqueous electrolytes in this study are labelled on their respective 3D graphs. It can be clearly observed that the light blue curve underestimates κ at lower temperature at most concentrations and it overestimates κ at high temperature at all concentrations. We acknowledge that the oversimplification of the problem into a two-parameter equation could be the main cause for the over/under estimation observed. However, despite the discrepancies having two parameters only offers several advantages that contribute to its practical utility. First, the simplicity of the model makes it more accessible and easier to interpret than models with a higher number of parameters. This ease of understanding

is particularly valuable for researchers and practitioners who require a straightforward yet effective tool for predicting conductivity in various applications. Second, the lower number of parameters in our model decreases the risk of overfitting, ensuring that it is more likely to generalize well to new, unseen data. This is an essential attribute for a model that aims to be applicable across a wide range of electrolytes.

Conclusions

In this work, we have studied the ionic conductivity of nitrate-salts/H_2O aqueous solutions over wide concentration and temperature ranges and correlated the observed trends to their respective liquid-solid phase diagrams. We showed that the structure of the electrolyte solutions can be connected to the binary phase diagram in many ways: First, the x_{max} in the conductivity vs concentration plot coincides with the near eutectic composition. Second, the heterogeneous structure of the solid in the phase diagram persists in the liquid. This implies that upon increasing the concentration of the salt in the electrolyte solution, a transition in solution structure from molten eutectic-in water to molten eutectic-in molten solvate or molten eutectic-in-molten salt takes place. The activation energy was calculated from the Arrhenius equations and showed a minimum around x_{max} and increased significantly thereafter. This was interpreted as the cause of the maximum and explained by the higher number of the ion-ion interactions at the expense of solvent-solvent and ion-solvent interactions and possibly changes in free volume. We also proposed a semiempirical model to correlate conductivity with molar concentration temperature; $\kappa = f(x, T)$ and verified its accuracy versus a wide concentration and temperature range. When compared to other conductivity models reported in the literature, ours proved to be of acceptable accuracy with fewer parameters; 2 versus at least 4 in other reported works. While our model may not achieve the same level of accuracy as more complex models with R^2 values above 99%, it still provides a reasonable approximation with R^2 values consistently above 95%. In many practical applications, this level of accuracy may be sufficient, particularly when considering the trade-offs in terms of simplicity, computational efficiency, and reduced overfitting risk.

Acknowledgments

The authors would like to thank Natural Resources Canada for partial financial support through the Program for Energy Research and Development (PERD) and Energy Innovation Program (EIP).

References

[1] J. Barthel, H. Krienke, W. Kunz, *Physical chemistry of electrolyte solutions: modern aspects*, **1998**.

[2] M. C. Smart, B. V Ratnakumar, S. Surampudi -, H. Duncan, N. Salem, Y. Abu-Lebdeh -, S. Takeuchi, R. Kokumai, J. E. Enderby, G. W. Neilson, *Reports Prog. Phys.* **1981**, *44*, 593.

[3] C. A. Angell, R. D. Bressel, *J. Phys. Chem.* **1972**, *76*, 3244.

[4] S. Smedley, *The interpretation of ionic conductivity in liquids*, **2012**.

[5] Y. Yamada, A. Yamada, *J. Electrochem. Soc.* **2015**, *162*, A2406.

[6] D. Aurbach, *Nonaqueous electrochemistry*, **1999**.

[7] C.-H. Yim, J. Tam, H. Soboleski, Y. Abu-Lebdeh, *J. Electrochem. Soc.* **2017**, *164*, A1002.

[8] M. Yoshizawa, W. Xu, C. A. Angell, *J. Am. Chem. Soc.* **2003**, *125*, 15411.

[9] C. J. Franko, C.-H. Yim, F. Årén, G. Åvall, P. S. Whitfield, P. Johansson, Y. A. Abu-Lebdeh, G. R. Goward, *J. Electrochem. Soc.* **2020**, *167*, 160532.

[10] C.-H. Yim, Y. A. Abu-Lebdeh, *J. Electrochem. Soc.* **2018**, *165*, A547.

[11] O. Borodin, L. Suo, M. Gobet, X. Ren, F. Wang, A. Faraone, J. Peng, M. Olguin, M. Schroeder, M. S. Ding, E. Gobrogge, A. Von Wald Cresce, S. Munoz, J. A. Dura, S. Greenbaum, C. Wang, K. Xu, *ACS Nano* **2017**, *11*, 10462.

[12] M. Špadina, J. F. Dufrêche, S. Pellet-Rostaing, S. Marčelja, T. Zemb, *Langmuir* **2021**, *37*, 10637.

[13] A. Wahab, S. Mahiuddin, *Can. J. Chem.* **2001**, *79*, 1207.

[14] B. B. Spencer, Simultaneous determination of nitric acid and uranium concentrations in aqueous solution from measurements of electrical conductivity, density, and temperature **1991**.

[15] W. Li, Y. Liu, Z. Zhang, R. Liu, J. Qiu, S. Wang, *J. Mater. Chem. A* **2021**, *9*, 15755.

[16] P. Fellner, I. Horsák, I. Koštenská, A. Žúžiová, A. Michalíková, .

[17] J. Eysseltová, V. T. Orlova, *J. Phys. Chem. Ref. Data* **2010**, *39*, 033104.

[18] H. Tizek, E. Knözinger, H. Grothe, *Phys. Chem. Chem. Phys.* **2002**, *4*, 5128.

[19] M. Kenisarin, K. Mahkamov, *Sol. Energy Mater. Sol. Cells* **2016**, *145*, 255.

[20] I. V. Gavrilin, *Russ. Metall.* **2022**, *2022*, 274.

[21] Rosemount Analytical, Conductance Data For Commonly Used Chemicals, **2010**, 44-6039/rev. B.

[22] K. D. Beyer, A. R. Hansen, M. Poston, *J. Phys. Chem A* **2003**.

[23] J. Han, A. Mariani, S. Passerini, A. Varzi, *Energy Environ. Sci.* **2023**.

[24] P. B. Calio, C. Li, G. A. Voth, *J. Phys. Chem. B* **2020**, *124*, 8868.

[25] W. Zhang, X. Chen, Y. Wang, L. Wu, Y. Hu, *ACS Omega* **2020**, *5*, 22465.

[26] H. Every, A. Bishop, M. Forsyth, D. M.-E. Acta, undefined 2000, *Elsevier*.

[27] A. Chagnes, S. Nicolis, B. Carré, P. Willmann, D. Lemordant, *ChemPhysChem* **2003**, *4*, 559.

[28] A. Wahab, S. Mahiuddin, *Can. J. Chem.* **2001**, *79*, 1207.

[29] P. Y. Lin, A. N. Soriano, R. B. Leron, M. H. Li, *J. Chem. Thermodyn.* **2010**, *42*, 994.

[30] Y. Fu, X. Cui, Y. Zhang, T. Feng, J. He, X. Zhang, X. Bai, Q. Cheng, *J. Chem. Eng. Data* **2018**, *63*, 1180.

Chapter 4: A polymer-rich quaternary composite solid-state electrolyte for lithium batteries

Adapted from: Al-Salih, H.; Huang, A.; Yim, C.-H.; Freytag, A. I.; Goward, G. R.; Baranova, E.; Abu-Lebdeh, Y. J. Electrochem. Soc. 2020, 167 (7), 070557.

Abstract

All-solid-state batteries continue to grow as an alternative to replace the traditional liquid-based ones not only because they provide increased safety but also higher power and energy densities. However, current solid-state electrolytes are either ceramics that are brittle but highly conducting (e.g. $Li_{0.33}La_{0.55}TiO_3$, LLTO) or polymer electrolytes that are poorly conducting but form flexible films with desired mechanical properties (e.g. Poly(ethylene oxide):Lithium bis(trifluoromethanesulfonyl)imide, PEO:LiTFSI). In this work, we have developed quaternary composite solid-state electrolytes (CSEs) to combine the benefits of the two types along with Succinonitrile (SN) as a solid plasticizer. CSEs with different compositions have been fully characterized over the whole compositional range. Guided by neural network simulation results it has been found that a polymer-rich CSE film gives the optimal ionic conductivity (10^{-3} S/cm at 55˚C) and mechanical properties (Tensile strength of 16.1 MPa; Elongation-at-break of 2360%.). Our solid-state coin-type cell which employs our in-house made cathode shows good cycling performance at C/20 and 55 °C maintaining specific discharge capacity at 143.2 mAh/g after 30 cycles. This new approach of formulating quaternary CSEs is proven to give the best combination of properties and should be universal and be applied to other CSEs with different chemistry.

Key words: solid-state battery; solid-state electrolyte; composites; Lithium batteries; ceramics; polymer electrolytes; interface

Introduction

High energy density, high output voltage and long cycle life with low capacity fading are the attractive characteristics that drove the world towards researching and utilizing lithium ion batteries.[1–4] Nowadays, they are the most commercially used batteries and are the leading power sources for electric vehicles (EV's) and other energy storage applications [3,4]. However, there are some safety hazards accompanying most commercial batteries and this is mainly attributed to the fact that they utilize organic liquid electrolytes which serves as a medium for dendrite formation and always possess the risks of leakage, volatilization, thermal instability and internal short circuiting. The radical solution to eliminate all the above mentioned risks has been found to be the utilization of solid-state electrolytes to form all solid-state batteries.[5–7] In addition to being safer, polymer-based solid-state electrolytes are flexible, mechanically strong and they offer higher power and energy densities as well as better thermal and electrochemical stability.[8,9] Noteworthy, being flexible allows their incorporation in various flexible electronics such as implantable biomedical devices, wearable electronics and sensors.[10] For the past decade, researchers have been proposing different strategies to create flexible battery components.[11–15] Although the use of liquid electrolytes in flexible batteries is possible, it is highly recommended to avoid the uses because of the above mentioned disadvantages.

One approach to calm the safety hazards associated with liquid electrolytes, is confining them in a solid polymer matrix. This gives the electrolyte mechanical strength yet, the ionic conductivity remains a function of the specific liquid electrolyte and its amount. This type of electrolyte is termed 'gel polymer electrolyte' or 'gel electrolytes'.[16–19] Unfortunately, the performance of gel electrolytes depends on the amount of liquid electrolytes in them and thus, they possess the same risk as the conventional liquid electrolyte especially under demanding operational conditions.[20] Consequently, researchers turned their attention towards the development of completely dry solid electrolytes to ensure total safety. Ionic conduction mechanism is the same in both solid and liquid lithium-ion batteries. In both, the lithium-ions de-intercalate from the cathodic side and gets transported through the electrode-electrolyte interfaces and the electrolyte until they reach the anode. The only difference between the two batteries is that there is no need for a separator in the solid-state battery because the electrolyte itself acts as one.[21] Solid-state electrolytes are mainly divided into two main classes, the inorganic solid electrolytes (ISE) and the solid polymer electrolytes (SPE). Different classes of ISE have been intensively researched. Although ISE have a generally lower ionic conductivity than liquid electrolytes, researchers have been able to explore a variety of ISE with

conductivities that are comparable and even higher than liquid electrolytes.[22–24] Perovskite ISE possess high oxidation potential and mechanical strength but, are unstable when in contact with lithium[25,26] and suffer from high grain boundary resistance.[27] Likewise, NASICON-like ISE show high oxidation potential, high ionic conductivity but are brittle and unstable against lithium metal.[28,29] On the other hand, garnet ISEs (e.g. LLZO) are stable with lithium metal but are hygroscopic and reactive with moisture.[30,31] Similarly, sulfides suffer from sensitivity towards moisture despite having impeccable ionic conductivity.[8,32] Further, high electrode/electrolyte interfacial resistance is observed when applying any kind of ISE, this is attributed to their crystalline structure. This, alongside their large-scale manufacturing difficulties impedes their large scale application.[28]

On the other hand, numerous SPEs based on high molecular weight polymers have been studied. All SPEs share the advantage of flexibility, easy processability and relatively better electrode/electrolyte interfacial compatibility when compared to ISE.[33] In particular, the polymer polyethylene oxide (PEO) has been found suitable for all-solid-state battery applications. It is applied in the form of a free standing film without major change in the current design of batteries.[34] Also, PEO is known for its ability to solvate various lithium salts by the interaction of ether oxygen bonds with lithium cations.[35,36] Nevertheless, its application is heavily hindered by the low room temperature conductivity (10^{-6}-10^{-8} S/cm) which is partly because of the high degree of crystallinity of PEO below its melting point ($\sim$ 60 °C).[37,38] To develop SPEs with good ionic conductivity and mechanical properties, researchers investigated methods to reduce PEO crystallinity at low temperature. Possible methods include the addition of inorganic ceramic fillers (ex. Al_2O_3, SiO_2)[37,38] or organic plasticizers (SN, PEG).[41–43] Those fillers are passive fillers as they provide no direct contribution to Li-ion conductivity. Differently, there are fillers termed ‘active fillers’ as they provide alternative pathways for Li-ion migration and thus directly contribute to a substantial increase in ionic conductivity [44,45]. Examples of active fillers are ISEs themselves when added in small amounts to SPEs creating what can be termed as composite solid electrolyte (CSE) or sometimes termed hybrid solid electrolyte (HSE). In the past decade, research has been directed towards different hybrid and CSE materials with a focus on exploring different fillers with SPEs and ISEs In general, CSEs can be classified into two types based on the relative amounts of ceramic and polymer in the CSE: (1) Polymer-rich or ceramic-in-polymer CSEs where the polymer is the primary phase and its amount is greater than that of the secondary phase ceramic (2) Ceramic-rich or polymer-in-ceramic where the ceramic is the primary phase and its amount in the composite is greater

than that of the secondary phase polymer. The properties of the CSE is then governed by those of the primary phase hence each type has its own pros and cons. For example, the polymer-rich CSE has the advantage of retaining the polymer's properties of ease of processability and flexibility and good contact with the electrodes while the ceramic-rich CSE retains the high ionic conductivity and non-flammability of the ceramic.

Most of the studies in the literature are focused on ternary CSEs compromised of a polymer, a ceramic and one of the fillers and seldom on quaternary CSEs. Therefore, in this work we report on a novel type of polymer-rich CSE where both active and passive fillers are used to produce a novel quaternary CSEs with enriched properties. The active filler used is the ISE fast-ionic conductor $Li_{0.34}La_{0.51}TiO_3$ (LLTO) perovskite ceramic and the passive filler is the organic plasticizer 'Succinonitrile' (SN), as depicted in the schematic in Fig 4.1 a. An investigation was executed to find out the appropriate compositions of PEO/LiTFSI/LLTO/SN (quaternary electrolytes) that would provide a highly conductive, free-standing CSE film as shown in Fig 4.1 b. Then, a full chemical, thermal, mechanical and electrochemical characterization of a selected composition was carried out and battery performance was evaluated in solid-state batteries.

Experimental

Materials

LLTO (NANOMYTE) was purchased from NEI corporation, PEO (average Mv = 600000 g/mol), LiTFSI salt and Acetonitrile were purchased from Sigma-Aldrich and Succinonitrile was purchased from Fluka. $Li(Ni_{0.5}Mn_{0.3}Co_{0.2})O_2$ (NMC532) was purchased from MTI Corp.

Preparation of CSE films

LiTFSI and LLTO powders were vacuum dried for 24 h at 80 °C while PEO and SN were dried under vacuum at 40 °C to prevent their melting. The thin CSE films were prepared using the traditional solution casting method. In a small vial, PEO powder was first dispersed in methanol in order to prevent agglomeration and then the main solvent acetonitrile was added to the vial to amount the PEO concentration to 7.3%. The PEO was then allowed to fully dissolve in acetonitrile using mechanical stirring for 2 h. LLTO and SN were then added to the solution and mechanically stirred for 24 h. Then, LiTFSI salt, in the 40:1 EO:Li ratio, was added and the solution continued to stir for another 4 hours before it was casted on circular mirror plates.

The film was then air dried for 12 h in a convection oven while covered with an acetonitrile wetted cloth to slow down evaporation in order to achieve homogenously looking films, as shown in Fig 4.1 c. Films were then dried under vacuum for 24 h to completely release any trapped solvent.

Sample characterization

The mechanical strength of the fully dried films was quantitatively measured by examining the stress-strain relationship using MTS Insight Electro-mechanical load frame. The films were cut into rectangular coupons that were 15 mm long and 100 mm wide. The test was carried out with a tensile speed of 1 mm/min.

X-ray diffraction (XRD) measurements were conducted in the Bruker D8 phaser diffractometer with Cu Kx radiation ($\lambda = 1.545$) from $2\theta = 10° - 80°$ with a step of magnitude 5° per minute. Further, Thermo-gravimetric analysis (TGA) was performed with Q5000 iR TA instrument. The CSE samples were heated in a sample pan from 25 °C to 600 °C. The heating was done in platinum pans under a N_2 purge gas flow of 25 cc/min at a rate of 10 °C/min. Differential Scanning Calorimetric (DSC) analysis was performed using Q2000 TA instrument. All the samples were sealed in aluminum hermetic pans and scanned from −90 to 100 °C at 10 °C/min rate under a N_2 purge gas flow of 50 cc/min.

Infrared spectra were recorded using Thermo Fisher Nicolet 6700 with a KBr beam splitter from 4000 to 500 cm^{-1} at 4 cm^{-1} resolution and 32 scans at room temperature. Attenuated total reflection (ATR) single bounce with diamond crystal was used as an accessory.

The ionic conductivity of the CSE film was calculated by running electrochemical impedance spectroscopy in the frequency range of 10^6 Hz to 1 Hz with an amplitude of 10 - 50 mV using solatron 1287 frequency analyzer. The CSE thin films were sandwiched between 2 symmetrical blocking stainless steel electrodes of diameter 22.8 mm and their ionic conductivity was determined as a function of temperature between 30 °C and 70°C with one hour rest time between measurements. The ionic conductivity was calculated using the following equation:

$$\sigma = \frac{L}{A}\frac{1}{R} \qquad \text{Eq.1}$$

Where σ (S/cm) is the ionic conductivity, L (cm) is the film thickness R (Ω) is the bulk resistance and A (cm^2) is the area of the symmetrical electrode. The activation energy was calculated from the Arrhenius plot using the Arrhenius equation:

$$\sigma = \sigma o \exp(\frac{-Ea}{RT})$$

Eq.2

Where σ (S/cm) is the ionic conductivity, σ_o is the pre-exponential factor, E_a is the activation energy, R is the universal gas constant and T is temperature.

All NMR measurements were performed on a 300 MHz spectrometer fitted with a variable temperature unit using a Diff50 probe. For ^{7}Li NMR measurements the CSE film was cut into a rectangular sheet and rolled up to fit inside a 4 mm magic angle spinning rotor. The rotor was then inserted into a 5 mm NMR tube. This allows for easy cleaning of the NMR tube and even distribution of the sample inside the spectrometer. The film was then heated at 75˚C for 4 hours inside the magnet before conducting diffusion measurements. Measurements were performed between 30-70˚ C. A 20-minute waiting period was included before running diffusion measurements to allow for the sample to equilibrate at the correct temperature (range: 30-70˚C). A stimulated echo gradient pulse sequence was used with the gradient length δ fixed at 2.5 ms and the diffusion time Δ set between 30-200 ms. The b values were kept constant for each temperature by varying the applied gradient strength and the diffusion time. The number of scans varied between 32 and 1024 scans with the gradient steps being kept constant at 32. Recycle delays were set between 1.0-2.5 s. T2 relaxation of LLTO is approximately an order of magnitude smaller than in LiTFSI, leading to a filtering of the LLTO signal under the above conditions. Solely the dynamics of LiTFSI in the polymer matrix is observed in this study. Diffusion data sets were fit using a single or (where applicable) multi-component fit in Matlab.

The electrochemical stability window was determined by linear sweep voltammetry (LSV) experiments which were run in a two-electrode cell fitted with stainless steel electrodes using Biologic VMP3 potentiostat. The scanning rate chosen was 50 mVs^{-1} at 55 °C from - 4 V to 4 V.

Battery Assembly and testing

To test the battery performance of these solid-state electrolytes, an all-solid-state 2325 coin-type half cells were assembled. Lithium metal discs were used as the counter electrode and a modified cathode was prepared to incorporate the PEO:LiTFSI electrolyte. The cathode composition (wt %) is as follows: 70% NMC 532, 15% PEO:LiTFSI (2:1), 10% Carbon C65 and 5% PVDF. The cathode slurry was prepared by adding pre-dissolved 2.5 wt% PVDF in NMP to 11.5 wt% PEO/LiTFSI in acetonitrile. C65 and NMC 532 are then added sequentially. The cathode was then cast on aluminum current collector and then dried at 80 °C for 24 h. The cathode was then calendared and was ready for use. 0.5'' diameter circular cuts were taken for coin-type cell assembly in an Argon filled glove box by sandwiching a 0.7'' solid electrolyte cut in between a 0.7'' Li disc and the cathode cut. The fabricated cells were then heated to 70 °C for 4 h, then cooled down and capacity measurements were performed by galvanostatic experiments carried out on a multichannel Arbin battery cycler (BT2000). This heating cycle is essential to homogenise the sample and stabilize the electrode/electrolyte interface. Charge-discharge tests were then carried out in the potential range of 2.5-4.2 V at 55 °C.

Results and discussion

The first step in the preparation of the polymer-rich quaternary CSEs is to select the PEO:LiTFSI (better known as EO:Li) molar ratio). This is better done by the aid of the PEO:LiTFSI phase diagram which is well documented and it shows the formation of three complex compounds at 2:1, 3:1 and 6:1 molar ratios with a crystallinity gap in the eutectic composition region between 12:1 and 6:1.[46] The conductivity isotherms (σ vs. T) are also known and similar to most liquid and solid electrolytes; it shows an increase in conductivity with salt addition but goes through a maximum near the eutectic composition and then drops thereafter till the saturation concentration. At room temperature, the conductivity increases from 10^{-8} S/cm at 48:1 EO:Li to reach a maximum of 10^{-5} S/cm at 10:1 EO:Li and decreases to 10^{-7} S/cm at 6:1 EO:Li. while at temperatures around the melting point of pure PEO, a similar trend is observed for the isotherm with an overall increase of one order of magnitude in conductivity values with a maximum still at 10:1. The eutectic composition seems to be a natural choice due to the maximum conductivity, but the mechanical properties are poor due to the crystallinity gap which prevents the formation of free-standing films. In this work, we selected an EO:Li ratio in the polymer-rich side of the phase diagram close to 40:1 where at room temperature pure, solid PEO coexists in equilibrium with either the liquid or (amorphous) solid 6:1 complex. Binary and ternary phase diagrams of PEO, LiTFSI and SN have also been

studied and eutectic-type phase diagrams are observed in the binary phases and coexistence regions in the ternary phase diagram have been identified at the end members with a wide isotropic liquid-like regions in the center indicative of the formation of ternary eutectics. [46]

Next, even though we decided to focus on polymer-rich CSE composites which means small amounts of LLTO and SN to act as fillers, CSEs were fabricated in different ratios, to cover the whole compositional range including CSEs with large amounts of LLTO and SN to map out and have an understanding of the structure/property relationship in these previously unknown quaternary CSEs. Then, the obtained properties (mechanical properties and ionic conductivity) were used as data points for non-linear fitting by using a neural network algorithm as described by Li *et al*. [47] The parameters obtained were used for simulating ternary diagrams. The simulation results were presented as two contour maps for each property, where light to dark orange color indicates free standing films and $\geq 10^{-3}$ S/cm conductivity and blue color indicates no film formation and $\leq 10^{-5}$ S/cm conductivity, respectively. As can be seen in Fig 4.2 (a) and (b), the ternary compositions that are best at film forming, are mainly concentrated in the polymer-rich or ceramic-in-polymer region, while the conductivity contour map indicates that the SN-rich region shows the highest ionic conductivity. This is expected as SN is known to act as a polymer plasticizer [42] and its high polarity allow for the ease of dissolution of lithium salts[45]. Based on this, the conclusion is that a quaternary composition in the polymer-rich region with small amounts of SN have the optimal combination of electrochemical and mechanical properties. Similar conclusions were drawn by Chen *et al* in a study that showed that the role of another ceramic LLZO in similar ceramic-in-polymer composites, but with no SN, is to enhance mechanical properties of the films while in the polymer-in-ceramic composites the ceramic provides a pathway for Li ions, while all improves the ability of the otherwise organic polymer to withstand stress from dendrites formed during lithium plating/stripping.[49]

The CSE film chosen for full characterization is sample ‘10S’ which lies in the red/orange regions of the two ternary composition diagrams showing the highest combination of conductivity and film forming ability. The composition of 10S is 70 wt% PEO, 12 wt% LiTFSI 9 wt%, LLTO and 9 wt% SN. The morphology and chemical composition of the sample was studied by SEM and EDS and images in Fig 4.3(a) and (b) indicate that LLTO particles (~ 2 μm) and LiTFSI salt are homogeneously dispersed in the porous polymer matrix.

Electrochemical Impedance Spectroscopy (EIS) was used to measure the conductivity of the 10S CSE film and found to be 1.9 x 10^{-4} S/cm at room temperature and 2.4 x 10^{-3} S/cm at 55˚C. These values are much higher than the reported values by Fan *et al* for PEO:LiTFSI:SN composites with 11:1 EO:Li ratio which is close to the eutectic composition and prone to produce liquid-like films. [42] The reported ionic conductivity at 30℃ reached 5 x 10^{-4} S/cm for the 50% SN-containing film and ~ 5 x 10^{-5} S/cm for the 16% SN-containing film. Even though it gives higher conductivity the use of larger amounts of SN introduces competition between SN (dielectric constant, ε = 38) and PEO (dielectric constant, ε = 8) and this results in blocking of ionic pathways. Fig 4.4 shows the σ vs. T "Arrhenius" plot for this CSE film. The activation energies of the film were calculated using the Arrhenius equation (eq 2) and the linear fitting for the data points in the low temperature region and the high temperature region as can be seen in fig 4.4. The activation energies were found to 37.6 ± 4 kJ/mol and 27.3 ± 1 kJ/mol, respectively. This drop in activation energy indicates an increase in the ease in which ions move at higher temperatures that is also expected in the molten state. In general, the activation energy values found in this work are similar to those reported by Fan *et al* [42] but way lower than those reported by Zhu *et al*[44] on PEO:LiTFSI:LLTO nano-composites. Activation energies higher than 40 kj/mol for composites with small amounts of LLTO fiber were reported that are close to those of PEO:LiTFSI (~ 50 kj/mol).[50] This indicates easier ionic conduction pathways in the quaternary composite compared to ternary composites specially the ones without SN as a plasticizer.

FTIR spectroscopy was utilized to observe and analyze the molecular interactions between the four components in the CSE film and the spectra are shown in Fig 4.5. PEO FTIR spectrum contains bands at around 842, 1100 and 1468 cm^{-1} which corresponds to CH_2 wagging mode, C-O-C stretching mode and CH_2 scissoring mode, respectively. [48] By means of comparison of the FTIR spectra of the 10S CSE film and its individual components, we can notice that the band at around 1470 cm^{-1} splits and becomes sharper which indicates a possible interaction between SN and Li cation of LiTFSI. Besides, we can also observe the broadening of the C-O-C stretching band at around 1100 cm^{-1}. This in turn indicates the coordination of Li^+ cation with the ether groups in PEO [49] .

^{7}Li NMR spectroscopy was also performed for the 10S CSE film to get more insight on this interaction and ion dynamics at different temperatures. The spectra shown in Fig 4.6 a reveal a single, broad peak throughout the heating and cooling cycles which is attributed to the

LiTFSI species. The linewidth decreases with increasing temperature indicating a change in ion mobility. Diffusion behavior of PEO-containing polymer electrolytes has been studied extensively in the past.[53] Detailed dynamic NMR studies have revealed the dependence of the cation mobility on the morphology of the polymer matrix.[51, 52] It has been shown that an increase in amorphous domains leads to a better-connected conductive networks. In particular, the polymer chain motion is essential in facilitating ionic diffusion in polymer electrolytes.[56,57] ^{7}Li pulsed field gradient (PFG) NMR was performed in order to investigate ionic diffusion in the 10S CSE film. Diffusion curves were obtained in the range of 30-70°C and are shown in Fig 4.6 b. At high temperatures a single diffusion process dominates, allowing for an accurate single-component fit while a single-component fit is not appropriate at lower temperatures. It is evident, that there is a significant change in the diffusion behavior between 45 °C to 55 °C. At high temperatures (55 °C to 70 °C) a linear dependence is apparent while at intermediate temperatures a coexistence of two components with slightly different diffusivities is apparent. This is in agreement with the change of morphology around the transition temperature, where presumably regions with varying degree of crystallinity are apparent. This gradual phase change is observed around 50 °C, which shows as a deviation from linear behavior in the Arrhenius plot in Fig 4.6 b. These two different regions have contrasting diffusion behavior with activation energies for region I and region II of 37.38 ±1 kJ/mol and 66.67 ±1 kJ/mol, respectively. However, the change in activation energy with temperature is in line with what was observed earlier in the Arrhenius plots obtained from ionic conductivity measurements and can be attributed to polymer morphology which has a significant influence on the diffusion pathways besides a possible role of SN. This might indicate that in polymer-rich CSE composites the ionic conductivity is dominated by the polymer dynamics and not the ceramic as was shown by Zheng *et al* [58] for LLZO:PEO composites where tracking of Li ion pathways at higher ceramic content proved the dominance of ceramic related pathways.

To further understand the effect of SN as a plasticizer, the phase transition behavior of 10S film was compared to that of a film made with the same ratios of 10S CSE film but without the SN, hereafter called '10S-SN'. Fig 4.7 shows the DSC scans which demonstrates a clear glass transition temperature (T_g) decrease from - 42.8 °C for 10S-SN to -53.1 °C for the 10S CSE film. A reduction in T_g enables faster ionic kinetics in polymer electrolytes [56]. Other features clear on the DSC curves of both samples is the endothermic peak shortly after 50 °C which corresponds to the melting of PEO. The 10S CSE film (SN containing) shows a marginal shift to the left because of the melting point reduction effect due to the presence of SN. Looking

closely, the melting peak of 10S-SN is also broader which is attributed to its higher crystallinity. To confirm this, the degree of crystallinity, X_c, was calculated using by using Eq. 3.

$$X_c = \frac{\Delta \boldsymbol{H_m}}{\Delta \boldsymbol{H_{PEO}} \cdot \boldsymbol{Y_{PEO}}} \quad \text{Eq. 3}$$

Where ΔH_m is the melting enthalpy of the sample, ΔH_{PEO} is the melting enthalpy of 100% crystalline PEO, 203 J g^{-1} [57][58] and Y_{PEO} is the weight fraction of PEO in the sample. X_c calculations show that 10S – SN is 51.8% crystalline while 10S is 42.6% crystalline. This significant decrease in crystallinity is solely caused by the addition of SN. Similar behavior was observed by Fan *et al* for similar compositions but without LLTO, and they showed that for much higher amounts of SN (50%) results in completely amorphous composites. [42]

PEO is a semi-crystalline polymer where the amorphous phase offers activated and more flexible chain segments which aid ion mobility [59]. Previous reports and studies have attributed PEO low ionic conductivity to slow polymer chains dynamics and inactive chain segments due to the crystalline phase domination. Hence, studies have been directed towards using fillers that increase the amorphous phase ratio, those are termed 'plasticizers'. XRD technique was used to investigate the crystal structure of 10S and 10S-SN CSE films. Before the characterization, the two samples underwent a heating cycle by heating to 70˚C for 4 hours then cooled back to ambient conditions. Fig 4.8 shows the clear disappearance of two major peaks related to PEO crystalline phase peaks at around 19˚and 23˚. This further proves the effectiveness of SN in the CSE as it plays both the role of Li^+ solvation and PEO chain plasticization which in turn explains the high ionic conductivity of this electrolyte.

Furthermore, the thermal stability of the 10S CSE film was investigated by means of TGA. Solid-state electrolytes must possess high degrees of thermal stability. This is to ensure safety and justify their use over liquid electrolytes. The TGA profile shown in Fig 4.9 indicates that there is a slight weight loss happening mainly after 100˚C but the 10S CSE film demonstrates good thermal stability till about 360˚C. Notably, the weight percentage remaining after heating to 600˚C is 12.3 wt% which is slightly higher than the ceramic content in the sample. This difference could correspond to carbon residues remaining after complete degradation. Echeverri *et al* [46] reported the TGA scans of PEO, LiTFSI and SN and showed

that while both neat PEO and LiTFSI have high thermal stability up to 380 °C the neat SN is only stable up to 130 °C upon prolonged heating. This can explain the small weight loss above 100 °C in the 10S CSE film.

The mechanical properties of 10S CSE film was measured by stress-strain testing. A good CSE film should be processed to withstand great forces of stress to ensure it does not fail either during cell packaging or when being charged/discharged. The stress-strain curve for the 10S CSE film is presented in Fig 4.10. The film exhibits a Young's modulus of ~ 155 MPa, a Tensile strength of 16.1 MPa and an elongation-at-break of 2360%. Thus, This CSE film possesses plastic behavior and can be applied as a separator and as an ionic conductor. Fan *et al* reported on the mechanical properties of similar composites without LLTO and showed that the addition of 50% SN to PEO:LiTFSI (11:1 EO:Li) resulted in a tensile strength of 0.5 MPa and an elongation-at-break of 550 %.[42] The values are way smaller than those of the 10S CSE film which could be attributed to the large amount of SN in the films along with the presence of LLTO in the 10S film which seems to improve the mechanical properties of the quaternary CSE.

Electrochemical stability is another key parameter to develop high energy density lithium batteries. By means of linear sweep voltammetry (LSV), we were able to determine the electrochemical stability window of the 10S CSE film at 55˚C as shown in Fig 4.11. We can observe the oxidation/reduction peaks starts to rise at 2.5 V and -2.5 V respectively which translates to an electrochemical stability window of 5V.

To assess the electrochemical performance of the 10S CSE film, 2325 coin-type cells were assembled by sandwiching the 10S film between commercial NMC 532 cathode (fabricated following common procedures of mixing NMC 532 powder with PVDF binder and a carbon additive) and a lithium disc. Charge-discharge tests were then carried out in the potential range of 2.5-4.2 V at 55 °C and at a cycling rate of C/20. These cells showed poor cycling performance and provided an initial discharge capacity of only 7 mAh/g. This is mainly attributed to the poor interfacial contact between the cathode and the electrolyte and the internal resistance inside the cell was calculated to be 2030 ± 10 Ω. To improve the interracial resistance, we assembled coin-type cells in the glove box following the procedure outlined in the experimental section of this paper which employs our in-house made cathode. The cathode used utilizes PEO:LiTFSI (2:1) as a co-binder to help improve the cathode/electrolyte interfacial

contact. Fig 4.12 shows the charge-discharge curve and the cycling performance of sample 10S. Notably, the specific discharge capacity improved significantly to values closer to the known experimental values (~ 150mAh/g). The initial capacity reached 112 mA/g then it kept on increasing for the first 16 cycles which indicates the continuous homogenization of the components inside the composite and at the interface inside the battery. After 30 cycles, the battery discharge capacity reached 143.2 mAh/g and the columbic efficiency achieved was 98.8%.

Conclusion

A polymer-rich quaternary composite solid-state electrolyte composed of PEO-LiTFSI-LLTO-SN was proposed and well characterized. Simulation done using neural network fitting technique helped us to choose a quaternary sample with an optimal combination of mechanical and electrochemical properties. The chosen CSE film with the following composition: 70%-PEO 12%-LiTFSI 9%-LLTO 9%-SN was made using traditional solution casting technique and its ionic conductivity reached slightly higher than 10^{-3} S/cm at 55˚C. Mechanical testing showed that the film has a Young modulus of ~ 155 MPa and can withstand a Yield strength of around 16 MPa and has a break-at-elongation point of over 2000%. FTIR, NMR, DSC and XRD techniques proved with evidence the role of Succinonitrile as a salt solvator and a polymer chain plasticizer, thus, explaining the high ionic conductivity. To fabricate the battery, incorporation of PEO:LiTFSI as a binder in the NMC 532-based cathode was essential to overcome the cathode-electrolyte interfacial resistance issue. The discharge capacity achieved by the battery Li/NMC/CSE after 30 cycles was 143.2 mAh/g at C/20 and 55˚C. Results conclude that this quaternary CSE is a promising candidate for next-generation solid-state lithium batteries.

Acknowledgments

We would like to thank Office of Energy Research and Development (OERD) at Natural Resources Canada for financial support.

References

[1] M. Armand, J. M. Tarascon, *Nature* **2008**, *451*, 652.

[2] J. W. Fergus, *J. Power Sources* **2010**, *195*, 939.

[3] C.-Y. Wang, G. Zhang, S. Ge, T. Xu, Y. Ji, X.-G. Yang, Y. Leng, *Nature* **2016**, *529*.

[4] E. Quartarone, P. Mustarelli, Electrolytes for solid-state lithium rechargeable batteries: Recent advances and perspectives. *Chem. Soc. Rev.* **2011**, *40*, 2525–2540.

[5] P. P. Soo, B. Huang, Y. I. I. Jang, Y. M. Chiang, D. R. Sadoway, A. M. Mayes, *J. Electrochem. Soc.* **1999**, *146*, 32.

[6] Y. Zhao, C. Wu, G. Peng, X. Chen, X. Yao, Y. Bai, F. Wu, S. Chen, X. Xu, *J. Power Sources* **2016**, *301*, 47.

[7] Q. Zhao, S. Stalin, C.-Z. Zhao, L. A. Archer, *Nat. Rev. Mater.* **2020**, 1.

[8] N. Kamaya, K. Homma, Y. Yamakawa, M. Hirayama, R. Kanno, M. Yonemura, T. Kamiyama, Y. Kato, S. Hama, K. Kawamoto, A. Mitsui, *Nat. Mater.* **2011**, *10*, 682.

[9] K. Xu, Electrolytes and interphases in Li-ion batteries and beyond. *Chem. Rev.* **2014**, *114*, 11503–11618.

[10] H. Nishide, K. Oyaizu, Toward flexible batteries. *Science (80-.).* **2008**, *319*, 737–738.

[11] A. Goyal, A. L. M. Reddy, P. M. Ajayan, *Small* **2011**, *7*, 1709.

[12] S. Y. Chew, S. H. Ng, J. Wang, P. Novák, F. Krumeich, S. L. Chou, J. Chen, H. K. Liu, *Carbon N. Y.* **2009**, *47*, 2976.

[13] J. Z. Wang, C. Zhong, S. L. Chou, H. K. Liu, *Electrochem. commun.* **2010**, *12*, 1467.

[14] N. Li, Z. Chen, W. Ren, F. Li, H. M. Cheng, *Proc. Natl. Acad. Sci. U. S. A.* **2012**, *109*, 17360.

[15] L. Noerochim, J. Z. Wang, S. L. Chou, D. Wexler, H. K. Liu, *Carbon N. Y.* **2012**, *50*, 1289.

[16] A. M. Stephan, Review on gel polymer electrolytes for lithium batteries. *Eur. Polym. J.* **2006**, *42*, 21–42.

[17] J. Y. Song, Y. Y. Wang, C. C. Wan, Review of gel-type polymer electrolytes for lithium-ion batteries. *J. Power Sources* **1999**, *77*, 183–197.

[18] A. Arya, A. L. Sharma, Polymer electrolytes for lithium ion batteries: a critical study. *Ionics (Kiel).* **2017**, *23*, 497–540.

[19] I. Osada, H. De Vries, B. Scrosati, S. Passerini, Ionic-Liquid-Based Polymer Electrolytes for Battery Applications. *Angew. Chemie - Int. Ed.* **2016**, *55*, 500–513.

[20] W. H. Meyer, *Adv. Mater.* **1998**, *10*, 439.

[21] F. Zheng, M. Kotobuki, S. Song, M. O. Lai, L. Lu, *J. Power Sources* **2018**, *389*, 198.

[22] Z. Ma, H. G. Xue, S. P. Guo, Recent achievements on sulfide-type solid electrolytes: crystal structures and electrochemical performance. *J. Mater. Sci.* **2018**, *53*, 3927–3938.

[23] J. C. Bachman, S. Muy, A. Grimaud, H. H. Chang, N. Pour, S. F. Lux, O. Paschos, F. Maglia, S. Lupart, P. Lamp, L. Giordano, Y. Shao-Horn, Inorganic Solid-State Electrolytes for Lithium Batteries: Mechanisms and Properties Governing Ion Conduction. *Chem. Rev.* **2016**, *116*, 140–162.

[24] A. Varzi, R. Raccichini, S. Passerini, B. Scrosati, *J. Mater. Chem. A* **2016**, *4*, 17251.

[25] C. H. Chen, K. Amine, *Solid State Ionics* **2001**, *144*, 51.

[26] Y. H. Cho, J. Wolfenstine, E. Rangasamy, H. Kim, H. Choe, J. Sakamoto, *J. Mater. Sci.* **2012**, *47*, 5970.

[27] C. Ma, K. Chen, C. Liang, C. W. Nan, R. Ishikawa, K. More, M. Chi, *Energy Environ. Sci.* **2014**, *7*, 1638.

[28] M. Keller, A. Varzi, S. Passerini, *J. Power Sources* **2018**, *392*, 206.

[29] P. Hartmann, T. Leichtweiss, M. R. Busche, M. Schneider, M. Reich, J. Sann, P. Adelhelm, J. Janek, *J. Phys. Chem. C* **2013**, *117*, 21064.

[30] A. Sharafi, E. Kazyak, A. L. Davis, S. Yu, T. Thompson, D. J. Siegel, N. P. Dasgupta, J. Sakamoto, *Chem. Mater.* **2017**, *29*, 7961.

[31] M. Wang, J. Sakamoto, *J. Power Sources* **2018**, *377*, 7.

[32] Q. Zhang, D. Cao, Y. Ma, A. Natan, P. Aurora, H. Zhu, *Adv. Mater.* **2019**, *31*, 1901131.

[33] C. Sun, J. Liu, Y. Gong, D. P. Wilkinson, J. Zhang, Recent advances in all-solid-state rechargeable lithium batteries. *Nano Energy* **2017**, *33*, 363–386.

[34] B. Scrosati, J. Garche, Lithium batteries: Status, prospects and future. *J. Power Sources* **2010**, *195*, 2419–2430.

[35] G. M. Stone, S. A. Mullin, A. A. Teran, D. T. Hallinan, A. M. Minor, A. Hexemer, N. P. Balsara, *J. Electrochem. Soc.* **2012**, *159*.

[36] K. J. Harry, D. T. Hallinan, D. Y. Parkinson, A. A. MacDowell, N. P. Balsara, *Nat. Mater.* **2014**, *13*, 69.

[37] S. K. Fullerton-Shirey, J. K. Maranas, *Macromolecules* **2009**, *42*, 2142.

[38] J. G. Kim, B. Son, S. Mukherjee, N. Schuppert, A. Bates, O. Kwon, M. J. Choi, H. Y. Chung, S. Park, A review of lithium and non-lithium based solid state batteries. *J. Power Sources* **2015**, *282*, 299–322.

[39] D. Lin, W. Liu, Y. Liu, H. R. Lee, P. C. Hsu, K. Liu, Y. Cui, *Nano Lett.* **2016**, *16*, 459.

[40] G. X. Wang, L. Yang, J. Z. Wang, H. K. Liu, S. X. Dou, *J. Nanosci. Nanotechnol.* **2005**, *5*, 1135.

[41] W. Liu, S. W. Lee, D. Lin, F. Shi, S. Wang, A. D. Sendek, Y. Cui, *Nat. Energy* **2017**, *2*.

[42] L. Z. Fan, Y. S. Hu, A. J. Bhattacharyya, J. Maier, *Adv. Funct. Mater.* **2007**, *17*, 2800.

[43] Y. Masuda, M. Nakayama, M. Wakihara, *Solid State Ionics* **2007**, *178*, 981.

[44] L. Zhu, P. Zhu, Q. Fang, M. Jing, X. Shen, L. Yang, *Electrochim. Acta* **2018**, *292*, 718.

[45] T. Pareek, S. Dwivedi, S. A. Ahmad, M. Badole, S. Kumar, *J. Alloys Compd.* **2020**, *824*, 153991.

[46] M. Echeverri, N. Kim, T. Kyu, *Macromolecules* **2012**, *45*, 6068.

[47] Z. Li, Z. Cheng, L. Xu, T. Li, Nonlinear Fitting by Using a Neural Net Algorithm, **1993**, https://pubs.acs.org/sharingguidelines.

[48] P. J. Alarco, Y. Abu-Lebdeh, A. Abouimrane, M. Armand, *Nat. Mater.* **2004**, *3*, 476.

[49] L. Chen, Y. Li, S. P. Li, L. Z. Fan, C. W. Nan, J. B. Goodenough, *Nano Energy* **2018**, *46*, 176.

[50] P. Zhu, C. Yan, M. Dirican, J. Zhu, J. Zang, R. K. Selvan, C. C. Chung, H. Jia, Y. Li, Y. Kiyak, N. Wu, X. Zhang, *J. Mater. Chem. A* **2018**, *6*, 4279.

[51] E. Morales, J. L. Acosta, *J. Appl. Polym. Sci.* **1998**, *69*, 2435.

[52] O. Borodin, G. D. Smith, *Macromolecules* **2006**, *39*, 1620.

[53] S. Munoz, S. Greenbaum, *Membranes (Basel).* **2018**, *8*, 120.

[54] W. Gorecki, M. Jeannin, E. Belorizky, C. Roux, M. Armand, *J. Phys. Condens. Matter* **1995**, *7*, 6823.

[55] C. Berthier, W. Gorecki, M. Minier, M. B. Armand, J. M. Chabagno, P. Rigaud, *Solid State Ionics* **1983**, *11*, 91.

[56] J. P. Donoso, T. J. Bonagamba, H. C. Panepucci, L. N. Oliveira, W. Gorecki, C. Berthier, M. Armand, *J. Chem. Phys.* **1993**, *98*, 10026.

[57] W. Gorecki, C. Roux, M. Clémancey, M. Armand, E. Belorizky, *ChemPhysChem* **2002**, *3*, 620.

[58] J. Zheng, M. Tang, Y.-Y. Hu, *Angew. Chemie Int. Ed.* **2016**, *55*, 12538.

[59] V. S. Kolosnitsyn, G. P. Dukhanin, S. A. Dumler, I. A. Novakov, Lithium-conducting polymer electrolytes for chemical power sources. *Russ. J. Appl. Chem.* **2005**, *78*, 1–18.

[60] X. L. Wu, S. Xin, H. H. Seo, J. Kim, Y. G. Guo, J. S. Lee, *Solid State Ionics* **2011**, *186*, 1.

[61] L. Hu, Z. Tang, Z. Zhang, *J. Power Sources* **2007**, *166*, 226.

[62] P. Johansson, *Polymer (Guildf).* **2001**, *42*, 4367.

Figure captions

Figure 4.1 (a) A schematic of the CSE film depicting all its components (b) A schematic of the casting process of the CSE film to slow down acetonitrile evaporation to achieve homogenous films as depicted in (c).

Figure 4.2 (a) Contour map indicating possible film forming quaternary compositions. PEO/LiTFSI ratio was fixed at 40:1. Orange and darker indicates compositions that made free standing films, blue means no film was formed. Green indicates weak self-sticking films were formed (b) similar map indicating the ionic conductivities of the compositions at 55 °C. Orange and darker indicates conductivities > 10^{-3} S/cm, blue indicates conductivities < 10^{-5} S/cm.

Figure 4.3 (a) SEM image of the 10S CSE film along with (b) layered EDS showing the distribution
of La (LLTO) and F (LiTFSI) throughout the film.

Figure 4.4 Conductivity vs. T, Arrhenius plot, of the 10S CSE film.

Figure 4.5 ATR FTIR spectra of the 10S CSE film and its components.

Figure 4.6 ^{7}Li NMR spectra of the 10S CSE film as a function of temperature during a) heating cycle, b) heating cycle) c) Diffusion coefficients of the 10S CSE film as a function of temperature. d) Arrhenius plot of the diffusion coefficient

Figure 4.7. DSC scans of the 10S CSE film with and without succinonitrile (10S-SN).

Figure 4.8 XRD patterns of the 10S CSE film with and without succinonitrile (10S-SN).

Figure 4.9 TGA scan of the 10S CSE film.

Figure 4.10 Stress strain test of the 10S CSE film.

Figure 4.11 LSV scan of the 10S CSE film.

Figure 4.12 (a) Charge-discharge curve of the 10S CSE film at 0.05C (C/20) and 55˚C (b) capacity cycling at 55˚C.

Figures

Figure 4.1

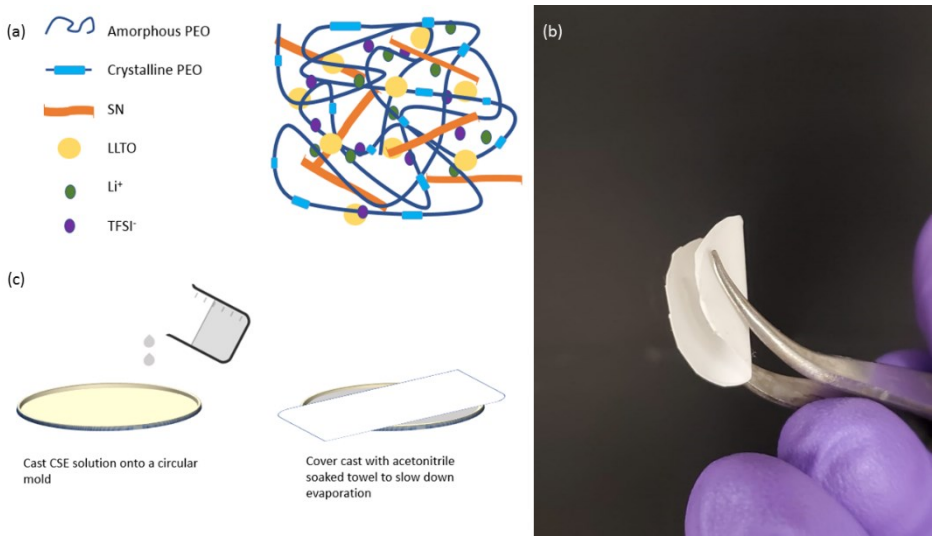

Figure 4.2

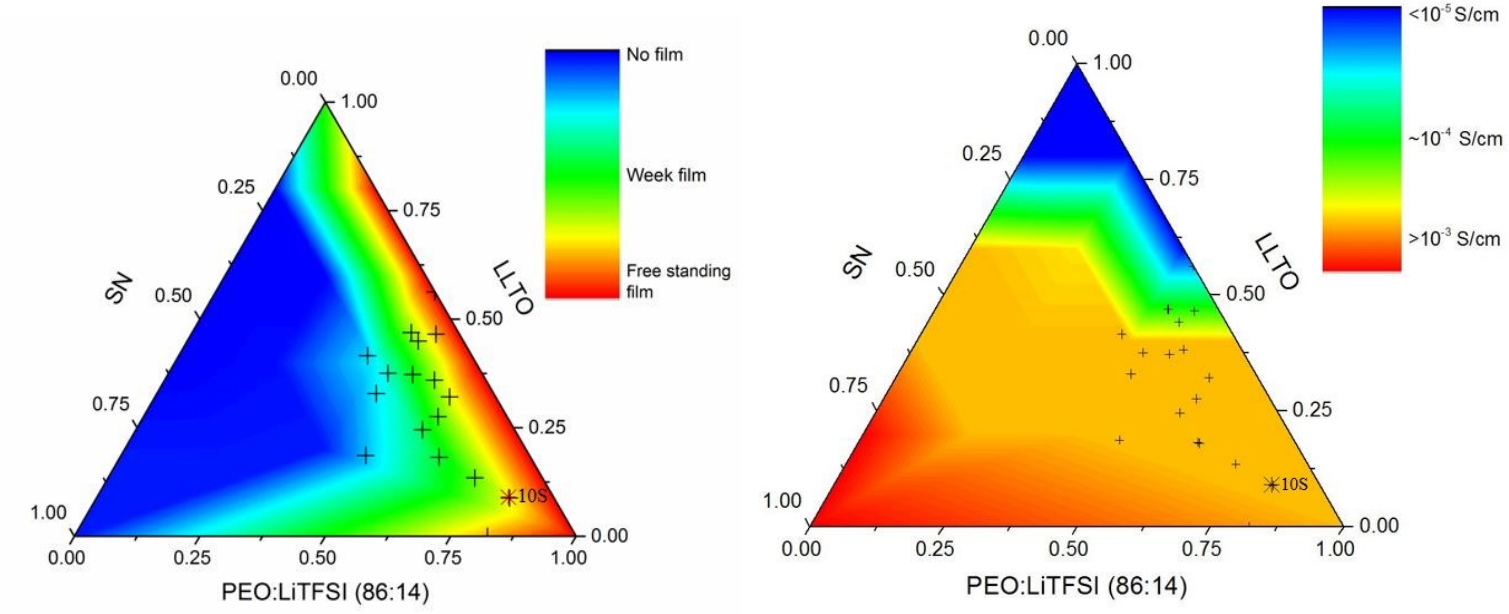

Figure 4.3

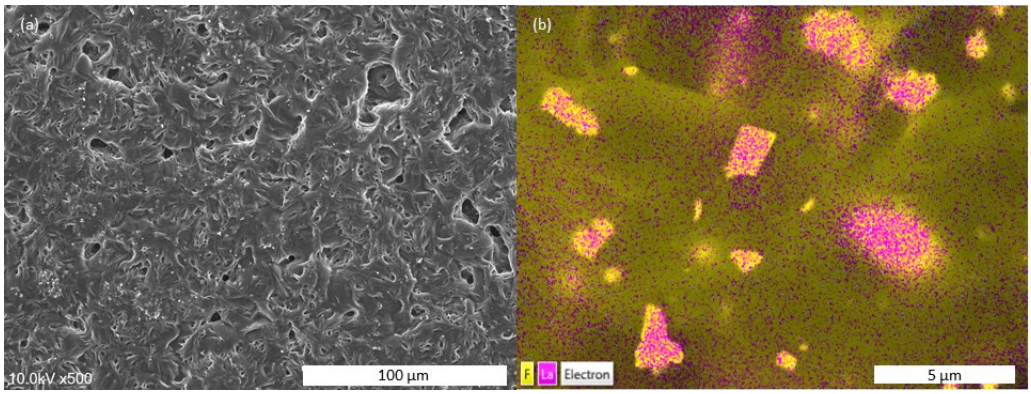

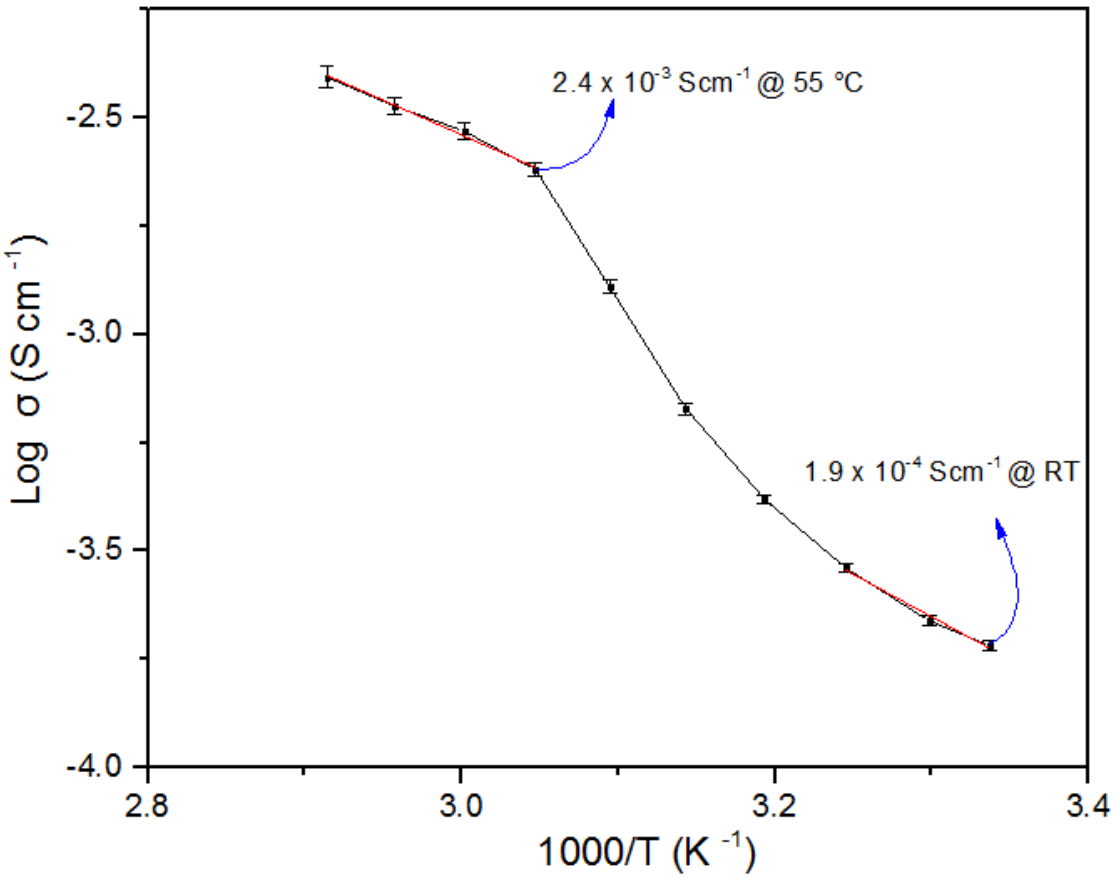

Figure 4.4

Figure 4.5

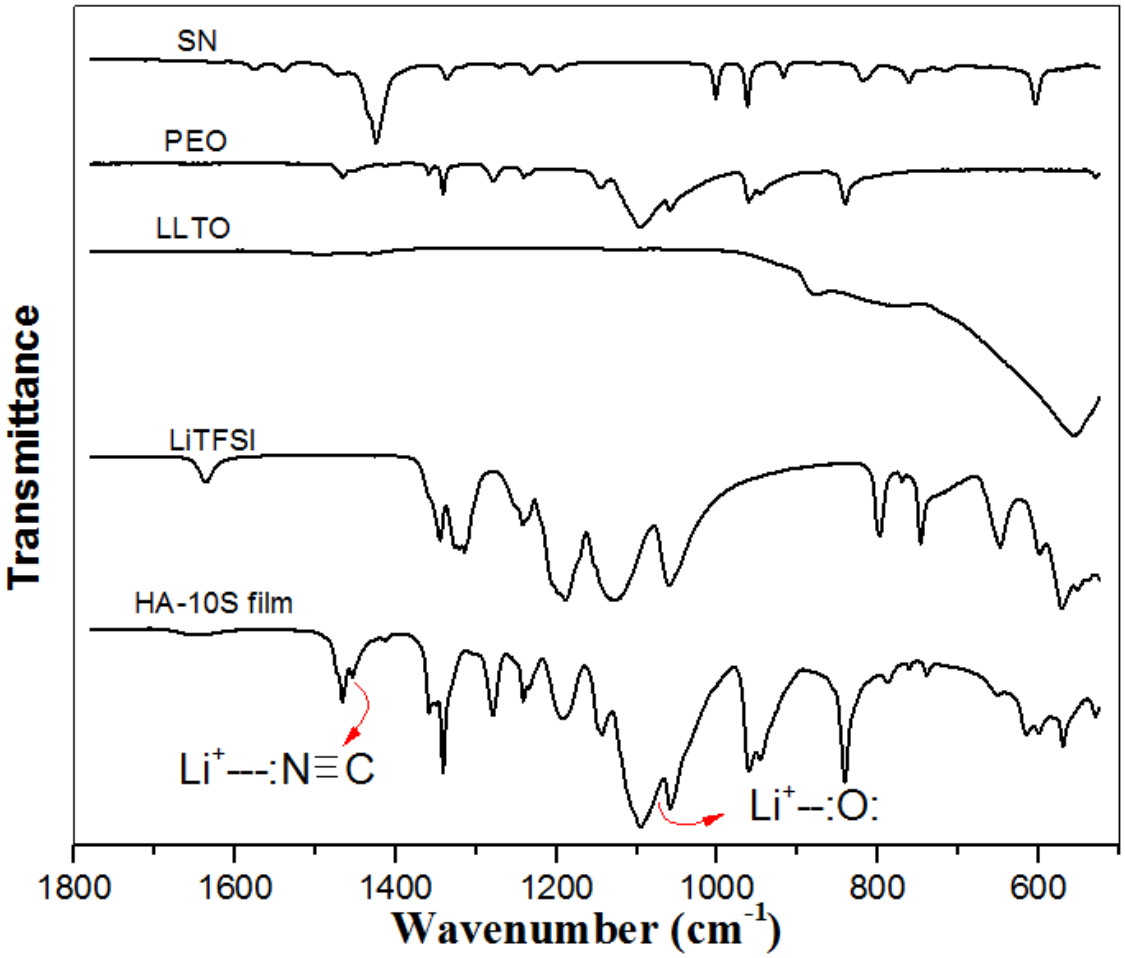
SN
PEO
LLTO
LiTFSI
HA-10S film
Li+---:N≡C
Li+--:O:
Transmittance
1800
1600
1400
1200
1000
800
600
Wavenumber (cm-1)

Figure 4.6

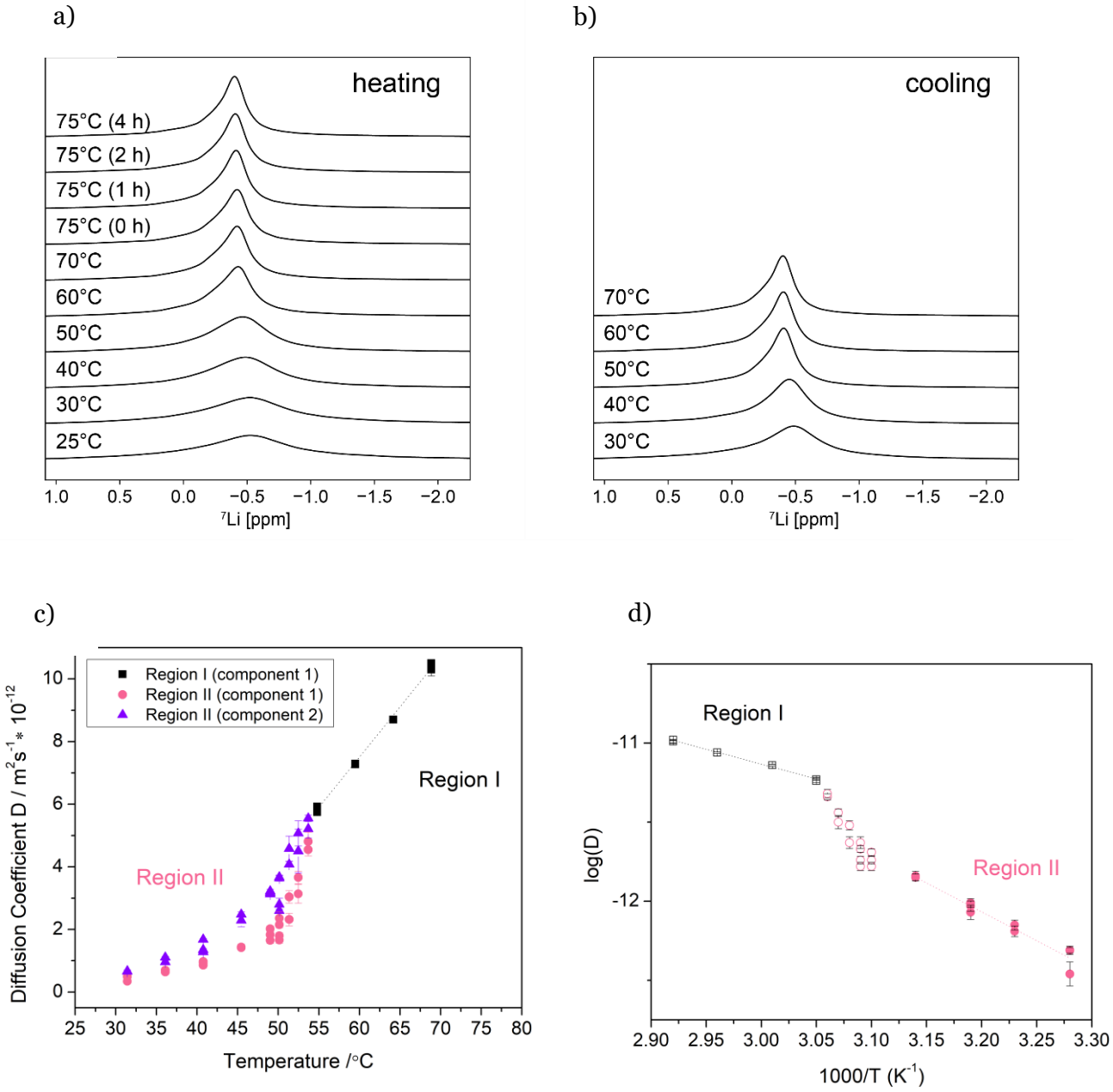
a)
heating
75°C (4 h)
75°C (2 h)
75°C (1 h)
75°C (0 h)
70°C
60°C
50°C
40°C
30°C
25°C
1.0 0.5 0.0 −0.5 −1.0 −1.5 −2.0
⁷Li [ppm]
b)
cooling
70°C
60°C
50°C
40°C
30°C
1.0 0.5 0.0 −0.5 −1.0 −1.5 −2.0
⁷Li [ppm]
c)
Region I (component 1)
Region II (component 1)
Region II (component 2)
Region I
Region II
Diffusion Coefficient D / m²s⁻¹ * 10⁻¹²
0 2 4 6 8 10
25 30 35 40 45 50 55 60 65 70 75 80
Temperature /°C
d)
Region I
Region II
log(D)
-11
-12
2.90 2.95 3.00 3.05 3.10 3.15 3.20 3.25 3.30
1000/T (K⁻¹)

Figure 4.7

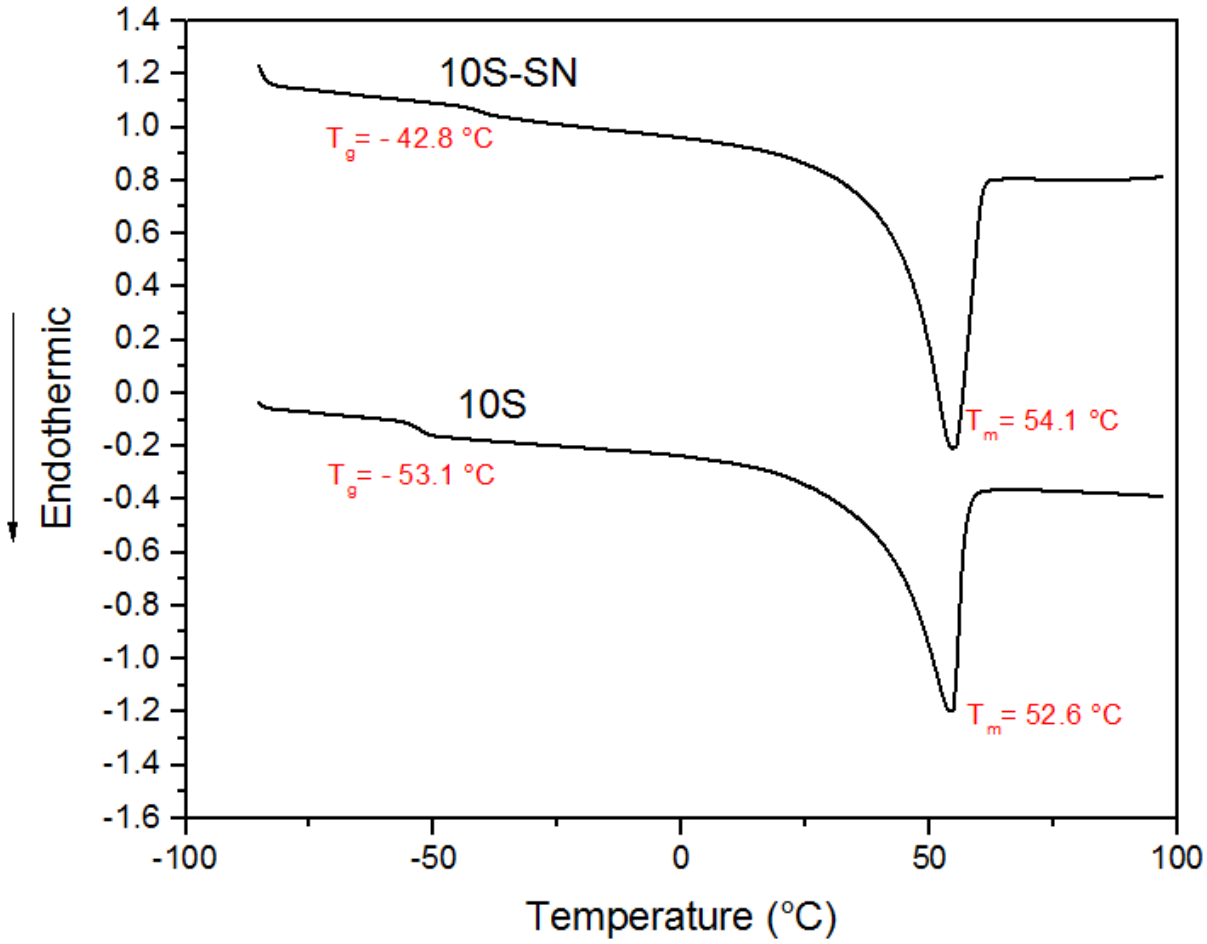
10S-SN
T_g= - 42.8 °C
T_m= 54.1 °C
10S
T_g= - 53.1 °C
T_m= 52.6 °C
Endothermic
Temperature (°C)
1.4
1.2
1.0
0.8
0.6
0.4
0.2
0.0
-0.2
-0.4
-0.6
-0.8
-1.0
-1.2
-1.4
-1.6
-100
-50
0
50
100

Figure 4.8

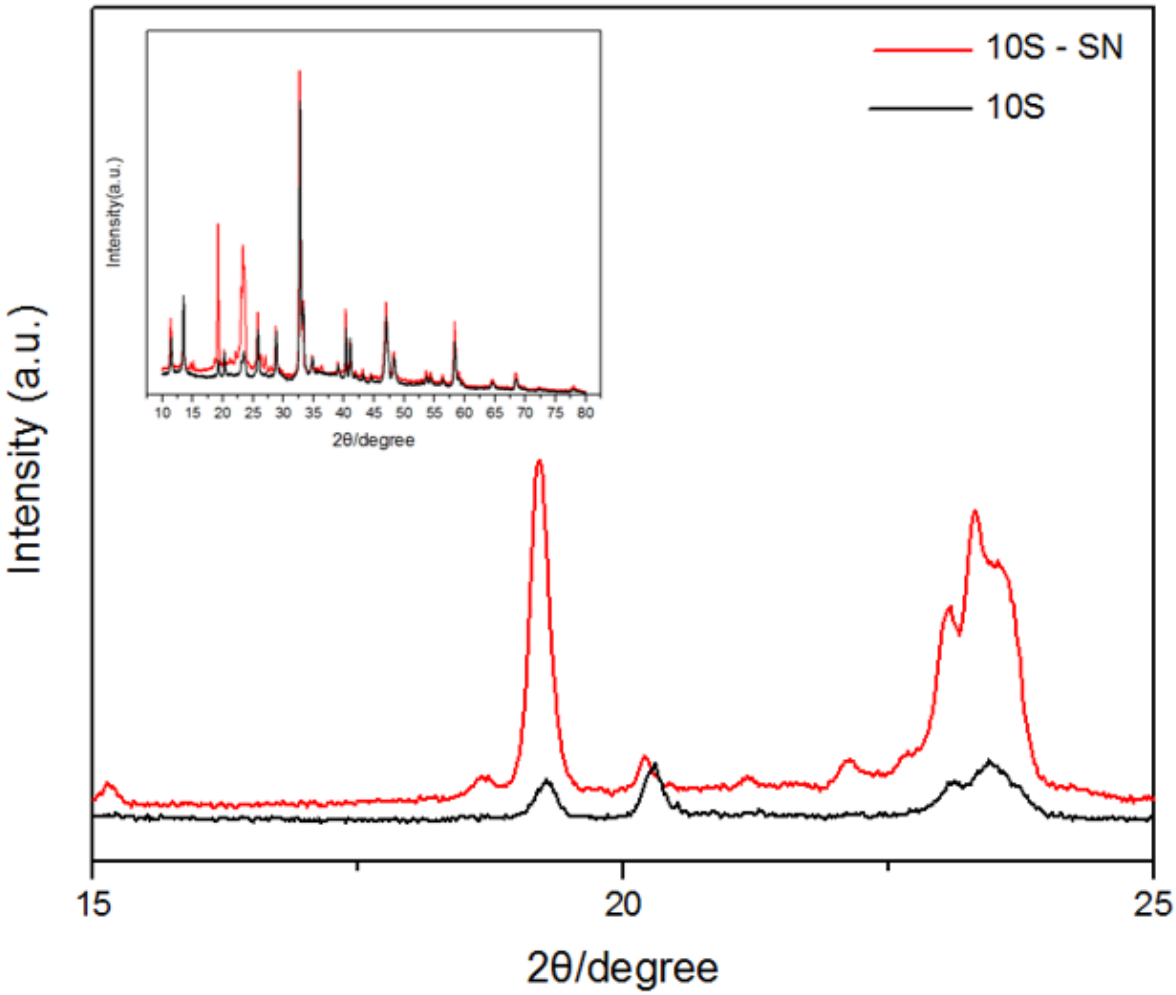
10S - SN
10S
Intensity (a.u.)
15
20
25
2θ/degree
Intensity(a.u.)
10 15 20 25 30 35 40 45 50 55 60 65 70 75 80
2θ/degree

Figure 4.9

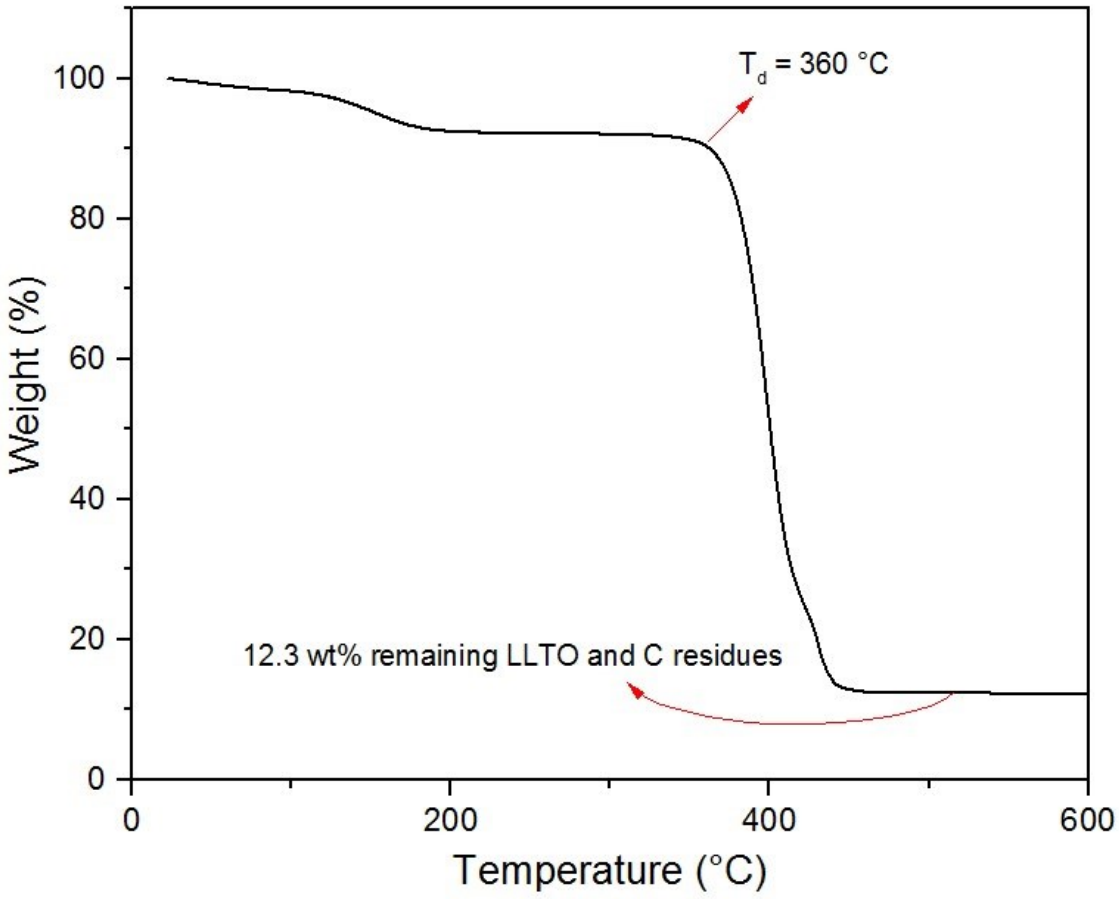
T_d = 360 °C
12.3 wt% remaining LLTO and C residues
Weight (%)
Temperature (°C)
100
80
60
40
20
0
0
200
400
600

Figure 4.10

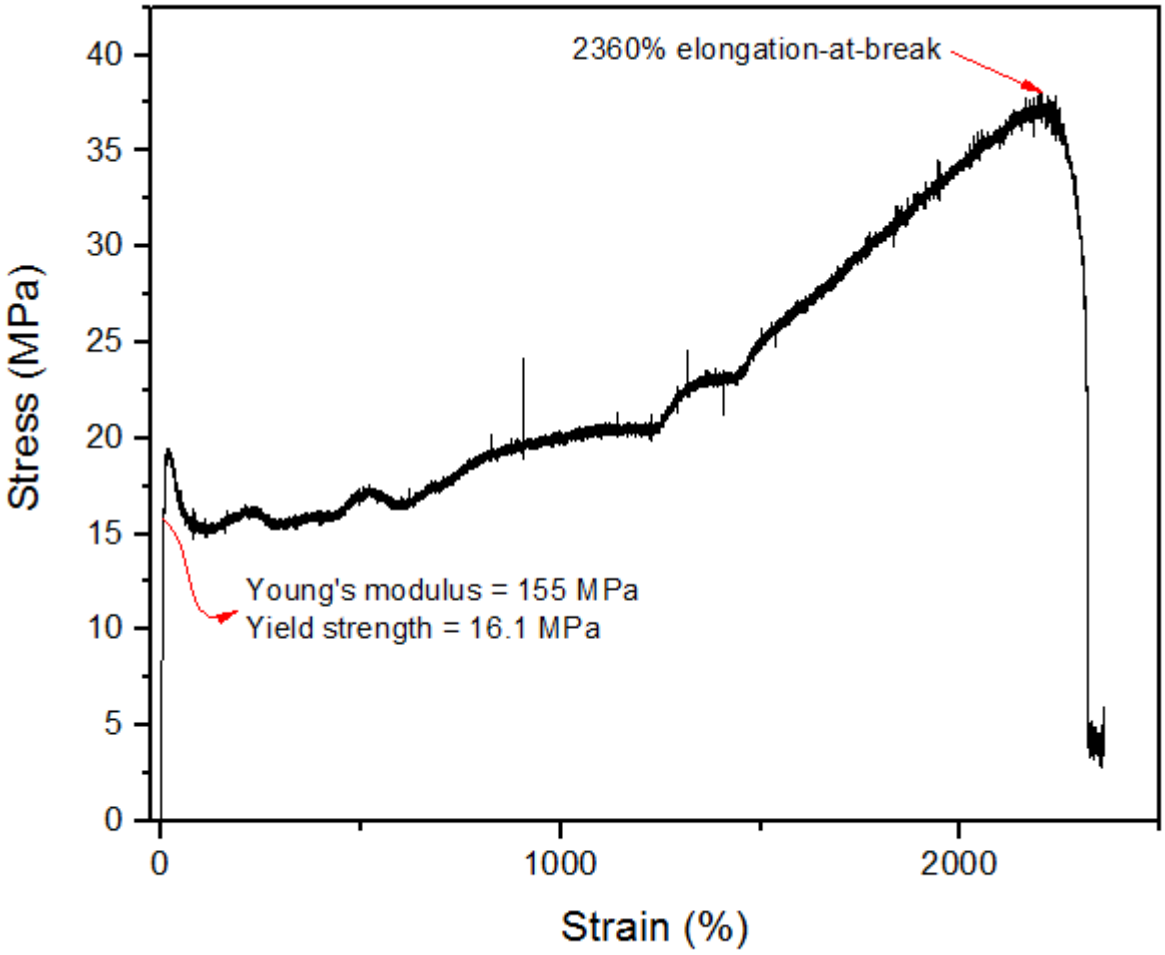
2360% elongation-at-break
Young's modulus = 155 MPa
Yield strength = 16.1 MPa
Stress (MPa)
Strain (%)
0
5
10
15
20
25
30
35
40
0
1000
2000

Figure 4.11

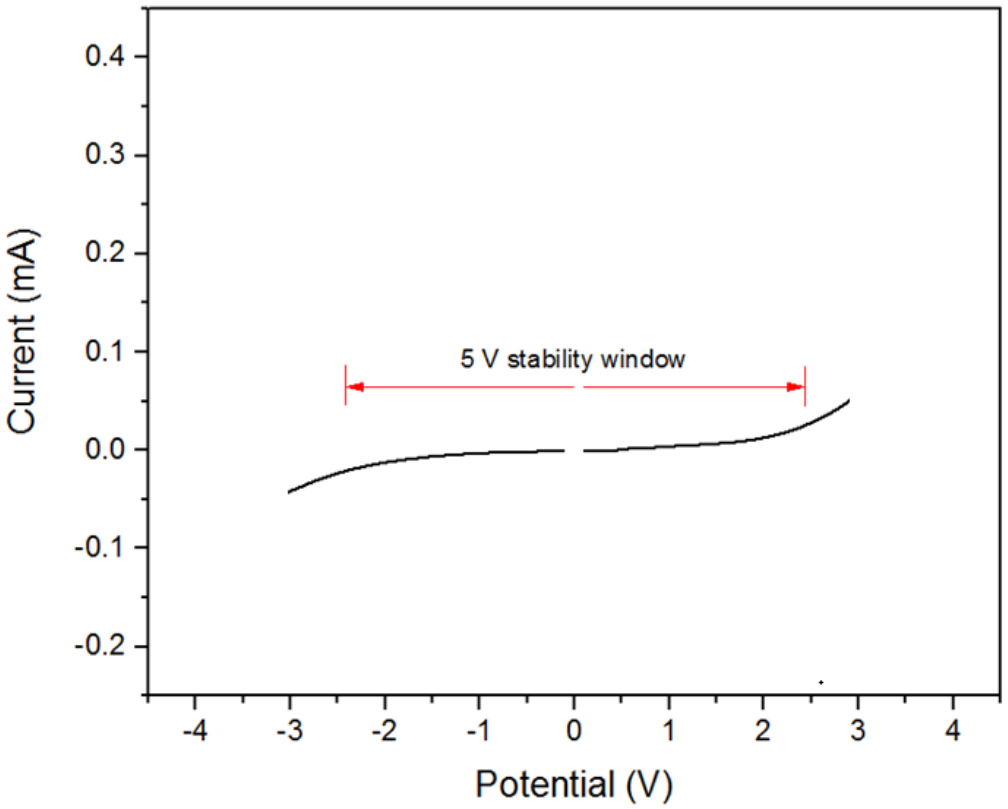

Figure 4.12

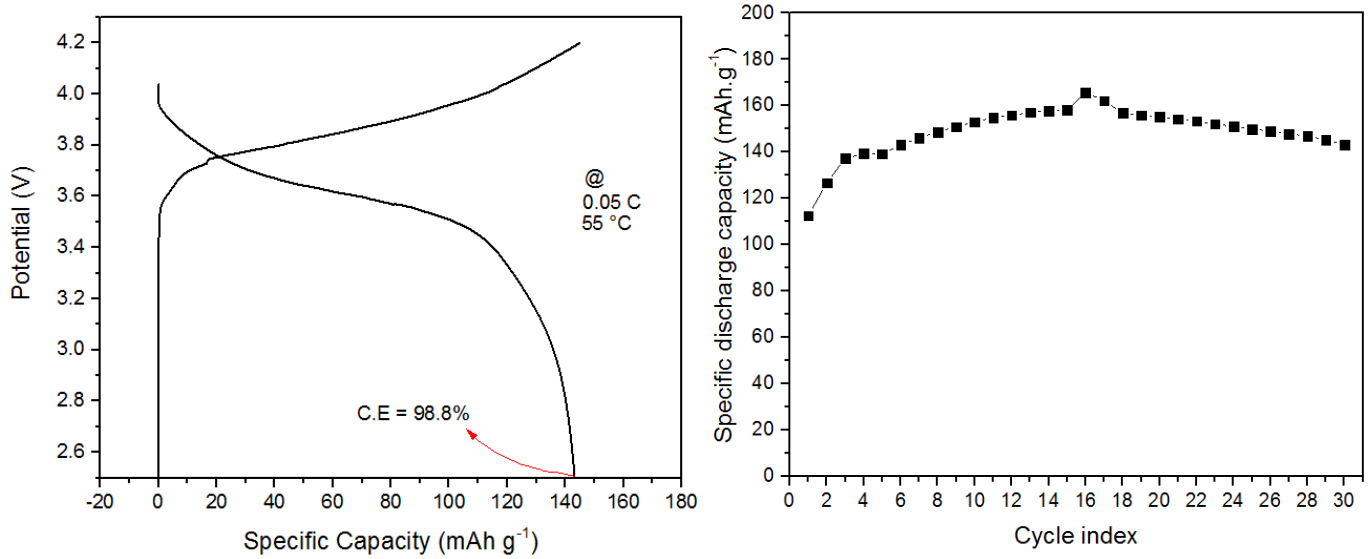

Chapter 5: A ceramic rich quaternary composite solid-state electrolyte for solid-state lithium metal batteries

Adapted from: Hilal Al-Salih, Mengyang Cui, Chae-Ho Yim, Zoya Sadighi, Shuo Yan, Zouina Karkar Gillian R. Goward, Elena A. Baranova, Yaser Abu-Lebdeh, J. Electrochem. Soc. 2022. **169** 080510

Abstract

Solid-state lithium metal batteries are one of the most promising candidates to take over the traditional liquid-based ones as they not only allow us to circumvent safety issues but also boost energy density far over the current limits imposed by the present chemistries. We have recently demonstrated that the combination of highly conductive inorganic solid electrolyte (ISE), Li0.33La0.55TiO3 (LLTO), with the mechanically durable solid polymer electrolyte (SPE), polyethylene oxide: Lithium bis(trifluoromethanesulfonyl)imide (PEO:LiTFSI), alongside a solid plasticizer, Succinonitrile, has proved to be successful in making highly performing polymer-rich (> 50% polymer) quaternary composite solid electrolytes (CSEs) that evade both the brittleness of ceramics and the poor conductivity of polymers. Herein, we extend the work to ceramic rich quaternary CSEs (70% ceramic). Ceramic-rich films were fabricated using tape casting technique and have reasonable ionic conductivity of 1.5×10^{-4} S cm^{-1} at 55˚C, decent mechanical properties and displays impressive endurance in Li || Li symmetrical cells (> 800 h). Solid-state coin-type cells assembled with optimized composite cathode show satisfactory cycling performance at 0.05 C and 55 °C reaching specific discharge capacity of 102.6 mAh g^{-1}, maintaining high Coulombic efficiency (> 95%) and high-capacity retention of 96.0% after 50 cycles.

Key words: solid-state battery; solid-state electrolyte; composites; Lithium metal batteries; polymer electrolytes; composite cathode; plasticizer

Introduction

Because of their high volumetric and gravimetric energy densities, Lithium-ion batteries (LIBs) have emerged as one of the most important storage technologies in response to the need for high energy density, high output voltage and long cycle life with low capacity fading.[1–4] Their commercialization back in 1991 led to a whole industrial revolution that we continue to benefit of till this day.[5] Currently, they power almost all kinds of portable electronics and wireless devices. [6,7] Additionally, LIBs are currently considered the best choice for powering the present and emerging electric vehicles (EVs) as they endure an adequate mile range.[8,9] Despite all of their numerous advantages, LIBs suffer from major drawbacks especially when considered for futuristic energy intensive application.[10,11] The major safety threats arise from the utilization of flammable non aqueous organic electrolytes that facilitate lithium dendrite formation and are susceptible to volatilization, leakages, thermal runaways and internal short circuits.[12,13] Additionally, these electrolytes are not stable against lithium metal anodes and have to be coupled with insertion compound anodes which resembles a huge sacrifice to the energy density of the battery. The electrochemical capacity of graphite for example is 0.37 Ah g^{-1} which is only ~ 10% that of lithium metal (3.86 Ah g^{-1}).[14,15] The use of solid-state electrolytes (SSEs) to form all solid-state batteries is a promising solution to eliminate the safety hazards and suppress lithium dendrite formation which in turn enables the use of lithium metal anodes.[16–18]. In addition, SSEs can form mechanically flexible and strong films that can offer better thermal and electrochemical stabilities as well.[19,20] In recent years, researchers have been trying to propose different strategies to enable flexible energy dense battery components for utilization in implantable biomedical devices, wearable electronics, and sensors. Indeed, solid-state batteries (SSBs) are emerging as the favorable candidates over the traditional LIBs for such applications owing to the above mentioned traits.[21–26] Noteworthy, the overall ionic conduction route in those batteries is not inherently different than the traditional LIBs. In both kind of batteries lithium ions depart the cathode to the electrolyte by deintercalation, travel through the electrolyte and then re-intercalate at the anode. The only noticeable difference is the absence of a separator in SSBs as the SSE acts as one. [27] Generally, SSEs are divided into two major classes, inorganic solid electrolytes (ISEs) and solid polymer electrolytes (SPEs).[28,29] ISEs or the ceramic-based solid electrolytes usually offer high lithium ion conductivity, high thermal and electrochemical stabilities, and are also effective in suppressing lithium dendrite growth.[30] Although liquid electrolytes generally possess higher ionic conductivities, when compared to SSEs researchers were able to explore ISEs with comparable and even higher ionic conductivities.[31–33] Despite having similar characteristics, different ISE

subclasses have different properties. For instance, perovskites are mechanically strong and retain high oxidation potentials yet suffer from high grain boundary resistance and are unstable against lithium.[34–36] Similarly, NASICON-type ISEs also retain high oxidation potentials, high ionic conductivity but are brittle and unstable against lithium.[37,38] In contrast, garnet-type ISEs are stable against lithium metal but impractical to handle because they are hygroscopic and reactive to air.[39,40] Likewise, sulfide ISEs possess exceptional ionic conductivity but are sensitive to air moisture.[19,41] However, all types of ISEs share some common drawbacks such as their large scale manufacturing economical infeasibility and high electrode-electrolyte interfacial resistance arising because of their crystalline lattice.[37]

On the other side, polymer-based solid electrolytes or SPEs generally possess lower ionic conductivity yet are superior in various other aspects. They have excellent mechanical properties, lower electrode-electrolyte interfacial resistance and they are easy to process.[42–44] Particularly, polyethylene oxide (PEO) is considered the most practical SPE mainly because it can be applied in the form of a free standing film in most current battery designs without modification.[45] Additionally, PEO polymer has good Li^+ solvation ability due to interactions between Li^+ and ether oxygen atoms found on PEO backbone.[46,47] Nonetheless, application of solid PEO films is largely impeded by its low ionic conductivity (10^{-6}-10^{-8} S/cm) which stems from PEO's high degree of crystallinity below its melting temperature ($\sim$ 60 °C).[48,49] Hence, researchers have investigated strategies to lower PEO's crystallinity at ambient operating conditions. Possible strategies include the use of inorganic (e.g., SiO_2, Al_2O_3, $Mg(ClO_4)_2$) [[50–52] and organic (e.g., polyethylene glycol (PEG), succinonitrile (SN)) [53–55] 'passive' fillers, sometimes known as plasticizers. The term 'passive' comes from the fact that they do not provide any direct contribution to ionic conductivity, rather they alter the structure of their host to allow for enhanced conductivity. Alternatively, there are 'active fillers' that directly contribute to enhancing ionic conductivity by providing alternative Li^+ migration pathways.[56–58] Ceramic ISEs are considered active fillers when added in small amounts to a polymer matrix which also creates the third major class of solid electrolytes, composite solid electrolytes (CSEs). The fruitful combination of SPEs and ISEs aims at combining the best properties of both worlds while evading the disadvantages on the way.[59,60] CSE class can further be divided into two sub-classes: (1) polymer rich or ceramic-in-polymer CSE where the polymer matrix is the primary phase of the electrolyte and (2) ceramic rich or polymer-in-ceramic where the ceramic crystalline structure is the primary phase of the electrolyte. Notably, each sub-class is different in terms of properties as their structures are inherently either polymeric or crystalline

depending on their primary phase. Polymer rich CSEs tend to retain most of the advantages of SPEs such as mechanical strength, low interfacial resistance and ease of processability whereas ceramic rich CSEs tend to possess ISE properties such as thermal and electrochemical stabilities, lithium dendrite suppression and ceramic non-flammability.

Our research group has reported on a novel quaternary CSE that employs both an active and a passive filler.[61] It is composed of PEO:LiTFSI as the primary phase, the perovskite ceramic $Li_{0.34}La_{0.51}TiO_3$ (LLTO) as the active filler, the plastic crystal organic plasticizer Succinonitrile (SN) as the passive filler. A thorough investigation was executed to find the quaternary SSE composition that acquire the optimal combination of the two main properties, namely, ionic conductivity and mechanical strength. After that, the selected electrolyte underwent a series of full electrochemical, mechanical, thermal and chemical characterization.[61] In this work, we have managed to prepare a ceramic rich CSE composed of the same four components as in the highly performing polymer rich one. The weight percentage of LLTO ceramic was fixed at 70% whilst keeping the ratio of PEO-LiTFSI-SN the same as in the polymer rich CSE produced in Al-Salih *et al*.[61] Precisely, the produced ceramic rich CSE has the following composition (wt. %): 70%-LLTO, 23.3%-PEO, 3.8%-LiTFSI and 2.9%-SN. Precisely, the aim of this work is to report on the properties of this quaternary ceramic rich CSE and to explain the properties variation induced by changing the primary phase of this SSE. In addition, we have managed to cycle an all-solid-state battery assembled with lithium metal anode, this PEO-containing SSE and the high-voltage cathode $LiNiMnCoO_2$ (NMC). The utilization of high voltage active materials such as NMC is key to achieving higher energy densities. To our knowledge, there are very few articles reporting cycles with PEO-containing electrolytes and NMC cathodes.[61–63]

Experimental

Materials

Granular and milled LLTO (Fig 5.1) with median particle size (D50) of ~ 40 μm and ~ 1 μm, respectively, were purchased from Toho titanium Co. PEO (average Mw = 600000 $gmol^{-1}$), LiTFSI salt and acetonitrile were purchased from Sigma-Aldrich and Succinonitrile was purchased from Fluka. $Li(Ni_{0.5}Mn_{0.3}Co_{0.2})O_2$ (NMC 532) was purchased from MTI Corp.

Preparation of Composite LLTO-PEO-LiTFSI-SN solid electrolyte film

To prepare LLTO particles to be used in CSE film fabrication, 95 wt. %- granular LLTO and 5 wt. %-milled LLTO were mixed in ethanol overnight and casted to dry at 110 °C for 24 hours. The purpose of mixing LLTO particles with different particle size is to minimize the grain boundary resistance between the particles. Next, the prepared LLTO powders and LiTFSI salt were vacuum dried for 24 h at 80 °C whereas PEO and SN were dried under vacuum at 40 °C to avert their melting. CSE films were prepared by using the well-known tape casting technique. To prepare the slurry, a planetary centrifugal mixer is used (THINKY). First PEO powder are added to the mixer container followed by a few drops of methanol to wet the added PEO. The addition of methanol is essential to enhance PEO solvation and prevents agglomeration. Next, LiTFSI, SN and LLTO are added in respective amounts until the total weight of powders reach to 1g. Acetonitrile solvent is then added until the slurry is 30% concentrated. The mixture is then ball milled with zirconia balls in the planetary centrifugal mixer for 9 minutes at 2000 rpm, followed by sonication for 15 minutes, mixing for another 9 minutes, and finally defoaming for 1 minute to release any trapped bubbles. The resulting slurry is then casted on a non-stick PTFE sheet using a 350 μm doctor blade. The spread slurry is then dried at room temperature for 24 h followed by vacuum drying at 40 °C to release any trapped solvent. The result is a white, smooth and flexible thin (~ 40 μm*)* film (Fig 5.2 (b)).

Sample characterization

The ceramic rich film, hereafter will be referred to as CR, underwent full characterization using various thermal and electrochemical techniques as fully described below.

Scanning electron microscopy imaging (SEM) was done using JEOL 840A instrument equipped with an Oxford Instruments 6560 INCA x-sight light element energy dispersive X-ray (EDX) spectrometer. X-ray diffraction (XRD) measurement was performed in the Bruker D8 phaser diffractometer with Cu K_α radiation ($\lambda = 1.545$) from $2\theta = 10 - 80°$ with a step of magnitude 5° per minute. Further, Thermo-gravimetric analysis (TGA) was performed using Q5000 iR TA instrument. The film was heated from 25 to 600 °C in a platinum pan under N_2 purge gas flow of 25 cc min^{-1} at a rate of 10 °C min^{-1}. Differential Scanning Calorimetric (DSC) analysis was performed using Q2000 TA instrument. The sample was sealed in an aluminum hermetic pan and scanned from −90 to 100 °C at 10 °C min^{-1} rate under N_2 purge gas flow of 50 cc min^{-1}.

Fourier transform Infrared spectra (FTIR) were also measured using Thermo Fisher Nicolet 6700 with a KBr beam splitter from 4000 to 500 cm^{-1} at 4 cm^{-1} resolution and 32 scans at room temperature. Attenuated total reflection (ATR) single bounce with diamond crystal was used as an accessory.

The ionic conductivity of the CR film was calculated by running electrochemical impedance spectroscopy (EIS) in the frequency range of 10^6 to 1 Hz with an amplitude of 10 mV using Solatron 1287 frequency analyzer. CR thin film was sandwiched between two symmetrical blocking stainless steel electrodes of diameter 22.8 mm and the ionic conductivity was determined as a function of temperature between 25 and 70 °C with a step magnitude of 5 °C and one hour rest time between measurements. The ionic conductivity was calculated using the following equation (eq. 1):

$$\sigma = \frac{L}{AR} \qquad \text{Eq.1}$$

Where σ (S cm^{-1}) is the calculated ionic conductivity, L (cm) is the film thickness R (Ω) is the bulk resistance, and A (cm^2) is the area of the symmetrical electrode. The activation energy was calculated from the Arrhenius plot using the Arrhenius equation (eq. 2):

$$\sigma = \sigma_o \exp(\frac{-Ea}{RT})$$

Eq. 2

Where σ (S cm^{-1}) is the ionic conductivity, σ_o is the pre-exponential factor, E_a is the activation energy, R is the universal gas constant and T is temperature.

^{7}Li NMR experiments were performed on Bruker Avance III wide-bore 300 MHz spectrometer, with a 5 mm ^{7}Li single resonance coil inserted in a Diff 50 double resonance gradient probe. The CSE film was rolled into a 4 mm magic-angle spinning rotor and further placed into a 5 mm Shigemi NMR microtube. The sample was firstly heated at around 75 ºC for 4 h before PFG measurements. ^{7}Li diffusion coefficients were acquired by fitting the PFG echo attenuation curves with Stejskal and Tanner equation (Eq. 3) using a MATLAB script.[64,65]

$$E = exp[-\gamma^2 G^2 \delta^2 D \left(\Delta - \frac{\delta}{3}\right)]$$

Where E is echo attenuation level; γ is gyromagnetic ratio of ^{7}Li; G is the gradient strength; δ represents the effective gradient pulse length; D is the measured ^{7}Li diffusivity, and Δ is the pre-set diffusion time. For the variable-temperature (VT) PFG experiments, a 20-minute waiting period was applied to achieve the equilibrate target temperature within the sample before NMR data collection. The target temperatures were calibrated by measuring the ^{1}H chemical shifts of 100 % ethylene glycol. The pulse gradient stimulated echo sequence was utilized, incorporated with longitudinal eddy current delay. δ were fixed from 1.2 – 1.5 ms with the gradient strengths varied from 23 – 27 T m^{-1} over the 32 gradient steps. Δvalues were kept as 100 ms for all the PFG experiments, and the number of scans were kept as 256. Recycle delays were set in between 1.5 – 2.3 s.

The electrochemical stability window was determined by linear sweep voltammetry (LSV) experiments which was run in a two-electrode cell fitted with stainless steel blocking electrodes using Biologic VMP3 potentiostat. The scanning rate was fixed at 50 mVs^{-1} at 55 °C from – 4 to 4 V.

Battery Assembly and electrochemical testing

In order to enable the CR electrolyte cycling against lithium metal in all-solid-state batteries, 18 mm solid electrolyte cuts were cold pressed with a thin PEO:LiTFSI:SN layers (See Fig 5.3). The thin polymer electrolyte layers are necessary as buffering layers for LLTO is extremely unstable against lithium metal [66] (Hereafter, this double layer CSE will be referred to as mod CR). To observe the lithium stripping/plating behaviour, Li || Li symmetrical cells were assembled with bare CR and CR with buffering thin polymer layers on both sides. The battery performance was tested using an all-solid-state lithium metal battery prepared with mod CR, 2325 coin-type half cells were assembled using 250 μm thick lithium metal discs as the counter electrode and an in-house modified NMC with incorporated PEO:LiTFSI as cathode. The cathode composition (wt. %) is as follows: 85% NMC 532, 10% PEO:LiTFSI (2:1), and 5% Carbon C65. The cathode slurry was prepared by mixing NMC and carbon C65 powders in NMP solvent followed by adding and mixing PEO:LiTFSI powders and acetonitrile solvent. Afterwards, the slurry was casted on aluminum current collector and dried at 80 °C for 24 h before calendaring (Hereafter, this cathode will be referred to as mod NMC 532). The active material mass loading achieved for this cathode was found to be 3.31 mg cm^{-2}. Next, 13

mm diameter cuts of this cathode were used for coin-type cells assembly in an Argon gas glove box where a 20 mm mod CR cut was placed in between the cathode cut and an 18 mm Lithium disk. The prepared Li | mod CR | mod NMC 532 coin type cells were heated to 70 °C for 4 h, and then cooled down prior to Galvanostatic cycling. This heating cycle is essential to homogenise the sample and stabilize the electrode/electrolyte interface. Charge-discharge tests and capacity measurements were then carried out in the potential range of 2.5-4.0 V at 55 °C and at different C-rates including C/20, C/10 and C/5 using a multichannel Arbin battery cycler (BT2000).

Results and discussion

In quest to find the quaternary composition with the optimal combination of mechanical properties and ionic conductivity, CSEs with different compositions were fabricated to cover all PEO:LiTFSI-LLTO-SN ternary compositional regions.[61] Film forming ability and ionic conductivity data for the prepared films was taken and fed to a neural network algorithm to create non-linear fitting for the data as described by Li *et al*. [67] The obtained parameters were used to simulate ternary diagrams which were subsequently used to determine the quaternary CSE with the best combination of properties. Fig 5.4 presents the resulting contour diagram of ionic conductivity and film forming ability. The CSE with best combination of properties is a polymer rich electrolyte that was fully characterized and reported on in our previous work and had the following composition: 70 wt.%-PEO, 12 wt.%-LiTFSI 9 wt.%-LLTO and 9 wt.%-SN.[61] In this work, a novel polymer-in-ceramic CSE was developed from the same components by increasing LLTO content to 70 wt. % yet keeping the PEO-LiTFSI-SN compositional ratio the same. This SSE film (CR) has the following composition: 70 wt. %-LLTO, 23.3 wt. %-PEO 3.8 wt. %-LiTFSI and 2.9 wt. %-SN. Fig 5.5 presents the SEM and EDX mapping of CR film showing homogenous and uniform particles and elemental distribution, respectively. Although developing batteries that use fully ceramic electrolytes is desirable due to the advantage of being the safest as opposed to organic-based electrolytes, there still lies challenges in terms of huge interfacial resistance at the electrode/electrolyte interfaces. Moreover, ceramic electrolyte utilization has only been feasible when coupled with liquid or gel electrolyte additives. In our approach, we increased the amount of non-flammable ceramic component compared to flammable organic polymers in the composite electrolyte which takes us one step closer to safe fully ceramic non-flammable electrolyte for solid-state batteries.

The ionic conductivity of CR was measured using Electrochemical Impedance Spectroscopy (EIS) and found to be 1.3×10^{-5} S cm^{-1} at 25 °C and 1.5×10^{-4} S cm^{-1} at 55 °C. These conductivity values are comparable to those reported by Zhu *et al* for their PEO/LLTO-nanowires SSE of 3.63×10^{-4} S cm^{-1} at 60 °C.[56] Although CR contains non-oriented LLTO particles, it encompasses PEO that is plasticized by SN which could explain the similarity in ionic conductivity. SN molecules are highly polar allowing for easier dissolution of Li^+ and play a critical role in mobilizing PEO chains by preventing their crystallization upon cooling down from elevated temperature.[54] Nonetheless, We have demonstrated that higher ionic conductivities can be achieved in CSE with a polymer matrix as primary phase. The polymer rich quaternary CSE composed of the same components has ionic conductivity that is one order of magnitude higher.[61] Similarly, Pila *et al.* have also demonstrated higher ionic conductivity for a polymer rich CSE composed of 90 wt. % $(PEO)_8$:$LiClO_4$ and 10 wt.% LLTO CSE.[68] Fig 5.6 presents the σ vs. T "Arrhenius" plot for CR. The activation energies of the film were evaluated using the Arrhenius equation (eq. 2) and linear fitting for data points in the low and high temperature regions and found to be 77.2 and 53.1 kJ/mol, respectively. This reduction in activation energy means that ions migrate more freely at higher temperatures, which is expected in the molten state of PEO. Overall, the activation energy values are similar to those reported by Zhu *et al.* [56] on PEO:LiTFSI:LLTO nano-composites but higher than those reported by Fan *et al.* and our group on polymer rich CSEs that contain SN in them. [54,61] Notably, bare LLTO pellets were prepared and characterized to compare their bulk and grain ionic conductivities with the composite electrolyte film and they were found to be 2.9×10^{-4} and 3.2×10^{-5} S cm^{-1} at 55 °C respectively. As expected, CR film is less ionically conductive than Li^+ conductivity in the bulk LLTO phase but it is more conductive than Li^+ conductivity in the grain boundary phase. This is because PEO-LiTFSI-SN complexes fill the grains between LLTO particles in the CSE film, Fig 5.7 is a schematic diagram that simplifies this observation

To understand the Li^+ dynamics of CR at the molecular level, ^{7}Li PFG-NMR was utilized to investigate the long-range Li^+ transport within the CSE. The PFG diffusion curves were acquired at the temperature range from ~ 50 – 70 °C. Clearly, CR contains more than one Li^+ chemical environment, namely, Li^+ in LLTO phase and in LiTFSI within the PEO matrix, thus, this implies the existence of more than one Li^+ motion. The two-component PFG data was fitted by breaking the echo attenuation curve into a superposition of two independent slopes. Fig 5.8 (a) shows the linearized echo attenuation curve, where a natural logarithm of ^{7}Li signal intensity is plotted against the gradient strength squared. The "breakpoint" of the two slopes is observed at around 1×10^6 G^2 cm^2. Data points below the breakpoint (orange) were fitted with

a single slope, while the rest data points (light blue) were fitted with the second slope. All the PFG measurments were examined and fitted with the same method. According to Stejskal and Tanner equation (Eq. 3),[69] a steeper slope indicates a faster diffusion coefficient, which could originate predominantly from the fast ^{7}Li diffusion in the amorphous PEO matrix. Diffusivity of the slower ^{7}Li motion is an order of magnitude lower than the fast motion, thus assigned to the ^{7}Li diffusion in the LLTO phase.

The Arrhenius plots of the two diffusion motions are generated in Figure 5.8 (b). The calculated activation energies are 43 ± 6 and 18 ± 3 kJ mol^{-1} for the fast and the slow motions, which correspond to Li^{+} motion of LiTFSI in PEO and Li^{+} motion in LLTO, respectively. Both the activation energy and the diffusivities acquired for the fast motion were very similar to the previously reported results under the similar temperature range.[61] In addition, it is noticed that the ^{7}Li diffusivities of the slower motion in LLTO phase are higher than expected, compared to other reported values for oxide ISEs (10^{-13} m^2 s^{-1}). This could be further supported by the results obtained from Hayamizu *et al*.[70] Similarly, the ^{7}Li PFG echo attenuation curve of tetragonal LLTO was fitted with two linear slopes, resulting in $D_{Li\text{-}fast}$ and $D_{Li\text{-}slow}$. The diffusivity values and the activation energy for the $D_{Li\text{-}fast}$ are very similar to the diffusion in LLTO acquired from this work (14 vs 18 ± 3 kJ mol^{-1}).[70] Generally speaking, under the diffusion time $\Delta \sim 100$ ms, the ^{7}Li diffusivities of oxide polycrystalline electrolytes obtained from PFG-NMR at the similar temperature ranges are usually at at the order of 10^{-13} m^2 s^{-1}[71,72] due to the sluggish Li^{+} transport across grain-boundaries.[73] However, a faster diffusivity can be observed when there is less grain-boundary transport (such as the Li^{+} transport in a single crystal). In this case, the high Li^{+} diffusivity of the LLTO phase can be attributed to the decrease in the grain-boundary transport, resulted from the aforementioned filling of the smaller PEO-LiTFSI-SN complexes at the LLTO grain boundaries (Fig 5.7).

Fig 5.9 (a) shows the thin electrolyte film X-ray diffraction pattern. The two PEO powder diffraction peaks at 19.2° and 23.3° look damped when compared to pure PEO crystalline plane diffraction peaks which indicate the effectiveness of SN as a polymer chain plasticizer.[74] The chemical interactions between the four components in CR were observed and analyzed by FTIR spectroscopy, as illustrated in Fig 5.9 (b). The bands at 842, 1100, and 1468 cm^{-1} in the PEO FTIR spectrum correspond to CH_2 wagging mode, C-O-C stretching mode, and CH_2 scissoring mode, respectively.[48] When comparing the FTIR spectra of CR and its individual constituents, we can see that the band at around 1470 cm^{-1} divides and gets sharper, indicating a probable interaction between SN and Li^{+} cation of LiTFSI. In addition, at roughly 1100 cm^{-1}, we can see the C-O-C stretching band widening. This, in turn, shows coordination

between Li^+ cations and ether groups on PEO chains.[49] These two interaction observations were also noted in the FTIR spectra of the polymer rich CSE which indicates that PEO and SN still play a major rule in facilitating Li^+ migration despite their lower content in this ceramic rich CSE.[61]

Thermal analysis of CR was done by means of DSC and TGA shown in Fig 5.10. The DSC reveals a glass transition at T_g = – 39.2 °C and an endothermic melting peak at T_m = 54.1 °C which are 13.9 and 1.5 °C higher, respectively, than that of the polymer rich CSE.[61] These T_g and T_m differences are expected since the ceramic rich CSE is more crystalline due to the higher perovskite-structured LLTO content. Higher T_g indicates slower ionic kinetics in CSEs which supports the ionic conductivity difference between the two films.[56] To quantitatively analyze the crystallinity difference, eq. 3 can be used to calculate the degree of crystallinity.

$$X_c = \frac{\Delta \boldsymbol{H_m}}{\Delta \boldsymbol{H_{PEO}} \cdot \boldsymbol{Y_{PEO}}} \qquad \text{Eq. 3}$$

Where ΔH_m is the sample melting enthalpy, obtained from TA universal analysis software, ΔH_{PEO} is the 100% crystalline PEO melting enthalpy of, 203 J g^{-1} [57][58] and Y_{PEO} is the PEO weight fraction in the sample. X_c calculations show that the ceramic rich CSE is 60.2% crystalline while the polymer rich are 42.6% crystalline.

TGA was used to test the thermal stability of the film. The thermal stability of solid-state electrolytes is critical to ensure their safety and justify their use as an alternative to liquid electrolytes. The TGA profile in Fig 5.10 (b) shows that there is a little weight loss at 100 °C. This weight loss is less pronounced than weight loss for the polymer rich film in the same temperature range.[61] This is expected since the polymer has more organic content. TGA analysis of PEO, LiTFSI, and SN by Echeverri *et al.* [80] showed that whereas pure PEO and LiTFSI exhibit great thermal stability up to 380 °C, pure SN is only stable up to 130 °C after extended heating. This could explain the film's slight weight loss over 100 °C. Overall, CR possess good thermal stability until approximately 360 °C which is similar behavior to the polymer rich electrolyte reported earlier.[61] It's worth noting that the weight percent of material left after heating to 700 °C is 70.8 wt. %, which is somewhat greater than the sample's ceramic content. This difference could be due to carbon residues that persist after complete decomposition.

Another important factor to consider while developing high-energy-density lithium batteries is electrochemical stability. We were able to measure the electrochemical stability window of the film at 55 °C using LSV, as shown in Fig 5.11. The oxidation/reduction peaks begin to climb at 2.7 V and -2.7 V, respectively, corresponding to a 5.4 V electrochemical stability window.

To assess the electrochemical performance of the ceramic rich electrolyte, Li | mod CR | mod NMC 532 batteries were fabricated in 2325 coin-type cells by sandwiching an electrolyte cut between our modified NMC 532 cathode and a lithium disc. Charge-discharge tests were then carried out in the potential range of 2.5-4.0 V at 55 °C and at different cycling rate of C/20, C/10 and C/5. The composite cathode utilizes PEO:LiTFSI (2:1) as a co-binder to improve the cathode/electrolyte interfacial contact and reduce resistance (R). Fig 5.12 (a) and (b) show the charge-discharge curve and the cyclic performance of the all-solid-state lithium metal battery, respectively. Poor initial specific discharge capacity (SDC) for the first cycle was noted at only 112.6 mAh g^{-1}. However, SDC kept increasing for the next 33 cycles until hitting a maximum SDC of 160.6 mAh g^{-1} while maintaining high columbic efficiency in all cycles (> 95%). This trend implies that homogenization of the solid-state battery components takes ample time. After arriving to peak SDC, reasonably slow capacity fading was observed afterwards. After 50 cycles, capacity retention was 96.0%. This electrochemical behavior is very similar to the all-solid-state battery employing the polymer rich electrolyte, except that the latter achieved higher SDC (> 140 mAh g^{-1}).[61] Moreover, Fig 5.12 displays the galvanostatic cycling stability of Li || Li symmetrical cells with mod CR and bare CR at 60 °C. The aim of this test is to study the lithium plating and stripping behavior at a typical current density of 0.1 mA cm^{-2}. The mod CR symmetrical cell displayed stable cycling performance for over 800 hr with negligible voltage drop while the bare CR symmetrical cell showed continuous resistance build up in the cell due to the SEI formation in the cell and ultimately failing at around 300 h mark. These results emphasize the rule of the polymer layer in enabling the electrochemical cycling of ceramic rich electrolytes in all-solid-state lithium metal batteries.

Conclusion

We have successfully synthesized and fully characterized polymer rich and ceramic rich quaternary solid-state electrolyte composed of LLTO-PEO-LiTFSI-SN. The CSE with the optimal combination of electrochemical and mechanical properties was reported on earlier in

Al-Salih *et al*.[61] and had the following composition: 70%-PEO 12%-LiTFSI 9%-LLTO 9%-SN. In this work, the ceramic content was fixed to 70 wt. % in the CSE whilst keeping the ratio of the other three components the same. This ceramic rich CSE was fabricated into 40 μm thin films using a tape casting technique and its ionic conductivity was found to be 1.5×10^{-4} S cm^{-1} at 55 °C which is almost one order of magnitude lower than that of the polymer rich film which had a conductivity of 2.4×10^{-3} S cm^{-1} at the same temperature. All-solid-state lithium metal batteries were assembled using the ceramic rich CSE, lithium metal anode, and an in-house made NMC 532 cathode that includes PEO:LiTFSI electrolyte in its composition. This step was essential to overcome the cathode-electrolyte interfacial resistance. Finally, the highest specific discharge capacity achieved by the Li | mod CR | mod NMC 532 was 102.6 mAh g^{-1} and the battery's capacity retention was 96.0% after 50 cycles.

Acknowledgments

We would like to thank Office of Energy Research and Development (OERD) at Natural Resources Canada for financial support.

References

[1] M. Armand, J. M. Tarascon, *Nature* **2008**, *451*, 652.

[2] J. W. Fergus, *J. Power Sources* **2010**, *195*, 939.

[3] C.-Y. Wang, G. Zhang, S. Ge, T. Xu, Y. Ji, X.-G. Yang, Y. Leng, *Nature* **2016**, *529*.

[4] E. Quartarone, P. Mustarelli, Electrolytes for solid-state lithium rechargeable batteries: Recent advances and perspectives. *Chem. Soc. Rev.* **2011**, *40*, 2525–2540.

[5] N. Nitta, F. Wu, J. T. Lee, G. Yushin, Li-ion battery materials: Present and future. *Mater. Today* **2015**, *18*, 252–264.

[6] G. Crabtree, Perspective: The energy-storage revolution. *Nature* **2015**, *526*, S92.

[7] P. Fairley, *Nature* **2015**, *526*, S102.

[8] A. Kwade, W. Haselrieder, R. Leithoff, A. Modlinger, F. Dietrich, K. Droeder, Current status and challenges for automotive battery production technologies. *Nat. Energy* **2018**, *3*, 290–300.

[9] Z. P. Cano, D. Banham, S. Ye, A. Hintennach, J. Lu, M. Fowler, Z. Chen, Batteries and fuel cells for emerging electric vehicle markets. *Nat. Energy* **2018**, *3*, 279–289.

[10] K. Turcheniuk, D. Bondarev, V. Singhal, G. Yushin, Ten years left to redesign lithium-ion batteries. *Nature* **2018**, *559*, 467–470.

[11] Y. Sun, N. Liu, Y. Cui, Promises and challenges of nanomaterials for lithium-based rechargeable batteries. *Nat. Energy* **2016**, *1*, 1–12.

[12] X. Yu, A. Manthiram, Electrode-electrolyte interfaces in lithium-based batteries. *Energy Environ. Sci.* **2018**, *11*, 527–543.

[13] A. Manthiram, X. Yu, S. Wang, Lithium battery chemistries enabled by solid-state electrolytes. *Nat. Rev. Mater.* **2017**, *2*, 1–16.

[14] J. B. Goodenough, *Acc. Chem. Res.* **2013**, *46*, 1053.

[15] X. Yu, A. Manthiram, *Acc. Chem. Res.* **2017**, *50*, 2653.

[16] P. P. Soo, B. Huang, Y. I. I. Jang, Y. M. Chiang, D. R. Sadoway, A. M. Mayes, *J. Electrochem. Soc.* **1999**, *146*, 32.

[17] Y. Zhao, C. Wu, G. Peng, X. Chen, X. Yao, Y. Bai, F. Wu, S. Chen, X. Xu, *J. Power Sources* **2016**, *301*, 47.

[18] Q. Zhao, S. Stalin, C.-Z. Zhao, L. A. Archer, *Nat. Rev. Mater.* **2020**, 1.

[19] N. Kamaya, K. Homma, Y. Yamakawa, M. Hirayama, R. Kanno, M. Yonemura, T. Kamiyama, Y. Kato, S. Hama, K. Kawamoto, A. Mitsui, *Nat. Mater.* **2011**, *10*, 682.

[20] K. Xu, Electrolytes and interphases in Li-ion batteries and beyond. *Chem. Rev.* **2014**, *114*, 11503–11618.

[21] A. Goyal, A. L. M. Reddy, P. M. Ajayan, *Small* **2011**, *7*, 1709.

[22] S. Y. Chew, S. H. Ng, J. Wang, P. Novák, F. Krumeich, S. L. Chou, J. Chen, H. K. Liu, *Carbon N. Y.* **2009**, *47*, 2976.

[23] J. Z. Wang, C. Zhong, S. L. Chou, H. K. Liu, *Electrochem. commun.* **2010**, *12*, 1467.

[24] N. Li, Z. Chen, W. Ren, F. Li, H. M. Cheng, *Proc. Natl. Acad. Sci. U. S. A.* **2012**, *109*, 17360.

[25] L. Noerochim, J. Z. Wang, S. L. Chou, D. Wexler, H. K. Liu, *Carbon N. Y.* **2012**, *50*, 1289.

[26] H. Nishide, K. Oyaizu, Toward flexible batteries. *Science (80-.).* **2008**, *319*, 737–738.

[27] F. Zheng, M. Kotobuki, S. Song, M. O. Lai, L. Lu, *J. Power Sources* **2018**, *389*, 198.

[28] V. Thangadurai, S. Narayanan, D. Pinzaru, Garnet-type solid-state fast Li ion conductors for Li batteries: Critical review. *Chem. Soc. Rev.* **2014**, *43*, 4714–4727.

[29] M. Forsyth, L. Porcarelli, X. Wang, N. Goujon, D. Mecerreyes, *Acc. Chem. Res.* **2019**, *52*, 686.

[30] R. Chen, Q. Li, X. Yu, L. Chen, H. Li, Approaching Practically Accessible Solid-State Batteries: Stability Issues Related to Solid Electrolytes and Interfaces. *Chem. Rev.* **2020**, *120*, 6820–6877.

[31] Z. Ma, H. G. Xue, S. P. Guo, Recent achievements on sulfide-type solid electrolytes: crystal structures and electrochemical performance. *J. Mater. Sci.* **2018**, *53*, 3927–3938.

[32] J. C. Bachman, S. Muy, A. Grimaud, H. H. Chang, N. Pour, S. F. Lux, O. Paschos, F. Maglia, S. Lupart, P. Lamp, L. Giordano, Y. Shao-Horn, Inorganic Solid-State Electrolytes for Lithium Batteries: Mechanisms and Properties Governing Ion Conduction. *Chem. Rev.* **2016**, *116*, 140–162.

[33] A. Varzi, R. Raccichini, S. Passerini, B. Scrosati, *J. Mater. Chem. A* **2016**, *4*, 17251.

[34] C. H. Chen, K. Amine, *Solid State Ionics* **2001**, *144*, 51.

[35] Y. H. Cho, J. Wolfenstine, E. Rangasamy, H. Kim, H. Choe, J. Sakamoto, *J. Mater. Sci.* **2012**, *47*, 5970.

[36] C. Ma, K. Chen, C. Liang, C. W. Nan, R. Ishikawa, K. More, M. Chi, *Energy Environ. Sci.* **2014**, *7*, 1638.

[37] M. Keller, A. Varzi, S. Passerini, *J. Power Sources* **2018**, *392*, 206.

[38] P. Hartmann, T. Leichtweiss, M. R. Busche, M. Schneider, M. Reich, J. Sann, P. Adelhelm, J. Janek, *J. Phys. Chem. C* **2013**, *117*, 21064.

[39] A. Sharafi, E. Kazyak, A. L. Davis, S. Yu, T. Thompson, D. J. Siegel, N. P. Dasgupta, J. Sakamoto, *Chem. Mater.* **2017**, *29*, 7961.

[40] M. Wang, J. Sakamoto, *J. Power Sources* **2018**, *377*, 7.

[41] Q. Zhang, D. Cao, Y. Ma, A. Natan, P. Aurora, H. Zhu, *Adv. Mater.* **2019**, *31*, 1901131.

[42] C. Sun, J. Liu, Y. Gong, D. P. Wilkinson, J. Zhang, Recent advances in all-solid-state rechargeable lithium batteries. *Nano Energy* **2017**, *33*, 363–386.

[43] D. Dong, B. Zhou, Y. Sun, H. Zhang, G. Zhong, Q. Dong, F. Fu, H. Qian, Z. Lin, D. Lu, Y. Shen, J. Wu, L. Chen, H. Chen, *Nano Lett.* **2019**, *19*, 2343.

[44] Y. Jiang, X. Yan, Z. Ma, P. Mei, W. Xiao, Q. You, Y. Zhang, Development of the PEO based solid polymer electrolytes for all-solid state lithium ion batteries. *Polymers (Basel).* **2018**, *10*, 1237.

[45] B. Scrosati, J. Garche, Lithium batteries: Status, prospects and future. *J. Power Sources* **2010**, *195*, 2419–2430.

[46] G. M. Stone, S. A. Mullin, A. A. Teran, D. T. Hallinan, A. M. Minor, A. Hexemer, N. P. Balsara, *J. Electrochem. Soc.* **2012**, *159*.

[47] K. J. Harry, D. T. Hallinan, D. Y. Parkinson, A. A. MacDowell, N. P. Balsara, *Nat. Mater.* **2014**, *13*, 69.

[48] S. K. Fullerton-Shirey, J. K. Maranas, *Macromolecules* **2009**, *42*, 2142.

[49] J. G. Kim, B. Son, S. Mukherjee, N. Schuppert, A. Bates, O. Kwon, M. J. Choi, H. Y. Chung, S. Park, A review of lithium and non-lithium based solid state batteries. *J. Power Sources* **2015**, *282*, 299–322.

[50] D. Lin, W. Liu, Y. Liu, H. R. Lee, P. C. Hsu, K. Liu, Y. Cui, *Nano Lett.* **2016**, *16*, 459.

[51] G. X. Wang, L. Yang, J. Z. Wang, H. K. Liu, S. X. Dou, *J. Nanosci. Nanotechnol.* **2005**, *5*, 1135.

[52] B. Xu, X. Li, C. Yang, Y. Li, N. S. Grundish, P. H. Chien, K. Dong, I. Manke, R. Fang, N. Wu, H. Xu, A. Dolocan, J. B. Goodenough, *J. Am. Chem. Soc.* **2021**, *143*, 6542.

[53] W. Liu, S. W. Lee, D. Lin, F. Shi, S. Wang, A. D. Sendek, Y. Cui, *Nat. Energy* **2017**, *2*.

[54] L. Z. Fan, Y. S. Hu, A. J. Bhattacharyya, J. Maier, *Adv. Funct. Mater.* **2007**, *17*, 2800.

[55] Y. Masuda, M. Nakayama, M. Wakihara, *Solid State Ionics* **2007**, *178*, 981.

[56] L. Zhu, P. Zhu, Q. Fang, M. Jing, X. Shen, L. Yang, *Electrochim. Acta* **2018**, *292*, 718.

[57] T. Pareek, S. Dwivedi, S. A. Ahmad, M. Badole, S. Kumar, *J. Alloys Compd.* **2020**, *824*, 153991.

[58] N. Wu, P. H. Chien, Y. Li, A. Dolocan, H. Xu, B. Xu, N. S. Grundish, H. Jin, Y. Y. Hu, J. B. Goodenough, *J. Am. Chem. Soc.* **2020**, *142*, 2497.

[59] Q. Guo, Y. Han, H. Wang, S. Xiong, Y. Li, S. Liu, K. Xie, *ACS Appl. Mater. Interfaces* **2017**, *9*, 41837.

[60] A. Li, X. Liao, H. Zhang, L. Shi, P. Wang, Q. Cheng, J. Borovilas, Z. Li, W. Huang, Z. Fu, M. Dontigny, K. Zaghib, K. Myers, X. Chuan, X. Chen, Y. Yang, *Adv. Mater.* **2020**, *32*, 1905517.

[61] H. Al-Salih, A. Huang, C.-H. Yim, A. I. Freytag, G. R. Goward, E. Baranova, Y. Abu-Lebdeh, *J. Electrochem. Soc.* **2020**, *167*, 070557.

[62] J. H. Choi, C. H. Lee, J. H. Yu, C. H. Doh, S. M. Lee, *J. Power Sources* **2015**, *274*, 458.

[63] P. López-Aranguren, X. Judez, M. Chakir, M. Armand, L. Buannic, *J. Electrochem. Soc.* **2020**, *167*, 020548.

[64] E. Stejskal, J. T.-T. journal of chemical physics, undefined 1965, *aip.scitation.org* **1965**, *42*, 288.

[65] W. P.-C. in M. R. A. Educational, undefined 1998, *Wiley Online Libr.*

[66] J. Z. Lee, Z. Wang, H. L. Xin, T. A. Wynn, Y. S. Meng, *J. Electrochem. Soc.* **2016**, *164*, A6268.

[67] Z. Li, Z. Cheng, L. Xu, T. Li, Nonlinear Fitting by Using a Neural Net Algorithm, **1993**, https://pubs.acs.org/sharingguidelines.

[68] C. R. Milian Pila, E. P. Cappe, N. D. S. Mohallem, O. L. Alves, M. A. Aguilar Frutis, N. Sánchez-Ramírez, R. M. Torresi, H. León Ramírez, Y. M. Laffita, *Solid State Sci.* **2019**, *88*, 41.

[69] C. J. J.-P. in nuclear magnetic resonance, undefined 1999, *nmr2.buffalo.edu*.

[70] K. Hayamizu, S. Seki, T. Haishi, *Solid State Ionics* **2018**, *326*, 37.

[71] K. Hayamizu, S. S.-P. C. C. Physics, undefined 2017, *pubs.rsc.org*.

[72] K. Hayamizu, Y. Matsuda, … M. M.-S. state nuclear, undefined 2015, *Elsevier*.

[73] K. Hayamizu, Y. Terada, K. Kataoka, J. Akimoto, *J. Chem. Phys.* **2019**, *150*.

[74] L.-Z. Fan, Y.-S. Hu, A. J. Bhattacharyya, J. Maier, *Adv. Funct. Mater.* **2007**, *17*, 2800.

[75] E. Morales, J. L. Acosta, *J. Appl. Polym. Sci.* **1998**, *69*, 2435.

[76] O. Borodin, G. D. Smith, *Macromolecules* **2006**, *39*, 1620.

[77] V. S. Kolosnitsyn, G. P. Dukhanin, S. A. Dumler, I. A. Novakov, Lithium-conducting polymer electrolytes for chemical power sources. *Russ. J. Appl. Chem.* **2005**, *78*, 1–18.

[78] X. L. Wu, S. Xin, H. H. Seo, J. Kim, Y. G. Guo, J. S. Lee, *Solid State Ionics* **2011**, *186*, 1.

[79] L. Hu, Z. Tang, Z. Zhang, *J. Power Sources* **2007**, *166*, 226.

[80] M. Echeverri, N. Kim, T. Kyu, *Macromolecules* **2012**, *45*, 6068.

[81] B. Li, Q. Su, L. Yu, D. Wang, S. Ding, M. Zhang, G. Du, B. Xu, *ACS Appl. Mater. Interfaces* **2019**, *11*, 42206.

Figure captions

Figures

Figure 5.1

(a)

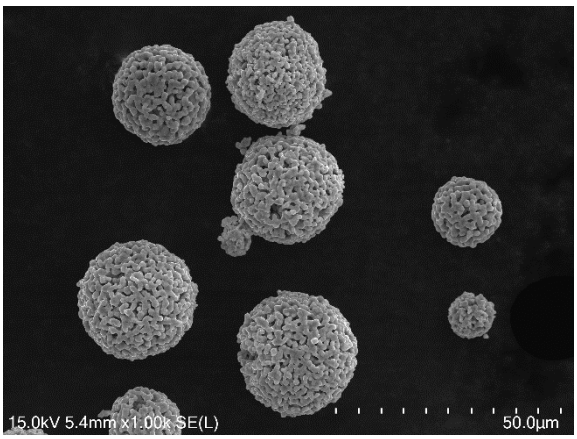

(b)

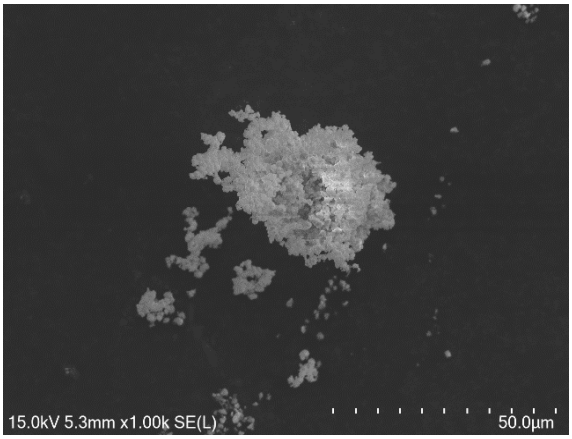

Figure 5.2

(a)

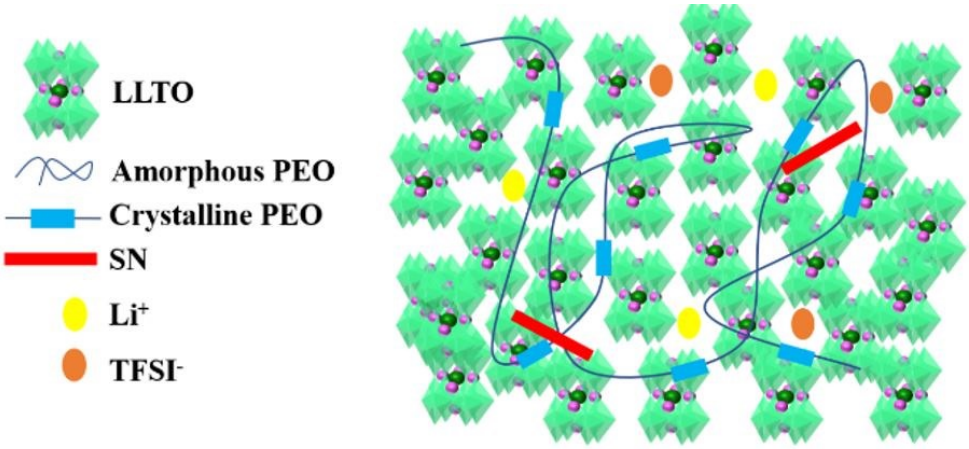

(b)

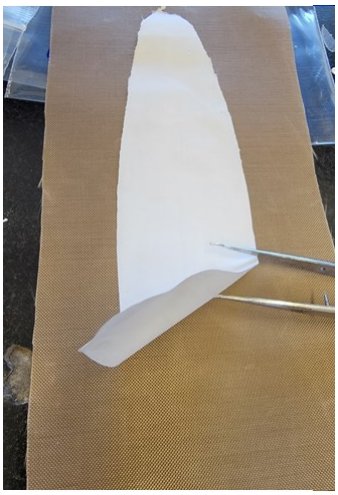

Figure 5.3

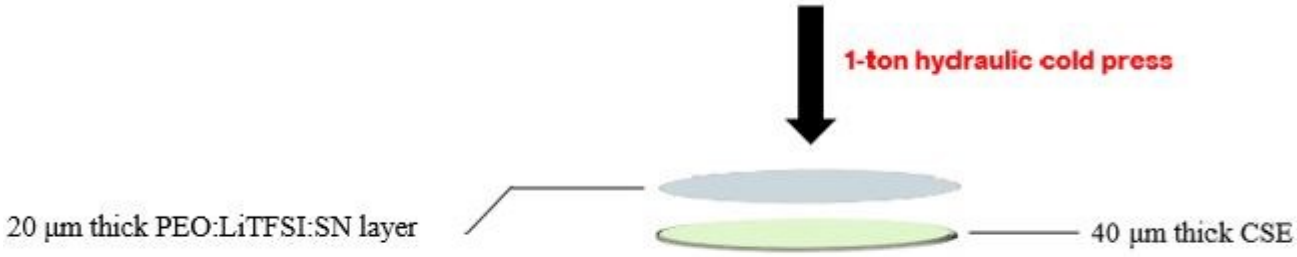
1-ton hydraulic cold press
20 µm thick PEO:LiTFSI:SN layer
40 µm thick CSE

Figure 5.4

(a)

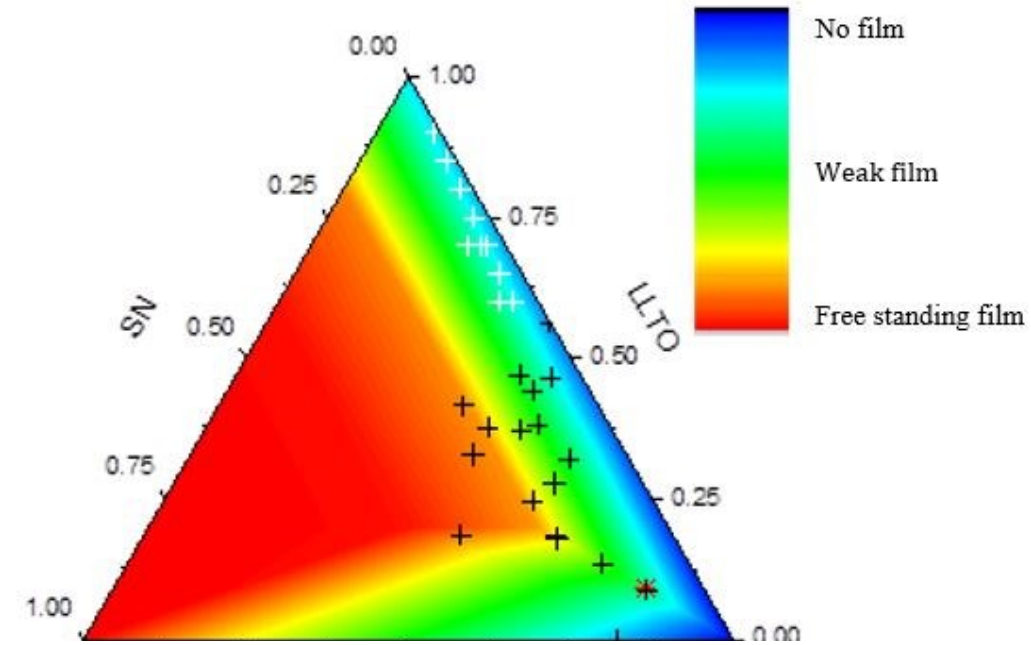
No film
Weak film
Free standing film
SN
LLTO
0.00
0.25
0.50
0.75
1.00

(b)

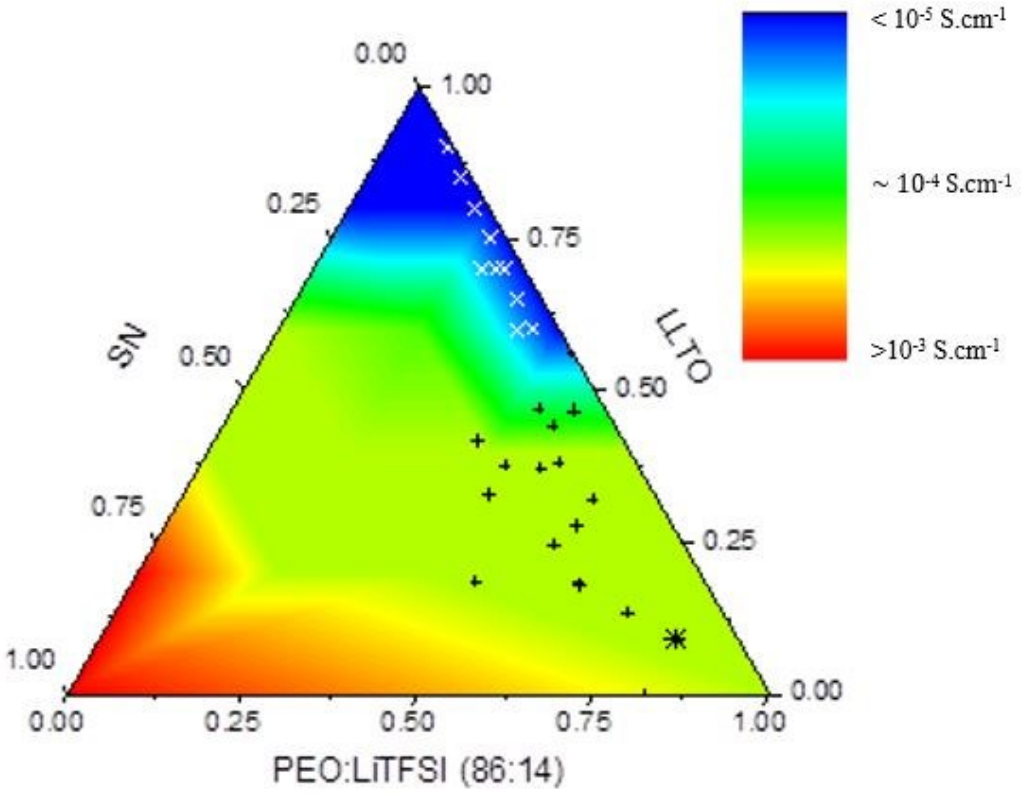
< 10-5 S.cm-1
~ 10-4 S.cm-1
>10-3 S.cm-1
SN
LLTO
PEO:LiTFSI (86:14)
0.00
0.25
0.50
0.75
1.00

Figure 5.5

(a)

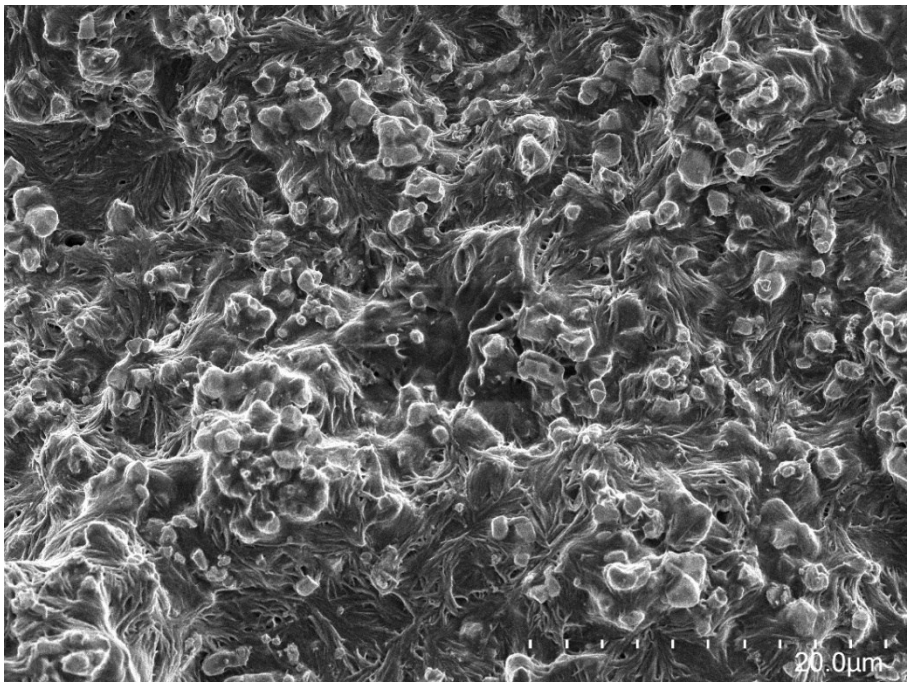

(b)

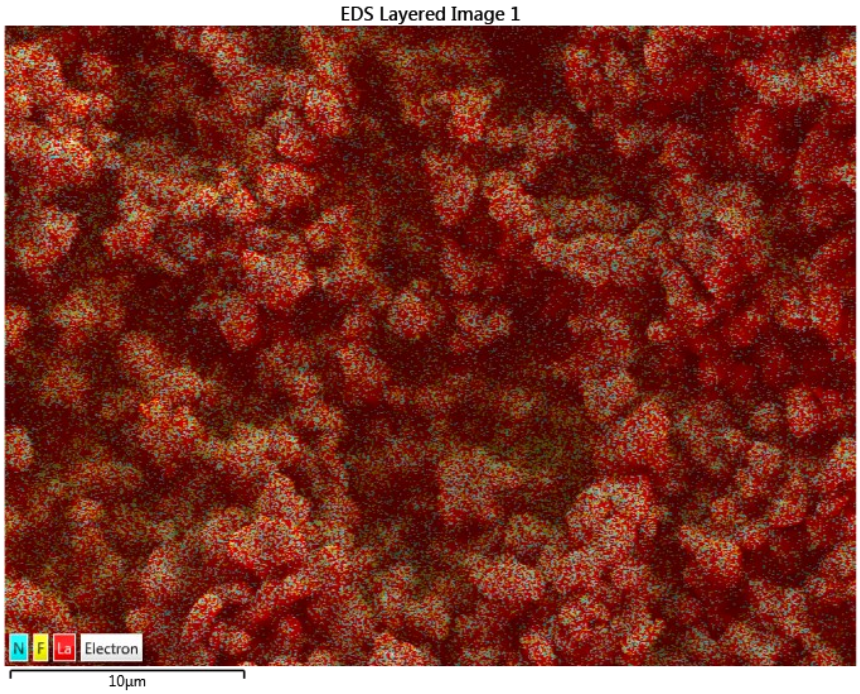

Figure 5.6

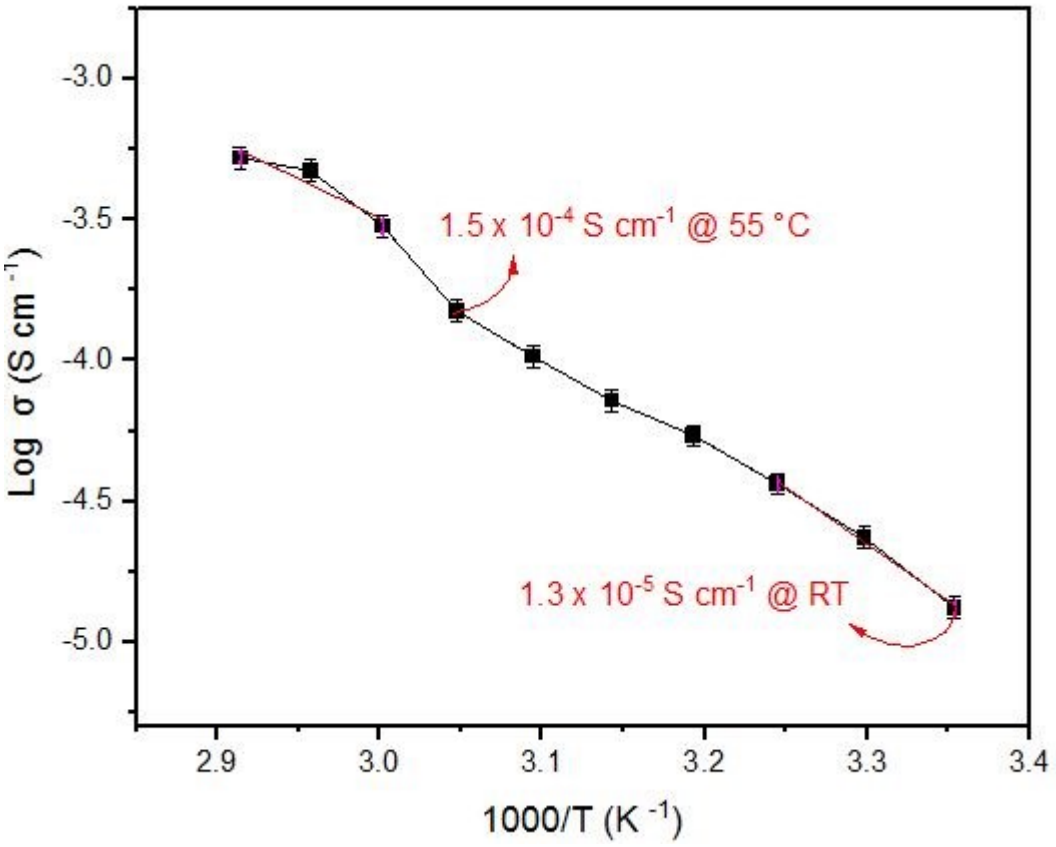

Figure 5.7

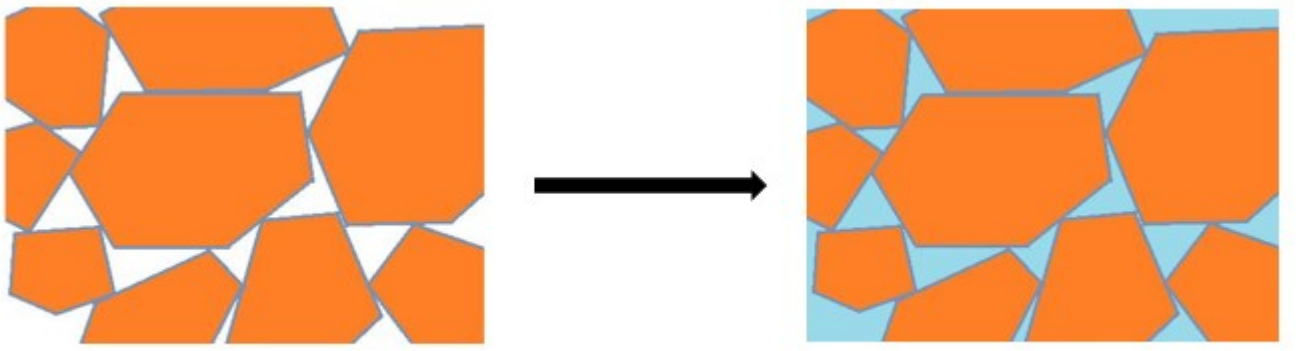

Figure 5.8

(a)

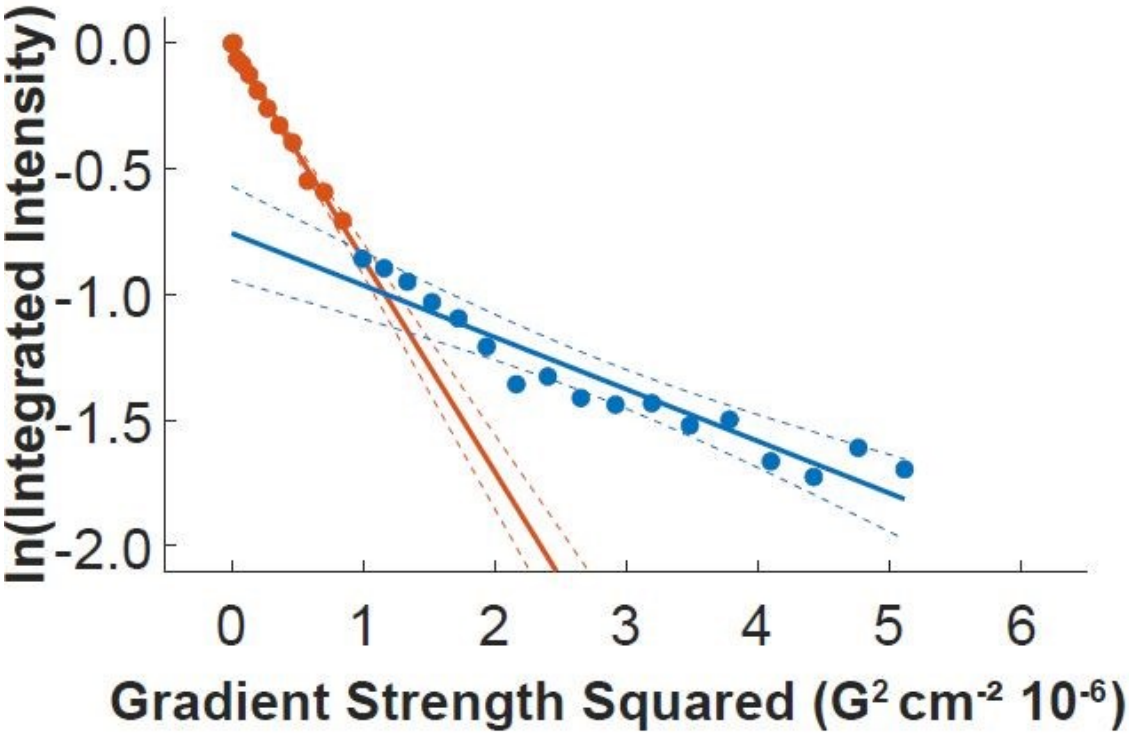
ln(Integrated Intensity)
0.0
-0.5
-1.0
-1.5
-2.0
0
1
2
3
4
5
6
Gradient Strength Squared (G² cm⁻² 10⁻⁶)

(b)

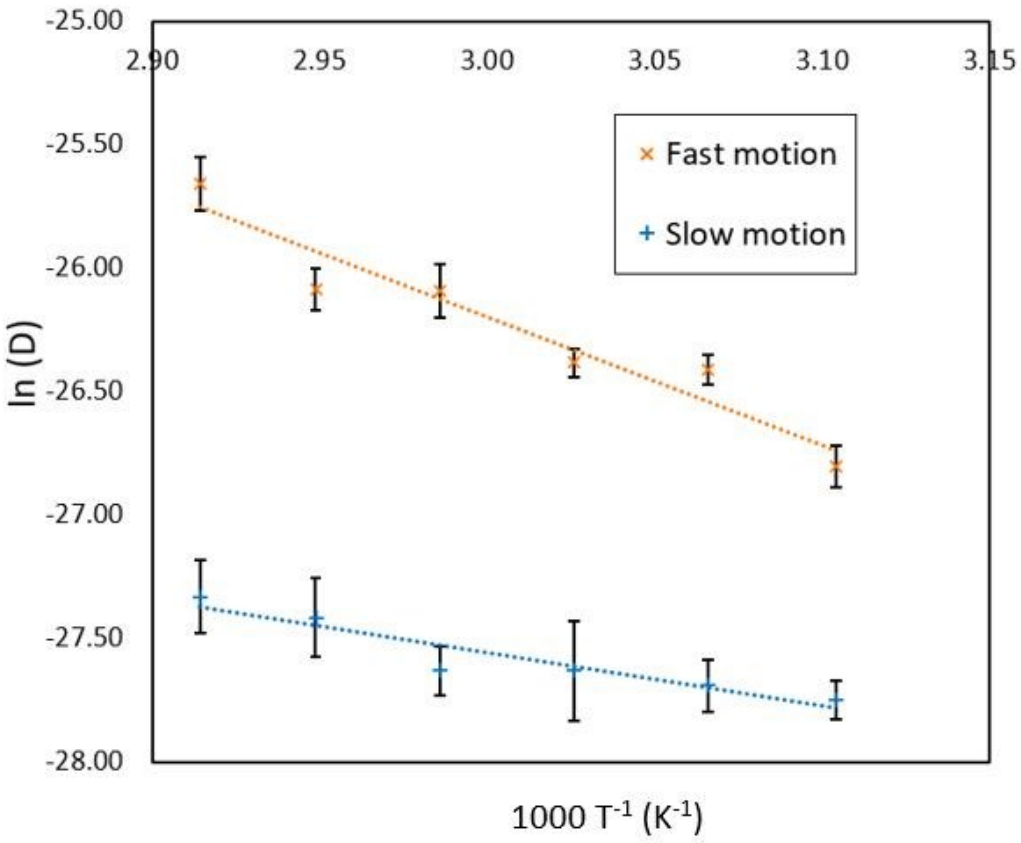
-25.00
-25.50
-26.00
-26.50
-27.00
-27.50
-28.00
ln (D)
2.90
2.95
3.00
3.05
3.10
3.15
1000 T-1 (K-1)
Fast motion
Slow motion

Figure 5.9

(a)

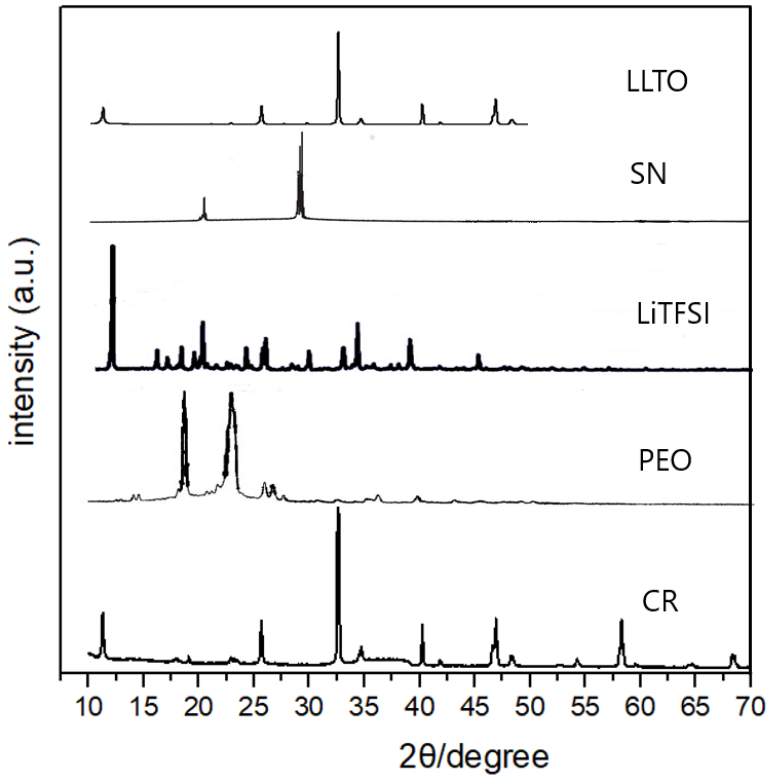
LLTO
SN
LiTFSI
PEO
CR
intensity (a.u.)
10 15 20 25 30 35 40 45 50 55 60 65 70
2θ/degree

(b)

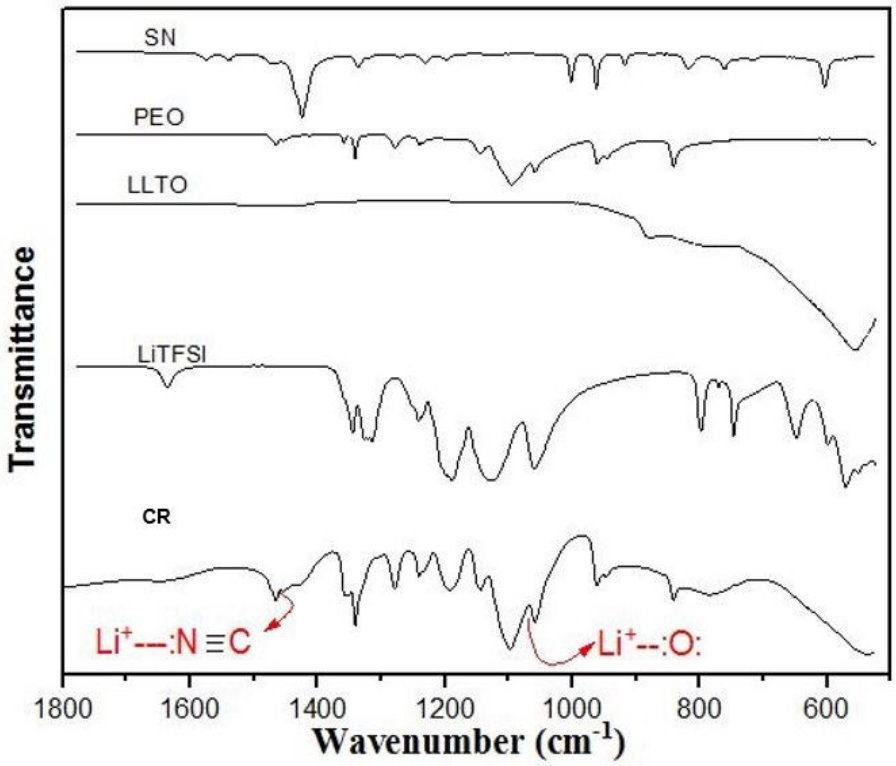
SN
PEO
LLTO
LiTFSI
CR
Li+---:N≡C
Li+--:O:
Transmittance
1800
1600
1400
1200
1000
800
600
Wavenumber (cm-1)

Figure 5.10

(a)

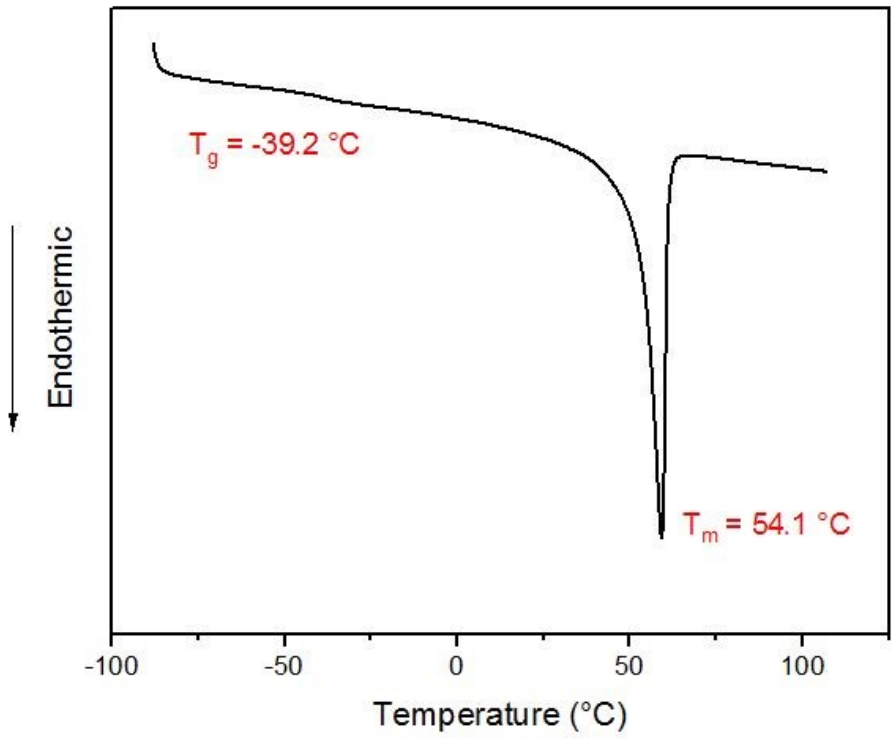

(b)

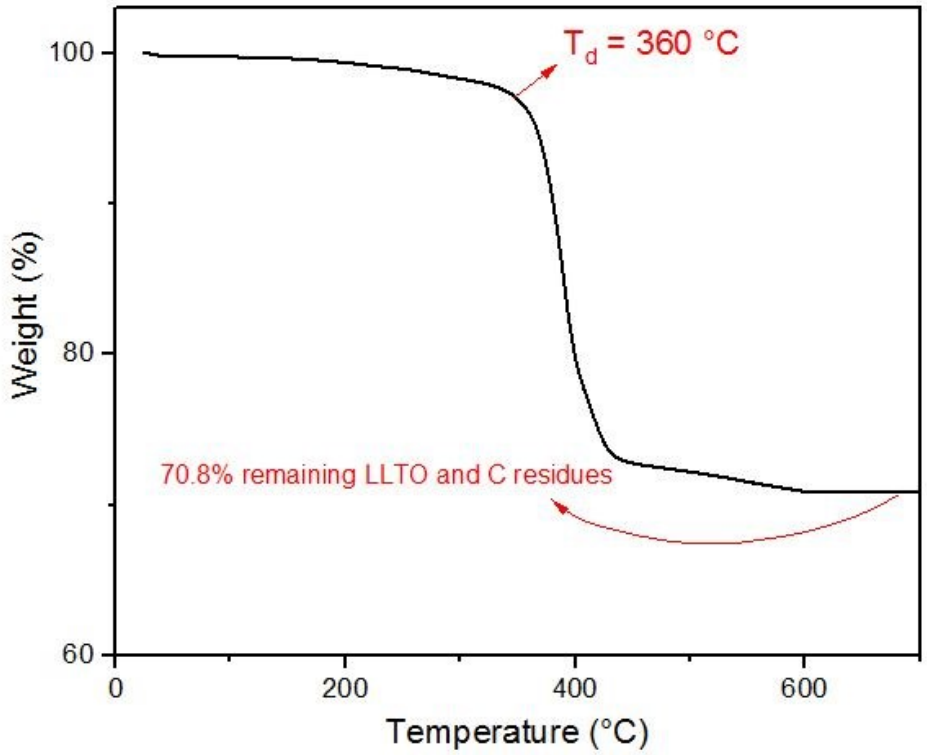

Figure 5.11

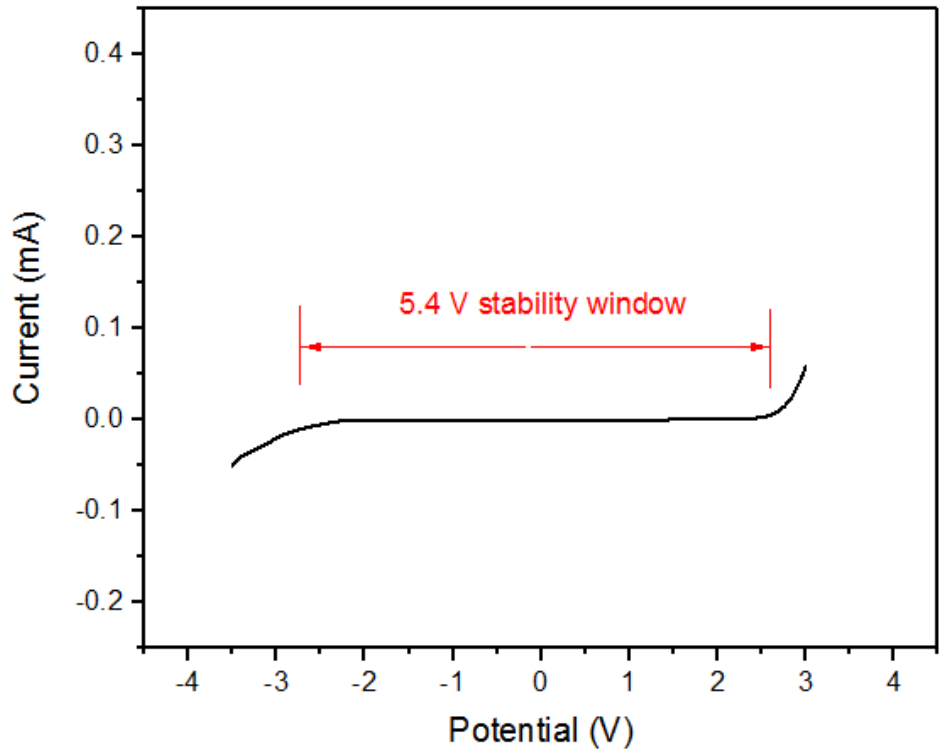

Figure 5.12

(a)

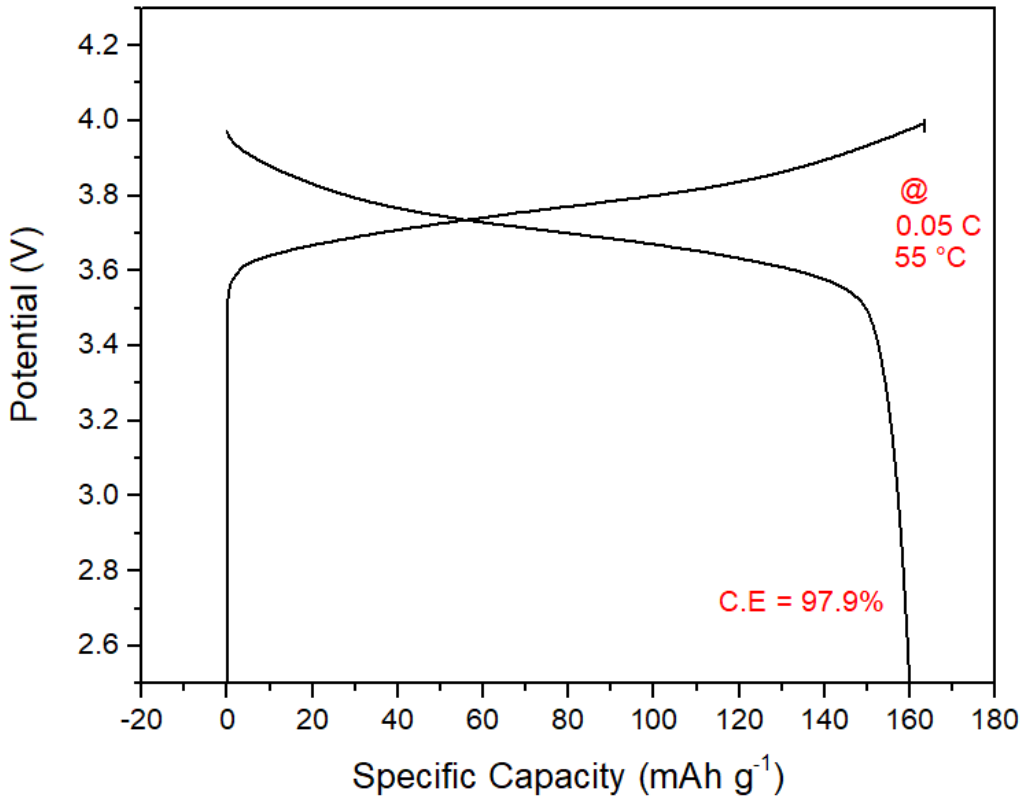

(b)

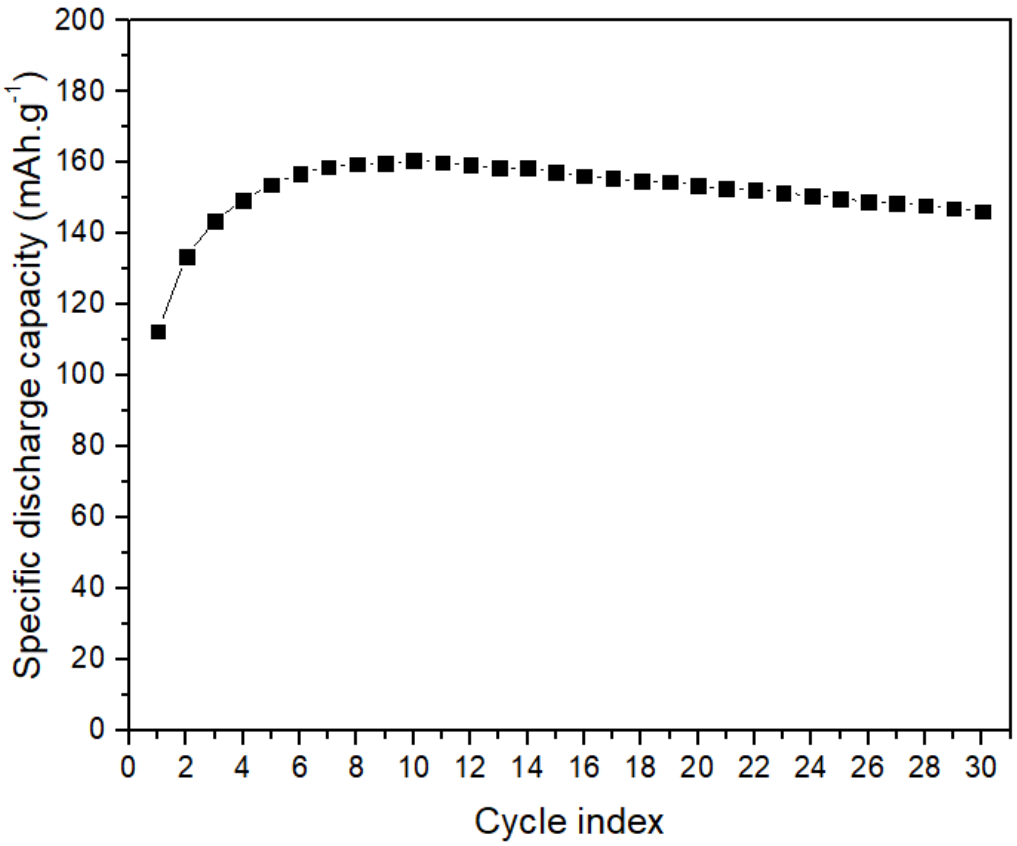
Specific discharge capacity (mAh.g-1)
Cycle index
0
20
40
60
80
100
120
140
160
180
200
0
2
4
6
8
10
12
14
16
18
20
22
24
26
28
30

(c)

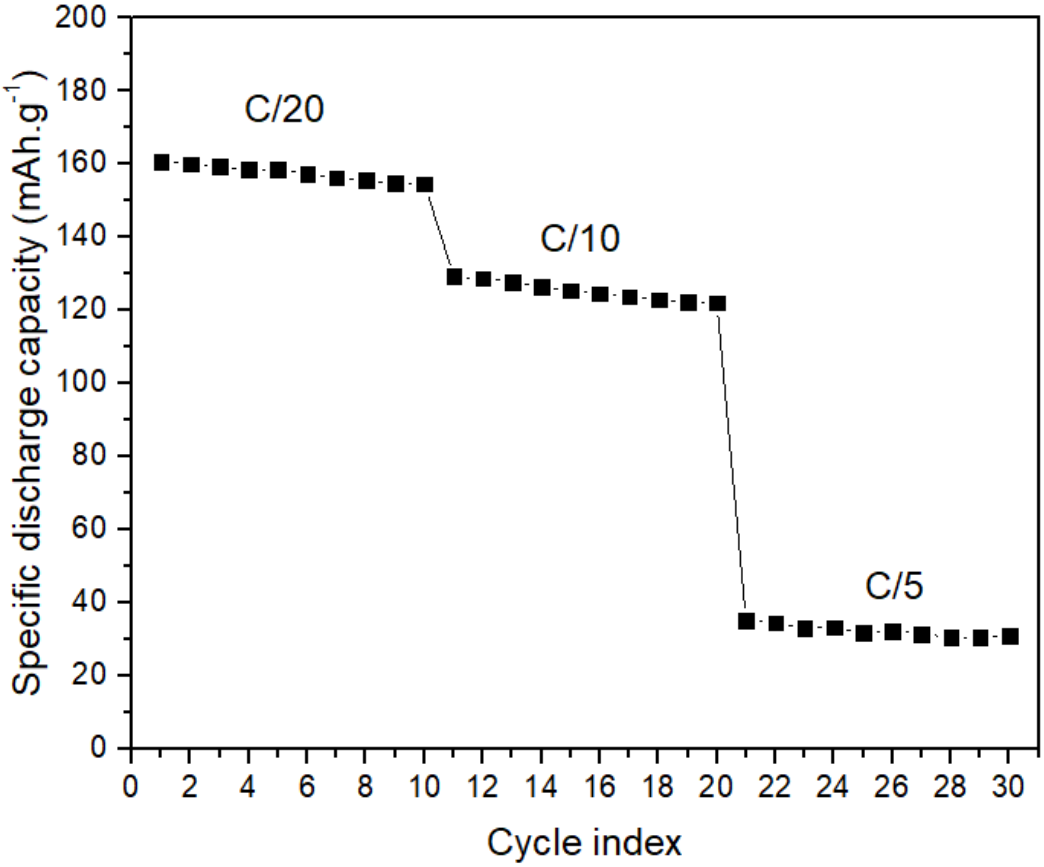
Specific discharge capacity (mAh.g-1)
Cycle index
C/20
C/10
C/5
0
20
40
60
80
100
120
140
160
180
200
0
2
4
6
8
10
12
14
16
18
20
22
24
26
28
30

(d)

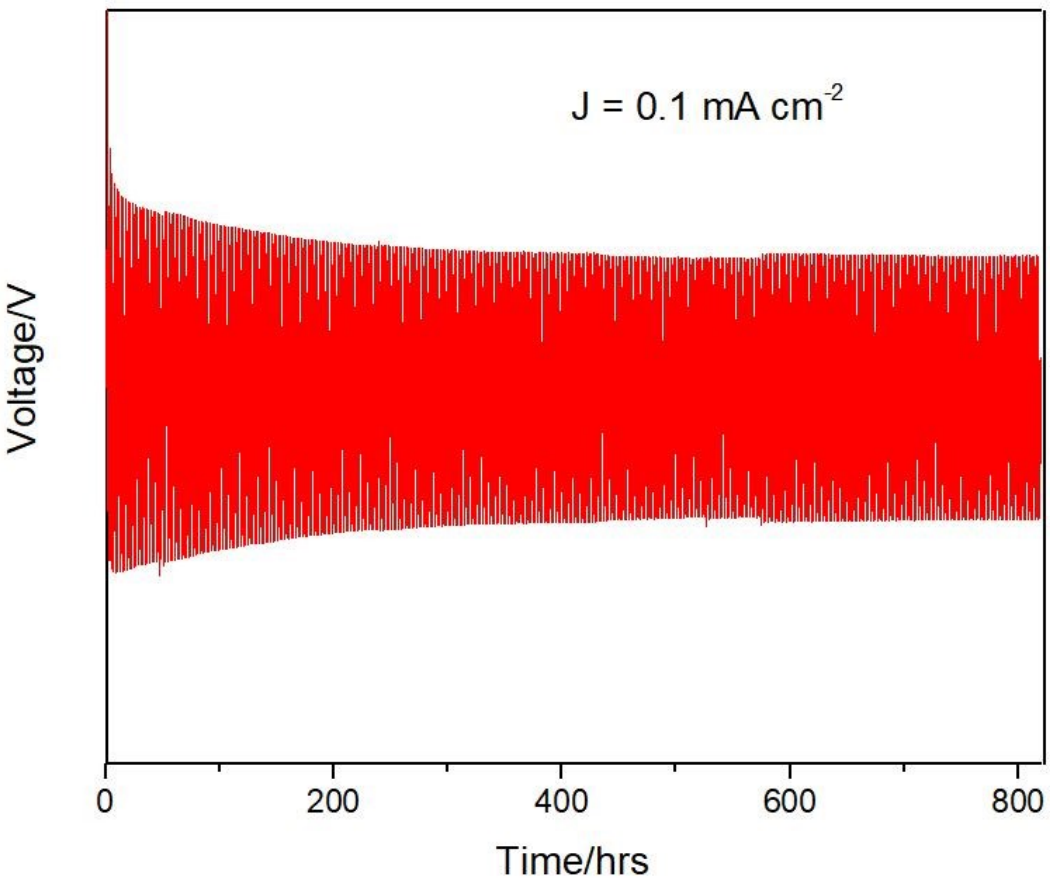
J = 0.1 mA cm-2
Voltage/V
Time/hrs
0
200
400
600
800

(e)

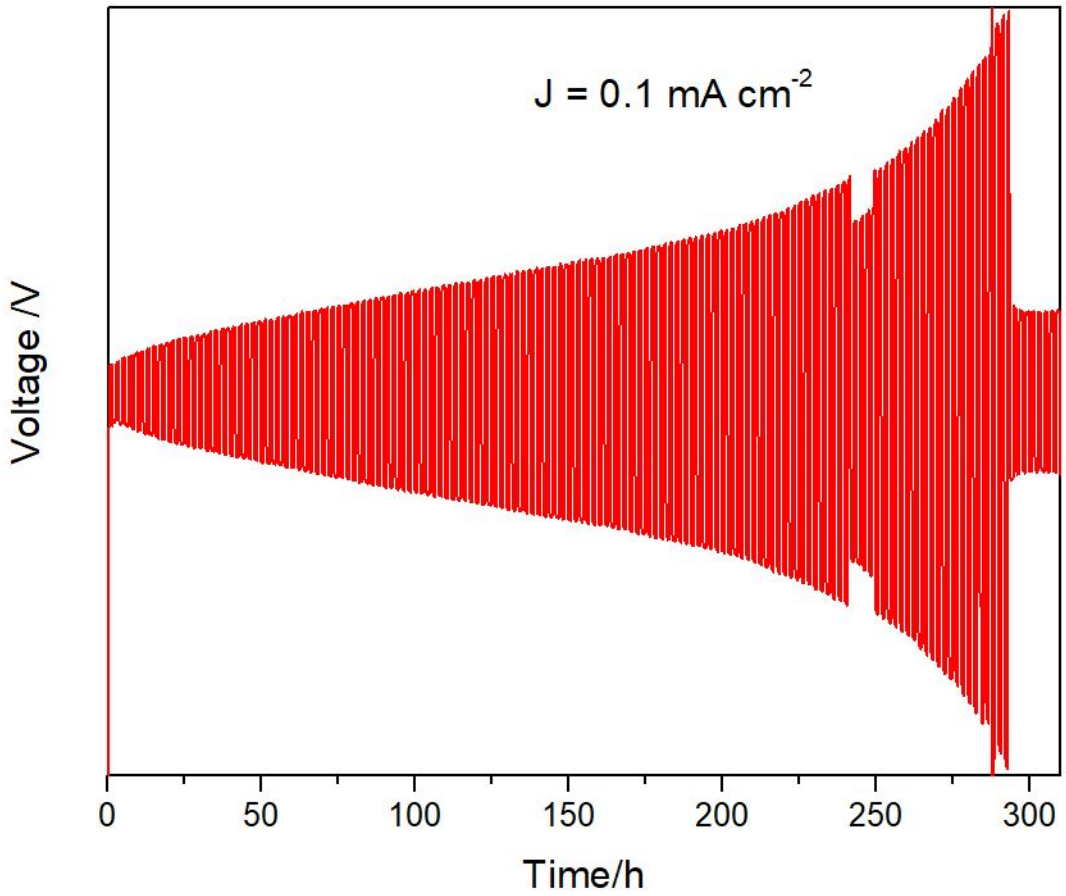

(f)

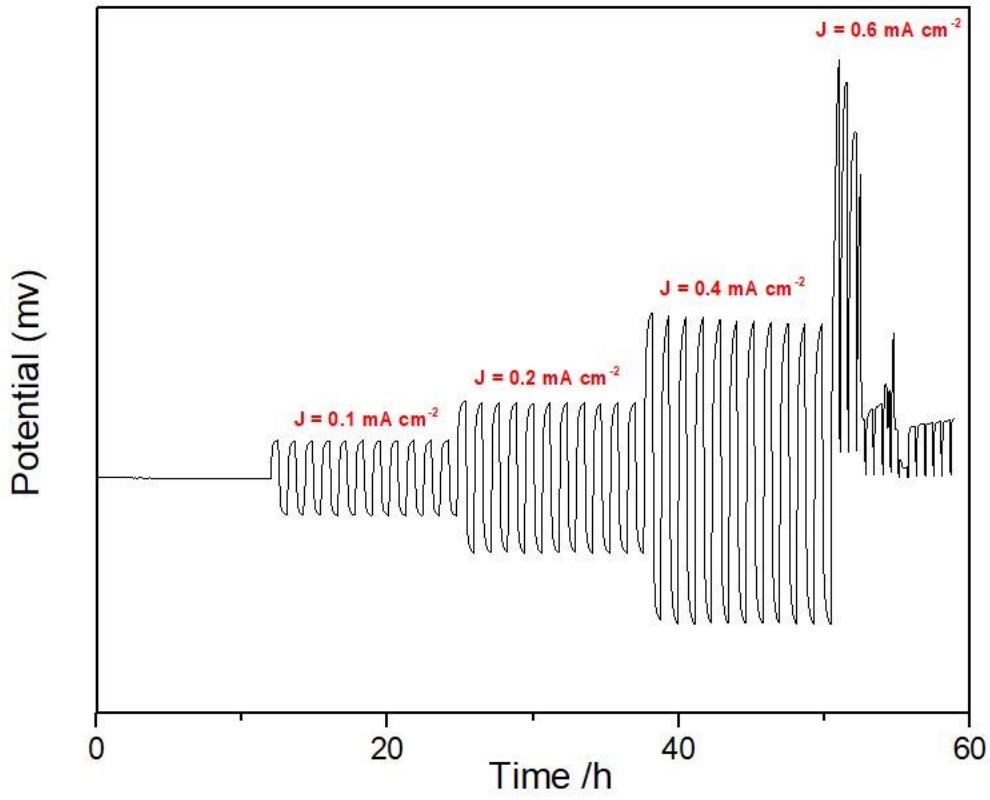
J = 0.6 mA cm-2
J = 0.4 mA cm-2
J = 0.2 mA cm-2
J = 0.1 mA cm-2
Potential (mv)
0
20
40
60
Time /h

Chapter 6: Conclusion, outlook, and recommendations

Conclusion

This thesis has explored the development of safe and high energy density batteries, focusing on electrolytes for aqueous lithium-ion batteries (ALIBs) and all-solid-state batteries (ASSBs). The increasing demand for efficient energy storage devices is driven mostly by electric vehicles (EVs). The global transition toward electric vehicles, prioritized by governments and the commitments of various countries to phase out the sale of internal combustion engine (ICE) vehicles in the coming years, has significantly increased the need for batteries that can deliver high energy density while ensuring safety and sustainability. This growing demand underscores the importance of developing advanced battery technologies to meet the performance requirements of electric vehicles and support the shift towards cleaner and more environmentally friendly transportation options.

The research in this thesis began in chapter 3 with an investigation into the microstructure of nitrate aqueous electrolytes and how the structure relates with ionic conductivity. This understanding is crucial for optimizing the energy density and cost of ALIBs, which offer advantages over conventional LIBs in terms of safety, affordability, and having a wider temperature range of operation. It has been found that the ionic conductivity isotherms of the nitrate-salt/H_2O solutions show a maximum around the concentration that coincides with the eutectic concentration in the phase diagram. This is most likely due to the minimum found in the activation energy vs concentration curve calculated from the Arrhenius equation. The electrochemical stability window for these electrolytes, however, remains bottleneck in their practicality because of the inherently low stability window for water.

For this reason, the thesis then shifted focus to the study of all-solid-state batteries (ASSBs), which have gathered significant interest due to their potential for higher energy density, improved safety, and longer cycle life compared to LIBs. ASSBs eliminate the need for flammable and volatile organic liquid electrolyte, reducing the risk of thermal runaway and preventing the growth of lithium dendrites, which can cause short circuits and capacity loss. Chapters 4 and 5 presented the development of two novel Composite Solid Electrolytes (CSEs) for use in ASSBs, consisting of Polyethylene oxide (PEO), Lithium bis(trifluoromethanesulfonyl)imide (LiTFSI) salt, Lithium Lanthanum Titanate (LLTO) Perovskite inorganic ceramic, and the polymer plasticizer Succinonitrile (SN). The polymer-rich CSE demonstrated superior characteristics compared to its ceramic-rich counterpart with the most notable difference being in terms of ionic conductivity; the ceramic rich ionic

conductivity was one order of magnitude lower. It had the following composition: 70%-PEO 12%-LiTFSI 9%-LLTO 9%-SN. Both electrolytes were successfully charged and discharged in ASSBs when coupled with a lithium metal anode and an in-lab prepared 'Catholyte' containing composite cathode.

The contributions of this thesis to the fields of ALIBs and ASSBs not only advance our understanding of battery technologies but also pave the way for safer, more efficient, and sustainable energy storage solutions. The novel insights and materials developed in this work have the potential to significantly impact the future design and optimization of batteries for various applications, ultimately contributing to the global transition towards clean and renewable energy sources.

Outlook and recommendations

The most important recommendations are listed below:

- Use of advanced computational techniques such as Molecular Dynamics (MD) simulations and ab initio modeling to corroborate the microstructure of highly concentrated aqueous electrolyte solutions as described by the phenomenological/empirical model proposed in chapter 3.
- Utilizing the novel understanding of liquid electrolytes microstructure into the exploration of more fluorine free salts to drive the cost of lithium batteries down and reduce their environmental footprint as well.
- Paying more attention to analysing failure roots (whether it is ununiform SEI growth, dendrite growth and/or electrolyte decomposition) and post-mortem analysis can offer valuable in literature and would help accelerate research in the field. Mentioning capacity fade and early failure without pinpointing the ‘why’ strips value from a work.
- Most reported solid electrolytes in literature and in chapters 4 and 5 still contain an organic flammable portion even if solid and non volatile. Investigation of novel anti-flammable additives would be of extreme benefit to the field.
- The electrolyte class with the highest potential to revolutionize batteries are ‘ceramic’ solid states electrolytes. Pure ceramic SSE can be very difficult to process and they are accompanied by interfacial and interfacial challenges. However, they have the potential to be the safest, and most energy dense chemistry due to their wide thermal and

electrochemical stability window.

Appendix A: Supplementary information for chapter 3

Figure *A*.1: Isothermal structural variation at high and low temperatures in a phase diagram with no solvate *formation.*

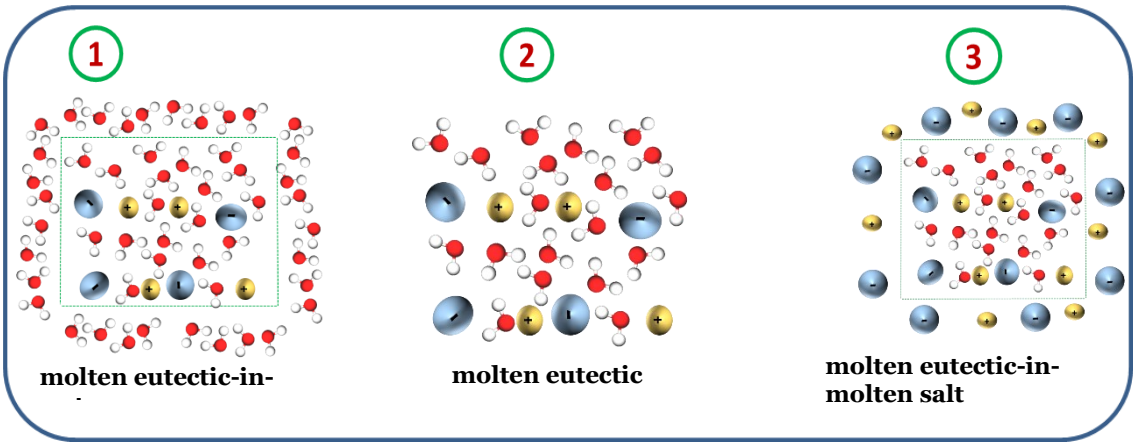

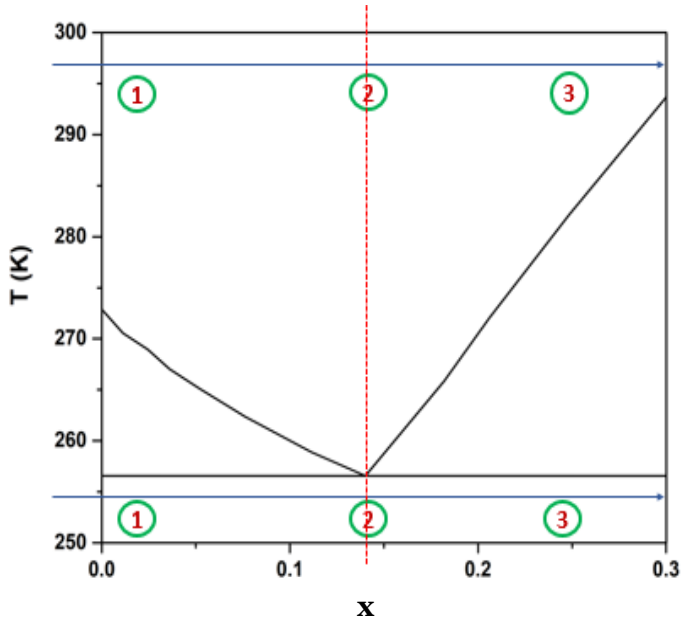

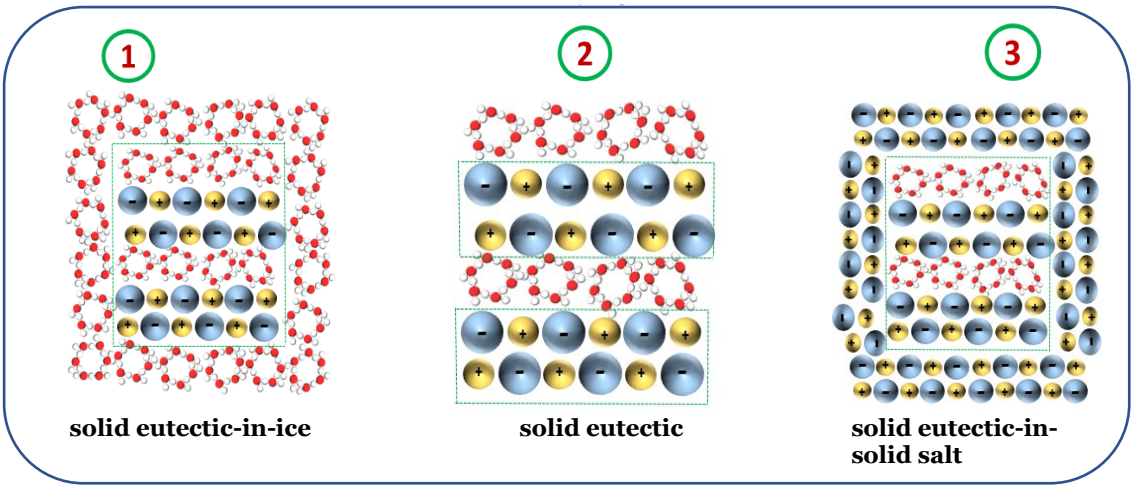

Figure A.2: Isothermal structural variation at high and low temperatures in a phase diagram with solvate formation

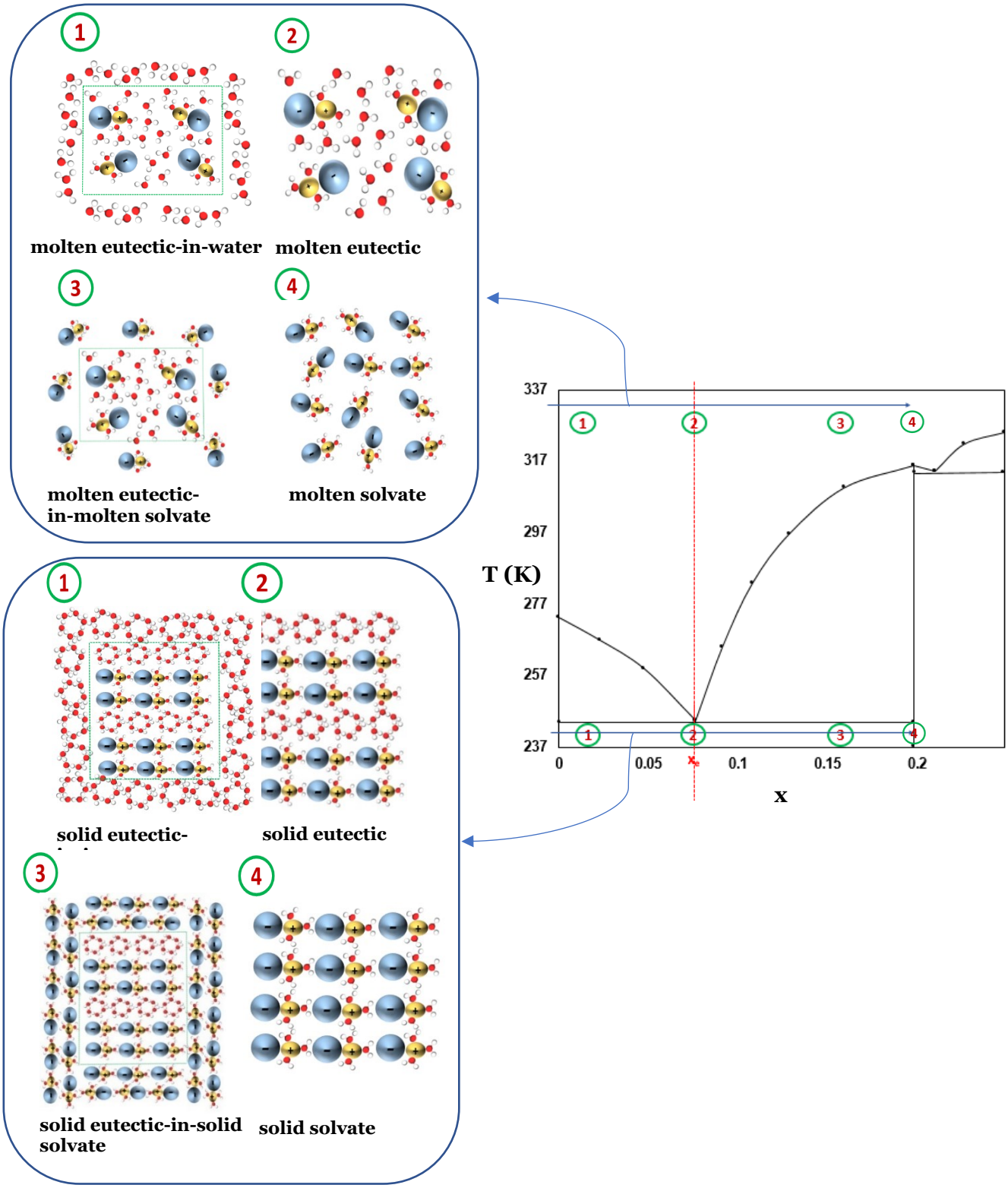

Fig. A.3: Microstructure schematic Illustration for every molar concentration/temperature

Iso-compositional structural variation in the case of:

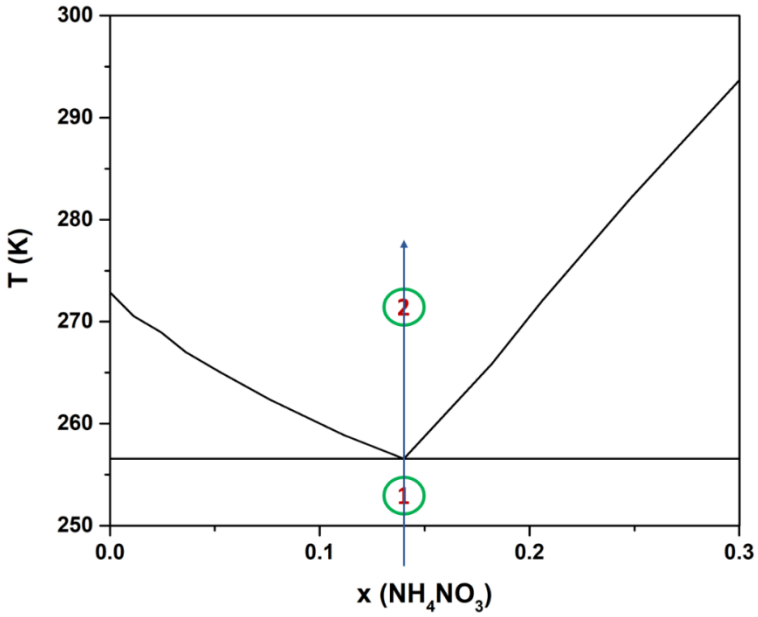

I. Phase diagram with no solvate formation

a. $x = x_e$

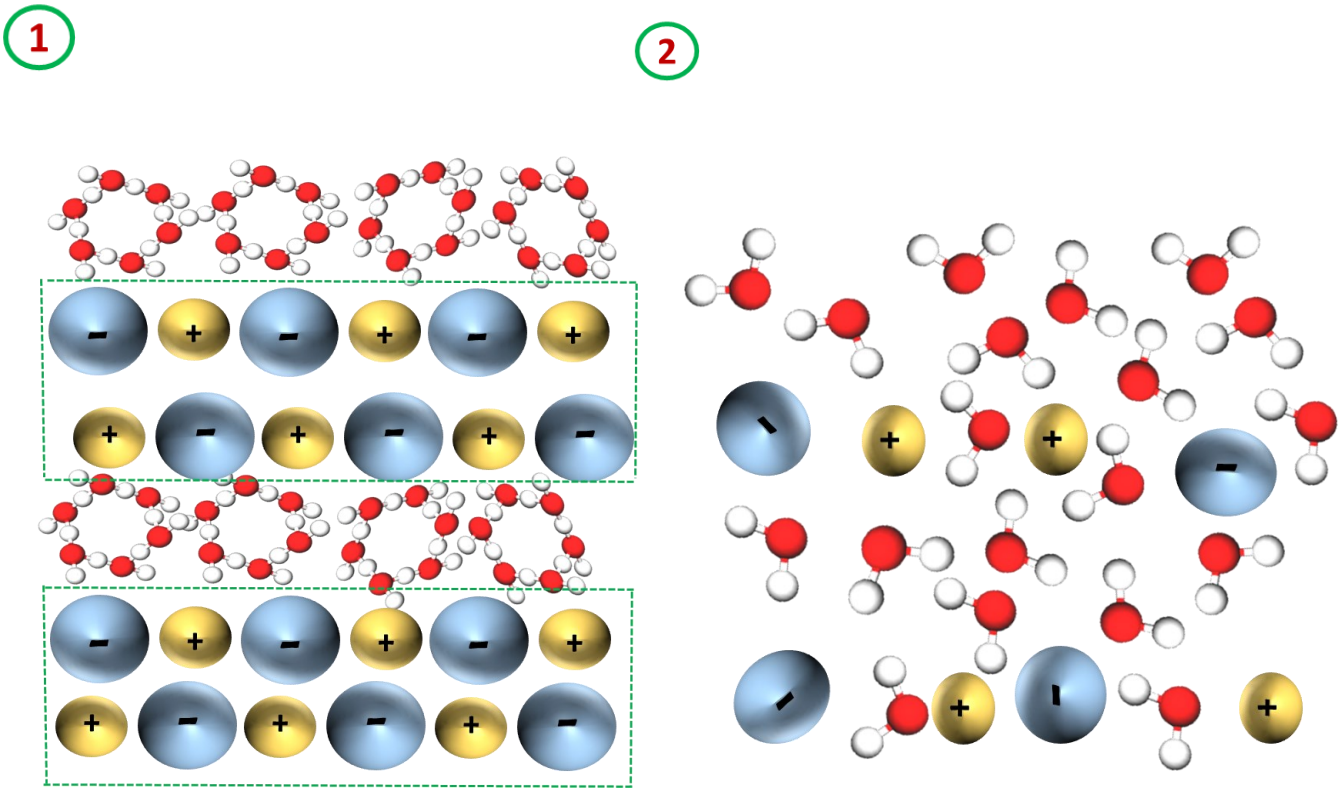

b. At $x<x_e$:

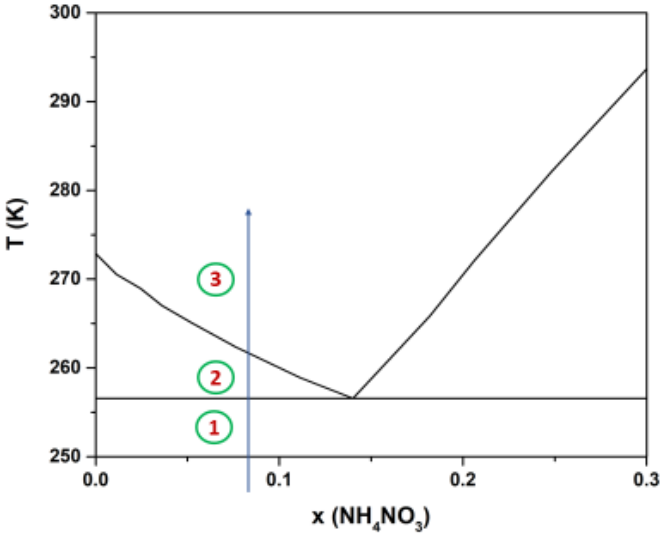

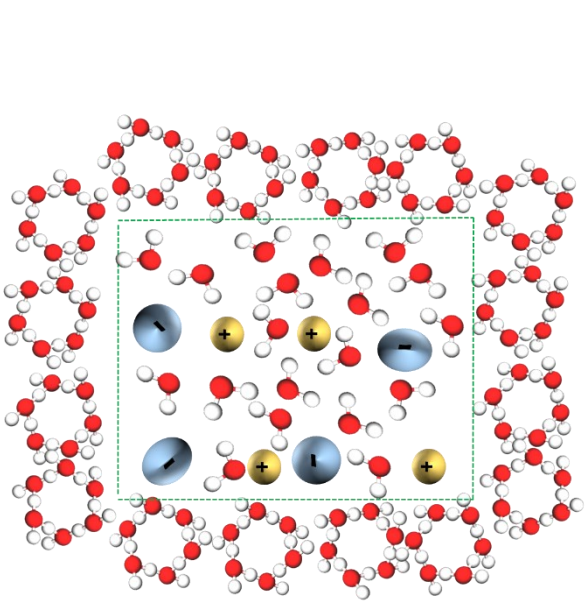

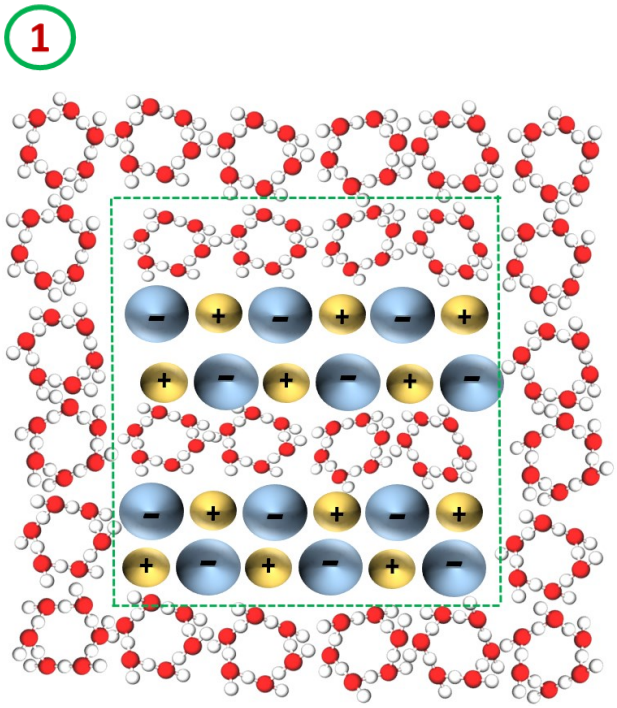

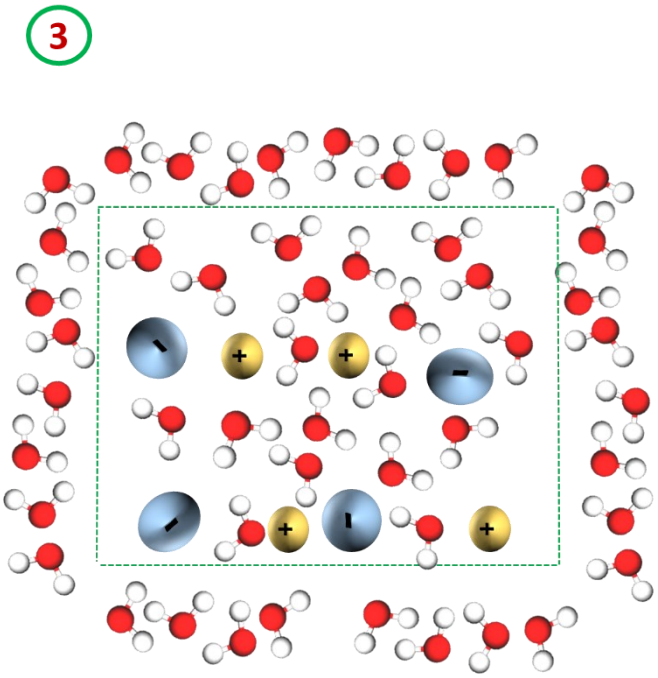

c. At $x > x_e$

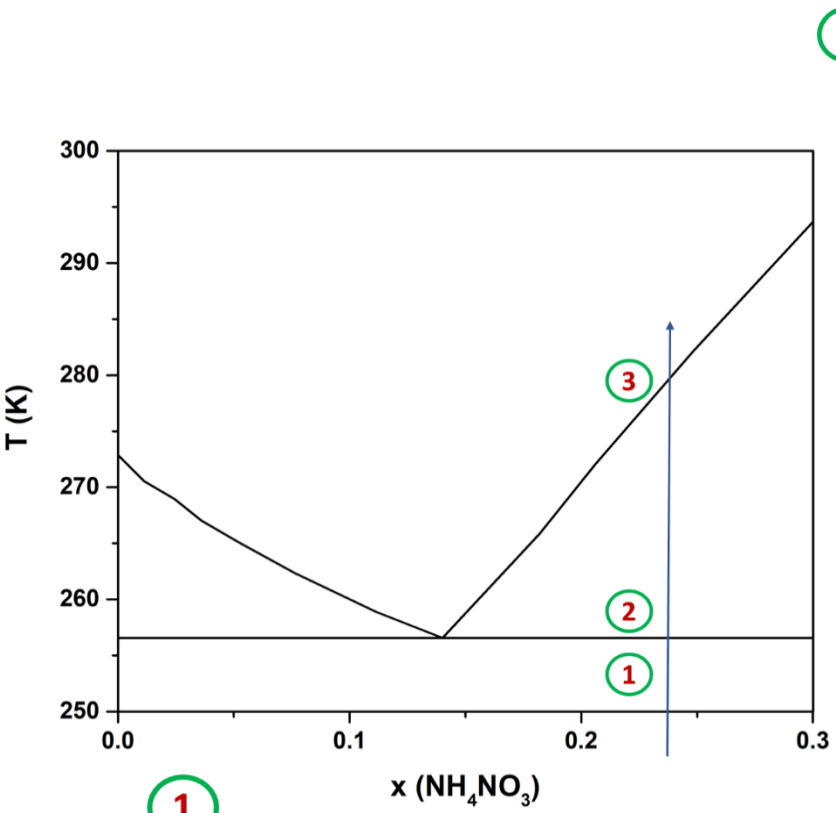

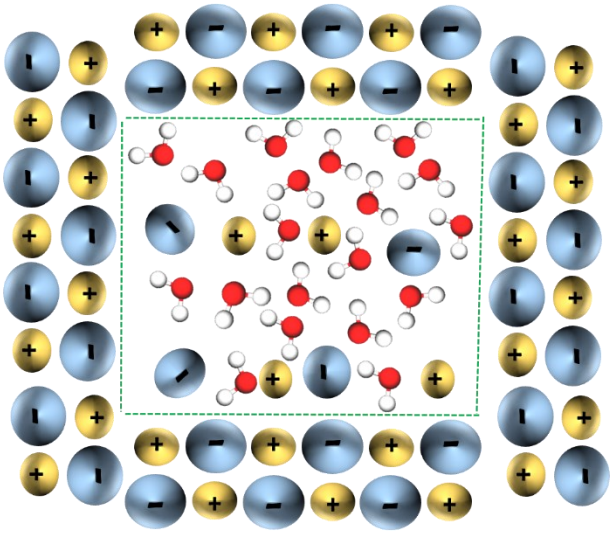

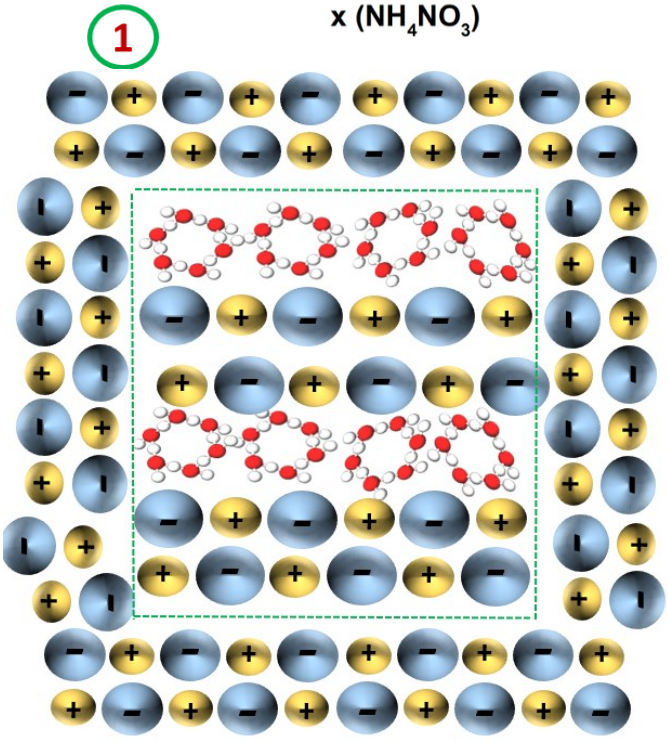

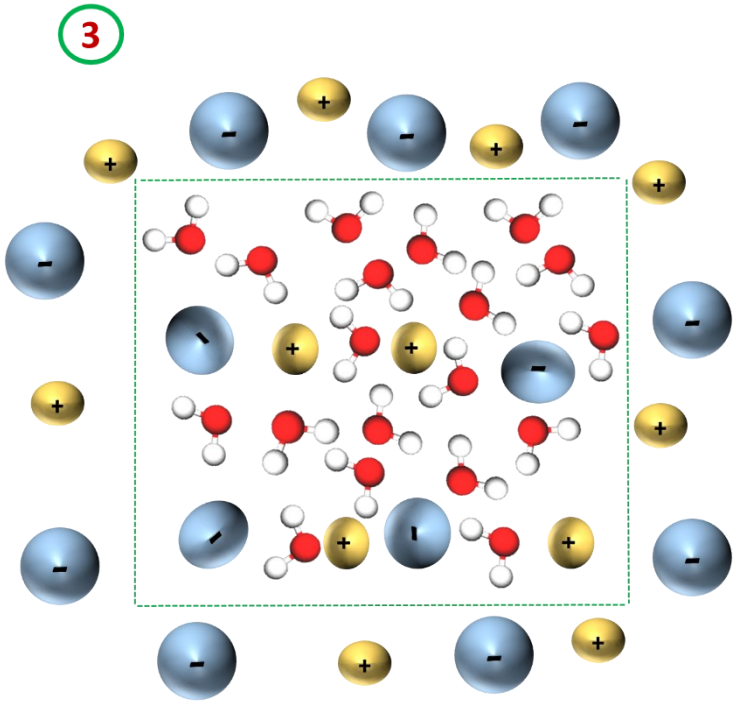

II. Phase diagram with solvate formation

a. $x = x_{e1}$

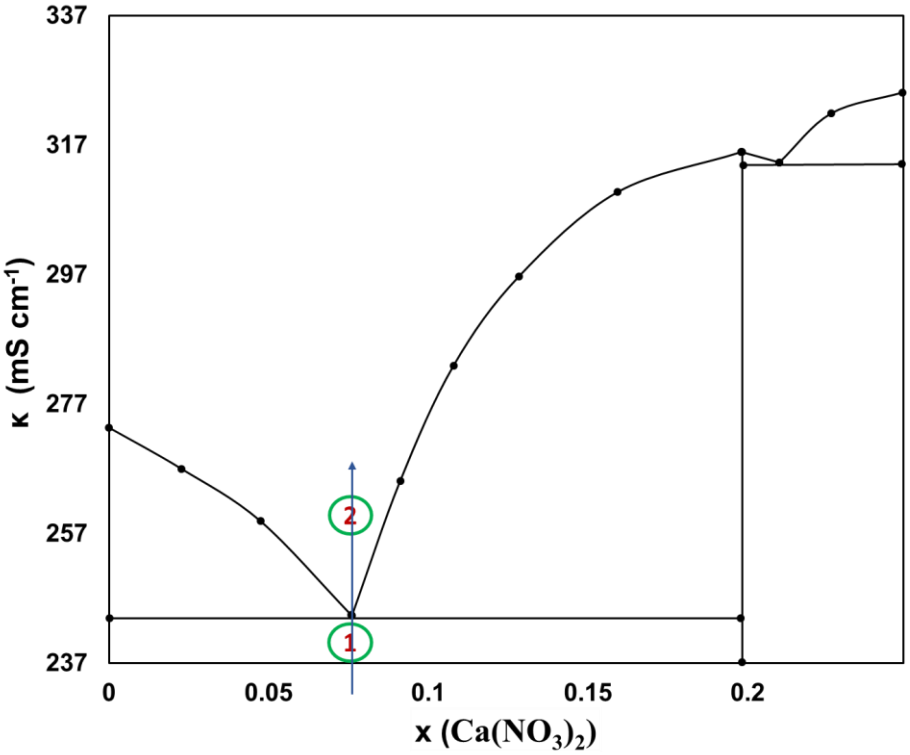

1

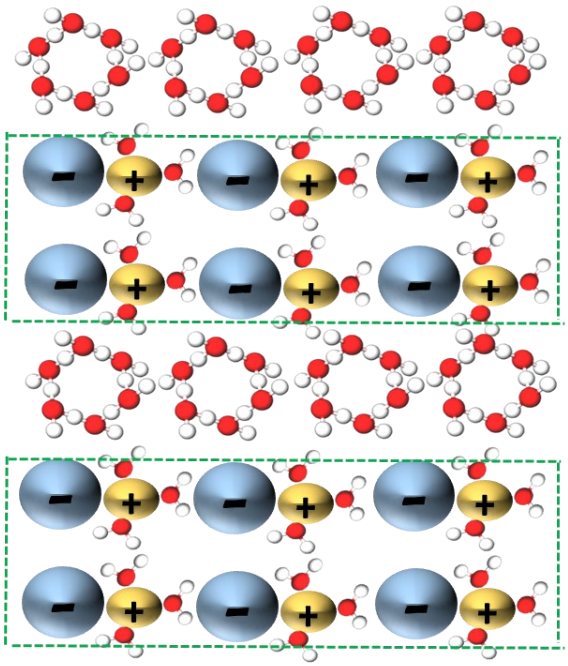

2

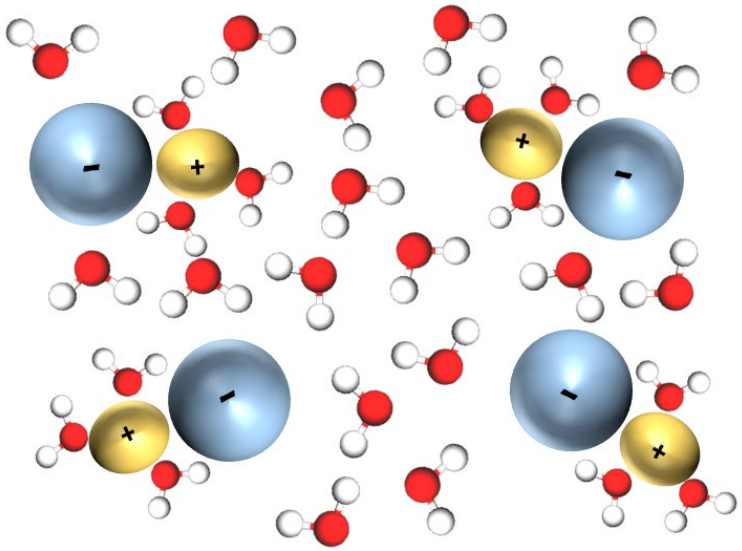

b. $x = x_s$

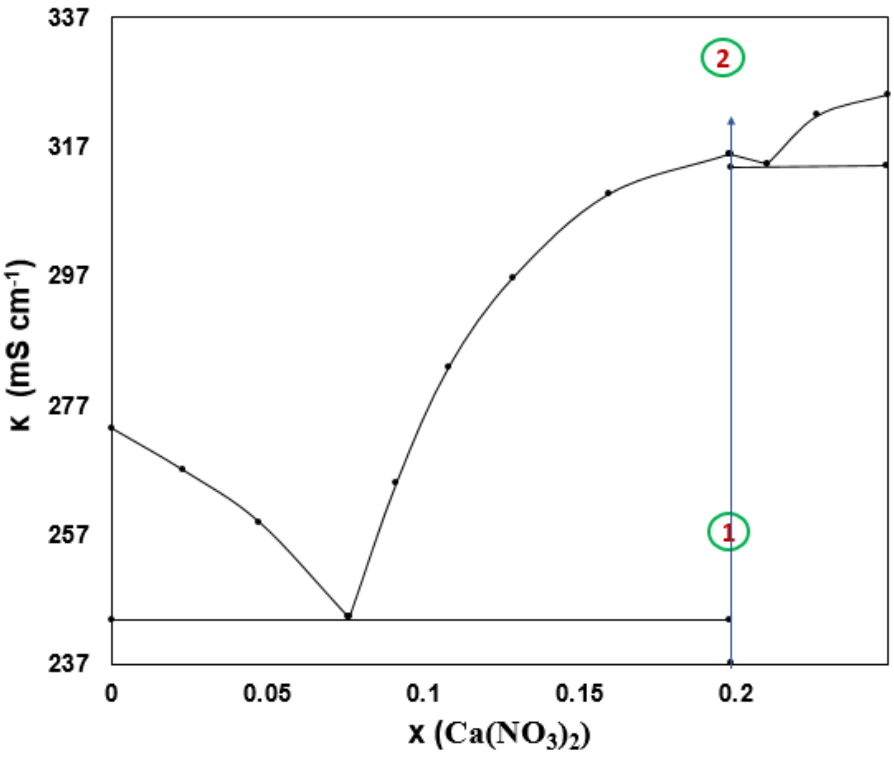

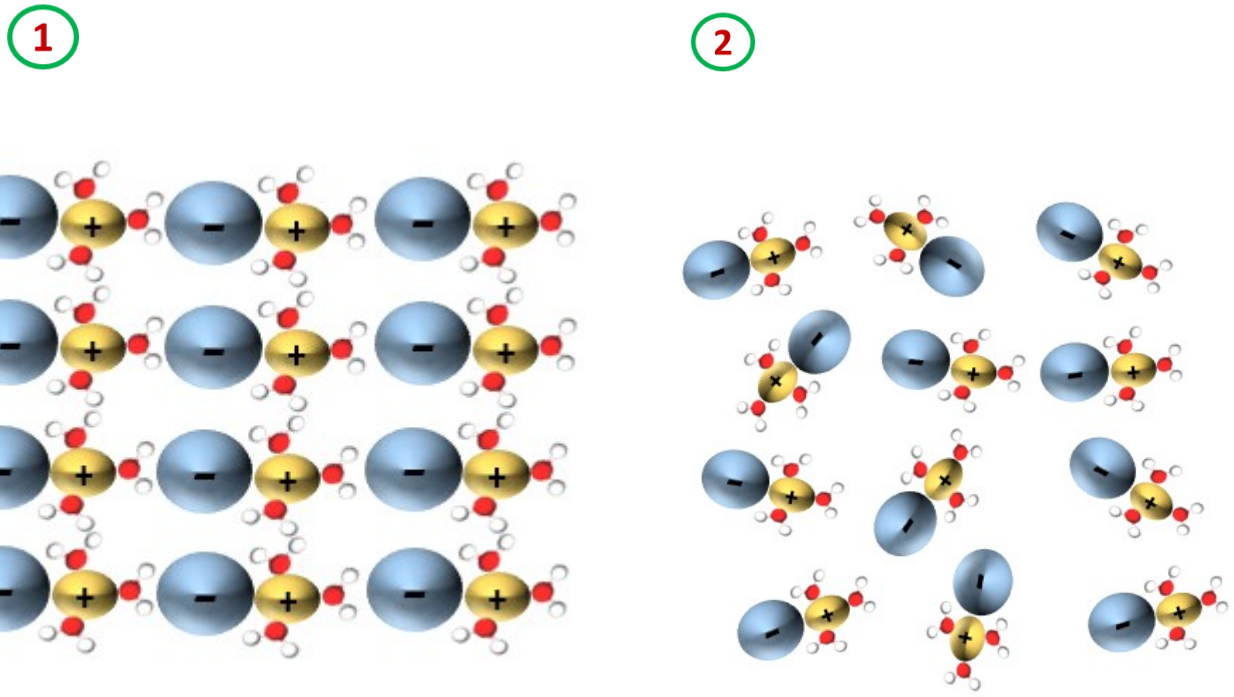

c. $x = x_{e2}$

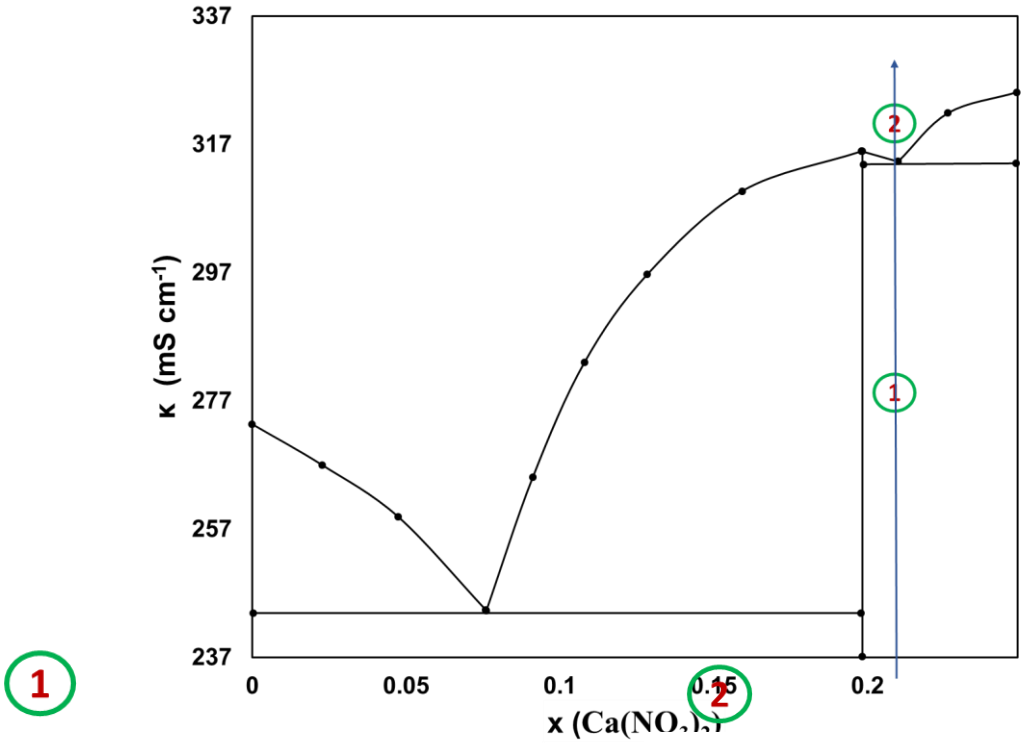

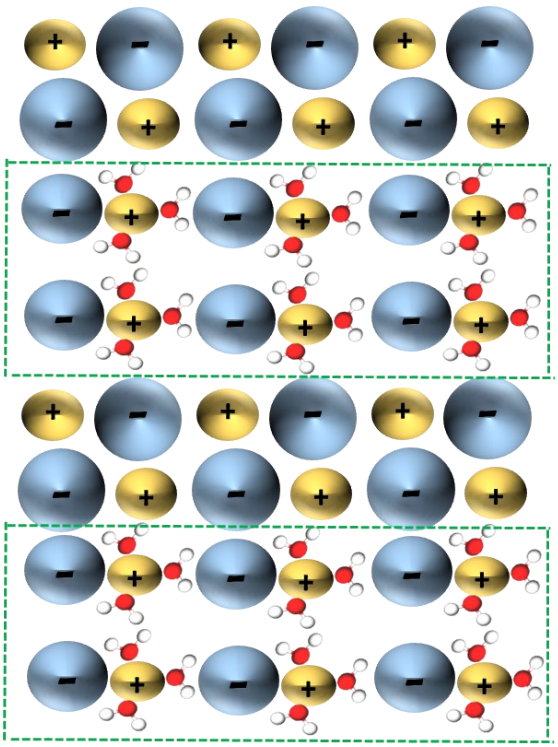

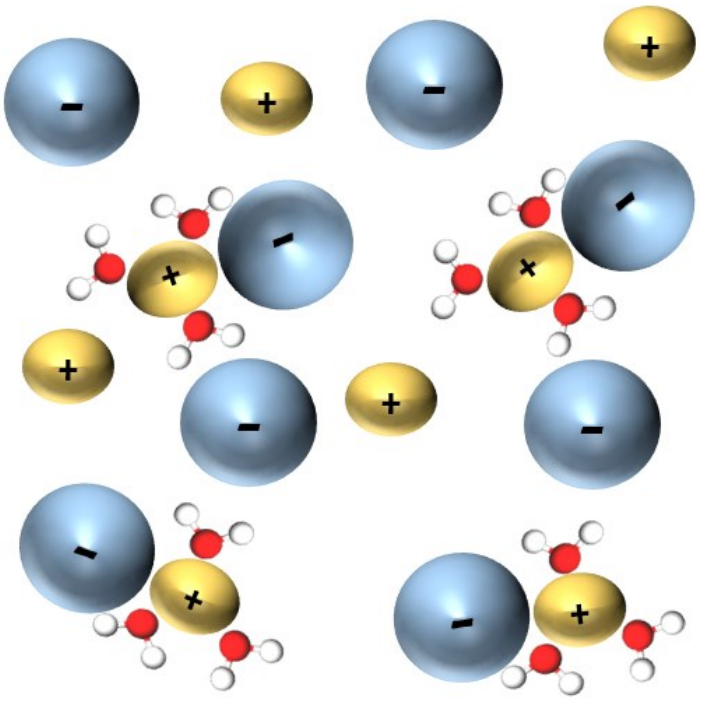

d. $x < x_{e1}$

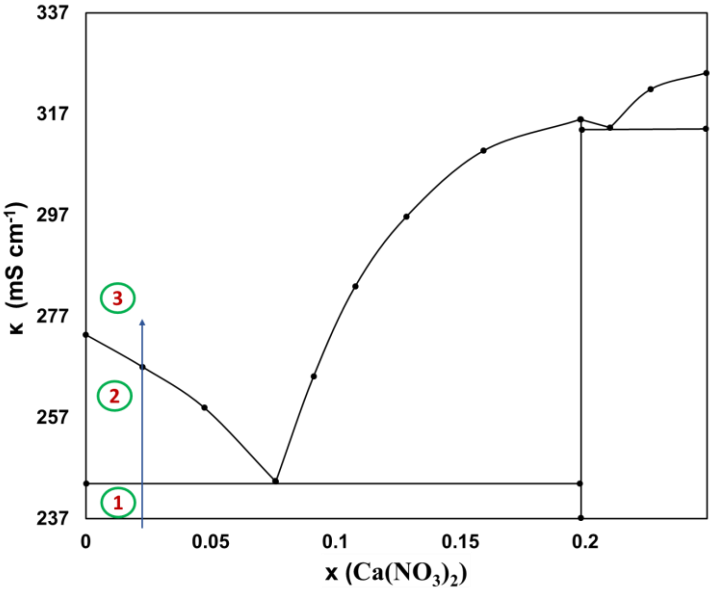

2

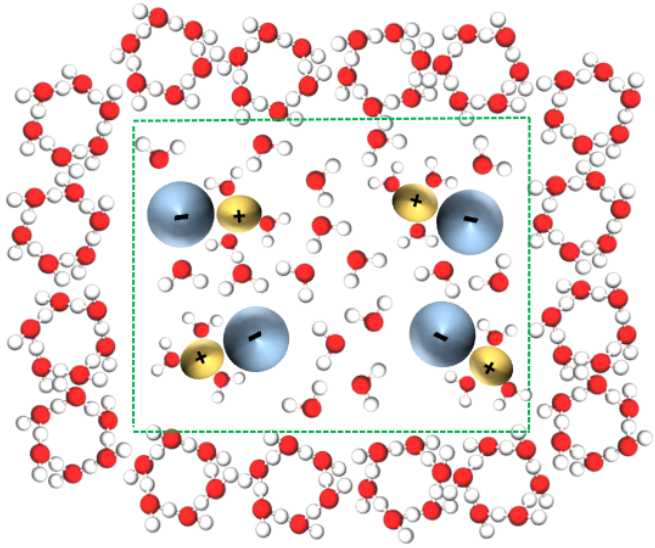

1

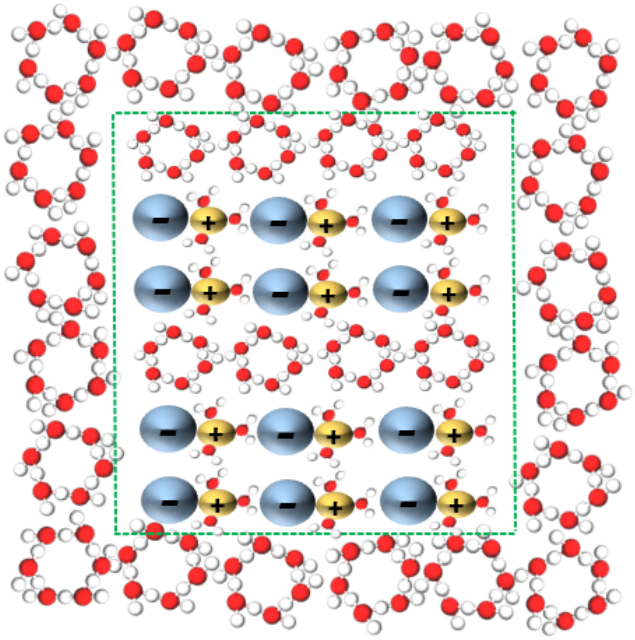

3

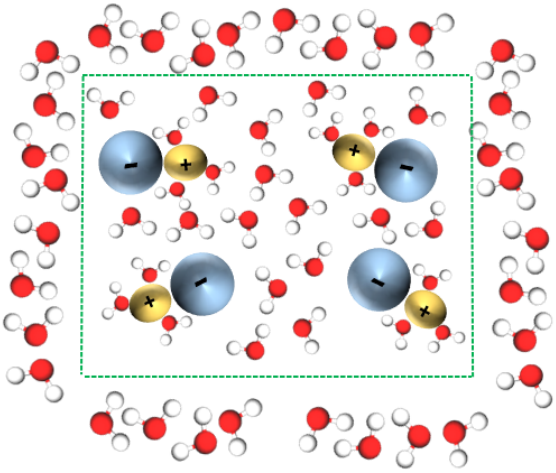

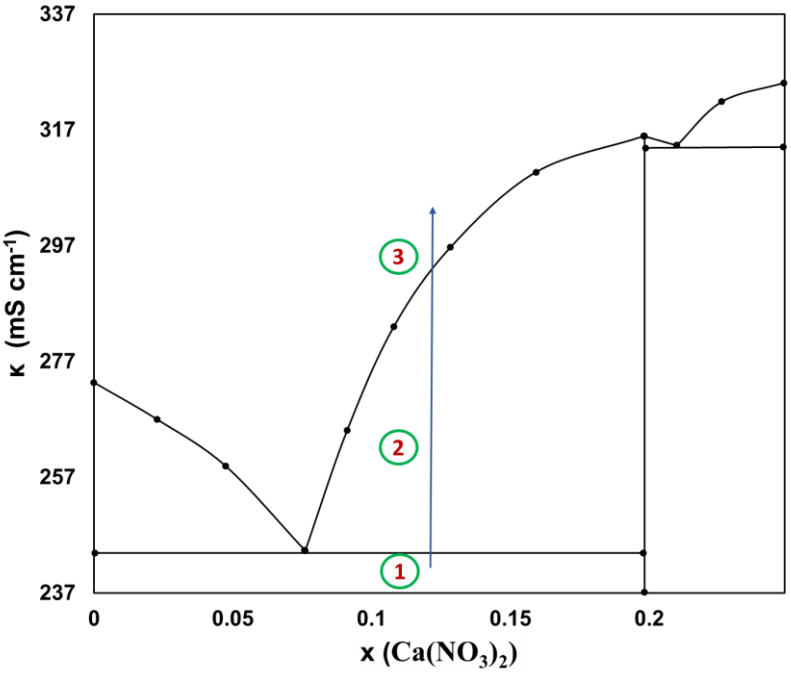

e. $x_{e1} < x < x_s$

2

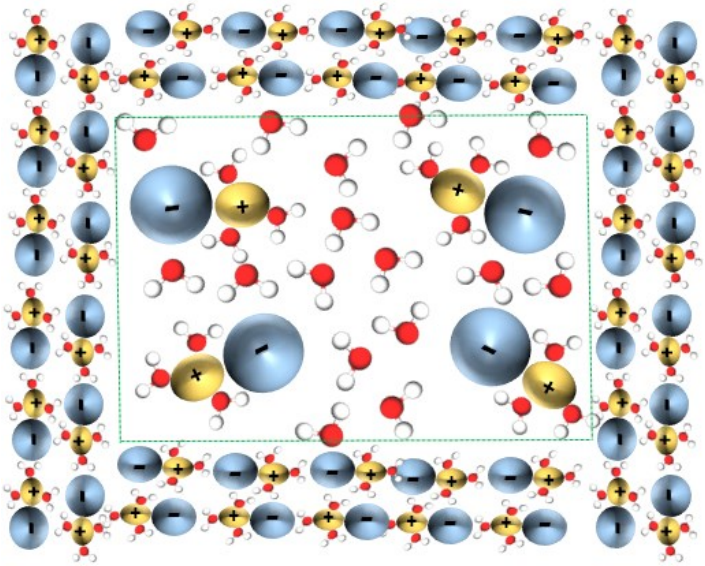

1

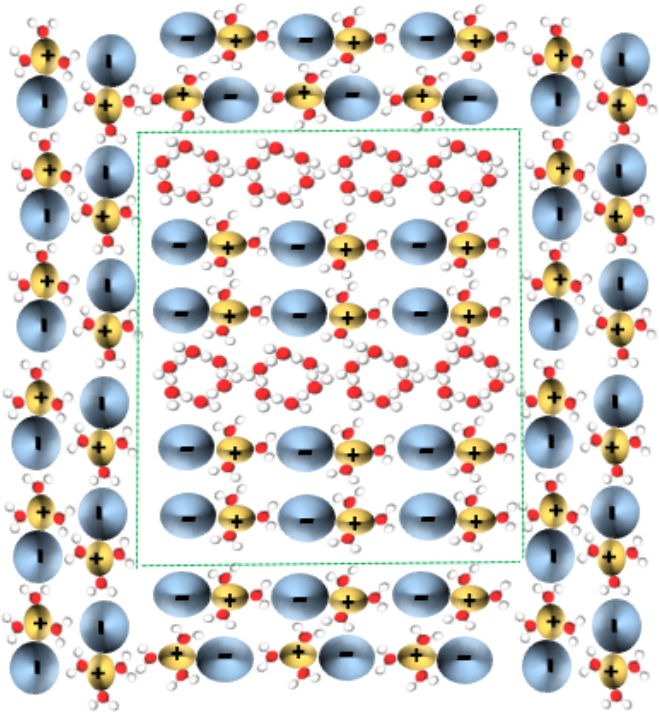

3

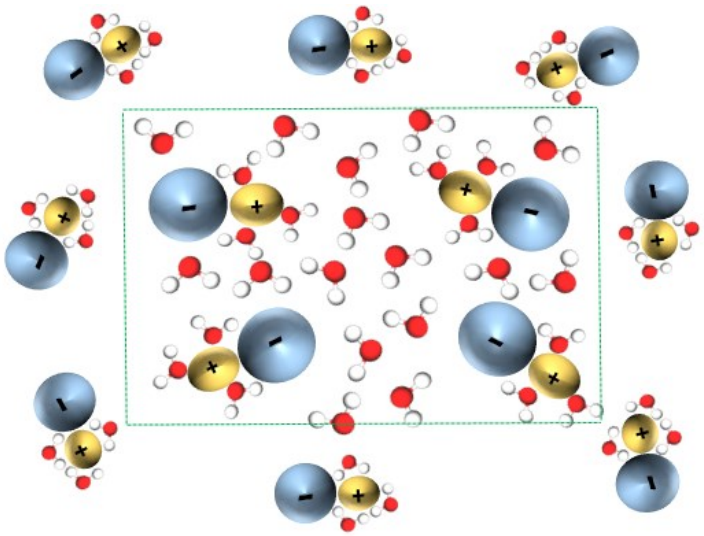

f. $x_s < x < x_{e2}$

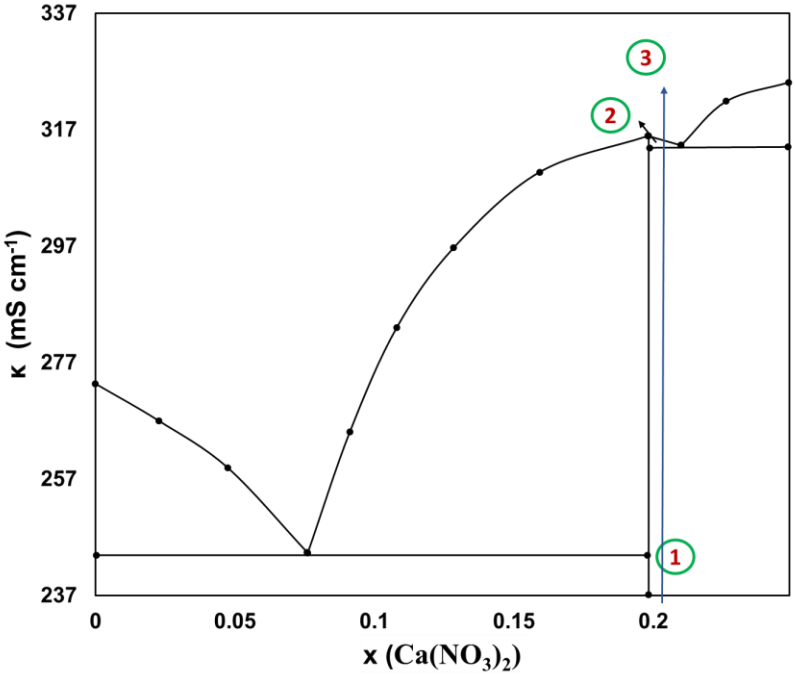

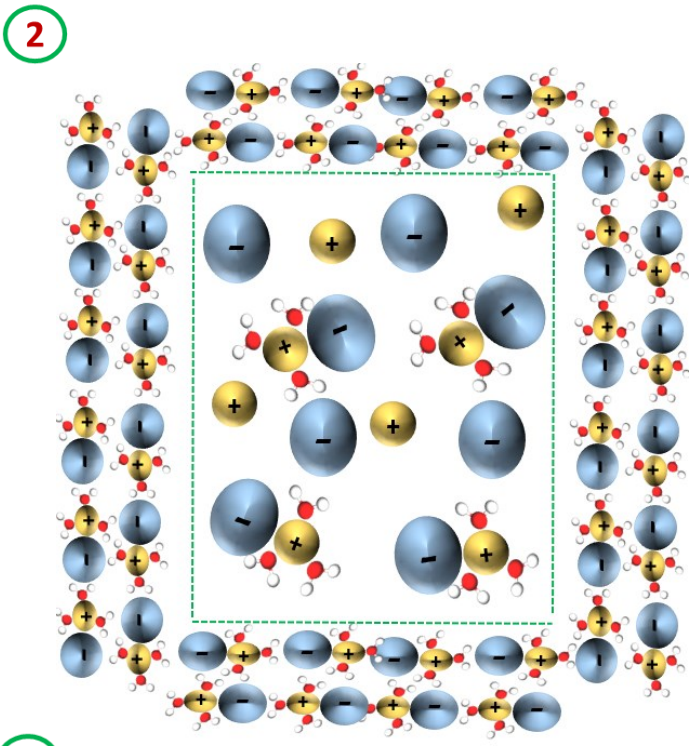

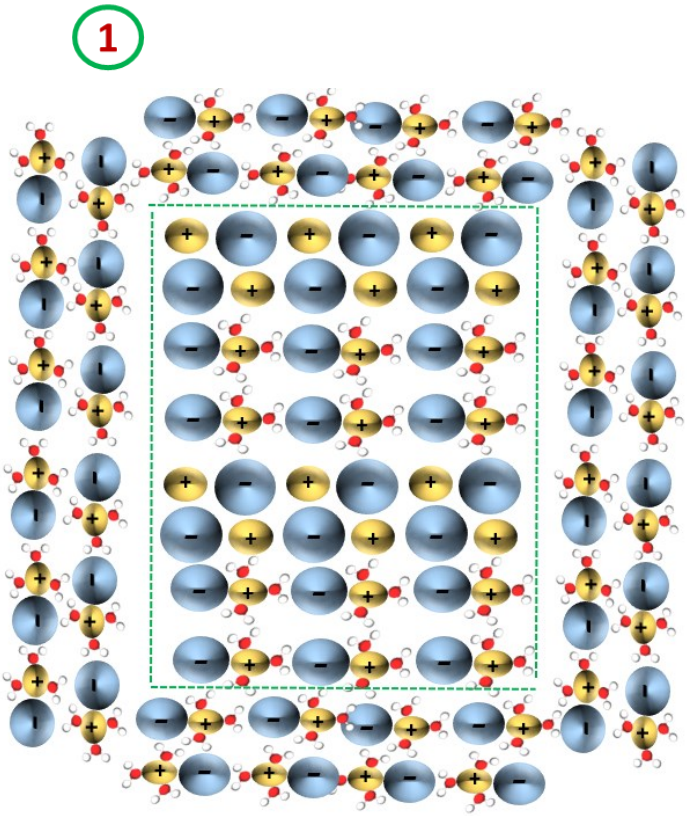

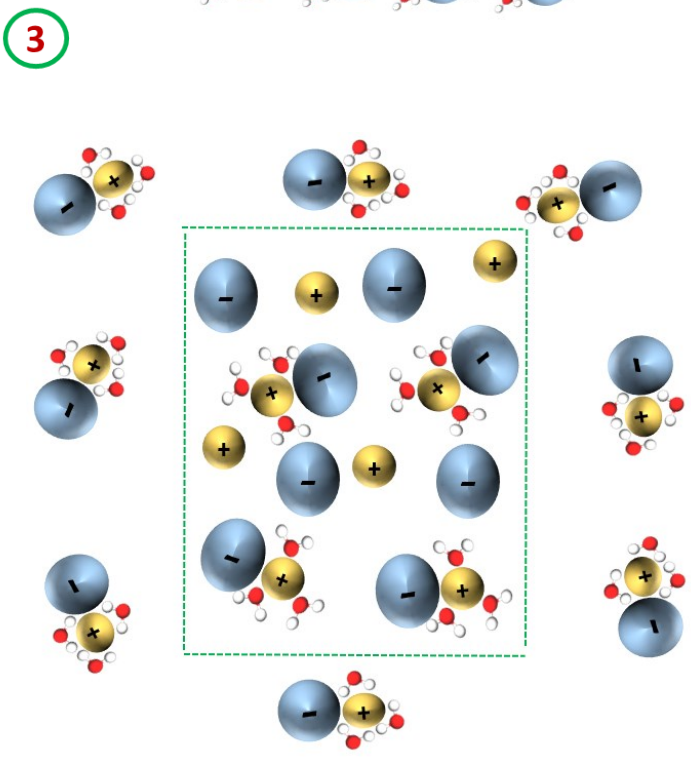

g. $x > x_{e2}$

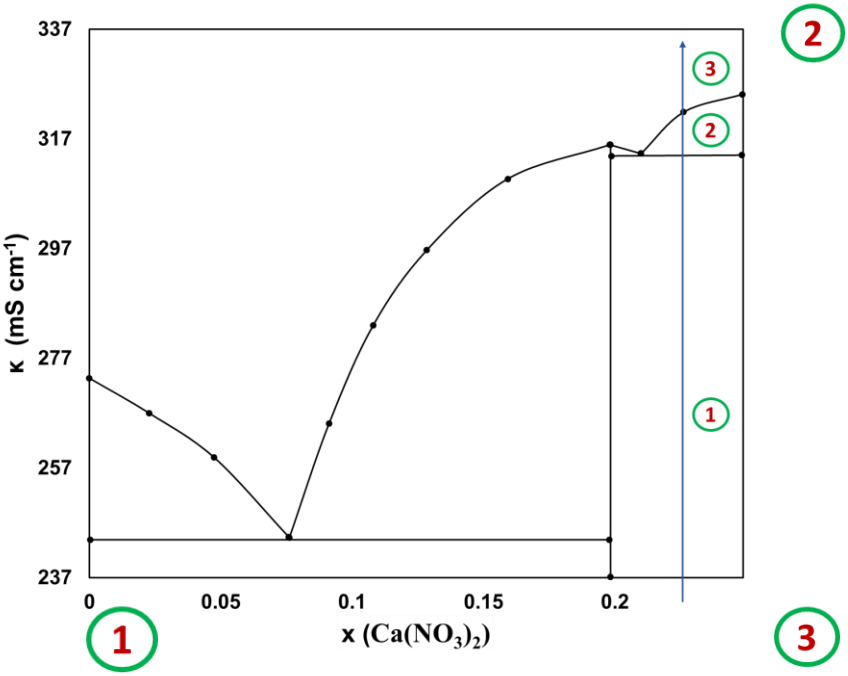

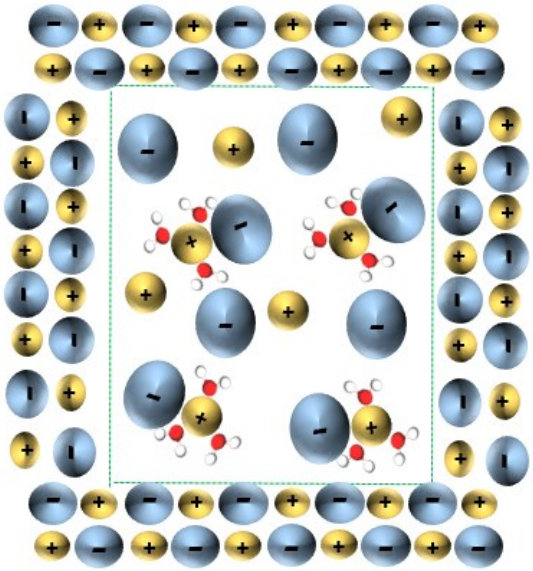

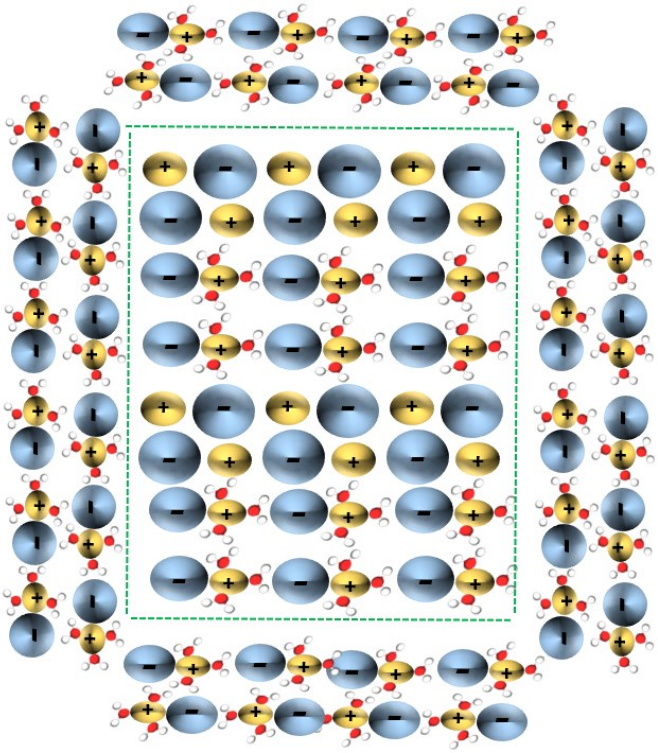

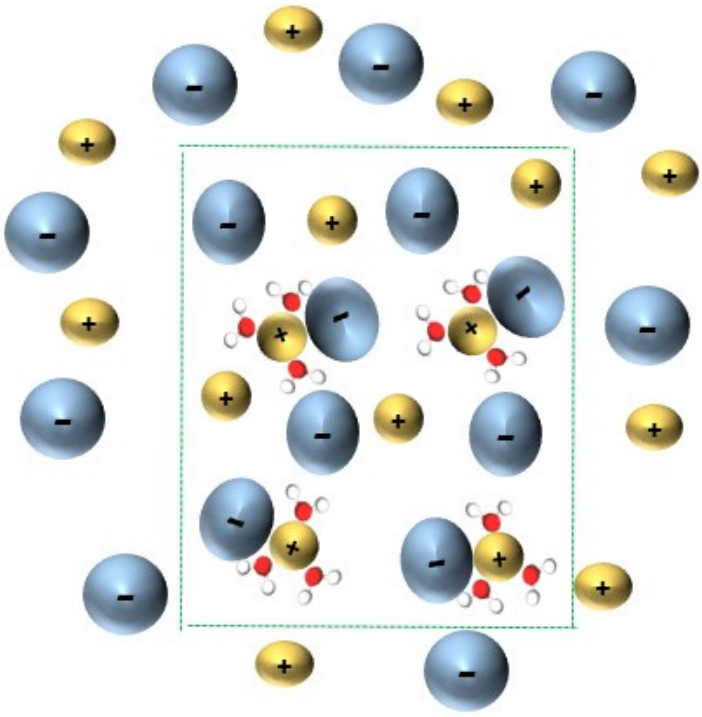

Appendix B: Composite Cathodes for Solid-State Lithium Batteries: “Catholytes” the Underrated Giants

Adapted from: H. Al-Salih, M.S.E. Houache, E.A. Baranova, Y. Abu-Lebdeh, advanced energy and sustainability research 2200032. 10.

Abstract

To expedite the large-scale adoption of electric vehicles (EVs), increasing the gravimetric energy density of batteries to at least 250 Wh kg^{-1} while sustaining a maximum cost of \$120 kWh^{-1} is of utmost importance. Solid-state lithium batteries are widely accepted as a promising candidate for application in the next generation of electric vehicles (EVs) as they promise safer and higher energy density batteries. Nonetheless, their development has been impeded by many challenges, including the resistive electrode-electrolyte interface originating from the removal of the liquid electrolyte that normally permeates through the porous cathode and insures efficient ionic conductivity through the cell. One way to tackle this challenge is by formulating composite cathodes that employ solid state ionic conductors as ‘catholytes’ in their structure. Herein, we attempt to shed light on this less studied and poorly understood approach. We present the different classes of catholytes that have been reported in literature alongside the most common fabrication techniques used to prepare composite cathodes. Next, the interplay between the microstructure and design parameters of composite cathodes with the electrochemical performance of SSBs and the techniques used to measure their transport properties are well documented. Finally, general guidelines surrounding composite cathode research are outlined.

Key words: Catholytes, Composite cathodes, Solid-state batteries, Solid-state electrolytes, composite solid electrolytes, Lithium metal batteries

Introduction

The growing need for long-lasting, high-power portable devices, as well as the widespread use of electric vehicles (EVs) and renewable energy storage, necessitate safe, lower-cost, higher-energy density batteries with improved cycle life to ensure the future global demands are well met.[1,2] Recent reviews have summarized progress in the developments of high-energy Li-ion cells, as shown in Figure B.1. Lithium ion batteries (LIBs) now on the market use liquid electrolytes (LEs), that are inexpensive, simple to make, and guarantee optimal electrode wetting, facilitating ionic pathways throughout the battery which minimizes internal resistance.[3] Using high potential cathode materials (> 4.5 V vs Li+/Li) in cells with LEs to achieve higher energy density may result in undesired reactions, despite the use of additives, compromising the stability and operational life.[4] Furthermore, attempting to reduce the thickness of the separator below 10 µm can result in safety issues, such as with the recent Samsung Galaxy smartphone problems.[2,5] Other limitations of LEs include the difficulty of designing flexible cells, the risk of leakage and flammability, the risk of short-circuiting due to dendrite penetration, constrained thermal stability, as well as low Li+ transference number (t_{Li+}, i.e. the fraction of Li+ ion conductivity relative to overall ionic conductivity) which leads to cell polarization.[2]

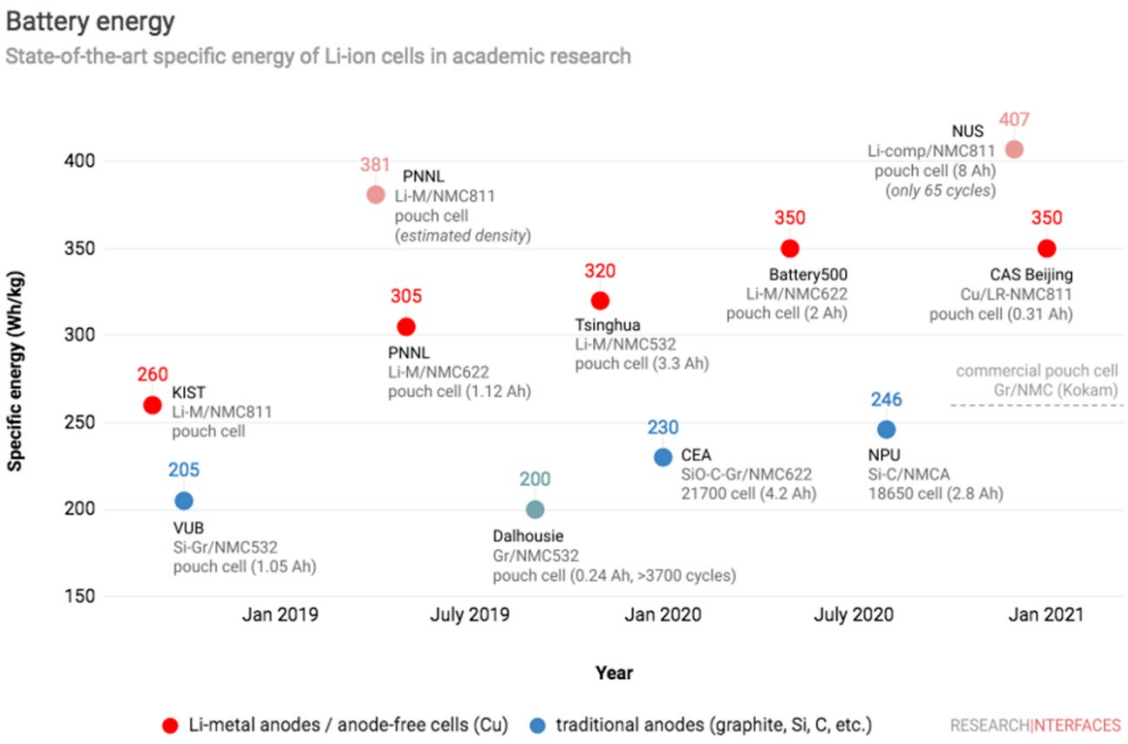

Figure B.1. Trends in Specific Energy for Advanced Batteries. Reproduced with permission.[6] 2022, Research Interfaces.

Numerous intriguing benefits arise by switching to a solid-state system.[7] First, by avoiding the use of flammable organic LEs, a solid-state system promises to eliminate most safety problems. Second, by blocking Li dendrites on one side, Solid-state electrolytes (SSEs) can potentially be effective in preventing short-circuits. Third, some Solid-state batteries (SSBs) can be twisted, punched, or even pierced without posing a safety danger. Finally, stable SSEs may allow for a broader electrochemical window, allowing for the adoption of higher voltage cathode materials. It is worth mentioning that a recent study found that the standard Li/solid electrolyte/inert metal cell test overestimates the electrochemical stability window of most inorganic solid electrolytes.[8] Overall, SSBs are anticipated to have a long cycle life, excellent reversibility, a larger operating temperature range, and other favorable characteristics. If the use of solid electrolytes is to be scaled up, four specific criteria must be met:[9–12] (i) High ionic conductivity $\sigma > 10^{-4}$ S cm^{-1}, (ii) Sufficient strength and minimum defects to prevent Li dendrite penetration, (iii) Inexpensive raw materials and (iv) Low activation energy for Li+ diffusion.

SSEs can generally be divided into two major classes: solid polymer electrolytes (SPEs), and Inorganic solid-state electrolytes (ISEs). Currently, the only large-scale SSBs on the market contain SPEs, namely the poly (ethylene oxide) (PEO)-based electrolyte is in the Bolloré Blue car's lithium metal batteries (LMB) manufactured by Blue solutions.[13] In SPEs, The Li+ ions hop from one void to another that are created during local rearrangements of polymer chain segments, resulting in ionic conduction. Polymers can have both amorphous and crystalline domains, and the predominant conduction mechanism is usually attributed to segmental motion in the amorphous regions, while there have been occasional reports of $LiXF_6$-PEO systems (X = Sb, As, P) with relatively significant crystalline phase conductivity.[14] Low room temperature (RT) (below 10^{-4} S cm^{-1}) and low oxidative degradation potential (below 4 V versus Li^+/Li) are the main limitations of SPEs, particularly PEO-based SPEs, restricting their use in high voltage cathodes.[2,15] In the case of the Blue solutions' cells the compatible lower voltage (3.4 V) $LiFePO_4$ is used. On the other hand, SPEs are often less expensive, lighter, more flexible, non-flammable, and have better lithium metal compatibility than LEs, allowing them to be used in LMBs.[16]

ISEs are crystalline, glassy, or glassy ceramic materials that possess excellent transport properties, such as t_{Li+} approaching 1 and high bulk ionic conductivity which have earned them

the moniker superionic conductors (for example, in the case of thio-LISICON type $Li_{9.54}Si_{1.74}P_{1.44}S_{11.7}Cl_{0.3}$, LSPSC, RT σ = 25 mS cm^{-1}).[17,18] Ions moving through a crystalline ISE must circumvent bottleneck sites, which are energy barriers between local minima along the diffusion paths. Diffusion channels having a low migration barrier and a high number of crystallographic sites over which the migrating ions can be spread are essential for triggering superionic conductivity. The former properties are linked to the anion sub-lattice, and it has been demonstrated that the body-centered cubic (bcc) anion packing provides the most favorable energy landscape with the lowest Li+ migration barrier (0.2 eV).[18] Glassy ISEs are made by rapidly quenching glass-forming melts with high ionic conductivity and low Li+ ion conduction activation energy. The structure of glasses is dependent on the structure of the corresponding melts, and the ionic conductivity of glassy SIEs is usually higher than that of crystals. To increase the ionic conductivity of glassy SIEs, network modifiers and lithium salts, as well as a mixture of glass formers with various anions, have been tested as promising solutions. The partial crystallization of super Li+ ion conductive crystalline phases from precursor glasses can be used to develop highly conductive glass ceramic materials.[19] Sulfide and oxide compounds are the most investigated ISEs. Some of them, such the thio-LISICON type $Li_{10}GeP_2S_{12}$ (LGPS, RT σ = 1.2 $\times 10^{-2}$ S cm^{-1}), contain costly non-abundant elements like Ge, making large-scale adoption very challenging. LGPS's incompatibility with Li metal is also due to the presence of Ge. Those containing Ti^{4+}, such as perovskite-type $Li_{3x}La_{2/3-x}TiO_3$ (LLTO, RT σ ≈ 10^{-3} S cm^{-1}) and NASICON-type $Li_{1+x}Al_xTi_{2x}$ $(PO4)_3$ (LATP, RT σ ≈ 10^{-3} S cm^{-1}), can be reduced at the contact with metallic Li, becoming good electronic conductors that causes rapid cell degradation and eventual short circuit of the cells. Sulfides are often particularly sensitive to moisture, resulting in the formation of H_2S, necessitating costly processing in an inert atmosphere. Sulfides also have a modest oxidative degradation potential (around 3 V vs. Li+/Li).[2,18,20,21]

Composite polymer electrolytes (CPEs) with ISEs as fillers have received a lot of attention in recent years as a way to utilize the superior transport characteristics of inorganic Li^+ conductors while simplifying the preparation process, improving the interfacial contact with the electrodes, and buffering mechanical stress during cycling. Conductive ISE fillers (sometimes known as '*active*' fillers) in SPEs significantly impact the ion transport mechanism in polymers, in ways that are currently not fully comprehended. The size, volume fraction, shape, and orientation of the conductive filler all influence the creation of a percolation network in the inorganic phase. In CPEs, the organic/inorganic interface has a significant impact on overall ionic conductivity. In addition, Lewis acid-base interactions between the organic and

inorganic phases can also alter charge carrier mobility and salt dissociation which is also observed in CPEs containing inert non-conductive particles such as SiO_2 and Al_2O_3 (sometimes known as '*passive*' fillers). The resistance to charge transfer across the two phases in CPEs with conductive inorganic fillers is influenced by multiple factors, including Li^+ solvation energy and the difference in Li^+ concentration and transference number in the two phases.[13,16,22] Recently, there have been a number of excellent extensive reviews of solid electrolytes for all-solid-state lithium batteries (ASSLBs).[13,23–27]

Despite the rapid development of solid electrolytes, the high interfacial resistance generated by inadequate contact and interfacial reactions is a substantial impediment to the adaptation of ASSLBs as illustrated in Figure B.2. It is difficult to achieve sufficient contact between a SSE and an electrode without a permeable liquid. In addition, the mechanical particle-to-particle contact is further deteriorated by the periodic electrode shrinking and expanding during cycling.[28] As a result, high polarization and low active material utilization are prominent in solid state lithium batteries. It is concluded from the preceding discussion that the key to realizing competitive ASSLBs is the establishment of decent stable contact between the SSE and the electrodes especially at the cathode/SSE interface where the interfacial impedance determines the rate capability and cycling stability of ASSLBs. The establishment of a good continuous ionic conduction path through the solid interface between the cathode and the electrolyte, as well as the reduction of strain/stress at the interface attributable to volume change during lithiation/delithiation, are both critical. To achieve this objective, several interfacial modification techniques have been visited such as using composite cathodes (CCs),[29–33] cathode coating,[29,34–37] Bi-layer electrolyte construction,[38,39] intermediate coating,[40,41] and thermal annealing.[42–44]

Here in this review, we will focus on the first technique which is the utilization of composite cathodes. Typically, composite cathodes are made by mixing the active material (AM), SSE as binder (also known as '*catholyte*'), and an electronically conductive additive. The first section will discuss the choice of catholytes and how the fraction of catholytes in composite cathodes enhance the overall cell performance. This is followed by Table 1 which summarizes the relevant work that has been done in literature so far followed by a discussion of the different fabrication techniques. Next, the microstructure of composite cathodes is explained alongside the design parameters influencing it such as catholyte content, particle dimension, voids, and tortuosity. The different techniques used to characterize the ionic and electronic conductivity (σ_i and $\sigma_{e)}$ are also presented and analyzed. Finally, the major obstacles

and challenges in the pursuit of optimized composite cathodes for SSB are documented together with the recommended guidelines to overcome them.

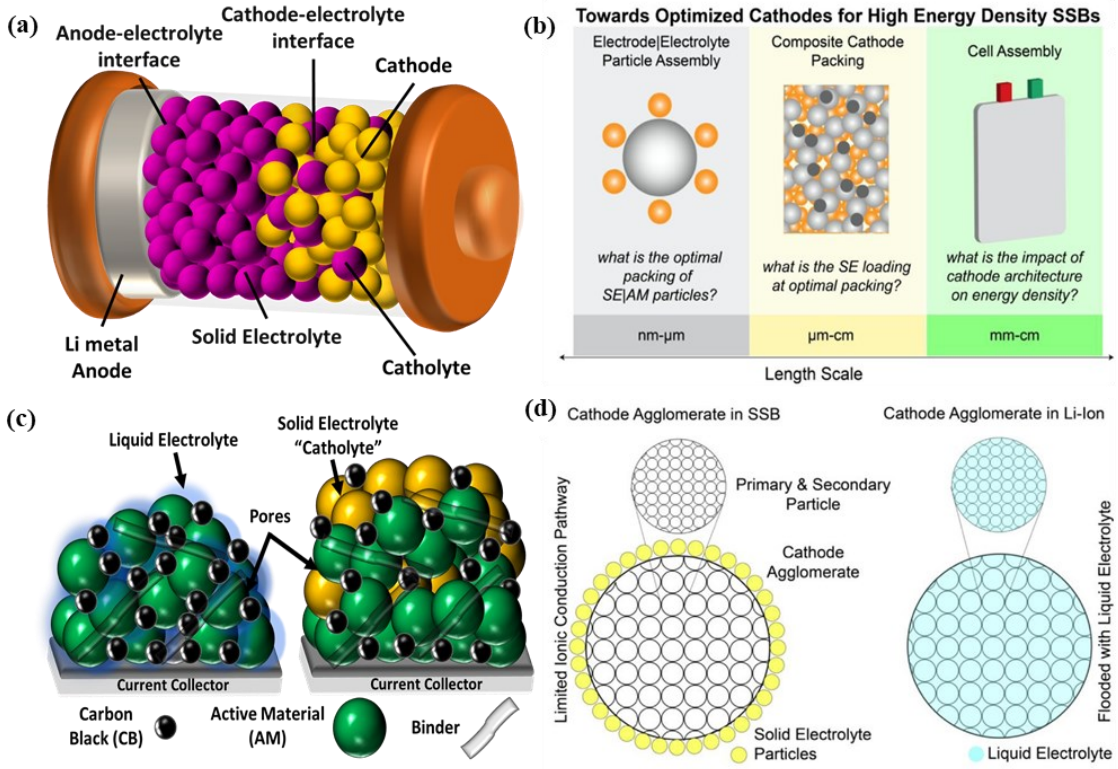

Figure B.2. a) Schematic of different interfaces in solid state batteries. b) Hierarchy of energy density model investigated. c) Schematic of conventional and composite cathodes microstructure .d) Cathode agglomerate and ion transport mechanism in cathode for SSB and conventional Li-ion battery. Reproduced with permission.[45] 2022, Copyright Energy Storage Materials.

Electrode design: Composite cathode formulation and preparation techniques

Formulation

The cathode in conventional LE based LIBs is a combination of AM particles, carbon particles, and an inert polymer binder where the LE in those batteries flows into the pores of this structure. In SSBs on the other hand, the LE is now replaced by a catholyte in an all-solid composite cathode, which functions as both a binder material for mechanical support and an electrolyte for ion transport. A mixture of catholyte and carbon particles is now sandwiched between the AMPs, ideally providing continuous electronic and ionic conduction channels. The inclusion of a SSE within the electrode, in particular, results in different heterogeneous

SSE/solid interfaces with the AMP, carbon particles, and metal current collector. Therefore, controlling the interfacial resistance at this additional inter-particle interface is essential to the overall ionic transport of the SSB.[1,46]

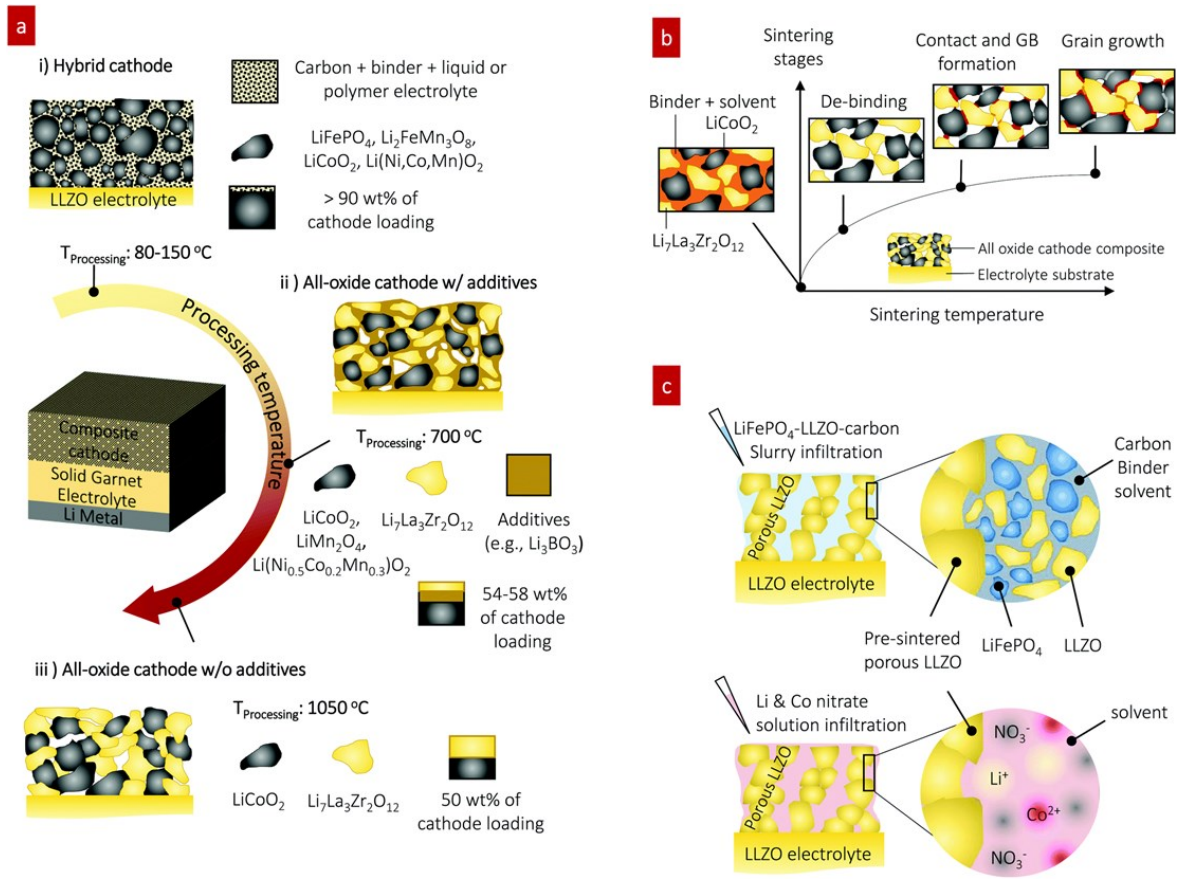

Figure B.3. Preparation of cathode composites for Li-garnet SSBs. a) Overview of the cathode composite processing, temperature, and components for each choice of design. b) Evolution of the microstructure and interface formation during conventional solid-state sintering as exemplified by the $LiCoO_2$–LLZO composite cathode. c) Preparation of the cathode composite used in this study. Reproduced with permission.[47] 2022, Energy & Environmental Science.

Notably, the majority of past decade literature publications surrounding lithium metal SSBs involve the use of composite cathodes to enable the electrochemical cycling of lab-scale coin and pouch cells. Table 1. Provides a comprehensive summary of the reported cell chemistry, type of composite cathode used and summary of their respective cycling conditions and electrochemical performances. ***The first common strategy*** when formulating a composite cathode is to use a catholyte that is made from the SSE components. In fact the only commercial SSB from Blue Solutions utilizes a catholyte of the same composition as the PEO:LiTFSI

electrolyte.[33,48–51] Passerini et al. reported on a Li/SPE/LFP SSB that achieved ~ 100% capacity retention after 100 cycles at 0.1 C. The composite cathode they used had the following formula 43% LFP, 50% SPE (PEO-LiTFSI-PYR_{14}LiTFSI) as an ionic conductor and mechanical binder, and 7% electronically conductive carbon.[50] PEO-LiTFSI-LLZO polymer-ceramic composite was also used as catholyte in Li/PEO-LiTFSI-LLZO/LFP reporting a peak specific discharge capacity of 137 mAh g^{-1} at 0.2C. Noticeably, the initial specific discharge capacity was only 94 mAh g^{-1} and it took 21 charge/discharge cycles to achieve the peak specific discharge capacity.[33] This behavior is observed in some other SSBs as well and it indicates that the cell requires a long time to achieve complete interlayer homogenization and full AMP activation.[52] One way to alleviate this phenomena was reported by López-Aranguren et al. and it involved a proprietary conditioning step prior to cycling by heating to 70 °C for 24 h.[51]

A second common strategy in composite cathode formulation is by using semi-crystalline polymer electrolytes as catholyte even when the SSE is composed of a polymer-ceramic composite. This is due to the fact that these polymers are more effective as binders than ceramics.[52–59] Zhang et al. reported on a highly performing Li/PEO-LLZTO-SN/LFP SSB that has the following composite cathode: 70% LFP 10% super P 15% PEO-LiTFSI 5% SN. Their assembled SSB achieved initial specific discharge capacity of 151.1 mAh g^{-1} at 0.5 C and 60 °C and retained 98% of its initial capacity after 200 cycles.[58] Furthermore, Succinonitrile (SN) which is a common polymer plasticizer has also proved effective as an ionic conductor in composite cathodes but cannot be used on its own as a binder as it does not provide mechanical stability. Thus, it is sometimes coupled with the conventional PVDF binder.[31,57,60] Li/SN-LLZNO/LFP with 35.7% SN content in the composite cathode formula were reported to achieve specific discharge capacity of 149.8 mAh g^{-1} and 99% capacity retention after 100 cycles at 0.05 C and room temperature conditions.

Another less common strategy is to develop all-ceramic oxide composite cathodes which are usually coupled with ceramic SSEs. The main advantage these cathodes hold over the aforementioned cathodes is increased safety as they are more capable of preventing thermal runaways by avoiding the use of any flammable organics.[61] However, recent data suggest that high active material loading is difficult to obtain (loading obtained ranges 50 – 58 wt. %), which complicates the realisation of high energy density batteries made with these type of cathodes.[47,62–67] Moreover, controlling the interfacial resistance within these cathodes' microstructure becomes tricky due to the poor binding properties of ceramics. Kim et al. have

summarized the different composite cathodes formulation and preparation techniques for application with Li-garnet electrolyte SSBs, as illustrated in Figure B.3 (a).[47]

Table B.5: Cell characteristics and electrochemical performance of SSBs utilizing composite cathodes reported in reviewed literature

Cell Configuration	CC formula	Discharge capacity/ cycle retention	T (°C)	Loading	Notes	Ref
Li/PEO-LiTFSI-LLZO/NMC622	75% NMC 622 5% C65 20% PEO-LiTFSI-LLZO	150 mAh g-1 (0.05C)	55	1.6 mAh cm^{-2}	-	[51]
Li/PEO-LiTFSI-SN-LLTO/NMC 532	70% NMC 532 15% PEO:LiTFSI 10% C65 5% PVDF	143.2 mAh g^{-1} (0.05C) - 98.8% (30^{th} cycle)	55	-	Peak specific discharge capacity is achieved after several cycles	[52]
Li/PVDF-LiTFSI/LFP + IC3	55%-70% LFP: super P: carbon black: PVDF-LiTFSI (8:1:1:0.5) 30%-45% IC3 (see notes)	157.7 mAh g^{-1} (0.05C) – 92.9% (160 cycles)	30	6.05 mg cm^{-2}	IC3: gel-like ionic conductor made of 20:1 molar ratio of SN-$LiClO_4$. IC3 was injected into the cathode sheet and fully covered the surface	[68]
Li/PVDF-LiTFSI/LCO + IC3	55%-70% LCO: super P: carbon black: PVDF-LiTFSI (8:1:1:0.5) 30%-45% IC3 (see notes	137 mAh g^{-1} (0.03C) – 92.6% (29 cycles)		12.0 mg cm^{-2}		
Li/SPE/NMC	43% NMC 50% PEO-LiTFSI-PYR_{14}TFSI 7% KJB	157 mAh g^{-1} (0.05C) – 66% (100^{th} cycle – 0.1C)	40	3-4 mg cm^{-2}	SPE = photo crosslinked PEO-LiTFSI-PYR_{14}TFSI KJ = ketjen black conductive carbon	[50]
Li/SPE/LFP	43% LFP 50% PEO-LiTFSI-PYR_{14}TFSI 7% KJB	161 mAh (0.05C) – 100 % (100^{th} cycle – 0.1C)		4-5 mg cm^{-2}		
Li/PEO-LiTFSI-LLZO/LFP	70.2% LFP 5.8% C65 24% PEO-LiTFSI-LLZO	144 mAh g^{-1} (0.1C) 140 mAh g^{-1} (0.2C)	70	1 mAh cm^{-2}	Peak specific discharge capacity is achieved after several cycles	[33]
Li/PEO-LLZTO/LFP	80% LFP 10% PVDF:SN:$LiClO_4$ 10% super P	153.3 mAh g^{-1} (0.05C) – 90% (200^{th} cycle)	60	1.46 mAh cm^{-2}	-	[69]
Li/SN-LLZNO/LFP	47.6% LFP 35.7% SN-LiTFSI 9.5% KJB 7.1% PVDF	149.8 mAh g^{-1} (0.05C) – 99% (100^{th} cycle)	RT	-	-	[31]
Li/PLLS15/LFP	LFPLS: 80% LFP:(PEO:LiTFSI):Super P (8:1:1) 10% Al-LLZO 10% SN	130 mAh g^{-1} (20 mA g^{-1}) – 89% (200 cycles)	25	1-2 mg cm^{-2}	PLLS15: 77.5% PEO:LiTFSI 7.5% Al-LLZO 15% SN	[70]
Li/PEO-LiTFSI/LFP	63% LFP 7% C65 30% SI-PPO-PEO-LiTFSI	168 mAh g^{-1} (0.1C) – 92% (100th cycle)	70	2.8 mg cm^{-2}	SI = Jeffamine-Succinimide	[71]
		141 mAh g^{-1} (0.1C) – 92% (140^{th} cycle)		4.9 mg cm^{-2}		
Li/PVDF-$LiClO_4$-LLZTO/LCO	80% LFP 10% super P 10% PVDF-LiTFSI + PEO/LiTFSI/EC (see notes)	150 mAh g^{-1} (0.1C) – 98% (120th cycle)	25	1.9 mg cm^{-2}	The prepared composite cathode was infilterated with homogeneous polymer electrolyte solution of PEO/LiTFSI/EC by syringe-dispensing method	[53]

Li/LAGP-PEO-LiTFSI /LFP	55% LFP 10% super P 35% PEO-$LiClO_4$	137.6 mAh g^{-1} (0.2 C) – 91.3% (100^{th} cycle)	55	3.6 mg cm^{-2}	-	[72]
Li/PEG-LiTFSI/LFP	60% LFP 20% Acetylene black 5% PVDF 15% PEG-$LiClO_4$	138 mAh g^{-1} (1C) – 91% (300^{th} cycle)	60	-	-	[73]
Li/PEO-LLZTO-SN/LFP	70% LFP 10% super P 15% PEO-LiTFSI 5% SN	151.1 mAh g^{-1} (0.5C) – 98% (200^{th} cycle)	60	-	-	[58]
Li/PEO-LiTFSI+LLZO nanowires/LFP	80% LFP 10% PEO-LiTFSI 10% carbon black	162.9 mAh g^{-1} (0.1C) – 97.4% (80^{th} cycle)	45	1.68 mg cm^{-2}	-	[59]
Li/PEO-LiTFSI-LLZO/LFP	70% LFP 20% super P 5% PEO-LiTFSI-LLZO	150.1 mAh g^{-1} (0.5C) – 93.2% (50^{th} cycle)	60	-	-	[74]
Li/PEO-LiTFSI-LLZO-SN/LFP	70% LFP 10% super P 15% LiTFSI 5% SN	135 mAh g^{-1} (1C) – 80% (500^{th} cycle)	60	3.5 – 4 mg cm^{-2}	-	[56]
Li/PEO-LiTFSI-LLZO-SN/LCO	70% LFP 10% super P 15% LiTFSI 5% SN	136 mAh g^{-1} (0.2C) – 96.3% (50^{th} cycle)	60		-	
Li/P(VDF-HFP)-LiTFSI-LLZTO/NMC 532	84% NMC 532 5% PVDF 5% super P 5% SN 1% LiTFSI	146.9 mAh g^{-1} (0.1C) – 86.9% (150^{th} cycle)	25	10.5 mg cm^{-2}	-	[57]
Li/PTEC-LiTFSI/LFP	80% LFP 10% super P 6.7% PTEC 3.3% P(VDF-HFP)	120.6 mAh g^{-1} (0.2C) – 100% (100^{th} cycle)	55	1.3-1.8 mAh g^{-1}	-	[75]
Li/PTEC-LiTFSI/LFMP	80% LFP 10% super P 6.7% PTEC 3.3% P(VDF-HFP)	105.1 mAh g^{-1} (0.2C) – 100% (100^{th} cycle)	55		-	
Li/PEO@GF/VL-LFP		145 mAh g^{-1} (0.1C) – 87.5% (50^{th} cycle)	80	10.5 mg cm^{-2}	PEO@GF: polymer electrolyte impregnated into a glassfiber (GF) scaffold by solution infiltration VL-LFP: Vertically aligned LFP fabricated by an ice-template freeze casting method	[76]
Li/PEO-$LiCF_3SO_3$-SiO_2/LFP	60% LFP 15% super P 25% PEO	140 mAh g^{-1} (0.2 mA cm^{-2}) – 60% (100^{th} cycle)	100	7 mg cm^{-2}	CC is solvent free: Prepared by dry blending followed by hot pressing and cold calendaring	[77]
Li/PVCA-LiDFOB/LCO	80% LCO 10% PVCA 10% acetylene black	146 mAh g^{-1} (0.1C) – 84% (150^{th} cycle)	50	1.5 mg cm^{-2}	Polymer electrolyte was in situ polymerized on Li. CC was solution casted on PVCA-LiDFOB/Li	[78]

Li/PEO-LiTFSI/PMA-LiTFSI/LCO	70.4% LCO 14.5% PMA 7% LiTFSI 8.5% carbon black	119 mAh g^{-1} (0.2C) – 91% (100^{th} cycle)	65	5 mg cm^{-2}	Double layer electrolyte	[79]
Li/LAGP/LFP	LFP/PEO-$LiClO_4$/super P (exact wt. % not reported)	158.4 mAh g^{-1} (0.1C) – 1.6% (200^{th} cycle)	60	-	CC was coated on LAGP pellet	[80]
Li/PEO-LPOS-LAGP/LFP		153.4 mAh g^{-1} (0.1C) – 99.9% (200^{th} cycle)				
Li/LSPC/LCO	89% - (97% LCO 1% PVDF 2% super P) 11% - Infiltrated LPSCl	141 mAh g^{-1} (0.5C) – 89% (50^{th} cycle)	30	10 mg cm^{-2}	LPSCl/EtOH solid state solution was infiltrated in LCO cathode	[81]
Li/LPS/NMC	76.2% NMC 19.0% LPS 1.9% Acetylene black 2.9% PPC	149 mAh g^{-1} (0.15 mA cm^{-2}) – 84% (175^{th} cycle)	30	-	-	[82]
Li/PEO-LiTFSI-LLZO/LFP	76% LFP 16% PEO-LiTFSI 8% ITO	160 mAh g^{-1} (0.1 mA cm^{-2}) – 100% (10^{th} cycle)	60	10.8 mAh cm^{-2}	ITO: indium tin oxide	[54]
Li/PEO-LiTFSI-SN-LGPS/LFP	70% LFP 20% super P 10% PEO-$LiClO_4$	160.6 mAh g^{-1} (0.1C) – 94.7% (60^{th} cycle)	40	-	-	[83]
Li/PEO-$LiClO_4$-SN-LAGP/LFP	50% LFP 10% super P 40% PEO-$LiClO_4$-SN	136.8 mAh g^{-1} (0.2C)	25	8 mg cm^{-2}	Capacity retention is not reported in numbers	[55]
Li/PEO-$LiClO_4$-LLZO/NMC 622	56% NMC 622 5% super P 39% PEO-$LiClO_4$-LLZO	166 mAh g^{-1} (0.02C)	55	2 mg cm^{-2}	Capacity retention is not reported in numbers	[49]
LTO/PPC-LiTFSI-LLZO/LFP	80% LFP 10% super P 10% PPC-LiTFSI-LLZO	123 mAh g^{-1} (0.1C) – 83.1% (80^{th} cycle)	RT	-	LTO was used as anode in this lithium metal free flexible solid state battery	[48]
Li/PEO-LiTFSI-LAGP/LFP	70% LFP 10% super P 10% PEO-LiTFSI-LAGP	166 mAh g^{-1} (0.1C) – 90% (50^{th} cycle)	60	-	-	[84]
Li/PVDF-LiFSI/LCO	75% LCO 11% PEO 10% super P 4% LiTFSI	141 mAh g^{-1} (0.15mA cm^{-2}) – 100% (200^{th} cycle)	25	2.8 mg cm^{-2}	-	[85]
Li/PI-LLZTO-PVDF/NMC 532	81.1% NMC 532 4% PVDF 6.75% super P 6.75% SN 1.4% LiTFSI	152.6 mAh g^{-1} (0.1C) – 94.9% (80^{th} cycle)	RT	9-10 mg cm^{-2}	-	[60]

Composite cathodes preparation techniques

Composite cathodes can be fabricated using a range of different techniques as researchers are not yet bound by an optimized technique that work for all kinds of battery chemistry. In fact, frequent improvisation of preparation techniques is not a surprise in this field. Nonetheless, some techniques are more often applied than others. One such example is ***solvent casting*** which is the same technique used to obtain PVDF-based cathodes for LIBs. It simply involves dissolving the AM particles, the catholyte, and the conductive carbon additive in the appropriate solvent followed by casting the resulting slurry on the current collector. The main drawback of this technique is the difficulty in drying the final traces of solvent which if present, could cause interfacial stability and unwanted reactivity with the lithium salt of the catholyte salt.[1,13]

Extrusion is a well-established and widely used method for obtaining composites for a wide range of applications; thus, it could be an appealing method for obtaining composite electrodes from an industrial standpoint. Appetecchi et al. produced and characterized PEO-based CEs using a dry, solvent-free method that involved hot extrusion of powder mixtures followed by roll mill calendaring. The obtained cathode films were between 100 and 180 μm thick. Prior to processing, all of the composite cathode's components were dried and sieved to remove or breakup macro-aggregates into smaller powder granules, including PEO, $LiCF_3SO_3$, super P conductive carbon, and $LiMn_2O_4$ (LMO). Finally, they were ball milled for at least 12 hours to gently blend them in the proper proportions. The electrodes made with this technique were thoroughly characterized using a range of techniques (e.g., TGA, DMTA, density, and porosity studies), and their composition was optimized based on their ionic and electronic conductivity obtained by EIS analysis. [1,86]

Another interesting preparation technique involves the ***infiltration*** of solution-processable SSE into conventional LIB cathodes. This is done by dipping the cathodes into the SE solution followed by drying in Argon environment. The SE-infiltrated composite cathodes are then vacuum dried at 180 °C. Finally they are cold pressed under 770 MPa.[81] A similar fabrication technique involved the injection of a gel ionic conductor into the voids of conventional PVDF based cathodes. Xin et al. managed to establish a stable cathode/electrolyte interface by injecting an ionic conductor gel into the cathode sheet at 80 °C and letting it cool down. The fraction of the ionic conductor in the obtained sheet ranged from 30 – 45 wt. %. The gel was termed '*IC3*'and is made by mechanically stirring LiTFSI powders into molten SN for 12 h at 80 °C.

Another utilized technique is ***hot pressing***. For example, NMC and LFP based composite cathodes were prepared by first mixing their AM particles with conductive carbon in a mortar. This was followed by blending this mix into a paste-like slurry made by mixing PEO and LiTFSI powders into $Pyr_{14}TFSI$ ionic liquid. The mixture is then annealed at 100 °C overnight and subsequently hot-pressed at 100 °C for a few minutes. Finally the resulting tape is cooledwn and calendared to obtain the final composite cathode which had an AM mass loading of 3 – 4 mg cm^{-2} for 4 – 5 mg cm^{-2} for LFP and NMC based cathodes respectively.[50] The same technique was also followed to make 7 mg cm^{-2} LFP composite cathode.[77]

As illustrated in Figure B.3 (b) and (c), one method to fabricate all ceramic composite cathodes is by screen printing the composite cathode slurry on a ceramic SSE substrate followed by ***sintering*** at high temperatures (> 1000 °C) to homogenize the solid-solid interfaces. Sintering additives can help lower sintering temperatures and improve the particles interconnection and densification of the cathode and electrolyte interfaces. [47] The addition of lithium borate (LBO) to LCO and NMC based composite cathodes, for example, lowers the sintering temperature from 1050 °C to 700 °C and accelerates densification kinetics.[42,87,88] Nonetheless, the addition of such additives could be detrimental to the cell performance as they increase the volumetric fraction of the "inactive" constituent in the composite cathode. Evidently, the utilization of ceramic components in composite cathodes creates major complications in terms of preparation methods and inter-particle interfacial resistance.

Composite Cathode Microstructure and Transport Properties

Composite cathode microstructure

An electrochemically active material (AM), a binder (typically a non-conducting polymer, such as PVdF), an electronically conductive carbon additive, and interconnecting porosity to allow the LE to permeate the cathode make up the conventional cathodes for currently available LIBs with LEs. Homogeneous electrode porosity is critical for stable battery performance as it promotes faster Li^+ diffusion and mitigates surface solid electrolyte interphase losses through passivation. An ideal electrode chemistry and architecture allows for maximum electrolyte access, facilitates ionic diffusion and charge transfer, provides continuous electron routes through excellent additive dispersion, and allows for volume expansion. Ion conduction in traditional batteries is enabled by LEs wetting porous electrodes, whereas if SSEs are employed, ion conduction is limited to the contact region between the solid electrolyte and the AM particles at the cathode/electrolyte interface. Hence, SSEs must be loaded onto the cathodes to provide continuous ionic pathways and ensure homogeneity in SSB.[89] AM particle size,

adhesion, and voids (related to material characteristics and preparation technique), as well as composition and thickness, all influence the microstructure of composite cathodes in SSBs. These variables affect the residual porosity of composite cathodes in one way or another. The impediment to Li^+ transport caused by the interconnected network of non-conductive phases (pores) is defined as tortuosity (τ) (see Figure B.4). τ is generally anisotropic, resulting in high macroscopic ohmic resistance, which reduces the battery's delivered energy and power density.[1] For LIBs, ionic diffusion within the LE in the porous cathode can be characterized by two properties: porosity ε and tortuosity τ (or κ; the tortuosity factor where $\kappa = \tau^2$). Porosity is defined as the volume fraction available for fluid or, equivalently, the volume fraction not filled by solid matrix while τ elucidate the convoluted and curving path that dissolved ions must take as they travel through the porous volume.[90] The effective ionic diffusion, D_{eff}^{ion}, throughout the complex microstructure can be given by:

$$D_{eff}^{ion} = \frac{\varepsilon}{\tau^2} D_{bulk}^{ion} = \frac{\varepsilon}{\kappa} D_{bulk}^{ion} \quad (1)$$

Where D_{bulk}^{ion} is the material's bulk ionic diffusion.

Despite the fact that SSBs do not contain any fluid and the predominant transport mechanism is ionic migration instead of diffusion, it is popular to apply fluid characteristics to SSB composite cathodes. The Nernst -Einstein equation may be used to link the lithium diffusion coefficient $D_{bulk,SSE}^{ion}$ and the ionic bulk conductivity of the SSE, $\sigma_{bulk,SSE}^{ion}$ on the assumption that interactions between lithium ions and lattice vacancies in the SE can be ignored.[91]

$$D_{bulk,SSE}^{ion} = \frac{\sigma_{bulk,SSE}^{ion} RT}{c_{bulk,SSE}^{ion} F^2} \quad (2)$$

Since conduction pathways in composite cathodes are tortuous as well. The effective ionic conductivity, σ_{eff}^{ion} may vary significantly from σ_{bulk}^{ion} according to the following equation:[92]

$$\sigma_{eff}^{ion} = \frac{\varepsilon_{SE}}{\tau^2} \sigma_{bulk,SSE}^{ion} \quad (3)$$

τ can also be defined geometrically as the shortest path Δl across the microstructure with respect to its length Δx:[93]

$$\tau = \frac{\Delta l}{\Delta x} \quad (4)$$

This tortuosity however, only accounts for the shortest path and overlooks broader but longer paths, which are also used by the ions and have an impact on effective diffusion. Hence, geometrical tortuosity measurements are underestimated when compared to experimental measurements of flux-based simulations.[93]

To practically determine τ for composite cathodes, bulk and effective conductivities could be measured and compared to equation 1.[90,92,94] Alternatively, electrochemical impedance spectroscopy (EIS) could be applied in a symmetrical cell configuration with a non-Li^+ electrolyte salt (Li^+ blocking configuration) to obtain τ information.[95,96] Trembacki et al. were able to calculate τ by means of 3D reconstruction of previously acquired X-ray tomography data.[97] Additionally, focused ion beam scanning electron microscopy (FIB-SEM) could also be used to perform τ calculations.[98]

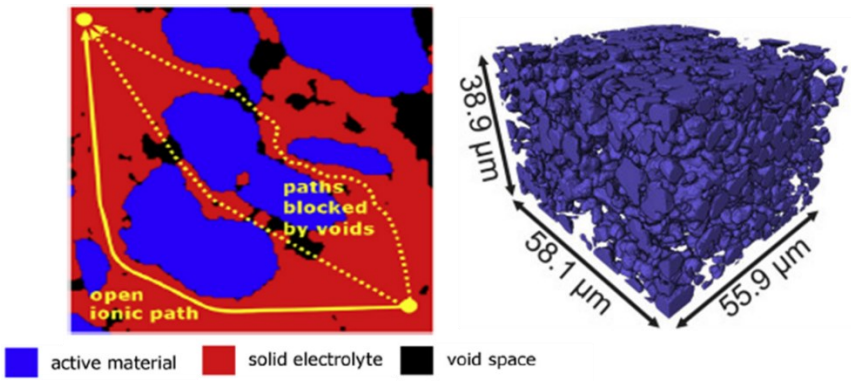

Figure B.4 Reconstruction of a LPS-LCO CE from FIB-SEM tomography. Reproduced with permission.[87] 2022, Journal of Power Sources.

Furthermore, there are only a few articles that report on the effect of changing the cathode composition on the electrochemical performance. Chen et al. studied the effect of varying PEO-LiTFSI catholyte content between 10 – 30 wt. % on the electrochemical performance of Li/PEO-LiTFSI-LLZO/LFP SSB. Batteries assembled with 30 wt. % show almost no capacity during cycling which is attributed to very low electronic conductivity. Reducing the catholyte fraction down to 15 wt. % raised the average discharge capacity to 155 mAh g^{-1} but reducing it further to 10 wt. % significantly decreased the average discharge capacity because of the absence of continuous Li^+ transportation pathways.[54] A similar study was conducted on Li/LGPS/LCO cells and it was found that at least 50 wt. % of LCO AM particles are needed to achieve solid electrochemical performance. Below this threshold, the contact amongst the AM particles is not sufficient to achieve the minimum required σ_e. This was confirmed by means of energy-dispersive X-ray (EDX) mapping and scanning electron microscopy (SEM) of the composite cathodes. Ultimately, it was revealed that ionic percolation pathways are more critical for achieving high rate capability (and thus power density), whereas electronic percolation appears to be the most important feature for high energy ASBs.

Under the test conditions, a 20 wt. % of SE in the composite cathode was sufficient to achieve good specific capacity values at low current densities.[99]

Furthermore, studies on the effect of varying the cathode loading on electrochemical performance of SSBs are seldom. In conventional LIBs, it was found that increasing cathode thickness does increase the overall energy density of the cell but only up to a limit. Exceeding that limit would lead to diminishing returns. For example, Singh et al. systematically studied NMC 333 cathodes with thicknesses varying from 70 -305 μm. The findings reported that NMC 333 cathodes thicker than 155 μm, demonstrated deteriorating cycling stability and higher kinetic energy losses at high C rates when compared to cathodes that are thinner than 155 μm.[100] Likewise, Wen et al. reported on the electrochemical performance of two Li/PVDF-LiTFSI/LFP SSB with the cathode loading of 6.05 mg cm^{-2} and 12.0 mg cm^{-2}. Their initial discharge capacities were found to be 157.7 and 137.0 mAh g-1, respectively, and achieved ~ 93% capacity retention after 160 and 129 cycles, respectively.[68] Similar discrepancy in electrochemical performance was reported for Li/PEO-LiTFSI/LFP cells with 2.8 mg cm^{-2} and 4.9 mg cm^{-2} cathode loading where the cell with lower thickness achieved higher initial specific discharge capacity and higher capacity retention over 100 cycles.[71] Despite the general observed superior electrochemical performance achieved at lower loadings, some articles have reported solid cycling stability with high loading composite cathodes. For instance, Zhang et al. were able to cycle Li/P(VDF-HFP)-LiTFSI-LLZTO/NMC 532 SSB that had a composite cathode loading of 10.5 mg cm^{-2} at room temperature and at a charging rate of 0.1C. The cell reported an initial specific discharge capacity of 146.9 mAh g^{-1} and retained 87% of this capacity after 150 cycles.[57] Li/LSPC/LCO cells with similar composite cathode loading were also reported to cycle at an even higher 0.5C rate reporting an initial specific discharge capacity of 141 mAh g^{-1} and a capacity retention of 89% after 50 cycles.[81]

The effect of AM particle size on cell performance was also investigated in a study done by Strauss et al. on composite cathodes made of NMC 622 and LPS ceramic SSE as the catholyte. The activity of the AM particles were studied using a combination of galvanostatic cycling and ex-situ XRD measurements on the cathode after they underwent charging. The wt. % of inactive AM particles was found to range from 2% (for smaller particles 4-5 ≈ μm) to 31% (larger particles 20 ≈ μm). Due to a lack of sufficient interconnection between large particles, conductivity tests show that σ_e is substantially influenced by particle size, declining by three orders of magnitude going from smaller to larger particles.[1,101] Polymer catholytes have significant advantages to ceramic catholytes in this regard, owing to their better adherence to the AM particles and this is demonstrated by the fact that the aforementioned composite cathode

prepared by hot extrusion which uses PEO-$LiCF_3SO_3$ catholyte reports negligible porosity in spite of the high catholyte weight content of 30 – 35 wt. %.

The microstructural electro-chemo-mechanics at the catholyte/AM interfaces are also often overlooked. As in conventional cathodes, AM particles suffer mechanical deformation during ion insertion and removal.[102] While cycling, the expansion and contraction of these particles could stress the catholyte matrix inducing microcracks (see Figure B.5) or even worse, causing delamination at the interface, isolating particles from conduction channels.[102–105] These interfaces can also be electrochemically unstable, resulting in the formation of higher-impedance interphases.[99,103,106–110] To enable rechargeable SSBs with long cycle lives, it is necessary to understand and control the chemical and mechanical behavior of interfaces within composite electrodes. For that, finite element modelling can be used in conjunction with other methods such as the kinetic Monte Carlo methods which account for diffusion or cohesive-zone fracture methods to asses crack propagation. These models have qualitatively highlighted common trends that facilitate the design of solid-state composite cathodes. AM particle size was found to play a critical in the mechanical stability at the interfaces; smaller particles have greater surface area to volume ratios, lowering their compressive stress in the particles during cycling which enhances the electronic conduction channels.[111,112] Modelling have also indicated that elastically compliant SSEs, like sulfides for example, can be both helpful and damaging to interfaces. Sulfides are less prone to delamination at the composite cathode/electrolyte interface during particle contraction, because they deform more readily in response to volume changes in AM particles.[113] On the other hand, according to nonlinear kinematic modelling, they may be more prone to microcrack development during particle expansion due to their ability to accommodate bigger deformations.[104]

Upon observing the literature, it can be concluded that the effect of the different parameters discussed above on the cell performance varies a lot depending on the battery chemistry in question and there is no universal optimized particle size, catholyte content, etc. Nonetheless, evaluating the σ_i and σ_e of composite cathode is of utmost importance when evaluating a composite cathode.

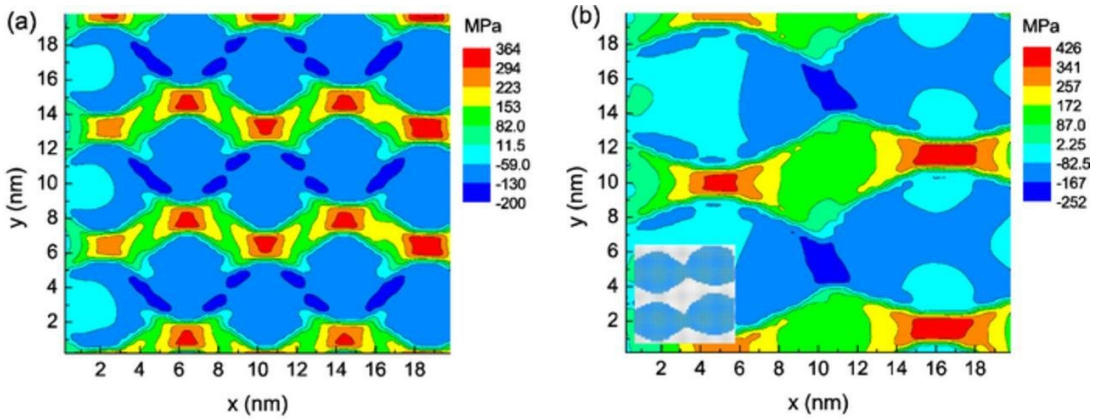

Figure B.5. Stress contour of the two systems after discharge: (a) the electrode particle of 4.7 nm and (b) the electrode particle of 9.2 nm. Reproduced with permission. [111] 2022, Journal of the Electrochemical Society.

Methods to calculate σ_i and σ_e

It has been established that an increase in the volumetric fraction of AM in composite cathodes is required to improve energy density. In today's SSBs, however, there has frequently been a trade-off between rate performance and AM ratio. This is most likely due to inefficient ionic conducting pathways in the composite rather than electronic conducting pathways. The intricacies of the rate limiting element, remain vague and unclear for researchers. As a result, quantitative analyses of the composite electrodes' ionic and electronic conductivities are required in order to develop advanced composite electrode designs with high AM content, high energy densities, and sufficient rate capability.

Researchers have recently reported using an AC impedance technique based on the transmission line model (TLM) to assess the ionic and electronic conductivities of composite cathodes. The electronic and ionic conductivities can both be measured using substrate/composite cathode/substrate configuration (ion blocking). Alternatively, DC polarization technique could be used but it requires the electron blocking configuration (SS/SSE/composite cathode/SSE/SS) as well as the ion blocking configuration to calculate σ_i and σ_e respectively.[114,115] The equivalent circuits for each configuration and the resulting impedance spectra are presented in Figure B.6. Falco et al. have reported on the most recent

models that use both AC impedance and DC polarization, explained the equivalent circuit of each and provided the equations for σ_i and σ_e extracted from these models[1] In a separate study, the σ_i and σ_e for NMC based composite cathodes formulated using LPS glass SSE as the catholyte were measured using both AC impedance and DC polarization techniques.[116] Conductivity values obtained from the two techniques were found to be similar. This finding implies that both DC and AC approaches may be used to assess electronic and ionic conductivities accurately. The electronic and ionic conductivities of the composite cathode were measured at state of charge (SOC) of 0% and 50%. The electronic conductivities were lower than the ionic conductivities before charging (SOC: 0%) but, at 50% SOC, on the other hand, electronic conductivities rose dramatically and eventually surpassed or equaled ion conductivities as theoretically expected. By examining the relationship between cell capacity and σ_i/σ_e, it was determined that the rate limiting element of the cells tested in this work was ionic conductivity in the cathodes. Furthermore, even in the charging state, both σ_i and σ_e of the composite electrode may be quantified. These findings indicate the usefulness of the conductivity measurements presented in this research, as well as the significance of identifying the rate limiting factor through the examination of the charged composite cathode's σ_i and σ_e. For NMC-LPS composite cathodes involved in this study, it was found that the composite with nearly identical ionic and electronic conductivities demonstrated the best rate performance while the theoretical energy density, on the other hand, is inversely proportional to the volume ratio of AM. Researchers must optimize the cathode composition in accordance with the desired performance. All in all, to achieve well-tailored composite cathodes, quantitative analyses of the conductivities of the composite electrodes for all-solid-state cells are critical.

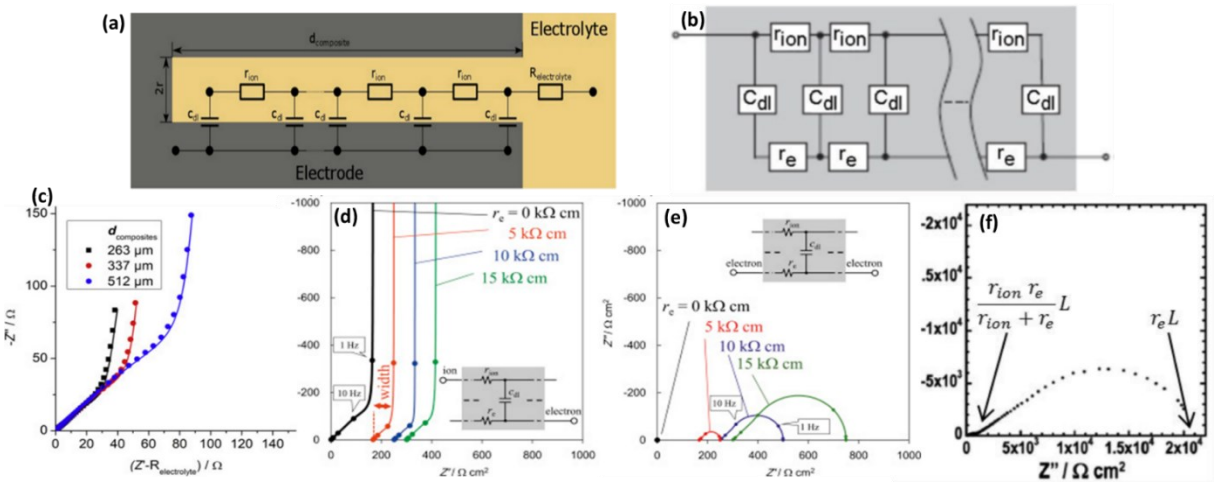

Figure B.6. a) TLM equivalent circuit for SS/CE/SE/CE/SS cells in the case of high b) and low. c) Simulation of the impedance spectra resulting from the TLM for high and (d) low σ_e. (e) Simulation of the impedance spectra for different values of r_{ion} and r_e. f) Nyquist plot of a SS/CE/SS for a CE consisting of NMC (48 % vol) and Li_3PS_4 (52 % vol) (here L stands for $d_{composite}$). Reproduced with permission. [114,115] 2022, Journal of Power Sources.[116] 2022, Journal of the Electrochemical Society.

Conclusion and outlook

All-solid-state batteries have drawn considerable attention as potential next-generation energy storage devices owing to their promises of higher energy density and better safer performances than the current state-of-the-art lithium ion batteries. However, developing low-cost, industrially scalable solid-state batteries with high energy density and stable cycling for large-scale energy storage and electric vehicle applications remains a daunting task especially in light of the large interfacial resistance arising from the insufficient solid-solid contact at cathode/electrolyte interface. Fundamentally, the absence of the fluidity characteristics of liquid electrolytes in SSB is to blame for the poor ionic conductivity in the cathode microstructure and the large impedances at the interface. Research efforts directed at understanding and minimizing the interfacial impedances are of critical importance at this stage in the advancement of the solid-state technology. To date, numerous interfacial modification techniques have been reported such as using composite cathodes, cathode active material coating, bi-layer electrolyte construction, intermediate coating, and thermal annealing.

In this mini-review, we reported and summarized the efforts surrounding the development of composite cathodes which are simply cathodes that employ ionic conductors as binders in addition to or instead of the conventional nonconductive binders (e.g. PVDF) that are currently used in LIBs cathodes. The fraction of ionic binders in composite cathodes is also

called '*the catholyte'*. Next, the different preparation techniques used to prepare composite cathodes such as solvent casting, extrusion, infiltration, in-situ polymerization, annealing and hot/cold pressing were briefly discussed. Despite the variety of the reported synthesis techniques, the ***solvent casting*** method, which is used to synthesize conventional cathodes, is still observed as the dominant technique reported for composite cathodes synthesis due to its cost efficiency and quick processability. Moreover, the parameters affecting the composite cathode structure at the micro-level were presented alongside a discussion of how they directly influence the electrochemical performance of SSBs. Namely, those are AM particle size, porosity, binder content and loading/thickness. There is no general guidelines established on those parameters that could be applied on different battery chemistry except for porosity which hinders the Li^+ transport in the cathode and thus, must always be minimized. However, sufficient ionic and electronic conductivities in the microstructure of composite cathodes are essential to achieve decent electrochemical performance in SSBs. AC Impedance and DC polarization using ion-blocking and electron blocking symmetrical cell configurations are the two most commonly used techniques to assess ionic and electronic conductivities.

To sum up, mechanical properties have a substantial impact on transport properties and consequently on, electrochemical performance. The microstructure is influenced by a number of elements, including the morphology of the starting materials, their compatibility and preparation methodology. Unfortunately, the optimization of the composite cathodes is often overlooked in favor of quick publishable findings. Typically, information related to composite cathodes are very briefly mentioned and the choice of the specific materials, loading or composition are seldom justified. Hence, It is recommended that full characterization of composite cathodes and detailed justification of its choice must be included in upcoming publications to help the research community better understand the interplay between the composite cathode microstructure and the overall SSBs properties and performance which will ultimately enable further rapid-paced advancements in the solid-state technology that will leap us closer to the new-era of green energy revolution.

Acknowledgements

We would like to thank Office of Energy Research and Development (OERD) at Natural Resources Canada for financial support.

References

[1] M. Falco, S. Ferrari, G. B. Appetecchi, C. Gerbaldi, *Mol. Syst. Des. Eng.* **2019**, *4*, 850.

[2] K. Ho Park, Q. Bai, D. Hyeon Kim, D. Yang Oh, Y. Zhu, Y. Mo, Y. Seok Jung, K. H. Park, D. H. Kim, D. Y. Oh, Y. S. Jung, Q. Bai, Y. Zhu, Y. Mo, *Adv. Energy Mater.* **2018**, *8*, 1800035.

[3] Y.-S. Hu, *Nat. Energy 2016 14* **2016**, *1*, 1.

[4] J. Cabana, B. J. Kwon, L. Hu, *Acc. Chem. Res.* **2018**, *51*, 299.

[5] M. J. Loveridge, G. Remy, N. Kourra, R. Genieser, A. Barai, M. J. Lain, Y. Guo, M. Amor-Segan, M. A. Williams, T. Amietszajew, M. Ellis, R. Bhagat, D. Greenwood, *Batter. 2018, Vol. 4, Page 3* **2018**, *4*, 3.

[6] "State-of-the-art specific energy of lithium-ion cells in academic research - Research Interfaces," accessed on January 23, 2022, https://researchinterfaces.com/state-of-the-art-specific-energy-of-lithium-ion-cells/.

[7] Y. Wang, W. D. Richards, S. P. Ong, L. J. Miara, J. C. Kim, Y. Mo, G. Ceder, *Nat. Mater. 2015 1410* **2015**, *14*, 1026.

[8] E. Stability of Li, F. Han, Y. Zhu, X. He, Y. Mo, C. Wang, F. Han, C. Wang, Y. Zhu, X. He, Y. Mo, *Adv. Energy Mater.* **2016**, *6*, 1501590.

[9] L. Xu, S. Tang, Y. Cheng, K. Wang, J. Liang, C. Liu, Y. C. Cao, F. Wei, L. Mai, Interfaces in Solid-State Lithium Batteries. *Joule* **2018**, *2*, 1991–2015.

[10] Y. Takeda, O. Yamamoto, N. Imanishi, *Electrochemistry* **2016**, *84*, 210.

[11] C. Yang, K. Fu, Y. Zhang, E. Hitz, L. Hu, C. Yang, K. Fu, Y. Zhang, E. Hitz, L. Hu, *Adv. Mater.* **2017**, *29*, 1701169.

[12] C. Monroe, J. Newman, *J. Electrochem. Soc.* **2005**, *152*, A396.

[13] M. Keller, A. Varzi, S. Passerini, *J. Power Sources* **2018**, *392*, 206.

[14] Z. Gadjourova, Y. G. Andreev, D. P. Tunstall, P. G. Bruce, *Nat. 2001 4126846* **2001**, *412*, 520.

[15] J. Mindemark, M. J. Lacey, T. Bowden, D. Brandell, *Prog. Polym. Sci.* **2018**, *81*, 114.

[16] M. Falco, S. Ferrari, … G. A.-M. S. D., undefined 2019, *pubs.rsc.org*.

[17] Y. Kato, S. Hori, T. Saito, K. Suzuki, M. Hirayama, A. Mitsui, M. Yonemura, H. Iba, R. Kanno, *Nat. Energy 2016 14* **2016**, *1*, 1.

[18] J. C. Bachman, S. Muy, A. Grimaud, H. H. Chang, N. Pour, S. F. Lux, O. Paschos, F. Maglia, S. Lupart, P. Lamp, L. Giordano, Y. Shao-Horn, Inorganic Solid-State Electrolytes for Lithium Batteries: Mechanisms and Properties Governing Ion

Conduction. *Chem. Rev.* **2016**, *116*, 140–162.

[19] C. Cao, Z. Bin Li, X. L. Wang, X. B. Zhao, W. Q. Han, *Front. Energy Res.* **2014**, *2*, 25.

[20] J. Schnell, T. Günther, T. Knoche, C. Vieider, L. Köhler, A. Just, M. Keller, S. Passerini, G. Reinhart, *J. Power Sources* **2018**, *382*, 160.

[21] Y. S. Jung, D. Y. Oh, Y. J. Nam, K. H. Park, *Isr. J. Chem.* **2015**, *55*, 472.

[22] D. T. Hallinan, I. Villaluenga, N. P. Balsara, *MRS Bull.* **2018**, *43*, 759.

[23] C. K. Chan, T. Yang, J. Mark Weller, *Electrochim. Acta* **2017**, *253*, 268.

[24] J. B. Goodenough, Y. Kim, *Chem. Mater.* **2009**, *22*, 587.

[25] K. Takada, *J. Power Sources* **2018**, *394*, 74.

[26] F. Zheng, M. Kotobuki, S. Song, M. O. Lai, L. Lu, *J. Power Sources* **2018**, *389*, 198.

[27] G. E. Blomgren, *J. Electrochem. Soc.* **2017**, *164*, A5019.

[28] K. Nie, Y. Hong, J. Qiu, Q. Li, X. Yu, H. Li, L. Chen, *Front. Chem.* **2018**, *6*, 616.

[29] Z. Ding, J. Li, J. Li, C. An, *J. Electrochem. Soc.* **2020**, *167*, 070541.

[30] F. Mizuno, A. Hayashi, K. Tadanaga, M. Tatsumisago, *J. Power Sources* **2005**, *146*, 711.

[31] M. He, Z. Cui, F. Han, X. Guo, *J. Alloys Compd.* **2018**, *762*, 157.

[32] W. Zha, Y. Xu, F. Chen, Q. Shen, L. Zhang, *Solid State Ionics* **2019**, *330*, 54.

[33] A. I. Pitillas Martinez, F. Aguesse, L. Otaegui, M. Schneider, A. Roters, A. Llordés, L. Buannic, *J. Phys. Chem. C* **2019**, *123*, 3270.

[34] C. Vinado, S. Wang, Y. He, X. Xiao, Y. Li, C. Wang, J. Yang, *J. Power Sources* **2018**, *396*, 824.

[35] X. Li, J. Liu, M. N. Banis, A. Lushington, R. Li, M. Cai, X. Sun, *Energy Environ. Sci.* **2014**, *7*, 768.

[36] S. Yubuchi, Y. Ito, T. Matsuyama, A. Hayashi, M. Tatsumisago, *Solid State Ionics* **2016**, *285*, 79.

[37] A. Sakuda, H. Kitaura, A. Hayashi, K. Tadanaga, M. Tatsumisago, *J. Electrochem. Soc.* **2008**, *156*, A27.

[38] J. E. Trevey, Y. S. Jung, S. H. Lee, *Electrochim. Acta* **2011**, *56*, 4243.

[39] Q. Zhang, J. P. Mwizerwa, H. Wan, L. Cai, X. Xu, X. Yao, *J. Mater. Chem. A* **2017**, *5*, 23919.

[40] K. H. Kim, Y. Iriyama, K. Yamamoto, S. Kumazaki, T. Asaka, K. Tanabe, C. A. J. Fisher, T. Hirayama, R. Murugan, Z. Ogumi, *J. Power Sources* **2011**, *196*, 764.

[41] T. Kato, T. Hamanaka, K. Yamamoto, T. Hirayama, F. Sagane, M. Motoyama, Y. Iriyama, *J. Power Sources* **2014**, *260*, 292.

[42] S. Ohta, S. Komagata, J. Seki, T. Saeki, S. Morishita, T. Asaoka, *J. Power Sources* **2013**,

238, 53.

[43] B. Liu, K. Fu, Y. Gong, C. Yang, Y. Yao, Y. Wang, C. Wang, Y. Kuang, G. Pastel, H. Xie, E. D. Wachsman, L. Hu, *Nano Lett.* **2017**, *17*, 4917.

[44] E. A. Il'ina, K. V. Druzhinin, N. S. Saetova, B. D. Antonov, V. I. Pryakhina, *Electrochim. Acta* **2018**, *285*, 326.

[45] M. B. Dixit, A. Parejiya, N. Muralidharan, R. Essehli, R. Amin, I. Belharouak, *Energy Storage Mater.* **2021**, *40*, 239.

[46] S. N. Patel, *ACS Macro Lett.* **2021**, *10*, 141.

[47] K. J. Kim, J. L. M. Rupp, *Energy Environ. Sci.* **2020**, *13*, 4930.

[48] J. Zhang, X. Zang, H. Wen, T. Dong, J. Chai, Y. Li, B. Chen, J. Zhao, S. Dong, J. Ma, L. Yue, Z. Liu, X. Guo, G. Cui, L. Chen, *J. Mater. Chem. A* **2017**, *5*, 4940.

[49] J. H. Choi, C. H. Lee, J. H. Yu, C. H. Doh, S. M. Lee, *J. Power Sources* **2015**, *274*, 458.

[50] M. Wetjen, G. T. Kim, M. Joost, G. B. Appetecchi, M. Winter, S. Passerini, *J. Power Sources* **2014**, *246*, 846.

[51] P. López-Aranguren, X. Judez, M. Chakir, M. Armand, L. Buannic, *J. Electrochem. Soc.* **2020**, *167*, 020548.

[52] H. Al-Salih, A. Huang, C.-H. Yim, A. I. Freytag, G. R. Goward, E. Baranova, Y. Abu-Lebdeh, *J. Electrochem. Soc.* **2020**, *167*, 070557.

[53] X. Zhang, T. Liu, S. Zhang, X. Huang, B. Xu, Y. Lin, B. Xu, L. Li, C. W. Nan, Y. Shen, *J. Am. Chem. Soc.* **2017**, *139*, 13779.

[54] R. J. Chen, Y. B. Zhang, T. Liu, B. Q. Xu, Y. H. Lin, C. W. Nan, Y. Shen, *ACS Appl. Mater. Interfaces* **2017**, *9*, 9654.

[55] Y. C. Jung, M. S. Park, C. H. Doh, D. W. Kim, *Electrochim. Acta* **2016**, *218*, 271.

[56] F. Chen, W. Zha, D. Yang, S. Cao, Q. Shen, L. Zhang, D. R. Sadoway, *J. Electrochem. Soc.* **2018**, *165*, A3558.

[57] B. Zhang, L. Chen, J. Hu, Y. Liu, Y. Liu, Q. Feng, G. Zhu, L. Z. Fan, *J. Power Sources* **2019**, *442*, 227230.

[58] W. Zha, F. Chen, D. Yang, Q. Shen, L. Zhang, *J. Power Sources* **2018**, *397*, 87.

[59] Z. Wan, D. Lei, W. Yang, C. Liu, K. Shi, X. Hao, L. Shen, W. Lv, B. Li, Q. H. Yang, F. Kang, Y. B. He, *Adv. Funct. Mater.* **2019**, *29*, 1805301.

[60] J. Hu, P. He, B. Zhang, B. Wang, L. Z. Fan, *Energy Storage Mater.* **2020**, *26*, 283.

[61] K. Liu, Y. Liu, D. Lin, A. Pei, Y. Cui, *Sci. Adv.* **2018**, *4*.

[62] F. Han, J. Yue, C. Chen, N. Zhao, X. Fan, Z. Ma, T. Gao, F. Wang, X. Guo, C. Wang, *Joule* **2018**, *2*, 497.

[63] T. Liu, Y. Ren, Y. Shen, S. X. Zhao, Y. Lin, C. W. Nan, *J. Power Sources* **2016**, *324*, 349.

[64] M. Shoji, H. Munakata, K. Kanamura, *Front. Energy Res.* **2016**, *4*, 32.

[65] S. Ohta, J. Seki, Y. Yagi, Y. Kihira, T. Tani, T. Asaoka, *J. Power Sources* **2014**, *265*, 40.

[66] K. Park, B. C. Yu, J. W. Jung, Y. Li, W. Zhou, H. Gao, S. Son, J. B. Goodenough, *Chem. Mater.* **2016**, *28*, 8051.

[67] C. L. Tsai, Q. Ma, C. Dellen, S. Lobe, F. Vondahlen, A. Windmüller, D. Grüner, H. Zheng, S. Uhlenbruck, M. Finsterbusch, F. Tietz, D. Fattakhova-Rohlfing, H. P. Buchkremer, O. Guillon, *Sustain. Energy Fuels* **2018**, *3*, 280.

[68] C. Xin, K. Wen, C. Xue, S. Wang, Y. Liang, X. Wu, L. Li, C.-W. Nan, *Batter. Supercaps* **2021**.

[69] J. Zhang, N. Zhao, M. Zhang, Y. Li, P. K. Chu, X. Guo, Z. Di, X. Wang, H. Li, *Nano Energy* **2016**, *28*, 447.

[70] V. T. Luu, Q. H. Nguyen, M. G. Park, H. L. Nguyen, M.-H. Seo, S.-K. Jeong, N. Cho, Y.-W. Lee, Y. Cho, S. N. Lim, Y.-S. Jun, W. Ahn, *J. Mater. Res. Technol.* **2021**, *15*, 5849.

[71] I. Aldalur, H. Zhang, M. Piszcz, U. Oteo, L. M. Rodriguez-Martinez, D. Shanmukaraj, T. Rojo, M. Armand, *J. Power Sources* **2017**, *347*, 37.

[72] Y.-C. Jung, S.-M. Lee, J.-H. Choi, S. S. Jang, D.-W. Kim, *J. Electrochem. Soc.* **2015**, *162*, A704.

[73] H. Zeng, X. Ji, F. Tsai, Q. Zhang, T. Jiang, R. K. Y. Li, H. Shi, S. Luan, D. Shi, *Solid State Ionics* **2018**, *320*, 92.

[74] F. Chen, D. Yang, W. Zha, B. Zhu, Y. Zhang, J. Li, Y. Gu, Q. Shen, L. Zhang, D. R. Sadoway, *Electrochim. Acta* **2017**, *258*, 1106.

[75] W. He, Z. Cui, X. Liu, Y. Cui, J. Chai, X. Zhou, Z. Liu, G. Cui, *Electrochim. Acta* **2017**, *225*, 151.

[76] X. Yang, Q. Sun, C. Zhao, X. Gao, K. R. Adair, Y. Liu, J. Luo, X. Lin, J. Liang, H. Huang, L. Zhang, R. Yang, S. Lu, R. Li, X. Sun, *Nano Energy* **2019**, *61*, 567.

[77] G. B. Appetecchi, J. Hassoun, B. Scrosati, F. Croce, F. Cassel, M. Salomon, *J. Power Sources* **2003**, *124*, 246.

[78] J. Chai, Z. Liu, J. Ma, J. Wang, X. Liu, H. Liu, J. Zhang, G. Cui, L. J. Chen Chai, Z. Liu, J. Ma, J. Wang, H. Liu, J. Zhang, G. Cui, J. Chai, X. Liu, L. Chen, *Adv. Sci.* **2017**, *4*, 1600377.

[79] W. Zhou, Z. Wang, Y. Pu, Y. Li, S. Xin, X. Li, J. Chen, J. B. Goodenough, W. Zhou, Y.

Pu, J. Chen, Z. Wang, X. Li, Y. Li, S. Xin, B. Goodenough, *Adv. Mater.* **2019**, *31*, 1805574.

[80] Z. Zhang, Y. Zhao, S. Chen, D. Xie, X. Yao, P. Cui, X. Xu, *J. Mater. Chem. A* **2017**, *5*, 16984.

[81] D. H. Kim, D. Y. Oh, K. H. Park, Y. E. Choi, Y. J. Nam, H. A. Lee, S. M. Lee, Y. S. Jung, *Nano Lett.* **2017**, *17*, 3013.

[82] M. Yamamoto, Y. Terauchi, A. Sakuda, M. Takahashi, *Sci. Reports 2018 81* **2018**, *8*, 1.

[83] B. Chen, Z. Huang, X. Chen, Y. Zhao, Q. Xu, P. Long, S. Chen, X. Xu, *Electrochim. Acta* **2016**, *210*, 905.

[84] Y. Zhao, Z. Huang, S. Chen, B. Chen, J. Yang, Q. Zhang, F. Ding, Y. Chen, X. Xu, *Solid State Ionics* **2016**, *295*, 65.

[85] X. Zhang, S. Wang, C. Xue, C. Xin, Y. Lin, Y. Shen, L. Li, C. W. Nan, *Adv. Mater.* **2019**, *31*, 1806082.

[86] G. B. Appetecchi, M. Carewska, F. Alessandrini, P. P. Prosini, S. Passerini, *J. Electrochem. Soc.* **2000**, *147*, 451.

[87] W. D. Kingery, M. D. Narasimhan, *J. Appl. Phys.* **2004**, *30*, 307.

[88] N. C. Rosero-Navarro, K. Tadanaga, *Solid Electrolytes Adv. Appl. Garnets Compet.* **2019**, 111.

[89] L. Bai, W. Xue, Y. Li, X. Liu, Y. Li, J. Sun, *Ceram. Int.* **2018**, *44*, 7319.

[90] A. Bielefeld, D. A. Weber, J. Janek, *ACS Appl. Mater. Interfaces* **2020**, *12*, 12821.

[91] M. Finsterbusch, T. Danner, C. L. Tsai, S. Uhlenbruck, A. Latz, O. Guillon, *ACS Appl. Mater. Interfaces* **2018**, *10*, 22329.

[92] Y. Kato, S. Shiotani, K. Morita, K. Suzuki, M. Hirayama, R. Kanno, *J. Phys. Chem. Lett.* **2018**, *9*, 607.

[93] B. Tjaden, D. J. L. Brett, P. R. Shearing, *https://doi.org/10.1080/09506608.2016.1249995* **2016**, *63*, 47.

[94] L. Froboese, J. F. van der Sichel, T. Loellhoeffel, L. Helmers, A. Kwade, *J. Electrochem. Soc.* **2019**, *166*, A318.

[95] J. Landesfeind, J. Hattendorff, A. Ehrl, W. A. Wall, H. A. Gasteiger, *J. Electrochem. Soc.* **2016**, *163*, A1373.

[96] J. Landesfeind, M. Ebner, A. Eldiven, V. Wood, H. A. Gasteiger, *J. Electrochem. Soc.* **2018**, *165*, A469.

[97] B. L. Trembacki, A. N. Mistry, D. R. Noble, M. E. Ferraro, P. P. Mukherjee, S. A. Roberts, *J. Electrochem. Soc.* **2018**, *165*, E725.

[98] L. Almar, J. Joos, A. Weber, E. Ivers-Tiffée, *J. Power Sources* **2019**, *427*, 1.

[99] W. Zhang, D. A. Weber, H. Weigand, T. Arlt, I. Manke, D. Schröder, R. Koerver, T. Leichtweiss, P. Hartmann, W. G. Zeier, J. Janek, *ACS Appl. Mater. Interfaces* **2017**, *9*, 17835.

[100] M. Singh, J. Kaiser, H. Hahn, *J. Electroanal. Chem.* **2016**, *782*, 245.

[101] F. Strauss, T. Bartsch, L. De Biasi, A. Y. Kim, J. Janek, P. Hartmann, T. Brezesinski, *ACS Energy Lett.* **2018**, *3*, 992.

[102] J. A. Lewis, J. Tippens, F. J. Q. Cortes, M. T. McDowell, *Trends Chem.* **2019**, *1*, 845.

[103] R. Koerver, I. Aygün, T. Leichtweiß, C. Dietrich, W. Zhang, J. O. Binder, P. Hartmann, W. G. Zeier, J. Janek, *Chem. Mater.* **2017**, *29*, 5574.

[104] G. Bucci, T. Swamy, Y. M. Chiang, W. C. Carter, *J. Mater. Chem. A* **2017**, *5*, 19422.

[105] W. Zhang, D. Schröder, T. Arlt, I. Manke, R. Koerver, R. Pinedo, D. A. Weber, J. Sann, W. G. Zeier, J. Janek, *J. Mater. Chem. A* **2017**, *5*, 9929.

[106] W. Zhang, F. H. Richter, S. P. Culver, T. Leichtweiss, J. G. Lozano, C. Dietrich, P. G. Bruce, W. G. Zeier, J. Janek, *ACS Appl. Mater. Interfaces* **2018**, *10*, 22226.

[107] C. Hänsel, S. Afyon, J. L. M. Rupp, *Nanoscale* **2016**, *8*, 18412.

[108] J. Auvergniot, A. Cassel, J. B. Ledeuil, V. Viallet, V. Seznec, R. Dedryvère, *Chem. Mater.* **2017**, *29*, 3883.

[109] A. Sakuda, A. Hayashi, M. Tatsumisago, *Chem. Mater.* **2009**, *22*, 949.

[110] R. Koerver, F. Walther, I. Aygün, J. Sann, C. Dietrich, W. G. Zeier, J. Janek, *J. Mater. Chem. A* **2017**, *5*, 22750.

[111] F. Hao, P. P. Mukherjee, *J. Electrochem. Soc.* **2018**, *165*, A1857.

[112] A. Bielefeld, D. A. Weber, J. Janek, *J. Phys. Chem. C* **2018**, *123*, 1626.

[113] G. Bucci, B. Talamini, A. Renuka Balakrishna, Y. M. Chiang, W. C. Carter, *Phys. Rev. Mater.* **2018**, *2*, 105407.

[114] Z. Siroma, T. Sato, T. Takeuchi, R. Nagai, A. Ota, T. Ioroi, *J. Power Sources* **2016**, *316*, 215.

[115] N. Kaiser, S. Spannenberger, M. Schmitt, M. Cronau, Y. Kato, B. Roling, *J. Power Sources* **2018**, *396*, 175.

[116] T. Asano, S. Yubuchi, A. Sakuda, A. Hayashi, M. Tatsumisago, *J. Electrochem. Soc.* **2017**, *164*, A3960.

Hilal Al-Salih received his Bachelor of Applied Science degree at the American University of Sharjah (U.A.E). Since 2018, he is working towards his Ph. D. at the University of Ottawa and the National Research Council of Canada (NRC) under the co-supervision of Dr. Elena Baranova and Dr. Yaser Abu-Lebdeh. His doctoral thesis focuses on developing novel composite solid-state electrolytes and on engineering the cathode/electrolyte interface within solid-state batteries.

Mohamed Houache received his Ph.D. in Chemical and Biological Engineering at the University of Ottawa in 2020. His current position is a research officer (Postdoc) at the National Research Council Canada (NRC). His research interests focus on Li-ion battery technology and beyond along with electrocatalysis for energy conversion and environmental technologies. Prior to joining NRC, he worked as a post-doctoral researcher leading a joint project between the Gbatteries and the University of Ottawa

Elena Baranova is a Full Professor in the Department of Chemical and Biological Engineering at the University of Ottawa. She received her Ph.D. from École Polytechnique Fédérale de Lausanne (EPFL) in 2005. She was an NSERC post-doctoral fellow with the National Research Council (NRC), Canada before joining UOttawa in 2008. Her field of research is Electrochemical Engineering and Catalysis. Dr. Baranova has authored over 130 publications, three book chapters and one US patent. She is an Executive Editor of the Journal of Chemical Technology and Biotechnology (JCTB, Wiley) and a Co-Director of Nexus for Quantum Technologies (NEXQT) Institute at UOttawa.

Yaser Abu-Lebdeh is a Senior Research Officer and Leader of the Battery Materials Innovation Team at the National Research Council of Canada in Ottawa. His research focuses on improving the performance and safety of existing and next generation materials for lithium batteries. He earned his Ph. D. in Electrochemistry from the University Of Southampton (UK), his Master's degree in Material Science from the University of Manchester (UK) and his bachelor's degree in Industrial Chemistry from Jordan University of Science and Technology. Before joining the NRC as an NSERC postdoctoral fellow he was a postdoctoral research fellow at the University of Montreal

Appendix C: Aqueous and Solid electrolyte electrochemical stability comparison

Figure C. 1: Comparison of the electrochemical stability window obtained through linear sweep voltammetry between (a) optimized aqueous electrolyte from chapter 3. (b) optimized solid-state electrolyte from chapter 4

(a)

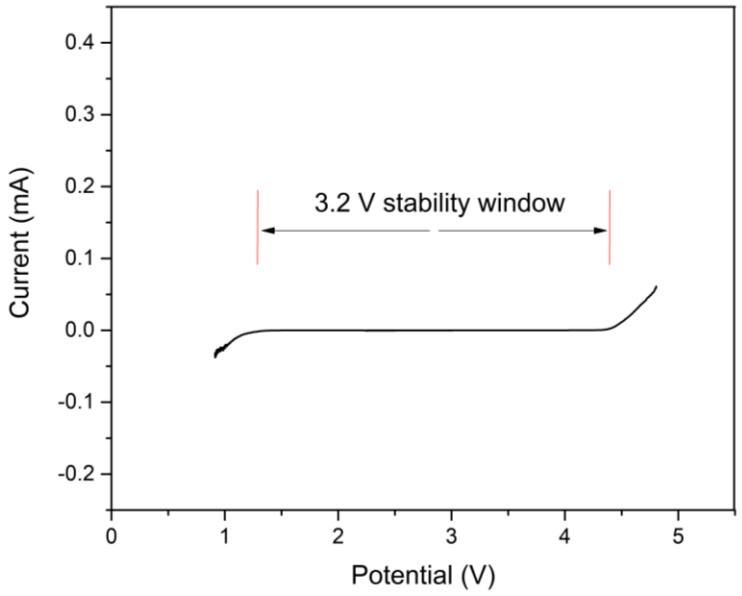

(b)

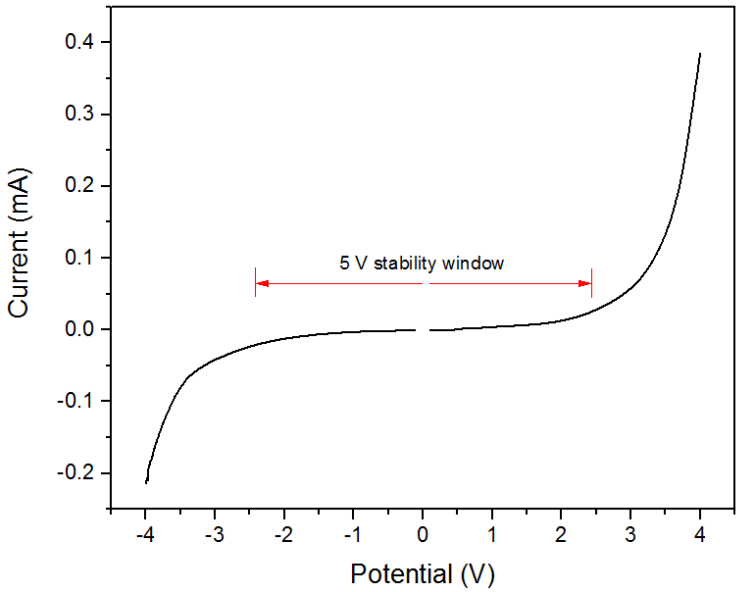

Appendix D: List of publications and conference participations

Published:

[1] **Hilal Al-Salih,** Mohamed Houache, Elena Baranova, Yaser Abu-Lebdeh, "Composite Cathodes for Solid-State Lithium Batteries:“Catholytes” the Underrated Giants", Advanced Energy and Sustainability Research, **2022,** 202200032.

[2] **Hilal Al-Salih**, Mengyang Cui, Chae-Ho Yim, Zoya Sadighi, Shuo Yan, Zouina Karkar Gillian R. Goward, Elena A. Baranova, Yaser Abu-Lebdeh "A ceramic rich quaternary composite solid-state electrolyte for solid-state lithium metal batteries", *J. Electrochem. Soc.* **2022.**

[3] **Hilal Al-Salih**, Allan Huang, Chae-Ho Yim, Annica I Freytag, Gillian R Goward, Elena Baranova, Yaser Abu-Lebdeh, "A Polymer-Rich Quaternary Composite Solid Electrolyte for Lithium Batteries", *J. Electrochem. Soc.* **2020**, *167*

[4] S. Yan, **H. Al-Salih**, C.-H. Yim, A. Merati, E. Baranova, A. Weck, Y. Abu-Lebdeh, "Engineered Interfaces between Perovskite La2/3xli3xtio3 Electrolyte and Li Metal for Solid-State Batteries", Frontiers in Chemistry. **2022,** 74.

submitted:

[5] **Hilal Al-Salih,** Elena Baranova, Yaser Abu-Lebdeh, " Connecting microstructure and ionic conductivity in aqueous electrolyte solutions: Towards a phenomenological structural and empirical conductivity model inspired by solid-liquid phase diagrams ", **2023,**

Conference participations:

[1] Syed Bukhari, Felix Selz, Runqi Wu, **Hilal Al-Salih**, Lingzi Sang, Yaser Abu-Lebdeh, and Mike Fleischauer "Platform for liquid, solid, and hybrid electrolyte characterization at controlled temperatures and pressures", **poster presentation**, Calgary, *CSC 2022*

[2] **Hilal Al-Salih**, Mohamed Houache, Elena Baranova, Yaser Abu-Lebdeh, "Exploring the Interplay between Composite Cathode Design and Cell Performance for Solid-State Lithium Batteries", **oral presentation**, Vancouver, *ECS 241st meeting*

[3] **Hilal Al-Salih**, Allan Huang, Chae-Ho Yim, Annica Freytag, Gillian Goward, Elena Baranova, Yaser Abu-Lebdeh, "High Performance Quaternary Solid Composite Electrolyte for Safe all-Solid Lithium Batteries", **poster presentation**. *virtual*, *CCCE 2021*

[4] **Hilal Al-Salih,** Chae-Ho Yim, Svetlana Niketic, Annica Freytag, Gillian R Goward, Elena A Baranova, Yaser Abu- Lebdeh, " A Novel Quaternary Composite Solid State Electrolyte for Li Batteries", **oral presentation**, Montreal, *ECS 237th meeting* (abstract accepted but meeting cancelled due to COVID-19 outbreak)